Towards quantum degenerate atomic Fermi mixtures

Thomas Salez

To cite this version:

Thomas Salez. Towards quantum degenerate atomic Fermi mixtures. Atomic Physics [physics.atom-ph]. Ecole Normale Supérieure de Paris - ENS Paris, 2011. English. NNT : 0309BRU00388 . tel-00636899v1

HAL Id: tel-00636899
https://theses.hal.science/tel-00636899v1

Submitted on 28 Oct 2011 (v1), last revised 10 Jan 2012 (v3)

ÉCOLE NORMALE SUPÉRIEURE
LABORATOIRE KASTLER BROSSEL

THÈSE DE DOCTORAT DE L'UNIVERSITÉ PARIS VI

Spécialité : Physique Quantique

présentée par

Thomas SALEZ[†]

Pour obtenir le grade de
Docteur de l'Université Pierre et Marie Curie (Paris VI)

Towards quantum degenerate atomic Fermi mixtures

Soutenue le mardi 27 septembre 2011
devant le jury composé de :

Philippe BOUYER	Rapporteur
Frédéric CHEVY	Membre Invité
Noël DIMARCQ	Président du Jury
Robin KAISER	Examinateur
Lev KHAYKOVICH	Examinateur
Hélène PERRIN	Rapportrice
Christophe SALOMON	Directeur de Thèse

[†] E-mail: thomas.salez@gmail.com

"I therefore believe it's true that with a suitable class of quantum machines you could imitate any quantum system, including the physical world."

Richard P. Feynman [1]

Synopsis

Au cours de ce travail de doctorat, j'ai participé au montage complet d'une expérience visant à refroidir et manipuler deux espèces atomiques alcalines fermioniques, ^{6}Li et ^{40}K. Le dispositif expérimental a pour objectifs l'étude des mélanges de fermions ultra-froids de masses différentes et la réalisation d'un simulateur analogique quantique flexible. En effet, là où certains problèmes quantiques à N corps en interaction, comme la supraconductivité à haute température critique ou l'antiferromagnétisme frustré, sont difficiles à aborder analytiquement et numériquement, les atomes froids, systèmes purs et contrôlables jusque dans leur interaction, offrent un point de vue complémentaire intéressant.

Lors de la conception du dispositif expérimental, nous avons assemblé une enceinte à ultra-vide, réalisé un système laser stabilisé complet pour chaque espèce et mis en place deux sources atomiques performantes, un ralentisseur Zeeman de ^{6}Li et un piège magnéto-optique bidimensionnel de ^{40}K; la plupart des grandeurs optiques et électriques ainsi que les diagnostiques d'imagerie étant contrôlés par voie informatique. Ces premières étapes ont permis l'obtention d'un piège magnéto-optique à deux espèces performant, contenant typiquement 5×10^9 atomes de ^{6}Li et 8×10^9 atomes de ^{40}K. Dans cette configuration, nous avons produit les premières molécules hétéronucléaires de $^6\mathrm{Li}^{40}\mathrm{K}^*$ par photoassociation, pour lesquelles nous avons observé et identifié 70 raies rovibrationnelles.

Dans une seconde partie, je décris en détail le transport magnétique du mélange atomique entre la cellule du piège magnéto-optique et une cellule d'expérience, où règne un vide poussé et bénéficiant d'un grand accès optique. Ce dispositif complet, de sa conception à son optimisation expérimentale, en passant par son assemblage mécanique et la mise en place du programme de contrôle et des diagnostiques numériques, constitue le coeur de mon travail. Son efficacité a pu être testée et optimisée, permettant ainsi un transfert performant du mélange vers la cellule finale.

Aussi, à l'issue de cette thèse, tous les outils sont opérationnels pour poursuivre le refroidissement du mélange par évaporation dans un piège magnétique, et par conséquent le champ est ouvert pour la simulation quantique et la compréhension de problèmes à N corps dans les mélanges de gaz de Fermi ultra-froids.

Abstract

During my PhD, I participated in the full setup from scratch of an experiment that aims at cooling down and manipulating two fermionic alkaline atomic species, ^{6}Li and ^{40}K. Our goal is to study ultracold Fermi mixtures with mass imbalance, and to realize a flexible quantum analog simulator. In fact, for certain quantum many-body problems, such as high critical temperature superconductivity and frustrated anti-ferromagnetism, there is neither complete analytical nor numerical solution. Therefore, cold atoms systems, due to their purity and their high degree of tunability, even on their interaction itself, offer an interesting complementary point of view in the study of those phenomena.

As far as the experimental setup is concerned, we built an ultra-high vacuum system, a complete and stable laser source for each species, as well as two performing atomic sources, a ^{6}Li Zeeman slower and a ^{40}K bidimensionnal magneto-optical trap; most of the optical and electrical quantities, as well as the imaging diagnostics, being computer controlled. Once those preliminary steps have been performed and optimized, we could obtain an efficient double magneto-optical trap, containing typically 5×10^{9} atoms of ^{6}Li and 8×10^{9} atoms of ^{40}K. In this configuration, we produced the first $^{6}\mathrm{Li}^{40}\mathrm{K}^{*}$ heteronuclear molecules by photoassociation, for which we identified 70 rovibrational lines.

In a second part, I describe in detail the magnetic transport of the atomic mixture, between the magneto-optical trap chamber and a science cell, located in an ultra-high vacuum region with large optical access. The complete setup, from its design to its experimental implementation and optimization, as well as the development of the program and the useful numerical diagnostics, are the heart of my work. The transport efficiency could be tested and optimized, allowing for an efficient transfer of the mixture in the science cell.

Thus, after this thesis, all the experimental tools are operational in order to allow for evaporative cooling of the mixture in an optically plugged magnetic trap. Therefore, the field is open for quantum simulation and understanding of many-body problems in ultracold Fermi mixtures.

Acknowledgments

Before starting, I would like to thank Philippe Bouyer, Noël Dimarcq, Robin Kaiser, Lev Khaykovich and Héléne Perrin, for having accepted to be in my thesis committee and for their useful remarks about the present dissertation.

This thesis work would not have been possible without the help of several persons that I want to thank here.

First, I would like to thank my supervisor Christophe Salomon for having welcomed me in his group, for having shared with me his great knowledge of experimental physics as well as for his talent in leading our team with strong optimism. I will always remember the time-spreading discussions we had about new physics and exciting prospects, as well as the moments he would come spontaneously in the lab in order to work with us on the experiment. Almost each time he suggested something, we finally realized he was right from the beginning.

Equivalently, I would like to thank my second supervisor Frédéric Chevy for is day-to-day help and his original teaching. He came almost everyday to the lab in order to help us, to give us precious pieces of advice and to work on the main program. We could also discuss with him about any subject in physics: his knowledge in general physics and his critical mind are uncommon. All along my PhD, I was amazed by his capability to put any given problem in simple equations in a short laps of time and thus to succeed in the extraction of a key piece of information for the experiment.

Then, I would like to thank my colleague and friend Armin Ridinger. It was a wonderful scientific and human adventure to build this new experiment together. I learned a lot from him, especially from his scientific rigor and his relentlessness in any aspect of the work, including the very choice of the laser names, but also from his unique soft skills. Above all, I really appreciated his open-minded attitude regarding cultural novelty.

I would like to thank as well Saptarishi Chaudhuri, who spent two years with us as a post-doctoral fellow. He brought his great experimental skills and performed a major work in the lab. Apart from his obvious talent in physics, what characterizes him the most is certainly his manner to do everything like a true gentleman, with such an incredible calm and such a wise indian philosophy that he could perfectly manage the young and excited PhD students we were. We should never change a working system.

Now, let me thank David Wilkowski, who spent a year in the team as a visitor, for his help in the lab in building performing 2D MOT and optical systems, and for the good mood he created in the team. Thanks a lot to Ulrich Eismann as well, for his help on the lithium table, his fine remarks, his skills in Catia, and for having shared the office with us. I would love to be a Berliner due to his influence. I also thank Kilvia Magalhães, post-doc of the early days, who helped me to build the first laser source and the first spectroscopic diagnostic of the experiment.

Then, I would like to thank the new dream team: Diogo Fernandes, Franz Sievers and Norman Kretzschmar, for brilliantly taking over and for the great help during transport debugging. I wish them to get several beautiful team results, and above all to have fun with our system. In the meantime, I thank Colin Parker who visited us during the last summer and who managed to solve smartly several issues in the experimental sequence. Many thanks also to the Fermix trainees: Eric Vernier, Cheng Zhang and Alexis Jouan, for their very useful jobs.

Jumping back to the early days, I wish to thank warmly David Guéry-Odelin for having nicely supervised me during my master's internship. I also thank his team, with whom we shared the office in P9: Gaël Reinaudi, Antoine Couvert, Gianluca Gattobigio, Tomasz Kawalec, Renaud Mathevet and Matthew Jeppesen. Thanks a lot for the good atmosphere of work.

The mechanical engineering part of my work could never be performed alone. Therefore, many thanks to the excellent workshop team: Jean-Michel Isac, José Romer, Richard Pescari, Michel Quidu, Saysavanh Souramasing, Thierry Bastien, Pascal Travers, Cyril Le Gallo, David Le Gallo, Georges Cornudet, Florence Tibou, Jack Olejnik, Nabil Garroum, Stefano Lun Kwong Leon, Jean-Claude Paindorge, as well as the others and the trainees.

I also thank the workshop of electronics, for the same reasons: Bernard Trégon, Lionel Pérennès, Toufik El Atmani, Denis Jaggi, Christophe Herrmann et Laurent Bonnet. Besides, I would like to thank the electricians for their support through high power issues: Franck Bouchereau, Jean-Marc Jusseau, Philippe Rousseau. I thank as well the computer engineers: Francis Hulin-Hubard, Christophe Bonnet, Frédéric Ayrault, Zaïre Dissi and Alain Launay, for having quickly solved my questions about networks and coding.

Naturally, I would like to thank the other teams of the laboratory for the scientific and friendly interactions we had, and for the borrowed components they never gave back to us, or the other way around: Tarik Yefsah, Clément Sayrin, Nir Navon, Andrew Grier, Trong Canh Nguyen, Juliette Simonet, Sylvain Nascimbène, Kenneth Maussang, Roger Gehr, Fabrice Gerbier, Félix Werner, Jérôme Beugnon, Sanjukta Roy, David Jacob, Luigi De Sarlo, Patrick Rath, Leticia Tarruel, Kaijun Jiang, Kenneth Günter, Rémi Desbuquois, Benno Rem, Igor Ferrier-Barbut, François Parmentier, Adrien Mahé...

This adventure was also a great human experience due to the wonderful administrative teams from LKB, IFRAF and the physics department. Therefore, thanks a lot to Linda Krikorian and Christophe Bernard for their help and their kindness as well as Dominique Giafferi, Thierry Tardieu, Pascale René-Kerber, Françoise David, France Lamette, Françoise Tarquis, Viviane Tia, Monique Granon, Emmanuelle André and Anne-France Seyer.

Let me thank also people from the Formation Interuniversitaire de Physique at ENS for having given me the opportunity to work in parallel as a teacher and for the new projects they helped me to build. I particularly thank my colleagues Jean-François Allemand, Antonin Marchand and Jean Hare, with whom I interacted a lot around analytical mechanics, as well as Xing Xing Zhou for the experimental project about Bell inequalities. I also thank the administrative team: Marie-Françoise Ducos,

Mascia Reato and Marie Bernabé, for their helpful and kind support. Finally, I thank my students for their interest and their rewarding questions, as well as my own teachers for having brought into being my passion for science.

I give a special thank to my two classmates and friends Vincent Ardourel and Bruno Deremble, for the numerous discussions we had during lunch break. They were the sunbeam in my basement lab.

Last but not least, I would like to thank a lot Florence Koch for being so exceptional, and for having accepted to share her life with me, as well as our two wonderful families; with a special mention for my brothers and my parents for being there, and for the freedom mind they embody. I am so lucky to have you.

Contents

Synopsis **5**

Abstract **7**

Acknowledgments **9**

Introduction **17**

I. Quantum degenerate gases 19
II. ^{6}Li-^{40}K experiments in the world 21
III. Outline of the dissertation 22

1 Experimental setup **25**

- 1.1 Vacuum system 26
  - 1.1.1 Description 26
  - 1.1.2 Assembly and baking 27
  - 1.1.3 Differential pumping 28
- 1.2 Optics 30
  - 1.2.1 General description 30
  - 1.2.2 Laser diode 33
  - 1.2.3 Frequency lock 33
  - 1.2.4 Tapered amplifier 35
- 1.3 ^{6}Li Zeeman slower 36
  - 1.3.1 Principle 37
  - 1.3.2 Magnetic profile 39
  - 1.3.3 Stability 41
  - 1.3.4 Jet divergence 43
  - 1.3.5 Atomic flux and efficiency 44
  - 1.3.6 Oven and vacuum 46
  - 1.3.7 Coils 48
  - 1.3.8 Laser beam 51
- 1.4 ^{40}K 2D magneto-optical trap 52
  - 1.4.1 Description 53
  - 1.4.2 Vacuum and pressure 54
  - 1.4.3 Laser system 55
  - 1.4.4 Atomic jet 56
- 1.5 Computer control 58
- 1.6 Summary 60

2 Magneto-optical trap **61**
- 2.1 Principle . . . 62
  - 2.1.1 Doppler cooling . . . 62
  - 2.1.2 Zeeman trapping . . . 62
  - 2.1.3 Total force . . . 63
  - 2.1.4 Doppler temperature . . . 65
  - 2.1.5 Light rescattering . . . 66
  - 2.1.6 Phase-space density . . . 67
  - 2.1.7 Capture velocity and trap depth . . . 67
- 2.2 Imaging and analysis . . . 67
  - 2.2.1 Fluorescence imaging . . . 67
  - 2.2.2 Absorption imaging . . . 69
  - 2.2.3 Analysis . . . 72
- 2.3 Experimental characterization . . . 74
  - 2.3.1 Practical aspects . . . 74
  - 2.3.2 Optimized parameters . . . 75
  - 2.3.3 Dark magneto-optical trap . . . 78
  - 2.3.4 Trap losses and lifetime . . . 81
  - 2.3.5 Double ^{6}Li-^{40}K magneto-optical trap . . . 83
- 2.4 Molecular photoassociation . . . 83
  - 2.4.1 Principle and setup . . . 85
  - 2.4.2 Theoretical aspects . . . 88
  - 2.4.3 Results . . . 89
- 2.5 Summary . . . 92

3 Magnetic trap **93**
- 3.1 Principle . . . 94
  - 3.1.1 Trapping potential . . . 94
  - 3.1.2 Majorana losses . . . 96
  - 3.1.3 Spin-relaxation . . . 97
- 3.2 Preliminary stages . . . 97
  - 3.2.1 Compressed magneto-optical trap . . . 98
  - 3.2.2 Cold magneto-optical trap . . . 99
  - 3.2.3 Optical pumping . . . 99
- 3.3 Experimental characterization . . . 103
  - 3.3.1 Technical overview . . . 103
  - 3.3.2 Atomic cloud properties . . . 104
  - 3.3.3 ^{40}K p-wave cross-section . . . 106
  - 3.3.4 Trap depth and gravity . . . 107
  - 3.3.5 Lifetime . . . 107
- 3.4 Next stages . . . 108
  - 3.4.1 Final quadrupole trap . . . 109
  - 3.4.2 Optically plugged magnetic trap . . . 110
  - 3.4.3 Evaporative cooling . . . 110
  - 3.4.4 Optical dipole trap . . . 111
  - 3.4.5 Feshbach coils . . . 115

3.4.6 High resolution imaging 116
3.5 Summary 118

4 Magnetic transport: design **119**
4.1 Statics 120
4.1.1 Algorithm 120
4.1.2 Injection 121
4.1.3 Elbow 122
4.1.4 Outcoupling 122
4.2 Atomic cloud properties 123
4.2.1 Adiabatic evolution 123
4.2.2 Size and temperature 124
4.3 Dynamics 128
4.3.1 Inertia 129
4.3.2 Adiabaticity 131
4.3.3 Trap trajectory 132
4.4 Results and checking 134
4.4.1 Currents 134
4.4.2 Checking the constraints 135
4.4.3 Numerical simulation of a default 135
4.4.4 Trap depth and gravity 138
4.5 Engineering 138
4.5.1 Mechanics and winding 139
4.5.2 Power supplies 141
4.5.3 Cooling system 142
4.5.4 Diagnostics and security 144
4.5.5 Logics 144
4.5.6 Computer control 148
4.6 Summary 149

5 Magnetic transport : characterization **151**
5.1 Hardware and software 152
5.1.1 Magnetic field 152
5.1.2 Currents 153
5.2 Dynamics 153
5.2.1 Injection 155
5.2.2 Inertia 155
5.2.3 Adiabaticity 156
5.3 Trap depth 157
5.3.1 Round-trip experiment 157
5.3.2 Truncation on the tube 160
5.3.3 Evaporative cooling in the tube 167
5.3.4 Longitudinal trap depth 168
5.4 Final results and evaporative cooling 169
5.4.1 Final results 171
5.4.2 Starting evaporative cooling 171

5.5 Summary 173

Conclusion **175**

A Appendix **177**
A.1 Atomic data 177
A.2 Magnetic field of a current loop 179
A.3 Transport routine 180
A.4 Adiabatic invariant of the quadrupole trap 181
A.5 Mechanical parameters of the transport 182
A.6 Engineering drawings 183

Bibliography **191**

Introduction

Quantum many body physics is an active research topic, since it generates rich and spectacular effects that are still difficult to understand. One commonly illustrates this through some puzzling condensed matter phenomena, such as high critical temperature superconductors, quantum Hall effect or frustrated Néel anti-ferromagnetism, but other exciting fields of physics involve those strongly interacting N-body systems as well; for instance, the quarks-gluons plasma in nuclear physics [2], or the neutron stars in astrophysics.

However, in spite of the numerous simplified hamiltonian models that have been developed along the years, those problems remain difficult to handle analytically and numerically. Therefore, in the early eighties, Richard Feynman suggested to develop a quantum analog simulator, in order to simulate the associated phenomena [1]. Such an apparatus would consist of an experimental system whose behavior would be controlled by the same hamiltonian as the one of interest, and whose parameters could be finely adjusted. Thus, similarly to the principle of classical analog simulators, that existed before our actual programmable computers (see Figure 1), the solution could be directly observed without any calculation.

Due to their high degree of purity, control, imaging and tunability, ultracold atomic systems have been proposed as a relevant choice for the creation of such a simulator [3]. For instance, it is already feasible to simulate Hubbard-like hamiltonians using ultracold atoms in optical lattices, as already demonstrated through the Mott insulator transition [4, 5]. In fact, focusing on fermions, such an hamiltonian is given by the expression:

$$H = -t \sum_{\langle i,\ j\rangle,\sigma} (c^{\dagger}_{i,\sigma} c_{j,\sigma} + c^{\dagger}_{j,\sigma} c_{i,\sigma}) + U \sum_{i} n_{i,\uparrow} n_{i,\downarrow} \ , \tag{1}$$

where t describes the tunneling between two neighboring sites, U quantifies the interaction on a given site, $c^{\dagger}_{i,\sigma}$ and $c_{i,\sigma}$ are the creation and annihilation operators on site i with spin σ, and $n_{i,\sigma} = c^{\dagger}_{i,\sigma} c_{i,\sigma}$ is the number operator on site i with spin σ. Therefore, this hamiltonian can be simulated by placing ultracold atoms in an optical lattice (see Figure 2), created by a stationary laser wave.

In the following, we recall the recent progresses in the field of ultracold quantum gases, before focusing on the particular topic of fermionic mixtures. Then, we give an overview of the existing experiments in the world that combine the ^{6}Li and ^{40}K fermions. Finally, we present the outline of this dissertation.

Figure 1: *An example of classical analog simulator: the astronomical clock of Notre Dame de Strasbourg. Built in the fourteenth century, this device simulates the motion of planets in the solar system.*

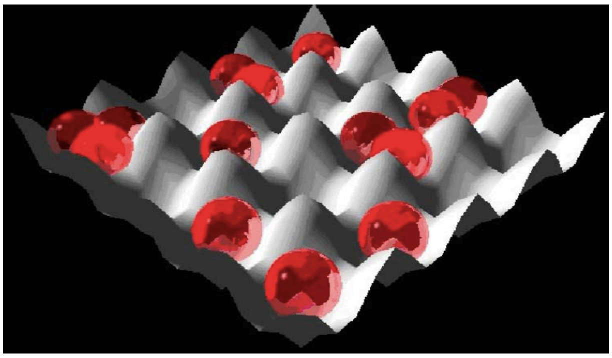

Figure 2: *An example of quantum analog simulator: the Hubbard simulator. Using cold atoms in an optical lattice, it simulates the Hubbard model (see equation 1).*

I. Quantum degenerate gases

A cold neutral atomic gas of density n can be described by two characteristic lengths. First, the classical average distance between two particles $n^{-1/3}$. Secondly, the quantum thermal de Broglie wavelength $\lambda_{\mathrm{dB}} = h/\sqrt{2\pi m k_{\mathrm{B}} T}$, where m is the atomic mass and T the temperature of the gas. This length represents the average size of the atomic wave function. At very low temperatures, when those quantities become of the same order, one can no longer distinguish two identical atoms. Depending on the atomic intrinsic angular momentum, the spin, nature allows two different kind of particles in 3D space. Bosons, of integer spin, obey Bose-Einstein statistics and tend to occupy the same fundamental state at ultra-low temperature. Thus, they form a single coherent macroscopic wave-function: the Bose-Einstein Condensate (BEC). Fermions, of half-integer spin, obey Fermi-Dirac statistics and can not occupy the same state according to Pauli's exclusion principle. At ultra-low temperature, they populate the energy states by order of increasing energy until the Fermi energy E_{F}, forming the so-called Fermi sea.

Bose-Einstein condensation

Bose-Einstein condensation was predicted for an ideal gas, by Satyendranath Bose [6] and Albert Einstein [7]. It was first observed experimentally through superfluidity of ^{4}He in 1938 [8]. This phase-transition was then observed for quasi-ideal gases in 1995 [9, 10, 11]. Afterwards, several major results were obtained and confirmed the coherence and the superfluidity of a BEC. Let us mention, for instance, the matter wave interferences [12], the observation of vortices [13] as well as dark and bright solitons [14, 15], the Mott insulator transition [4], and the Anderson localization of matter waves [16, 17]. Moreover, Feshbach resonances [18] that allow to change the scattering length a, or equivalently the s-wave elastic cross-section $\sigma = 4\pi a^2$, were observed in a BEC [19], opening the way to the study and control of interactions at ultra-low temperatures, as well as the formation of molecular bound states.

Degenerate Fermi gases

In contrast with the Bose-Einstein condensation in 3D, there is no phase transition for an ideal Fermi gas. It is degenerate when its temperature becomes lower than the Fermi temperature $T_{\mathrm{F}} = E_{\mathrm{F}}/k_{\mathrm{B}}$. The first degenerate quasi-ideal Fermi gas was observed in 1999 [20]. The reason why it was achieved after the BEC is due to its more complex cooling procedure. In fact, according to Pauli's exclusion principle, the s-wave collisions are suppressed for undistinguishable fermions. Moreover, the collisions with higher momentum orders, such as p-wave collisions, reduce drastically with temperature, since more and more states are occupied below the Fermi energy. This mechanism is known as Pauli blocking and was nicely observed in [21]. Both effects tend to suppress the collisions, and thus the crucial thermalization in the evaporative cooling process. A solution was to cool down the fermions in two distinguishable spin states [20]. Sympathetic cooling of fermions by evaporatively cooled bosons was demonstrated as well [22]. The characterization of ideal Fermi gases continued with

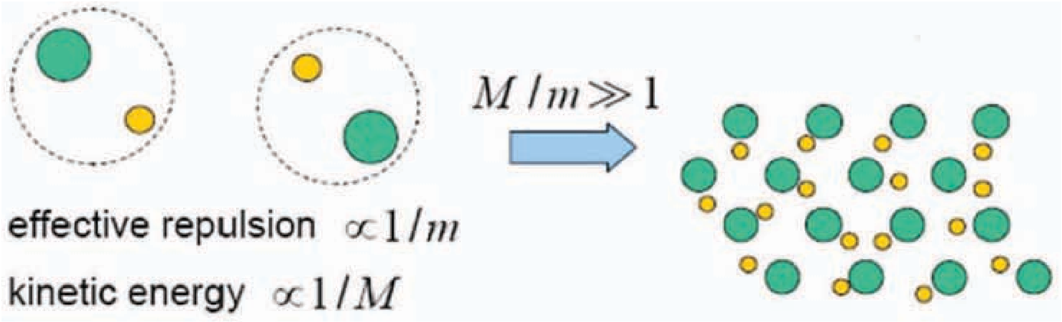

Figure 3: *Weakly bound molecules of heavy and light fermionic atoms were theoretically demonstrated to be characterized by a long-range intermolecular repulsion and to undergo a gas-crystal quantum transition if the mass ratio exceeds a critical value [49].*

the observation of Fermi pressure [23], for instance.

In presence of attractive interactions, fermions can form bosonic pairs and undergo a BEC phase transition as well. This was observed for the first time in 1911 through superconductivity of mercury [24], which was then explained by the Cooper pairing and the BCS theory of superconductors [25]. In 1972, the same mechanism was observed through superfluidity of ^{3}He [26]. Interacting Fermi gases were studied as well, using Feshbach resonances [18]. Long-lived weakly-bound molecules were created [27, 28, 29, 30, 31], which allowed to create the first molecular BEC [27, 32, 33]. Then, the first Fermi superfluids were observed [34, 35, 36], and the superfluid character was demonstrated through the observation of vortices [37]. The cross-over between those two phases was explored [36, 38]. Recent studies allowed to measure the velocity of sound in a Fermi gas [39], and the critical velocity for a superfluid flow across the BEC-BCS crossover [40]. A fermionic Mott insulator was also created in an optical lattice [5, 41], and a direct measurement of the equation of state of a strongly interacting Fermi gas was obtained [42, 43], opening the way to thermodynamical studies of ultracold gases.

Ultracold Fermi mixtures

The study of ultracold Fermi mixtures started with spin population imbalance and the observation of the associated phase separation [44, 45]. Mixtures of fermions with different masses are also of interest in the understanding of pairing mechanisms, due to their resulting unmatched Fermi surfaces. New exotic quantum phases, such as the Fulde-Ferrell-Larkin-Ovchinnikov (FFLO) phase [46, 47], or the breached pair phase [48], have been predicted theoretically but have not been observed so far. A Wigner-type crystalline phase transition (see Figure 3) has been predicted as well [49]. Optical lattices and species-specific potentials could allow to study disorder and Anderson localization [50], or mixed dimensions physics [51]. Furthermore, another exciting topic is the formation of ultracold polar molecules [52, 53]. They are of interest in the study of ultracold dipolar gases, where the long-range interaction would allow for new quantum phases as well.

II. ^{6}Li-^{40}K experiments in the world

^{6}Li and ^{40}K are the favorite candidates in the study of Fermi mixtures with mass imbalance, since they are the only stable alkali fermionic isotopes, and since the associated heteronuclear molecules have a large dipolar moment in their ground-state [54]. At the time of this thesis, four other groups in the world are studying ultracold Fermi mixtures: the group of Kai Dieckman in Singapore [55], the group of Jook Walraven in Amsterdam [56], the group of Rudolf Grimm in Innsbruck [57], and the group of Martin Zwierlein in Boston [58]. In each case, this is performed with the particular ^{6}Li and ^{40}K species, demonstrating the interest of such a mixture. So far, quantum degeneracy has been observed with typically 10^5 atoms of each species at a fraction of T_{F} [59, 57, 58], interspecies Feshbach resonances have been identified [60, 61], weakly-bound molecules have been produced by magnetoassociation [62], and a strongly interacting Fermi mixture has been characterized [63]. While designing our experiment, we had interesting discussions with people from these groups, and it was useful to study and compare their strategies. Here are the main characteristics of those experiments.

The Singapore group studies a triple mixture of ^{6}Li, ^{40}K and ^{87}Rb. The atomic sources are a Zeeman slower of ^{6}Li, and a vapor for ^{40}K and ^{87}Rb. They allow to load a MOT containing 3.2×10^7 atoms of ^{6}Li, 1.5×10^7 atoms of ^{40}K and 5.4×10^9 atoms of ^{87}Rb. Then, after a triple magnetic trap stage, the mixture is magnetically transferred towards a ultra-high vacuum chamber, where it is loaded into a Ioffe-Pritchard magnetic trap. There, the bosonic ^{87}Rb is cooled down further by evaporation, leading to sympathetic cooling of the fermions ^{6}Li and ^{40}K.

The Amsterdam group studies a mixture of ^{6}Li and ^{40}K. The double MOT is loaded from two single-species 2D-MOTs. It contains 3×10^9 atoms of ^{6}Li, and 2×10^9 atoms of ^{40}K. In the same chamber, the cloud is then transferred into an optically plugged magnetic trap in which evaporative cooling of ^{40}K in three spin states is performed, leading to sympathetic cooling of ^{6}Li. Finally, the mixture is optically transferred towards an ultra high vacuum region.

The Innsbruck group studies a mixture of ^{6}Li and ^{40}K. The experiment allows to add a third species, ^{87}Sr, as well. The MOT is loaded from a single Zeeman slower for all the species. It contains 10^9 atoms of ^{6}Li, and 10^7 atoms of ^{40}K. Then, in the same chamber, the cloud is transferred into an optical dipole trap, where it is cooled down by evaporative cooling of ^{6}Li in two spin states, and by sympathetic cooling of ^{40}K.

The Boston group studies a triple mixture of ^{6}Li, ^{40}K and ^{41}K. The MOT is loaded from a ^{6}Li Zeeman slower and a potassium Zeeman slower. It contains 10^9 atoms of ^{6}Li, and 5×10^7 atoms of ^{40}K. The cloud is transferred into an optically plugged magnetic trap, where evaporative cooling is performed on the bosonic ^{41}K, leading to sympathetic cooling of the fermions ^{6}Li and ^{40}K.

Our group, in Paris, studies a double mixture of ^{6}Li and ^{40}K. The double MOT is loaded from a ^{6}Li Zeeman slower and a ^{40}K 2D-MOT. It contains 5×10^9 atoms of ^{6}Li, and 8×10^9 atoms of ^{40}K. Then, the cloud is transferred into a magnetic trap before being magnetically transported towards a ultra-high vacuum chamber. There, it is transferred into an optically plugged magnetic trap, where evaporative cooling will be started and pursued in an optical trap. A possible strategy of evaporative cooling relies on evaporation of ^{40}K in two spin states, and sympathetic cooling of ^{6}Li. However, our system is flexible and we could explore other possibilities as well.

III. Outline of the dissertation

During this thesis, we designed and assembled from scratch the complete experimental setup that allows to produce, control and study ultracold atomic Fermi mixtures of ^{6}Li and ^{40}K. (see Figure 4). The main goal of our design was to produce a degenerate fermionic mixture with large atom numbers, in order to reach a high Fermi temperature, which allows to observe quantum behaviors at higher temperature, and to have a large signal-to-noise ratio. Moreover, this allows to have a high flexibility in the evaporative cooling process and a versatility in the studied phenomena.

Figure 4: *The lab at the beginning (left), and at the end of my PhD (right).*

The outline of this dissertation follows the natural chronology of a cooled atomic gas, from a hot vapor to its evaporative cooling in an optically plugged magnetic trap. In chapter 1, we describe the experimental setup, including the ultra-high vacuum chamber, the optics and the atomic sources. In chapter 2, we present our large double ^{6}Li-^{40}K magneto-optical trap, including the imaging device and the recent photoassociation of ^{40}K^{40}K* and ^{6}Li^{40}K* molecules. In chapter 3, we describe the magnetic trap, as well as its preliminary stages. We also give an overview of the next steps: evaporative cooling in an optically plugged magnetic trap, optical dipole trapping and high resolution imaging. In chapter 4, we present the design of the magnetic transport from a theoretical point of view. We characterize it experimentally in chapter 5.

Chapter 1 - Experimental Setup

We describe our ultra-high vacuum chamber, with a residual pressure inferior to 10^{-11} mbar in the final cell. Then, we present a powerful laser system giving typical powers of 500 mW for each species, at several stabilized frequencies, as well as two performing atomic sources: a ^{6}Li Zeeman slower and a ^{40}K 2D-MOT, with respective MOT loading rates of 1.2×10^9 atoms.s^{-1} and 1.4×10^9 atoms.s^{-1}.

Chapter 2 - Magneto-optical trap

After recalling the principles and limits of magneto-optical trapping of neutral atoms, we focus on our performing single-species and double-species MOTs of ^{6}Li-^{40}K, as well as the imaging diagnostics. In single species operation, we obtain 8.9×10^9 ^{40}K atoms at a temperature of 290 μK with a central density of 3×10^{10} atoms.cm^{-3}, and 5.4×10^9 ^{6}Li atoms at a temperature of 1.4 mK with a central density of 2×10^{10} atoms.cm^{-3}. In double species operation, we obtain 8×10^9 atoms of ^{40}K and 5×10^9 atoms of ^{6}Li. Those values are optimized by reducing the inelastic losses through a Dark MOT scheme. Then, we present the the first photoassociation of homonuclear ^{40}K^{40}K* and heteronuclear ^{6}Li^{40}K* molecules.

Chapter 3 - Magnetic trap

We present the magnetic trapping, from its principle and loss mechanisms to its experimental characterization. After compression and spin-polarization of the cloud, we load the magnetic trap, with an axial magnetic gradient of 85 G.cm^{-1}, and we obtain typically 10^9 atoms of each species, after 1 s of trapping. The temperatures are 400 μK for ^{40}K, and 1.3 mK for ^{6}Li. The design of the forthcoming stages are described as well. They consist of an optically plugged magnetic trap in the science cell and an optical dipole trap, where quantum degeneracy will be reached by evaporative and sympathetic coolings. In addition, we present our high-resolution imaging scheme involving a 404 nm ^{40}K transition.

Chapter 4 - Magnetic transport: theoretical aspects and engineering

We designed, assembled an studied a complete magnetic transport system allowing to move the magnetically trapped cloud to a region of ultra-high vacuum, and large optical access. In this chapter, we focus first on the theoretical aspects, such as the static algorithm that allows to control the shape of the trap at a given position of its center, and the dynamical issues linked to Majorana losses, adiabaticity, and inertia. Then, we describe the engineering part, through the mechanics, the winding, the logics, the security and the computer control.

Chapter 5 - Magnetic transport: experimental characterization

We present the experimental characterization of magnetic transport. The normalized full efficiency is calculated, measured and optimized to expected values of 80 % for ^{40}K, and 30 % for ^{6}Li. In addition, the lifetime is measured to be 30 s in the science cell. Finally, we show that our results enable evaporative cooling for ^{40}K in one single spin state, and sympathetic cooling of ^{6}Li.

Chapter 1

Experimental setup

During this thesis, we have built from scratch a complete system of production, control and study of ultra-cold atomic Fermi mixtures of ^{6}Li and ^{40}K. The main objective was to allow for large atomic numbers in the quantum degenerate regime. In order to achieve this, a special care has been taken on comparing the existing techniques and choosing the more relevant for our system. As detailed in the introduction of this dissertation, four similar experiments in the world study ultracold atomic Fermi mixtures with ^{6}Li and ^{40}K [55, 56, 57, 58].

In this chapter, we describe successively the vacuum assembly, the optics, the two atomic sources, ^{40}K 2D-MOT and ^{6}Li Zeeman slower, and the computer control. We present both the design aspects and the experimental characterization.

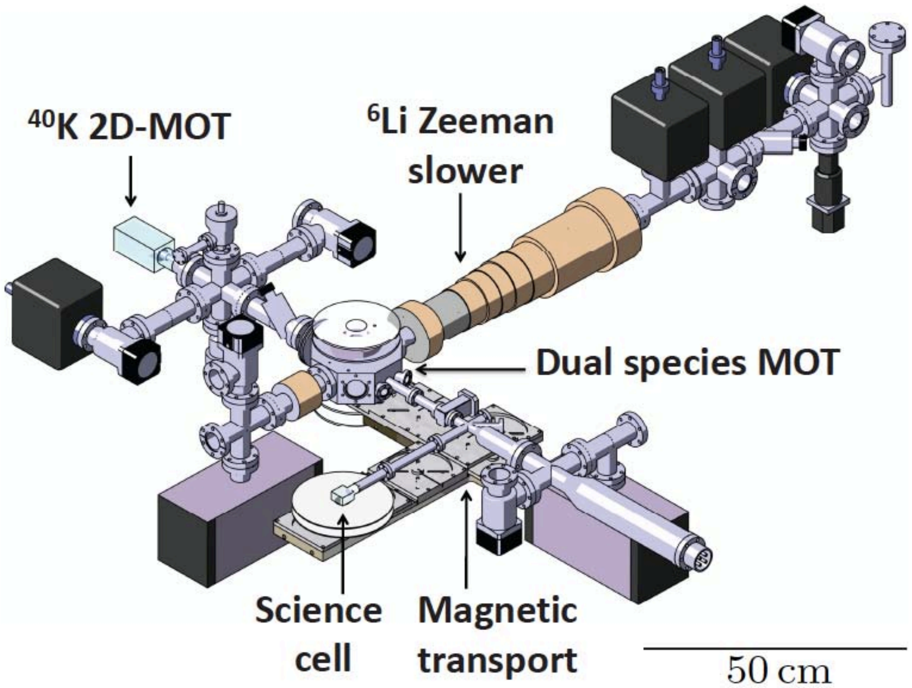

Figure 1.1: *Schematics of the vacuum assembly (see also Figure 1.2). The dual-species MOT is loaded from a 2D-MOT for* ^{40}K *and a Zeeman slower for* ^{6}Li*. A magnetic transport allows to transfer the cloud to a UHV science cell with large optical access.*

1.1 Vacuum system

This section is dedicated to the description of the vacuum chamber, from its design and assembly to its baking out, in order to create an ultra-high vacuum environment.

1.1.1 Description

A three-dimensional Catia view of the vacuum system and a picture of the experimental setup are shown in Figures 1.1 and 1.2. The vacuum manifold consists of two trap chambers and three flux regions, essentially made from MDC-Caburn vacuum elements. The first trap chamber is a central octagonal cell (see engineering drawing in appendix A.6) where the ^{6}Li-^{40}K dual-species MOT is prepared. The second chamber is a glass science cell (see engineering drawing in appendix A.6), in which we will evaporatively cool the mixture down to quantum degeneracy.

The three flux regions are all connected to the octagonal chamber and are divided in two parts: first, the atom sources, namely a 2D-MOT for ^{40}K and a Zeeman slower for ^{6}Li; secondly, a magnetic transport connecting the octagonal chamber to the final science cell. The magnetic transport consists of a spatially fixed assembly of magnetic coils which creates a moving trapping potential of constant shape by applying time-varying currents, as explained in chapter 4.

The octagonal chamber can be isolated from the source regions and the science cell by all-metal UHV valves, which allow for separate baking and trouble-shooting. The

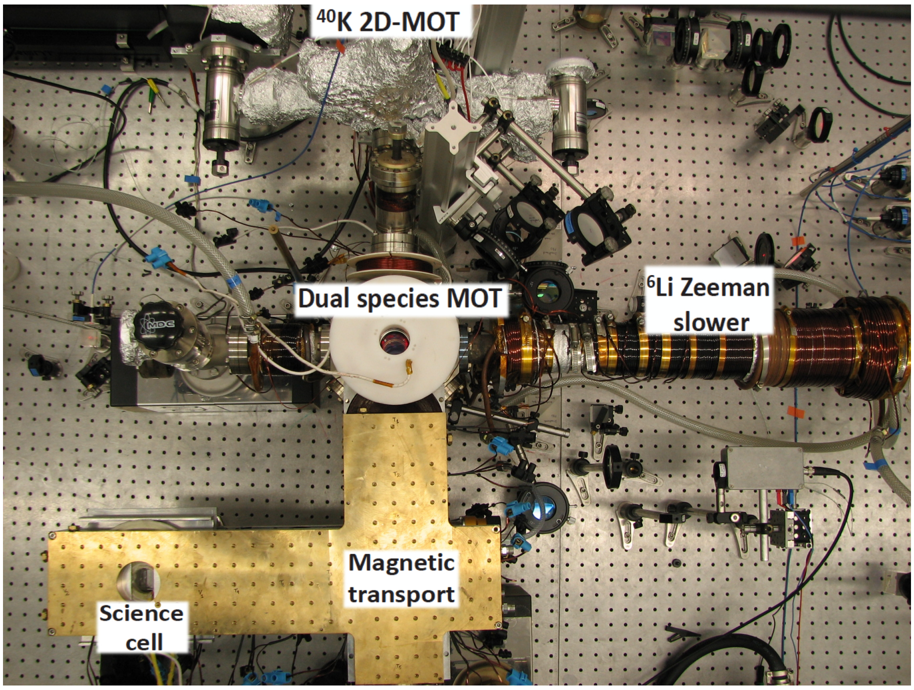

Figure 1.2: *Picture of the experimental setup from top (see also Figure 1.1).*

2D-MOT and the Zeeman slower regions are pumped by one and three 20 L.s^{-1} Varian ion pumps, respectively. The octagonal chamber is pumped by a 40 L.s^{-1} Varian ion pump and the science chamber by a 40 L.s^{-1} Varian ion pump and a Varian titanium sublimation pump. Two differential pumping tubes connect the two source regions to the octagonal chamber, in order to create a high vacuum environment in the octagonal cell. In a similar way, the science chamber is connected to the octagonal chamber via a combination of standard DN16 and DN10 vacuum tubes to further increase the vacuum quality, as explained in part 1.1.3.

The Hellma glass science cell benefits from a large optical access. It is made of fused silica dioxide (Vycor). Its thickness is constant and equals 4 mm, with a 10 μm precision. Apart from a DN 16 flange, a metal-to-glass adapter and a glass tube, it consists of a rectangular parallelepiped of $23 \times 23 \times 10$ mm^3 inner volume (see Figure 1.3 and engineering drawing in appendix A.6). Hellma guarantees a maximal deformation of 770 nm between the center and the edges of the windows, due to the 1 bar difference of pressure.

1.1.2 Assembly and baking

We mounted the vacuum chamber as explained in the following. First, we cleaned up the dirty components with acetone in an ultrasonic bath before baking them in an oven. Then, wearing clean latex gloves we assembled all the parts using copper gaskets and making sure that no couple of force was applied to the gaskets. We installed a turbomolecular pump as well as a Residual Gas Analyzer (RGA), after a dedicated valve in order to remove them once the baking procedure is over. Then, we ran the

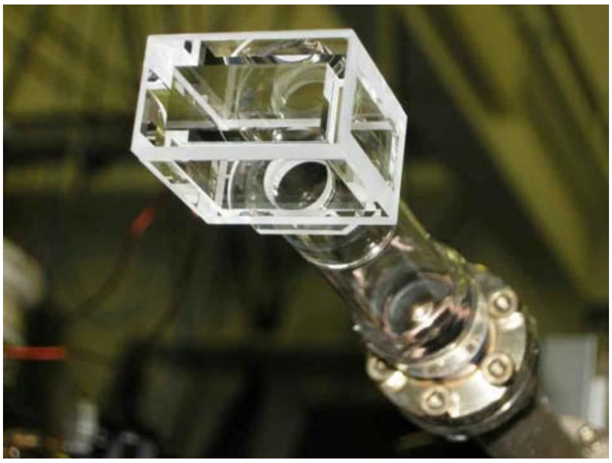

Figure 1.3: *Picture of the Hellma science cell connected to a standard DN16 tube. It consists of a rectangular parallelepiped of* $23 \times 23 \times 10$ *mm*^{3} *inner volume.*

turbomolecular pump during a few hours before starting the baking, while recording the partial pressures for different molecular masses.

The principle of baking is the following. First, we placed thermocouples (Hanna SFILS1) on key points such as valves and chambers. Then, we wrapped the complete vacuum system with some resistive heater tape connected to AC transformers (Variacs), and we covered the whole with aluminum foils, including the ion pumps. We then ramped up the voltage slowly, in order to ensure a smooth heating of the chamber to prevent the view-ports and other fragile elements from breaking. We reached 250° C after a day. There, we waited two days before launching the titanium sublimation pump during two hours. Then, we switched this pump off and launched the ion pumps. We stayed in this configuration during an additional week. Finally, we ramped the heating down to zero over a day. At room temperature of 22°C, the RGA indicated a total residual pressure of 10^{-10} mbar in the region of the octagonal chamber. We finally disconnected the RGA and the turbomolecular pump using the associated valve.

1.1.3 Differential pumping

Collisions of trapped atoms with background impurities limit the lifetime in a trap. Therefore, we now estimate the background pressure in the final science cell. For this purpose, let us introduce a simple model of gas conductance in a channel by analogy to Ohm's law in electricity:

$$Q = C\Delta P \ ,$$

where Q is the PV-flux, C is the channel conductance and ΔP is the difference of pressure along the channel. In the balistic regime, the conductance C (expressed in L.s^{-1}) of a cylindrical channel of length L and diameter D (expressed in cm) is given by the expression [64]:

$$C \approx 2.6 \times 10^{-4} \frac{D^3}{L} < v > \ , \tag{1.1}$$

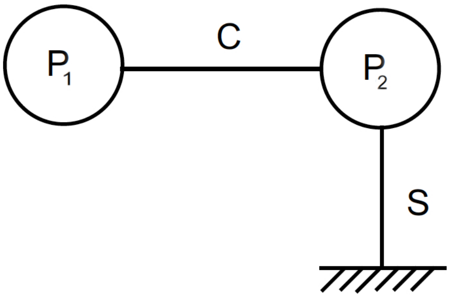

Figure 1.4: *Schematics of the differential pumping of the science cell. P_1 is the MOT pressure, P_2 is the pressure in the science cell, C is the conductance of the tube between the MOT chamber and the pump located at the elbow, and S is the effective pumping speed at the elbow.*

where $< v >= \sqrt{8k_\mathrm{B}T/\pi m}$ is the average atomic speed (expressed in cm.s^{-1}) in the considered gas (usually air) of atoms with mass m. Using this electrical analogy we can describe the differential pumping between the MOT and the science cell as a pressure divider (see Figure 1.4). P_1 is the MOT pressure. Since the transport pump is located at the elbow, we assume that there is no flow in the second arm of the transport, that is between the elbow and the science cell, as for an electrical resistor with one unconnected extremity. This hypothesis is valid if the outgasing speed of the second arm walls is negligible compared to the effective pumping speed of the pump. In this model, the pressure P_2 at the elbow is the same as the one in the science cell. We describe the elbow pump as a pressure ground ($P = 0$) connected to the elbow through a conductance S, where S is the effective pumping speed at the elbow which takes into account the commercial one $S_\mathrm{p} = 40$ L.s^{-1} in series with the conductance C_p of the tee connector of the pump:

$$S = \frac{C_\mathrm{p} S_\mathrm{p}}{C_\mathrm{p} + S_\mathrm{p}} \ , \tag{1.2}$$

where $C_\mathrm{p} \approx 34$ L.s^{-1}, for background air thermalized with the walls at room temperature of 22°C, using our real dimensions: $D = 3.8$ cm and $L = 19.7$ cm in equation 1.1. Thus, we find $S \approx 18$ L.s^{-1}. We can now estimate the pressure ratio as follows:

$$\frac{P_2}{P_1} = \frac{C}{S + C} \ .$$

Using three consecutive tubes of respectively 1.6 cm, 1 cm and 1.6 cm diameters, and 4.7 cm, 15.6 cm and 7.6 cm lengths, we can estimate this ratio to be 3.4 %, leading to a final pressure of $P_2 = 3.4 \times 10^{-12}$ mbar, with $P_1 = 1 \times 10^{-10}$ mbar (see part 1.1.2). Note that replacing the differential pumping tube (the second tube, with diameter 1 cm) by a standard DN16 one would have increased this final pressure by a factor 2.6.

The collision rate involving background impurities is proportional to the background density and thus to the pressure. Therefore, the lifetime in a trap due to collisions with background impurities is proportional to the inverse of the background pressure. As detailed in parts 3.3.5 and 5.4.1, we measured a lifetime of 3 s for the magnetic trap in the octagonal chamber (see Figure 3.10), and a lifetime of 30 s in the science chamber (see Figure 5.20). Then, there is a factor 3 missing with respect to the previous calculation, indicating a probable outgasing in the second arm.

1.2 Optics

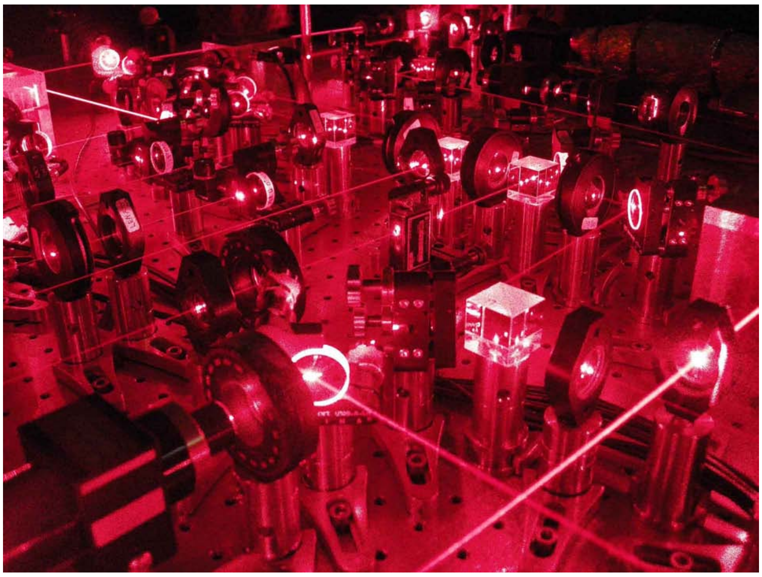

Figure 1.5: *Picture of a part of the lithium optical table.*

In this section, we describe the optical system. The hyperfine structures of ^{6}Li and ^{40}K D2 lines are shown in Figure 1.6 [65, 66]. Since we work with two different atomic species, we built two separate laser systems. Each one is located on a dedicated sealed hole optical table with tuned damping (Newport RS2000/RL2000). Then, the beams are independently sent through single-mode polarization-maintaining optical fibers (Oz Optics, LPSC-03) towards the main table, where the vacuum chamber is located (see part 1.1.1).

After a general description of the two optical systems, we focus on three key stages of the laser light production: first, the emission of a narrow linewidth laser beam by an extended cavity laser diode; secondly, its frequency stabilization through saturated absorption spectroscopy and electronic locking; thirdly, its amplification by a tapered amplifier.

1.2.1 General description

A scheme of the optical table for each species is given in Figure 1.7. The collimated light emitted by an extended cavity laser diode (see part 1.2.2) is locked to a saturated absorption line using a phase modulation through an Electro-Optical Modulator (see part 1.2.3). It is then amplified through a tapered amplifier (see part 1.2.4), before passing through a single-mode polarization-maintaining optical fiber, for spatial filtering and decoupling of the alignment stages. Then, due to the several applications

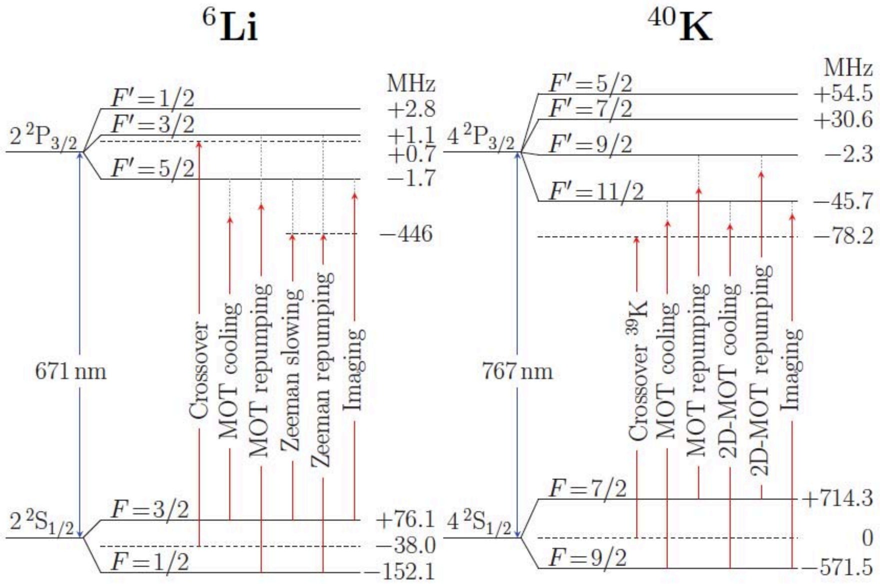

Figure 1.6: *Hyperfine structures of* ^{6}*Li and* ^{40}*K D2 lines. The laser diodes are locked to the indicated crossover frequencies. For potassium, due to the low natural abundance of* ^{40}*K, the lock is performed on a* ^{39}*K crossover line (see appendix A.1 for the* ^{39}*K hyperfine spectrum).*

such as cooling, repumping, spin-polarization, imaging or trapping, it is split in several parts which are shifted in frequency through Acousto-Optic Modulators (AOM). Such a modulator is a crystal excited by a radio-frequency signal of frequency f, coming from a home-made Voltage Control Oscillator and amplified using a 1 W amplifier (Minicircuits ZHL-1-2W). This creates a traveling density wave which modulates the refractive index. The modulation wavelength Λ is given by:

$$\Lambda = c_s/f \ ,$$

where c_s is the speed of sound in the crystal. Thus, the crystal acts as a Bragg grating. We generally use the positive and negative first orders of diffraction since they correspond to a more efficient transmission. Two configurations can be used: the single-pass one is used for switching on and off the beam, whereas the double-pass one [67] is used for scanning the frequency. In fact, in the double-pass method we place a lens and a mirror after the crystal, in a cat's eye configuration, which ensures that the reflected beam goes back in parallel with the incident one for any AOM frequency. With Crystal Technology and IntraAction AOMs, we reach typical efficiencies of 75% after spatial filtering in the first optical fiber. The fact that these tunings can be achieved with AOM, and do not request any additional master diode, is a direct consequence of the small hyperfine splittings in the spectra of both atoms (see Figure 1.6). After modulation, some of the beams are recombined (cooling and repumping frequencies for instance) and amplified using tapered amplifiers (see part 1.2.4), and they are all sent to the main table through optical fibers. Optical components (CVI-Melles-Griot) such as cubes, waveplates or lenses, are anti-reflexion coated.

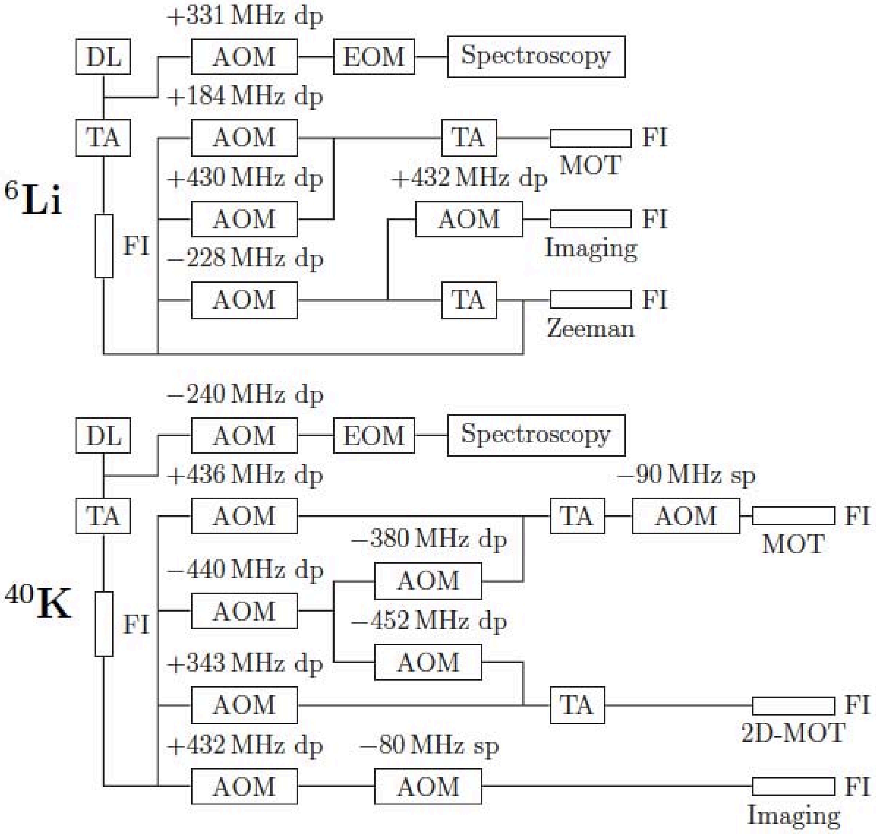

Figure 1.7: *Schematics of the laser systems of* ^{6}*Li and* ^{40}*K. The light emitted by a collimated laser diode (DL) is locked to a saturated absorption line (see part 1.2.3) using a phase modulation through an Electro-Optic Modulator (EOM). It is then amplified through a tapered amplifier (TA), before passing through a single-mode polarization-maintaining optical fiber (FI), for spatial filtering and decoupling of the alignment stages. Then, it is split in several parts which are, depending on their purpose, shifted in frequency through Acousto-Optic Modulators (AOM) in single-pass (sp) or double-pass (dp) configuration. Some of them are reamplified using TA, and they are all sent to the main table through FI.*

1.2.2 Laser diode

The master laser diodes are home-made external cavity diodes [68]. They are mounted in Littrow configuration where the first order beam diffracted by a grating serves as a feedback into the diode. Apart from its coarse tuning with current and temperature, the output frequency can be finely tuned by moving the grating using a piezoelectric actuator (Piezomechanik). We decided to use this configuration instead of the Littman-Metcalf one, where the output direction is fixed and an external feedback mirror is moved, because of its higher output power.

For ^{6}Li, the chip is a Mitsubishi diode (ML101J27) which is commonly used in the DVD industry. Therefore, it is not expensive due to its high production. The wavelength at room temperature is in the 654-664 nm range, and it can be shifted to the desired 671 nm (see Figure 1.6) by heating to 70-80°C. To reach these temperatures, we pass current trough two resistors with radiators fixed on the mount of the laser diode, we cover the inside of the mount with PET foils (Mylar) and we wrap the whole with an isolating foam. We finally get 40 mW of output power at a 150 mA driving current, and a spectral width smaller than 500 kHz. The typical lifetime of such a diode is six months, at these current and temperature.

For ^{40}K, the chip is an Eagleyard antireflexion-coated diode (EYP-RWE-0790-0400-0750-SOT03-0000). Its wavelength at room temperature is in the 760-780 nm range. Thus, we do not need to heat the mount in that case. We get 35 mW of output power at a 90 mA driving current, and a spectral width smaller than 500 kHz. The typical lifetime of such a diode is one year, at these current and temperature.

In both cases, the driving currents of the diodes are controlled via home-made current supplies, built in the electronics workshop of Laboratoire Kastler Brossel by Bernard Trégon and Lionel Pérennès. The temperature is also controlled via a home-made PID box, where the error signal is the voltage of a Wheatstone bridge. This voltage differs from zero when a 10 kΩ thermistance (Thorlabs, TH10K) placed in the laser mount is different from the chosen set-point resistance. The subsequent correction of temperature is then performed by a Peltier device (Roithner Lasertechnik, TEC1-12705T125) placed under the mount.

1.2.3 Frequency lock

On each optical table, a small part of the light emitted by the master diode, less than a milliwatt, is collected on a polarizing beam splitter in order to pass through a saturated absorption spectroscopy arm (see Figure 1.7). There, the beam is absorbed by an atomic vapor of the corresponding species contained inside a dedicated cell, before being collected by a 125 MHz low noise photodiode (New Focus 1801). In addition, the light is phase-modulated through a 20 MHz electro-optic modulator. This allows to generate the derivative of the absorption signal with a Pound-Drever-Hall device (Toptica PDD110). This box works like a synchronous demodulator: it multiplies the signal by the synchronous modulation signal and averages it. The obtained derivative signal serves as an error signal. It is sent in a PID device (Toptica PID110) that displaces the grating through another box (Toptica SC110) which drives the high voltage of the piezoelectric (see part 1.2.2). Thus, the master laser diode can be efficiently locked to an absorption line. The overall resolution of this spectroscopy is limited by

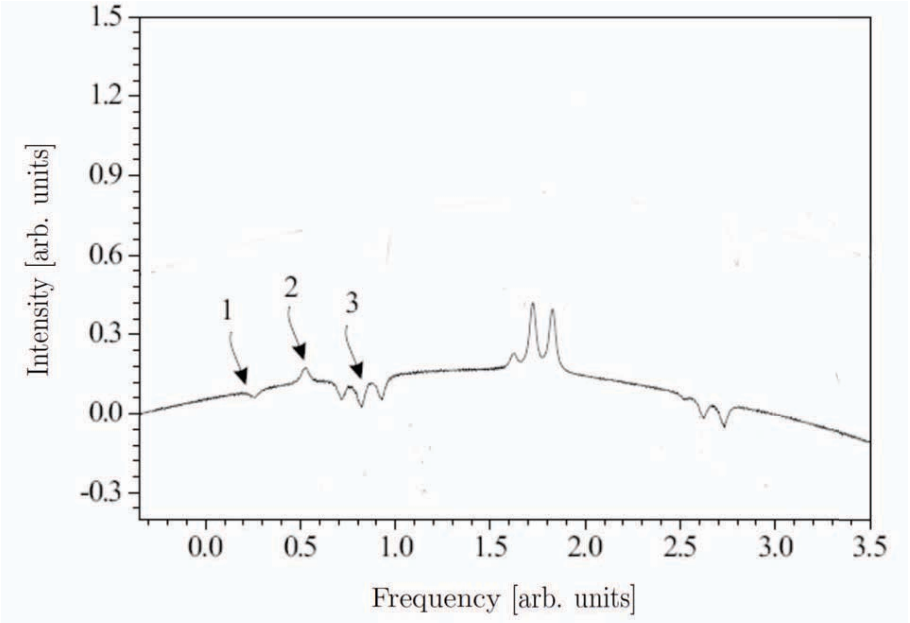

Figure 1.8: *Saturated absorption D2 lines of* ^6Li*. Peak 2 is the crossover peak used for lock. Peaks 1 and 3 correspond to transitions from the two hyperfine ground-states to the upper unresolved multiplet (see Figure 1.6). The unmarked peaks are the D1 lines of* ^7Li*.*

the intensity broadening of the lines to approximately 20-30 MHz. Therefore, we do not resolve the $P_{3/2}$ hyperfine substructures, since their widths equal 4.5 MHz for ^{6}Li (see Figure 1.6), and 33.8 MHz for ^{39}K [56], which is the isotope used for the locking of the ^{40}K master diode, as explained below.

For ^{6}Li, the laser is locked -331 MHz (see Figure 1.7) away from the crossover line shown in Figure 1.6. The saturated absorption D2 lines of ^{6}Li is shown in Figure 1.8, where peak 2 is the crossover peak used for lock. The absorption cell consists of a 50 cm MDC-Caburn DN38 pipe, heated to 350°C since the saturated vapor pressure of lithium at room temperature is low [69]. At each end of the tube there is a window. Inside, a solid lithium sample has been placed. The whole is heated by two thermocoax wires with opposite currents in order to avoid the creation of a bias magnetic field, that would lead to Zeeman shifting of the lines. As the lithium can chemically reacts with glass and obstruct the viewports, an argon buffer gas at 0.1 mbar has been added inside the tube. In addition, water cooling is performed in the vicinity of the windows. Finally, to avoid the fixation of lithium on those cold points, a stainless steel mesh (Alpha Aesar, 013477) covers the inside of the pipe. Thus, since lithium surface tension decreases with temperature, capillary forces tend to bring back the lithium towards hot regions [70].

Due to the very low natural isotopic abundance of ^{40}K (^{39}K: 93.36 %, ^{40}K: 0.012 %, ^{41}K: 6.73 %), its lines are not visible in the absorption cell at room temperature. Therefore, the laser is locked $+240$ MHz (see Figure 1.7) away from the crossover line of ^{39}K (see Figure 1.6). Figure 1.9 shows the saturated absorption D2 lines of ^{39}K (see appendix A.1 for the ^{39}K hyperfine spectrum). The middle peak is the crossover peak

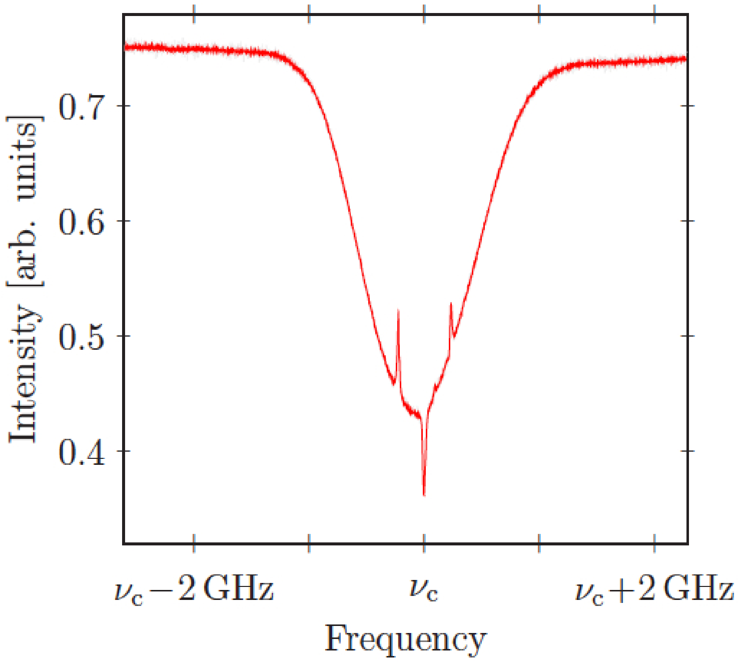

Figure 1.9: *Saturated absorption D2 lines of* ^{39}K *(see appendix A.1 for the* ^{39}K *hyperfine spectrum). The middle peak is the crossover peak used for lock. The two others correspond to the transitions from the two hyperfine ground-states to the upper unresolved multiplet (see Figure 1.6).*

used for lock. The two others correspond to the transitions from the two hyperfine ground-states to the upper unresolved multiplet. The absorption cell consists of a 5 cm long cylindrical ampoule containing natural potassium and heated to 40°C, by passing current inside two resistors and radiators fixed on a copper bracelet surrounding the ampoule. The ampoule has been prepared by engineer Florence Thibout from Laboratoire Kastler Brossel.

1.2.4 Tapered amplifier

In parts 1.2.2 and 1.2.3 we saw how to generate and stabilize in frequency the laser light. Let us now turn to its amplification. We need typically 600 mW for potassium 2D and 3D MOTs and 300 mW for lithium Zeeman slower and 3D MOT, whereas we have only 40 mW after a single laser diode. In addition, we loose power in the numerous fiber couplings and AOM (see Figure 1.7). Therefore, amplification is necessary. For both optical tables we decided to preamplify the laser beam before the spatial filtering in the first fiber and the shiftings in the AOMs, and to amplify it again afterwards, before it is sent to the main table through optical fiber (see Figure 1.7).

The device we use is a tapered amplifier [68, 71] which is driven by a current supply (Newport 525B) and whose temperature is regulated by a similar combination of home-made PID circuit and Peltier device as the one used for the master diodes (see part 1.2.2). It consists of a semiconducting device where the light is amplified by electro-photoluminescence and where the size of the medium increases in space so that the intensity remains constant. For lithium, the chip is a Toptica one (TA-670-0500-5) which gives 500 mW output power at 1 A of driving current, for a 20 mW input optical power. For potassium, the chip is an Eagleyard one (EYP-TPA-0765-01500-3006-CMT03-0000) which gives 1.5 W output power at 2.5 A of driving current, for a 20 mW input optical power. Since the chips are mounted on different heatsinks, depending on their supplier, we used slightly different designs for the two models but the principle remains similar. The chip is placed in between two aspherical collimation lenses of 4.5 mm focal length (Thorlabs, C230TME-B). In addition, since its output is astigmatic, it requires a special collimation assembly. For optimal mode matching with the filtering optical fiber (50 % coupling efficiency) we need to have a gaussian beam of 1.1 mm waist. Thus, we use two additional lenses placed outside the mounts : first a spherical one ($f^{\mathrm{K}} = 4$ cm and $f^{\mathrm{Li}} = 15$ cm), secondly a cylindrical one ($f^{\mathrm{K}} = 2.5$ cm and $f^{\mathrm{Li}} = 8$ cm) with only one direction of collimation, the other one not affecting the beam.

As a remark, such a tapered amplifier is a non-linear medium [71]. Parametric amplification can occur between close frequencies, leading to sidebands that reduce the power in the main mode and that can correspond to harmful resonant transitions in the experiment. Since we combine cooling and repumping light (see Figure 1.7) before injecting the four final tapered amplifiers for ^{40}K and ^{6}Li MOTs, ^{40}K 2D-MOT and ^{6}Li Zeeman slower, this could be an issue. For MOTs this is not harmful, because the two frequencies are sufficiently different with a spacing of 1.3 GHz for ^{40}K and 228 MHz for ^{6}Li, and because the sidebands do not correspond to any resonant transition. We measured the power lost in the sidebands, with a Fabry-Pérot cavity, to be 5 % in the case of ^{6}Li and 0.2% in the case of ^{40}K. For instance, Figure 1.10 shows the output spectrum of ^{40}K MOT tapered amplifier, for various input power ratios between principal cooling frequency (P) and repumping (R) one. However, as far as the Zeeman slower tapered amplifier is concerned, the two beams are separated by 228 MHz and are both red-detuned by 446 MHz (see Figure 1.6). Since the detuning equals approximately two times 228 MHz, this leads to a resonant sideband. Thus we decided to amplify only the cooling frequency in that case (see Figure 1.7 and part 1.3.8).

1.3 ^{6}Li Zeeman slower

In previous sections we described the vacuum manifold and the optics, let us turn now to the atomic sources. We focus here on ^{6}Li. Since we wish to get high atom numbers in the MOT, it would not be efficient to proceed with a lithium vapor directly inside the MOT chamber. In fact, due to the low saturated vapor pressure of ^{6}Li, this requires to heat the chamber a lot. We thus decided to implement a Zeeman slower [72] since it is nicely working and mastered in the lithium group at ENS [65].

We recall here first the well-known principle of Zeeman slowing and we describe the magnetic profile, as well as the stability of such a method, before characterizing the jet itself. In our case, we use a spin-flip Zeeman slower in order to avoid interactions between the slowing beam and the MOT. Then, we present the technical and experimental aspects concerning the oven, the vacuum, the coils and the laser beam, that allow us to get a flux of 1.2×10^9 atoms.s^{-1}.

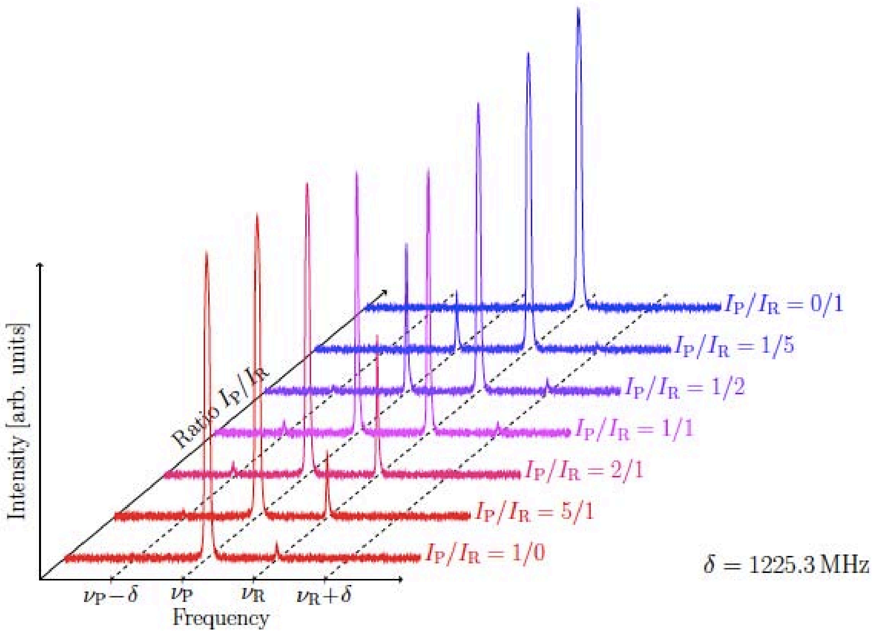

Figure 1.10: *Output spectrum of* ^{40}*K MOT tapered amplifier, for various input power ratios between principal cooling frequency (P) and repumping (R) one.*

1.3.1 Principle

In this part, we present the theoretical principle of Zeeman slowing. We first calculate the maximal acceleration induced by a resonant laser beam, from which we deduce typical size and time of slowing. Then, we estimate the Doppler effect in order to understand why we need an additional Zeeman effect to compensate it.

Maximal acceleration

The Zeeman slower technique relies on the radiative pressure. As depicted in Figure 1.11, an atomic jet coming out from an oven through a small hole is slowed down by a counter-propagating resonant laser beam.

In order to understand the slowing efficiency of such a laser beam, we estimate an order of magnitude of the distance and time needed to slow down the atomic jet. Let us consider a ^{6}Li atom of mass m escaping the oven at temperature T with the initial speed $v^* = \sqrt{3k_\mathrm{B}T/m}$ in the laser direction. On resonance, the maximal radiative pressure force F along the jet direction is given by:

$$F = -\frac{\Gamma\hbar k}{2} \ ,$$

with k the wave vector of the laser. Thus, the acceleration is constant and equals:

$$a = -\frac{\Gamma\hbar k}{2m} \ . \tag{1.3}$$

Putting numbers (see appendix A.1) gives $a \approx 2 \times 10^6$ m.s^{-2}. We already see that this acceleration is approximately 2×10^5 times gravity. With such a constant acceleration,

Figure 1.11: *An atomic jet coming out from an oven through a small hole is slowed down by a counter-propagating resonant laser beam. Picture taken from [73].*

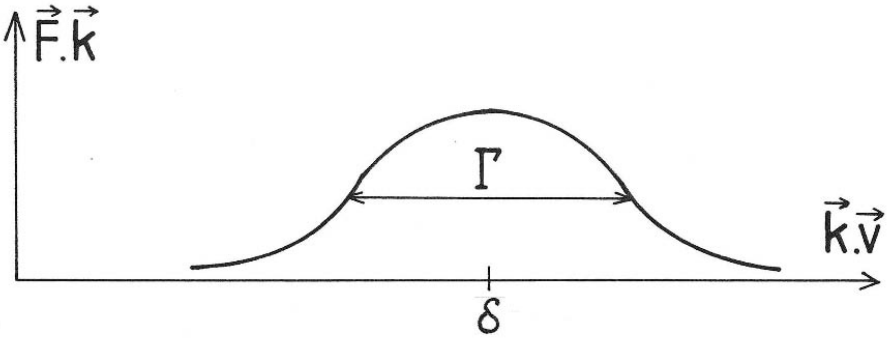

Figure 1.12: *The radiative pressure is a lorentzian function in frequency (see equation 2.1 and Figure 2.4), with a full width* Γ*. Picture taken from [73].*

the velocity v evolves as:

$$v = v^* + at \ . \tag{1.4}$$

Thus, using equations 1.3 and 1.4, we find that the atom is stopped after a time:

$$\tau_0 = -\frac{v^*}{a} = \frac{12mk_\mathrm{B}T}{\Gamma\hbar k} \ ,$$

and a length:

$$l_0 = -\frac{v^{*2}}{2a} = \frac{3k_\mathrm{B}T}{\Gamma\hbar k} \ .$$

With a resonant beam we thus can stop a ^{6}Li atom, escaping from an oven at 500 °C with a typical speed $v^* \approx 2000$ m.s^{-1}, in 1 ms over 90 cm.

Doppler effect

In the previous estimate, we assumed that the laser beam was resonant. However, since we are stopping atoms which have a typical initial speed of 2000 m.s^{-1}, the Doppler effect must play a significant role. Indeed, the radiative pressure is a lorentzian function in frequency (see equation 2.1) since it is based on the imaginary part of the polarizability. The associated full width is given by Γ, as shown in Figure 1.12. Thus, the typical width in velocity Δv_z for which the beam is resonant is given through the Doppler correspondence :

$$k\Delta v_z = \Gamma \ ,$$

which gives $\Delta v_z \approx 4$ m.s^{-1}. This result means that after a diminution of 0.2% of its initial speed the atom is not slowed down anymore. Therefore, it is impossible to slow down a jet with a simple laser beam of fixed frequency. Three solutions to this issue exist. First, we can use another tuning effect : the linear Zeeman shift induced by a bias field [72]. Secondly, we can tune the laser in a time-dependent way, in order to maintain the resonance with the slowed atoms [74]. Thirdly, we can use a controlled Stark shift to maintain the resonance along the path [75]. In our experiment, we use the first method as described in the following.

1.3.2 Magnetic profile

In this part, we calculate the magnetic profile $B(z)$ allowing for a constant acceleration αa along the slower, with $\alpha < 1$, where α is a positive safety factor that we explain in part 1.3.3, and where a is the maximal acceleration given at equation 1.3. On the jet axis, one can write by conservation of energy:

$$v^2 = v_{\mathrm{c}}^2 + 2\alpha a z \ , \tag{1.5}$$

where we have introduced the capture speed v_{c}, which corresponds to the speed for which the resonance condition is verified at the entrance in the slower. We explain its role further at the end of this part. Let us define as well, from equation 1.5, the final velocity v_{f} at the exit of the slower:

$$v_{\mathrm{f}}^2 = v_{\mathrm{c}}^2 + 2\alpha a l \ , \tag{1.6}$$

where l is the length of the slower.

To maintain a constant acceleration, the Doppler effect should be exactly compensated, at any point, by the Zeeman effect. We consider in the following a closed σ^+ transition between the states $|F = 3/2, m_F = 3/2\rangle$ and $|F' = 5/2, m_{F'} = 5/2\rangle$ for which atoms can always see the slowing beam, since there is no connexion to any dark F or m_F state. Furthermore, for those stretched states the Zeeman energy shift is linear with the field $B(z)$, even for high fields (see Figures 1.6 and 3.2), and equals respectively $-\mu_{\mathrm{B}}B(z)$ and $-2\mu_{\mathrm{B}}B(z)$ (see equation 3.2). Thus, the resonance condition expresses as follows:

$$\hbar\delta - \mu_{\mathrm{B}}B(z) + \hbar k v(z) = 0 \ . \tag{1.7}$$

We see through this equation that in the σ^+ case the field decreases with z. Using equations 1.5, 1.6 and 1.7, we find:

$$B(z) = \frac{\Delta B}{1 - \frac{v_{\mathrm{f}}}{v_{\mathrm{c}}}} \left[\delta' + \sqrt{1 - \left(1 - \frac{v_{\mathrm{f}}^2}{v_{\mathrm{c}}^2}\right) \frac{z}{l}} \right] \ , \tag{1.8}$$

where we have introduced the undimensioned detuning:

$$\delta' = \frac{\delta}{k v_{\mathrm{c}}} \ ,$$

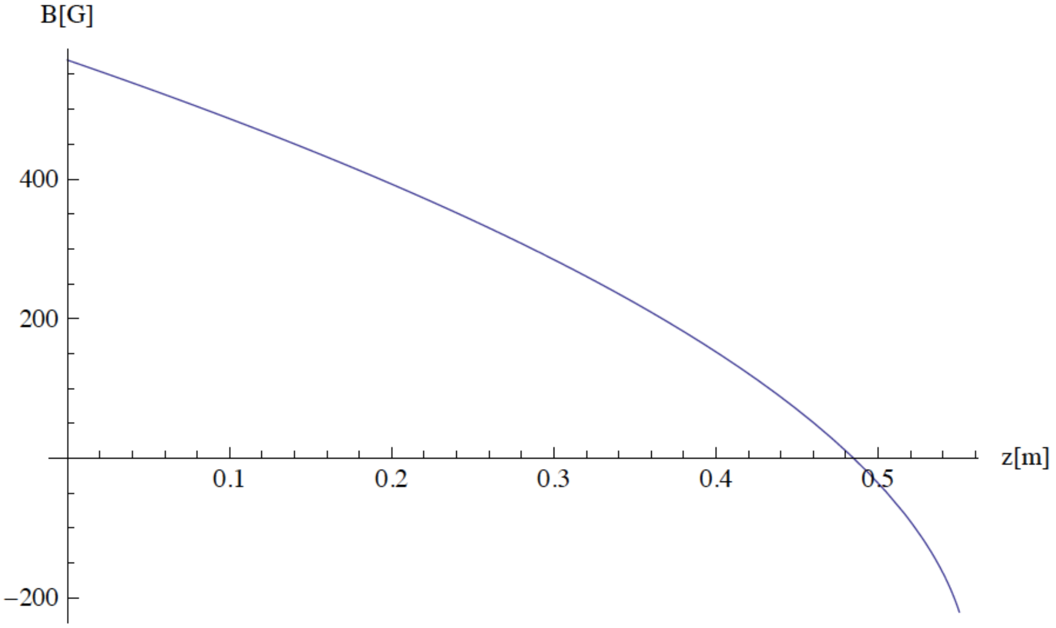

Figure 1.13: *Ideal magnetic profile of the* ^{6}*Li Zeeman slower, plotted from equation 1.8 with* $v_c = 838\ m.s^{-1}$, $l = 55\ cm$, $\delta = -75\ \Gamma$ *and* $\alpha = 0.34$.

and the magnetic amplitude of the slower:

$$\Delta B = B(0) - B(l) = \frac{\hbar k v_{\mathrm{c}}}{\mu_{\mathrm{B}}}\left(1 - \frac{v_{\mathrm{f}}}{v_{\mathrm{c}}}\right) \ .$$

Choosing $\delta' = 0$ would be harmful since the beam would be resonant with the MOT atoms, leading to consequent losses in this trap. Thus, we need to have a high detuning. Experimentally we chose $\delta = -75\ \Gamma$. Then B vanishes at $z = l(1 - \delta'^2)/(1 - v_{\mathrm{f}}^2/v_{\mathrm{c}}^2)$ and becomes negative until $z = l$, as plotted in Figure 1.13. The chosen parameters are $v_{\mathrm{c}} = 838$ m.s^{-1}, $l = 55$ cm, and $\alpha = 0.34$ (see part 1.3.3). This implies $v_{\mathrm{f}} = 95$ m.s^{-1} (see equation 1.6). We see that the final speed is larger than the capture speed of the ^{6}Li MOT, which is estimated to be approximately 20 m.s^{-1} (see part 2.1.7). However, the atoms are still decelerated significantly in the region between the slower exit and the MOT and are thus expected to be captured by the MOT, as finally observed experimentally. Atoms with an initial speed higher than v_{c} will never fulfill the resonance condition 1.7 an thus can not be slowed down. On the contrary, atoms with an initial speed smaller than v_{c}, but bigger than v_{f}, will be on resonance somewhere inside the slower, and thus will be slowed down as well until v_{f}. The capture speed is thus the maximal speed of the atoms for which the slower is efficient. Note that our capture speed is smaller than the most probable speed in the jet $v_{\mathrm{p}} = \sqrt{3k_{\mathrm{B}}T/m} \approx 2000$ m.s^{-1} (see part 1.3.5), which reduces the overall efficiency. However, due to the square root dependency of v_{c} in the length l (see equation 1.6), it would have required a 4.5 bigger slower to obtain a capture speed of the order of this most probable speed, which would have raised other issues linked with the jet divergence. An interesting additional feature of the Zeeman slower comes at this point. Since almost all the speeds smaller than v_c are reduced to v_f by the slower, there is a reduction of the width of the velocity distribution, and thus a cooling effect in the direction of the slower. Therefore, a Zeeman slower is a cooling device.

The $\delta' < 0$ configuration is a so called "spin-flip Zeeman slower" [76] since the sign of the magnetic field changes. As detailed in part 1.3.7, it consists of two coils: one big Zeeman slower creating a positive field up to $B(0) = 570$ G and one small inverted slower creating a negative field down to $B(l) = -220$ G. In the ideal case, the absolute spin orientation remains constant and anti-parallel to the entrance field and only the magnetic field flips. This technique is performing since it avoids the use of high fields at the entrance of the slower. In fact, had we used a simple Zeeman slower with $\delta' > 0$, the entrance field would have been of the order of $B(0) \approx 570 + 2 \times 220 \approx 1000$ G (see equation 1.7) in order to get a similar amplitude ΔB and a same final detuning. This means a two times higher current and then a four times higher dissipated Joule power, demonstrating the interest of our spin-flip configuration. However, it requires additional care. First, it is compulsory to add a counter Zeeman coil (see part 1.3.7) to compensate the bias field created by the inverted slower at the MOT position. Secondly, in the region of zero field, at the junction of the two slowers, the atoms can be depolarized to the wrong hyperfine ground-state $F = 1/2$, thus a repumping beam is required as well (see part 1.3.8). This region is also harmful since crossings of Zeeman levels can occur under $B \approx 2$ G.

1.3.3 Stability

We already introduced the safety factor α in part 1.3.2. The Zeeman slower is a robust system if $\alpha < 1$. We explain this point here, with similar arguments as [77].

For fixed geometry, field profile and capture speed, α is completely determined by the derivative of $B(z)$. For instance in $z = 0$, according to equations 1.5 and 1.7, we have the following relationship:

$$\alpha = \frac{\mu_\mathrm{B} v_\mathrm{c}}{\hbar k a} \left(\frac{\mathrm{d}B}{\mathrm{d}z}\right)_{z=0} . \tag{1.9}$$

Thus, whatever the used laser intensity, α is fixed, which means that the slower is in fact efficient somewhere away from exact resonance. More precisely, one can write:

$$\alpha = \frac{s}{1+s} = \frac{s_0}{1 + s_0 + 4\frac{\delta''^2}{\Gamma^2}} , \tag{1.10}$$

where δ'' is the real detuning seen by an atom in the operating regime of acceleration αa, and where:

$$s = \frac{s_0}{1 + 4\frac{\delta''^2}{\Gamma^2}} , \tag{1.11}$$

is the saturation parameter, which equals $s_0 = I/I_{sat}$ on resonance. Since $\alpha \approx 1/3$, we find with equation 1.10 that $s \approx 1/2$. In our case the slowing laser beam of 50 mW power is focused around the oven and has a waist of 1.5 cm at the MOT center (see part 1.3.8). Using the approximative dimensions of the system (see scale in Figure 1.1) we thus estimate the radius to be of the order of 1 cm in the Zeeman slower, which gives

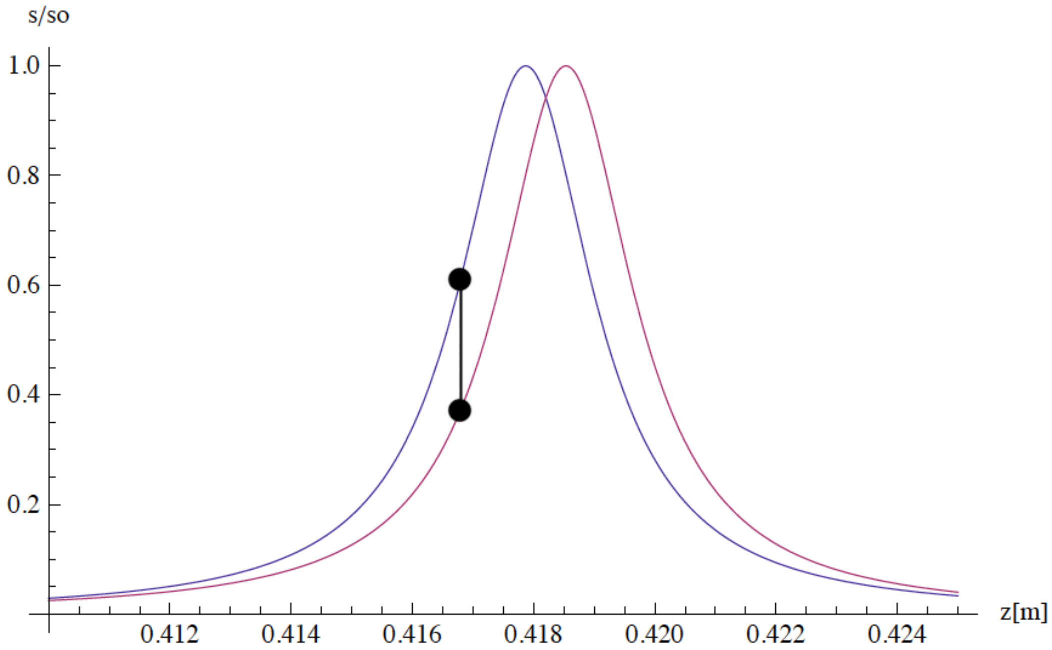

Figure 1.14: *Evolution of the normalized saturation parameter with distance for a speed* $v_c/2$ *(blue) and* $v_c/2-1$ *m.s*$^{-1}$ *(pink). In the operating regime (blue), an atom experiencing an unexpected deceleration (pink) will be less resonant and thus will be less decelerated by the slower. Therefore, it will move forward until it reaches the good* s/s_0 *value and stick back to the operating regime downstream.*

$s_0 \approx 6$ using appendix A.1 for the saturation intensity value. Thus, with equation 1.11 we deduce that an atom is away from resonance by typically $\delta'' = 2\,\Gamma$ in the operating regime.

We can understand the interest of such a security factor α. On Figure 1.14, the blue curve shows s/s_0 as a function the distance z in the slower for a fixed speed $v_c/2$. Note that the resonance condition happens after ~ 40 cm in the slower, for this particular speed. The pink curve shows the same function but for a speed 1 m.s^{-1} smaller. We place the atom on the blue curve for s/s_0 corresponding to our fixed value of α (here for pedagogical purposes the picture is wrong since actually $s/s_0 \approx 1/12$). Let us now consider an irregularity in the process: for instance a field deviation from the theoretical value or too much absorption with respect to the average acceleration. This can cause the speed to be reduced by 1 m.s^{-1}, for instance, from its expected value at this point. Thus, the atom (see the pink curve) will be less resonant and thus will be less decelerated. Therefore, it will move forward until it reaches the good s/s_0 value again, and stick back to the operating regime downstream. Inversely, a slight increase in speed, would bring the atom closer to resonance which will decelerate it more until it sticks back to the operating regime downstream. In conclusion, we see that such a Zeeman slower is stable. On the contrary, a choice of $\alpha = 1$ would be critical. In fact, it implies a perfect resonance $\delta'' = 0$. Then, an atom in the operating regime which, for a practical reason, is not decelerated as it should be, will get a higher velocity than the maximal authorized one at this point and will be definitely lost. Quantitatively, let us express the fact that the decceleration $-\alpha a$ can not exceed the maximal one $-a$:

$$-\alpha a = -\frac{\mathrm{d}v}{\mathrm{d}t} = -\frac{\mathrm{d}v}{\mathrm{d}z}v = -\frac{\mu_\mathrm{B} v}{\hbar k}\frac{\mathrm{d}B}{\mathrm{d}z} \leq -a \ ,$$

where we have used equation 1.7 to connect v and B. If $\alpha = 1$, the last inequality becomes an equality. Thus, any slight local increase of magnetic gradient reduces the maximal authorized speed v at this point. Therefore, an atom initially in the operating regime will be lost since its velocity is higher than the new maximal one. We thus need to reduce α for stability reasons. However, for fixed geometry and field profile, reducing α implies a reduction of the capture speed according to equation 1.9, and thus a reduction of the overall efficiency. Our chosen value $\alpha \approx 1/3$ is a typical trade-off value.

1.3.4 Jet divergence

An important aspect of the Zeeman slower is the divergence of the atomic jet. In order to estimate this number, we first quantify the initial jet divergence due to the collimation and pumping tubes, as well as the transverse heating due to spontaneous emission phenomena.

Between the oven and the slower, there is a collimation tube of 80 mm length and 3 mm radius (see engineering drawing in appendix A.6), as well as two differential pumping tubes which both have a 100 mm length and respective diameters of 5 mm and 10 mm (see part 1.3.6). This ensemble creates a selection cone, of $r = 5$ mm radius and $L \approx 300$ mm length, that limits the transverse velocity with respect to the longitudinal one. For a longitudinal velocity v_c, we find a maximal transverse velocity of:

$$v_\perp \approx v_\mathrm{c} r/L \ , \tag{1.12}$$

which is of the order of 15 m.s^{-1}.

In contrast with the longitudinal cooling effect explained in part 1.3.2, a transverse heating is induced all along the trajectory inside the slower. It is due to the spontaneous emission that follows each absorption of photon. In fact, by isotropy of emission, a photon can be reemitted in a transverse direction where there is no cooling effect. By conservation of linear momentum, this induces a recoil kick on the atomic linear momentum in this direction. We estimate the associated heating now. This random process can be described as a random walk in velocity space (see part 2.1.4), for which the evolution of the variance of one transverse component v_x is given by:

$$\frac{\mathrm{d}\langle v_x^2\rangle}{\mathrm{d}t} = 2D \ , \tag{1.13}$$

where D is the 1D diffusion coefficient in velocity. Let us estimate it with simple arguments. D should be homogenous to a speed squared divided by a time. The typical 1D speed of this problem is the recoil one $v_\mathrm{r} = \hbar k/m$, and the typical time is the inverse of the cycling rate $\alpha\Gamma/2$, including the safety factor α that reduces the intensity. Thus, we can write:

$$D = \frac{1}{3}\frac{(\hbar k)^2 \alpha\Gamma}{2m^2} \ , \tag{1.14}$$

where the factor 1/3 accounts for the average fact that only a third of the photons are emitted in the x-direction. Using equations 1.13 and 1.14 it follows:

$$\frac{\Delta\langle v_x^2\rangle}{\langle v_x^2\rangle(0)} = \frac{\langle v_x^2\rangle(t) - \langle v_x^2\rangle(0)}{\langle v_x^2\rangle(0)} = \frac{(\hbar k)^2\alpha\Gamma}{3m^2\langle v_x^2\rangle(0)}t\ . \tag{1.15}$$

Then, we can express $\langle v_x^2\rangle(0)$ using the temperature. However, as in equation 1.12, we must add a geometrical factor that takes into account the spatial limitation of the inner tube:

$$\langle v_x^2\rangle(0) \approx \frac{r^2}{L^2}\langle v_z^2\rangle(0) = \frac{k_\mathrm{B}Tr^2}{mL^2}\ . \tag{1.16}$$

Since the acceleration αa is constant, the total time τ spent in the slower for an atom of initial speed v_c is given by:

$$\tau = -\frac{v_\mathrm{c} - v_\mathrm{f}}{\alpha a}\ . \tag{1.17}$$

Thus, combining equations 1.3, 1.15, 1.16 and 1.17, we find:

$$\frac{\Delta\langle v_x^2\rangle}{\langle v_x^2\rangle(0)} = 2\frac{L^2}{r^2}\frac{(v_\mathrm{c} - v_\mathrm{f})v_\mathrm{r}}{v^{*2}}\ ,$$

where we have introduced the 3D RMS velocity of the oven $v^* = \sqrt{3k_\mathrm{B}T/m}$. Putting numbers leads to a transverse heating of approximately 16 % in variance, and thus 8 % in RMS velocity, which means an increase in transverse velocity of approximately 2.5 m.s^{-1}.

Thus, we can neglect the contribution of the transverse heating in comparison with the initial transverse velocity and use $v_\perp$ to estimate the final divergence. Let us consider an atom entering the slower with a longitudinal velocity v_c and a transverse one $v_\perp$. From equation 1.17, the time spent in the oven by the atom is approximately 1.2 ms. It exits with a longitudinal velocity v_f and then moves freely over approximately 20 cm, before reaching the MOT center (see Figure 1.1), which requires approximately 2 additional milliseconds. The total time to consider is thus around 3.2 ms, which gives with $v_\perp \approx 15$ m.s^{-1} a transverse spreading of approximately 5 cm in radius at the MOT center.

In conclusion, this divergence is not negligible. We reduce it experimentally by focusing the slowing beam around the oven (see part 1.3.8), since this creates a balanced transverse absorption and thus a transverse cooling [76]. Moreover, we use large 2 inches MOT optics in order to create a large capture volume in the MOT.

1.3.5 Atomic flux and efficiency

By measuring the MOT loading rate for small loading times (in order to neglect the MOT losses, see part 2.3.4), we found an optimum loading rate of 1.2×10^9 atoms. s^{-1}. In the following, we give simple arguments in order to understand this number and to connect it to the flux of the atomic jet. We thus estimate the overall efficiency of MOT loading by our Zeeman slower.

We describe the lithium oven by a 500°C thermalized box with an output tube of radius $\sqrt{A/\pi} \approx 2.5$ mm and length $d = 200$ mm, in order to describe the collimation tube (see engineering drawing in appendix A.6) and the first differential pumping tube that limit the jet extension (see part 1.3.6). The flux of atoms Φ_i entering the tube is simply given by:

$$\Phi_\mathrm{i} = \frac{n\bar{v}A}{2} \ , \tag{1.18}$$

where n is the density in the oven, $\bar{v} = \sqrt{8k_\mathrm{B}T/\pi m}$ the average speed in the oven, and where the factor 2 accounts for the fact that, by isotropy, only half of the atoms have a positive longitudinal velocity in the direction of the tube. To get the flux Φ_o at the end of the tube, we just multiply Φ_i by the portion of solid angle corresponding to the exit of the tube:

$$\Phi_\mathrm{o} = \Phi_\mathrm{i}\frac{A}{2\pi d^2} = \frac{n\bar{v}A^2}{4\pi d^2} \ . \tag{1.19}$$

Putting numbers gives $\Phi_\mathrm{o} \approx 5 \times 10^{13}$ atoms.s^{-1}.

Then, we need to multiply this flux Φ_o by the probability $R(T)$ for an atom to have a speed inferior to v_c. To calculate $R(T)$, we assume a Maxwell-Boltzmann distribution in the oven, at temperature T:

$$f(\boldsymbol{v}) = n\left(\frac{m}{2\pi k_\mathrm{B}T}\right)^{3/2} \exp\left[-\frac{m\boldsymbol{v}^2}{2k_\mathrm{B}T}\right] \ ,$$

where $n = \int d^3v f(\boldsymbol{v})$ is the density in the oven. Then, the number $d^4N(\boldsymbol{v})$ of atoms that escape the oven, through a hole of area A, with a velocity $\boldsymbol{v}$, during an infinitesimal time dt, is given by:

$$d^4N(\boldsymbol{v}) = f(\boldsymbol{v})vAv_zd^3dt \ ,$$

where $v_z = \boldsymbol{v}\cdot\boldsymbol{u_z}$ is the component of the velocity in the jet direction, v_z being positive if the atom escapes the oven. We can now rewrite this in spherical coordinates and integrate over the possible angles given by the geometry of the collimation tube. Apart from a constant factor, the distribution $P(v)$ of atoms escaping the oven per time unit with speed v is given by the expression:

$$P(v) \propto v^3 \exp\left[-\frac{mv^2}{2k_\mathrm{B}T}\right] \ . \tag{1.20}$$

This function is plotted in Figure 1.15. It is maximal for the most probable speed in the jet: $v_\mathrm{p} = \sqrt{3k_\mathrm{B}T/m}$, which happens to be equal to the 3D RMS speed of the oven. Using equation 1.20, we find the probability $R(T)$ for an atom to have a speed inferior to v_c:

$$R(T) = \frac{\int_0^{v_\mathrm{c}} dv v^3 \exp\left(-\frac{mv^2}{k_\mathrm{B}T}\right)}{\int_0^{\infty} dv v^3 \exp\left(-\frac{mv^2}{k_\mathrm{B}T}\right)} \approx 14\% \ . \tag{1.21}$$

We have seen in part 1.3.4 that the final transverse spreading of the jet is of the order of 5 cm in radius, which is typically five times bigger than the radius of the MOT beams (see part 2.3.1). Thus, we should add a capture factor in section of $R' \approx 4\%$.

In addition, we can assume that the two Zeeman sub-levels of $F = 1/2$ and the four Zeeman sub-levels of $F = 3/2$ are all equally populated at the entrance of the slower. In fact, for a maximal field of 570 G (see part 1.3.2) the Zeeman shift in energy corresponds

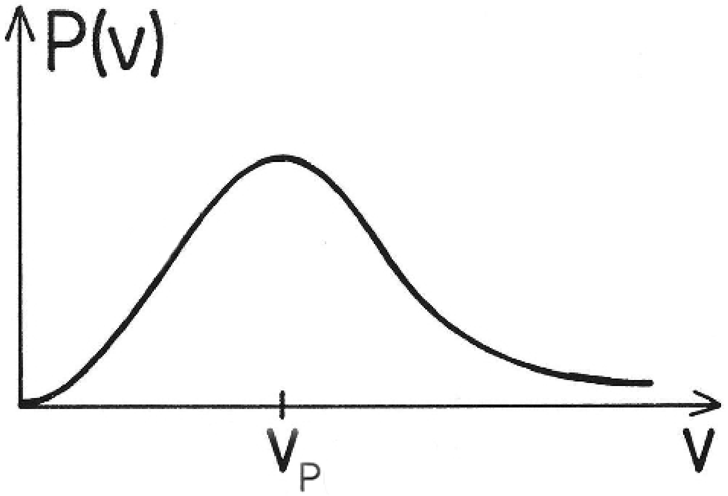

Figure 1.15: *Distribution of speed in the atomic jet (see expression 1.20). Its maximum corresponds to the most probable speed in the jet:* $v_p = \sqrt{3k_BT/m}$. *Picture taken from [73].*

to ~ 50 mK, which is very small compared to the oven temperature (773 K), leading to a Boltzmann ratio of ~ 1. Therefore, only an average fraction $R'' \approx 1/6$ of the atoms is initially in the appropriate $|F = 3/2, m_F = 3/2\rangle$ state for the Zeeman slower.

Finally, assuming that the gas in the oven is an ideal gas at $T = 773$ K, we can calculate the density $n = P_{\mathrm{s}}(T)/k_{\mathrm{B}}T \approx 4.5 \times 10^{19}$ m^{-3}, where we have introduced the saturated vapor pressure in the oven $P_{\mathrm{s}}(773) = 4.8 \times 10^{-3}$ mbar [78]. Consequently, the expected loading rate is $\Phi_{\mathrm{o}}RR'R'' \approx 5 \times 10^{10}$ atoms.s^{-1}. However, our experimental loading rate equals only ~ 2.5 % of this value, but we assumed a ballistic flight in this estimate, and we neglected the collisions between the MOT atoms and the unslowed hot atoms which occur above 475°C [79], and which reduce the MOT loading efficiency. For temperatures below 475°C, with the same arguments, we find an experimental flux which equals ~ 15 % of the theoretical one (see Figure 1.16). At those lower temperatures, we attribute the remaining factor ~ 6 to a partial capture of the slowed atoms crossing the MOT capture region.

1.3.6 Oven and vacuum

The lithium oven consists of a vertical reservoir tube connected to an horizontal collimation tube (see Figure 1.1 and engineering drawing in appendix A.6). The vertical tube has a 16 mm diameter and a 180 mm length. Its open extremity, on the top, is sealed with a blank DN38 stop that can be replaced by a turbomolecular pump in case of prebaking. The horizontal tube has a 6 mm diameter and a 80 mm length. Its open extremity DN38 is connected to the Zeeman slower. After prebaking at 600°C during a day, in order to eliminate the remaining LiH impurities from the ^{6}Li sample provided by Cambridge Isotope Laboratory, the oven contains nearly 3 g of pure solid ^{6}Li. In working conditions, it is heated to 500°C using a Thermocoax heating wire (SEI 10/50-25/2xCM10) connected to an AC transformer (Variac) that can provide a 110 V voltage. We thus used nickel gaskets, instead of copper ones that react with hot lithium and that can not sustain such high temperatures. In addition, the ensemble is covered by glass wool and aluminum foils, and the heating circuit contains a thermostated regulation system (Omega CN1501-TC-1) linked to a thermocouple (Hanna SFILS1), in order to stabilize the temperature and thus the atomic flux (see part 1.3.5). Finally, we placed a mechanical shutter (Danaher Motion BRM-27503) inside the vacuum to allow for blocking of the jet. It has a subsidiary task which is to serve as an alignment target for the Zeeman laser beam.

In order to isolate the MOT chamber from the high pressure in the oven of typically 5×10^{-3} mbar, we added two differential pumping tubes of both 100 mm length and respectively 5 mm and 10 mm diameters. Note that the collimation tube is playing a differential pumping role as well. After each of these three tubes we placed a Varian ion pump of 20 L.s^{-1}. Thus, the pressure in the MOT chamber remains inferior to 10^{-8} mbar when the oven is on (see part 1.1.3 for similar calculations).

Let us now estimate the lifetime of the oven. First, we assume that all the atoms entering the collimation tube are lost. Thus, using equation 1.18 we find a mass loss rate of:

$$\Gamma_{\mathrm{m}} = \Phi_{\mathrm{i}} m \approx 7 \times 10^{-6} \mathrm{g.s}^{-1} \ ,$$

where we used, as in part 1.3.5, the ideal gas law $n = P_{\mathrm{s}}(T)/k_{\mathrm{B}}T \approx 4.5 \times 10^{19}$ atoms.m^{-3}, with $P_{\mathrm{s}}(773) = 4.8 \times 10^{-3}$ mbar [78]. Therefore, in approximately ten operating days, all the lithium would have been expelled from the oven.

However, since most of the lithium atoms in this calculation are sent to the collimation tube walls and not far away in the experiment walls, we can recycle them. As for the absorption cell (see part 1.2.3), we actually covered the collimation tube inner walls with a stainless steel mesh (Alpha Aesar 013477). Thus, since lithium surface tension decreases with temperature, capillary forces bring back the lithium towards the oven [70]. The mass loss rate is thus rather given by the mass flux coming out of the collimation pipe, similarly to equation 1.19:

$$\Gamma_{\mathrm{m}} = \frac{n m \bar{v} A^2}{4\pi d'^2} \approx 4 \times 10^{-9} \mathrm{g.s}^{-1} \ ,$$

where $\sqrt{A/\pi} \approx 2.5$ mm is the effective radius, since the capillarity meshing reduces the radius by 0.5 mm, and $d' = 80$ mm is the length of the collimation tube. This corresponds to a lifetime of ~ 50 years. Therefore, we could in principle increase the oven temperature, in order to increase exponentially the atomic flux, and thus the loading rate of the MOT. However, above 475°C, collisions of the unslowed atoms of the oven with the MOT atoms start to play a significant role and are harmful for the MOT lifetime. Then, we decided not to exceed 500°C. This effect of collisions has been observed by blocking the jet with the mechanical shutter, for different temperatures, while measuring the MOT lifetime. We also see it on Figure 1.16, where we plot the ^{6}Li-MOT capture rate as a function of the lithium oven temperature. The solid curve is a fit from expression $L(T) \propto \Phi_0(T)R(T)R'R''$ found for the theoretical flux in the previous part (see equations 1.18 and 1.21). The fit is good until 475°C, where it starts to diverge from the experimental data, showing that our ballistic model is not valid anymore above this temperature: intrabeam collisions inside the collimation tube and collisions with MOT atoms become probable.

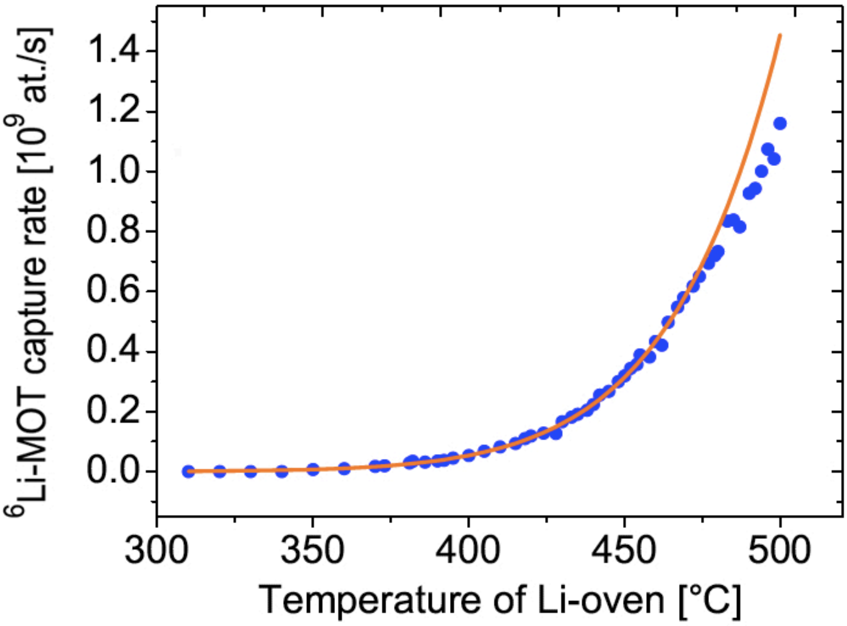

Figure 1.16: *^{6}Li MOT loading rate as a function of oven temperature. The solid curve is a fit using the theoretical flux of the Zeeman slower (see equations 1.18 and 1.21). The fit is good until 475° C, where it starts to diverge from the experimental data, showing that our ballistic model is not valid anymore: intrabeam collisions inside the collimation tube and collisions with MOT atoms occur.*

1.3.7 Coils

As explained in part 1.3.2, we choose the following parameters for the Zeeman slower: $v_c = 838$ m.s^{-1}, $l = 55$ cm, $\delta = -75\ \Gamma$ and $\alpha = 0.34$. This leads to the theoretical profile shown in Figure 1.13.

To design the assembly of coils that can generate such profile, we proceeded the following way. In a Mathematica program, for each of the two parts of the spin-flip slower, we superimpose on top of each other N solenoids of lengths l_i and radii a_i ($i = 1, N$), those quantities being *a priori* different for the two sides (see Figure 1.17). The current I and the number of loops per meter n are identical for all the layers and for the two sides of the slower. The quantities n and a_i are fixed by the size of the square wire (APX France copper CL H 1.6 mm × 2.5 mm with a 0.5 mm insulation layer), by the internal radius of the slower, fixed to be 3.3 cm, and by the fact that the layers are on top of each other. In the normal Zeeman side, all the layers start at $z_i^{\mathrm{s}} = 0$ and end at $z_i^{\mathrm{e}} = l_i$. In the inverted Zeeman side, the layers start at $z_i^{\mathrm{s}} = l$ and end at $z_i^{\mathrm{e}} = l - l_i$. For given numbers of layers, we fit the theoretical profile of Figure 1.13 by the sum of the fields generated by each layer i:

$$B_i(z) = \frac{\mu_0 n I}{2}\left[\frac{z - z_i^{\mathrm{s}}}{\sqrt{a_i^2 + (z - z_i^{\mathrm{s}})^2}} - \frac{z - z_i^{\mathrm{e}}}{\sqrt{a_i^2 + (z - z_i^{\mathrm{e}})^2}}\right] .$$

The fit variables are the common current I and the lengths l_i. We then optimize the results by changing the numbers of layers. This give us a final current of $I = 12$ A, 18

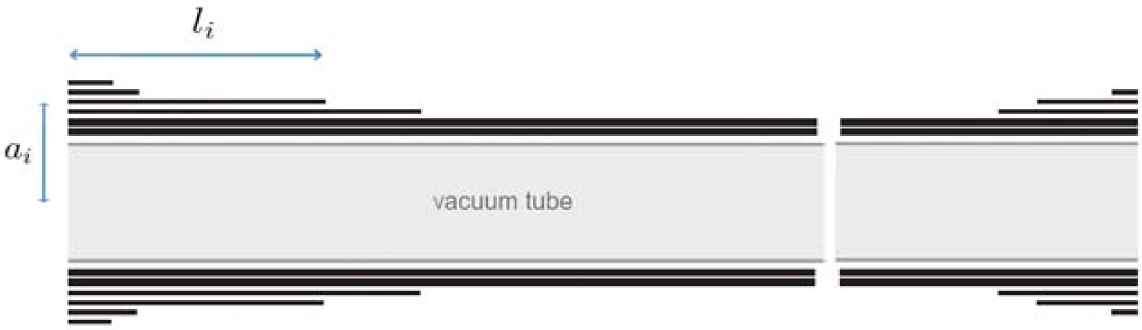

Figure 1.17: *Sectional drawing of the numerical model of the* ^{6}*Li Zeeman slower. Each side of the spin-flip Zeeman slower is made from superimposed solenoids of length* l_i *and radius* a_i *(*$i = 1, N$*).*

layers for the normal slower and 8 layers for the inverted one. The numbers of turns of each layer are respectively for the two sides (136, 134, 129, 117, 106, 94, 81, 65, 51, 17, 16, 16, 16, 16, 16, 16, 16, 16) and (18, 17, 16, 16, 15, 14, 13, 11). In order to compensate the bias field created at the MOT center by the inverted Zeeman, we added a counter Zeeman coil 12.7 cm after the MOT (see Figure 1.1). It consists of 4 layers, over a 10 cm total length. The field obtained with this design, as well as a Catia view of the coils assembly are shown in Figure 1.18.

Before we started winding the Zeeman slower, we performed a numerical simulation in order to check the effect of this magnetic field on the atoms. It is based on a simple dynamic simulation, where the force is the radiative pressure, including the Zeeman shift calculated from the profile $B(z)$ of Figure 1.18, and the Doppler shift kv. We used a uniform random assignation of the initial positions and a thermal-gaussian random assignation of the initial velocities. This simulation confirmed our choice by giving an efficiency close to the theoretical one (see part 1.3.5).

We then assembled the slower (see Figure 1.19) and measured the axial field with a home-made Hall probe (from chip UGM3503U). Results are in perfect agreement with the theoretical field, as shown in Figure 1.18.

The total coil assembly is mounted in series and fed with a common Delta Power supply in constant current (CC) mode. This supply is remote controlled via an analog output of the main computer (see part 1.5). In addition, a metal-oxide semiconductor field-effect transistor (MOSFET) such as the one used for transport (see part 4.5.2) allows to switch the Zeeman field on and off. The counter Zeeman has an additional power supply placed in parallel, to allow for fine adjustments of the bias field. By observing the ^{40}K MOT position in pulsed mode for the Zeeman currents we could tune this offset current to 6 A, so that the MOT remains at the same position, whether the Zeeman field is on or off.

Since the Zeeman coils can not be easily wound on the vacuum system, we wound it on the tube before assembling the vacuum chamber. Thus, it required special care as far as the baking was concerned. First, the wire insulation can stand 200°C and there is a thermal insulating Kapton layer just under the coils. Secondly, a Garnisch heating cable (GGCb250-K5-19) was wound around the vacuum tube for heating. We

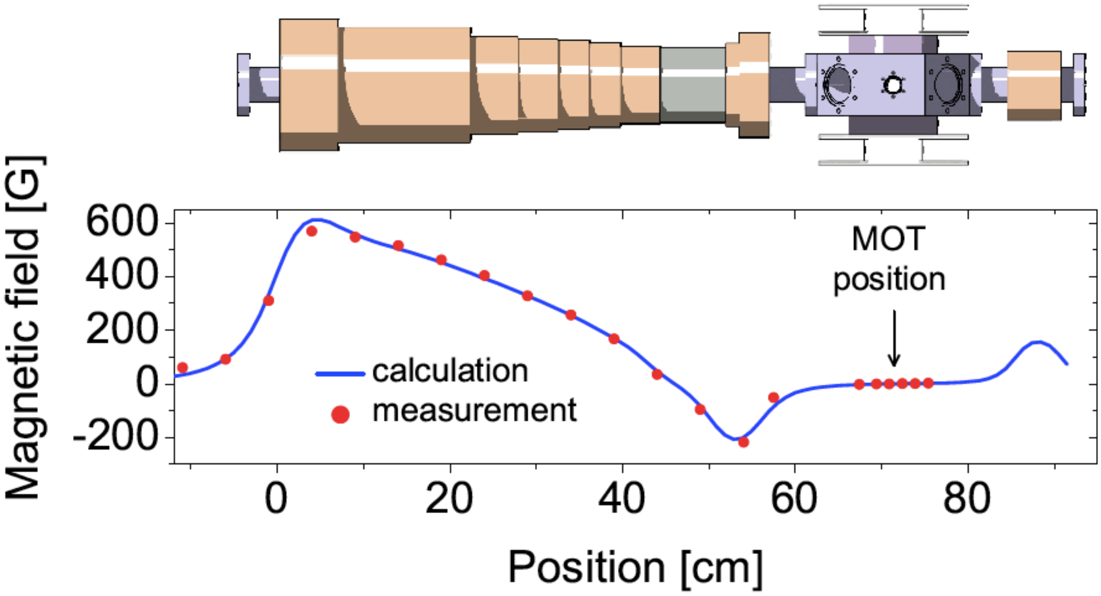

Figure 1.18: ^{6}*Li Zeeman slower magnetic field as a function of the position in the slower. The solid line is the theoretical magnetic field obtained with the assembly of solenoids in order to be close from the desired profile of Figure 1.13. The dots are the measurements inside the Zeeman tube, performed before assembling the vacuum system with a home-made Hall probe. In addition, we superimpose a Catia view of the coil assembly. Note the presence of a normal slower, an inverted one, as well as a compensating counter slower placed after the MOT in order to reduce the bias field of the inverted Zeeman slower.*

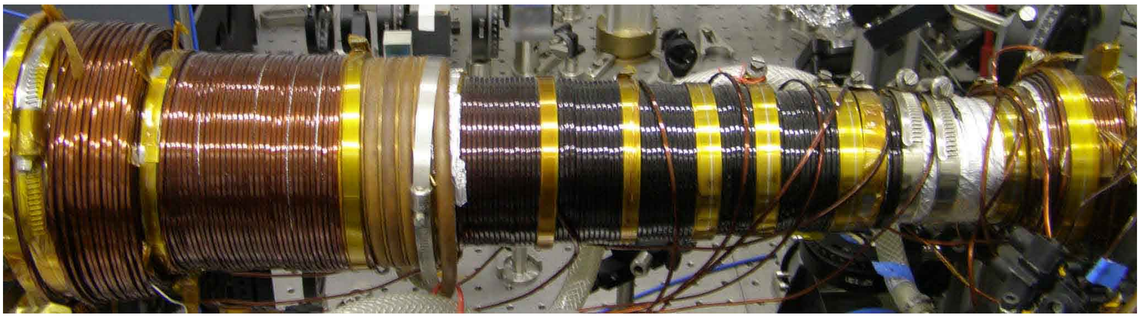

Figure 1.19: ^{6}*Li Zeeman slower.*

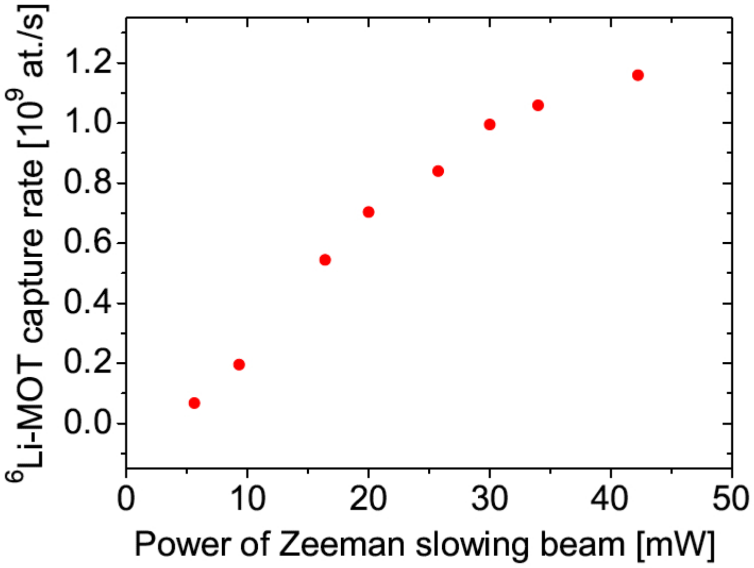

Figure 1.20: *^{6}Li capture rate as a function of the Zeeman slowing power. The repumping power is kept to 5.5 mW. With our 45 mW value we are in the saturation regime. The fact that this curve does not saturate around 8 mW, which corresponds to I_{sat} in the Zeeman slower, is due to the security factor α that shifts the atoms from resonance in the operating regime of the slower (see part 1.3.3), and to the gaussian beam profile that reduces the intensity seen by the atoms away from the axis of the slower.*

then covered it by two layers of water tubing, before winding the solenoids, to allow for efficient cooling during experimental operation.

1.3.8 Laser beam

As explained in part 1.3.2, the slowing laser beam is a bichromatic beam containing both the slowing and repumping frequencies. The first is amplified through a dedicated tapered amplifier, whereas the second is not amplified, as shown in Figure 1.7. Both beams are recombined on the lithium optical table (see part 1.2.1) and transferred towards the main table through a polarization maintaining single-mode optical fiber. The total power equals 50 mW, with 8 times more slowing than repumping power in the optimal case (see Figures 1.20 and 1.21). In order to take into account the divergence of the jet, and to add a transverse cooling effect, the slowing beam is first extended and then focalized on the oven. Thus, the diameter equals 31 mm at the MOT center. Using those numbers we estimated the resonant saturation parameter s_0 to be of the order of 6. Both frequencies are red detuned by $\delta = -75\,\Gamma$ (see Figure 1.6) and their linear polarizations are converted into a σ^+ one, with respect to the entrance field of the Zeeman, using a polarizing beam-splitter and a quarter-wave plate. Note that, due to the different Zeeman effects occurring for the two hyperfine ground-states [69], the repumper light is resonant only in the inversion region where $B = 0$. Note also that, since the polarizations of both frequencies are orthogonal due to their recombination on a polarizing beam-splitter before the fiber, we loose 50 % of the power on the polarizing

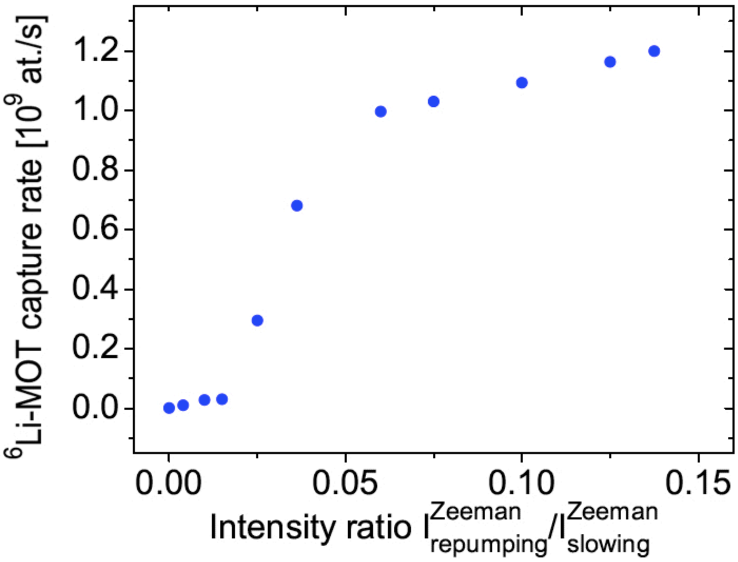

Figure 1.21: *^{6}Li capture rate as a function of the ratio between Zeeman repumping and slowing intensities. The slowing power is kept to 45 mW. We see that without repumping the efficiency of the slower is very small, which we attribute to the zero field depolarizing region of the spin-flip slower. On the other hand, we only need a few milliwatts of repumper light since the efficiency saturates quickly.*

beam-splitter that is placed after the fiber and before the quarter-wave plate. Even if we did not have any lack of optical power at the time of this thesis, we could avoid this loss in the future by mixing both frequencies with the same linear polarization before the fiber, using a small angle between the beams.

1.4 ^{40}K 2D magneto-optical trap

As for ^{6}Li, due to the low saturated vapor pressure of ^{40}K, we can not use a direct 3D magneto-optical trap loading from a vapor in the case of ^{40}K. Moreover, the natural isotopic abundance of ^{40}K equals 0.012 % (see part 1.2.3), thus the other isotopes would pollute strongly the vacuum quality. Thus, we also need an atomic source for ^{40}K. Nevertheless, the Zeeman slowing technique presented in section 1.3 would not be a relevant choice due to the low abundance of ^{40}K. Even with an enrichment of a few percent, the Zeeman slower would require a strong heating and thus a large consumption of the expensive enriched ^{40}K. We thus decided to a implement another efficient loading technique, requiring a smaller temperature : the 2D magneto-optical trap (2D-MOT) [80, 81]. Even if it is less robust than a Zeeman slower, since it depends on precise beam alignment and power, it offers the advantage of avoiding the bias magnetic field of an inverted slower (see part 1.3.2). Once our 2D-MOT was optimized, we could get a ^{40}K flux of 1.4×10^9 atoms.s^{-1}.

In this section, we present first a description of the 2D-MOT, including our coils design. Then, we turn to technical aspects about the vacuum, before giving an experimental characterization of the 2D-MOT optics and the atomic jet.

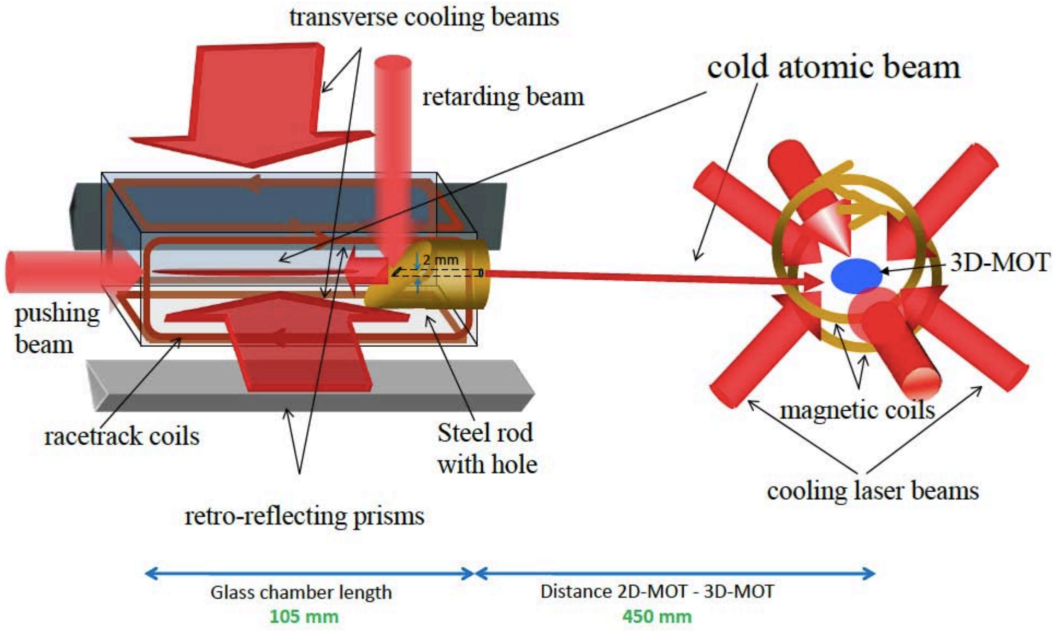

Figure 1.22: *Scheme of the ^{40}K 2D-MOT loading of the MOT.*

1.4.1 Description

A schematic drawing of our 2D-MOT is given in Figure 1.22. The principle is similar to the one of the 3D MOT (see part 2.1): a combination of red-detuned counter propagating laser beams slows down the atoms at the center of a magnetic quadrupole trap. However, as indicated by its name, the 2D-MOT works in two dimensions, transversally to the jet axis. In the longitudinal direction there is *a priori* no cooling effect, and the central line is characterized by a zero field so that there is no trapping along this axis. Nevertheless, in our case we add a 1D optical molasses in this direction [80] in order to cool down the sample further, and we increase the power of the pushing beam with respect to the one of the retarding beam, in order to push the atoms towards the MOT region, 45 cm further. For this purpose, there is a 2 mm hole placed on the 45° retro-reflecting mirror of the retarding beam to allow for the atoms to pass through.

The hole in the retro-reflecting mirror plays two additional roles. First, it serves as differential pumping tube, as described in part 1.4.2. Secondly, it collimates the atomic jet by spatial filtering of the transverse velocities, similarly to the Zeeman slower tubes (see part 1.3.4). Note that this transverse filtering ensures as well that the exiting atoms are longitudinally cooled. In fact, an atom with a small longitudinal velocity will spend a longer time in the transverse cooling region than an atom with a higher longitudinal velocity. Therefore, its transverse velocity will be more efficiently reduced. Thus, in average, longitudinally slow atoms will be less filtered out by the hole than the others, inducing an effective cooling effect of the distribution after the hole.

The 2D-MOT chamber consists of a rectangular parallelepipedic glass cell of $110 \times 55 \times 55$ mm^3 (see Figure 1.22). It is connected to the octagonal MOT chamber through a 45 cm DN38 tubing (see Figure 1.1), including an inner differential pumping tube and a separation Ultra-High Vacuum (UHV) valve from MDC-Caburn. The retro-reflecting mirror, inside the glass cell, is a 45° polished stainless steel mirror, with 50 % nominal reflectivity. It has a 2 mm hole at its center in order to let the atomic jet exiting the cell towards the MOT.

Four home-made rectangular coils are placed around the cell in a PVC cage system. They create a transverse quadrupole profile which is invariant by longitudinal translation, if we neglect the border effects. Each coil is connected by an individual 15 V-10 A Delta power supply for fine tuning of the field profile, as explained in part 1.4.3. The transverse gradient around the central line equals 11 G.cm^{-1}.

1.4.2 Vacuum and pressure

The potassium atoms originate from a 100 mg Technical Glass ampoule with an enriched vapor of 4 % in ^{40}K. This sample costs around 1000 € per milligramme of ^{40}K which is expensive. The ampoule is placed inside the vacuum in a soft DN16 bellow appendix connected through a UHV valve to the intermediate region in between 2D-MOT and MOT (see Figure 1.1). However, note that due to the presence of a differential pumping tube (see engineering drawing in appendix A.6), there is no direct connexion between the ampoule and the MOT region, without passing by the 2D-MOT cell. The ampoule could be broken after baking by simply bending the bellow.

The partial pressure of ^{40}K is of the order of 10^{-9} mbar at room temperature [56], which is not sufficient enough to have a good atomic flux exiting from the Zeeman. Our pressure measurements by absorption in the cell [82] showed that the optimum loading rate of the MOT is obtained for a 2.3×10^{-7} mbar total potassium pressure, which corresponds to 45°C. Under this value, the rate increases linearly with the pressure. Above, it decreases because of the collisions that start to play a role. Thus, we heat the 2D-MOT region to 45°C using a similar system as the one used for the lithium oven (see part 1.3.6), including the regulating circuit and thermocouple, as well as the thermocoax connected to an AC Transformer (Variac).

Due to the heating of the potassium ampoule, the vacuum quality would reduce in the MOT region. Therefore, in order to prevent the 2D-MOT region from polluting the MOT region, it is compulsory to add a differential pumping stage in between. It consists of three joined pipes (see engineering drawing in appendix A.6): the cylinder hole in the mirror (see part 1.4.1) of 2 mm diameter and 20 mm length, a tube of 5 mm diameter and 116 mm length, and a tube of 10 mm diameter and 86 mm length. Then, there is a standard DN38 tube over a distance of $\sim$ 25 cm, including the separation valve, until the center of the MOT chamber, the latter being pumped by a 40 L.s^{-1} Varian ion pump. Using similar calculations as the one developed in part 1.1.3, we estimate the MOT pressure to be approximately 340 times lower than the 2D-MOT one, that is of the order of 7×10^{-10} mbar, which is reasonable for MOT operation.

Let us finally estimate the lifetime of our potassium reservoir. Since the 2D-MOT region is connected to a 20 L.s^{-1} ion pump and isolated from the MOT region by the differential pumping tube described above, the lifetime of the potassium is directly given by the effective pumping speed S of the pump. Assuming an ideal gas law, as in part 1.3.5, the mass loss rate is given by:

$$\Gamma_{\mathrm{m}} = \frac{P_{\mathrm{sat}}(T)}{k_{\mathrm{B}}T} mS \ ,$$

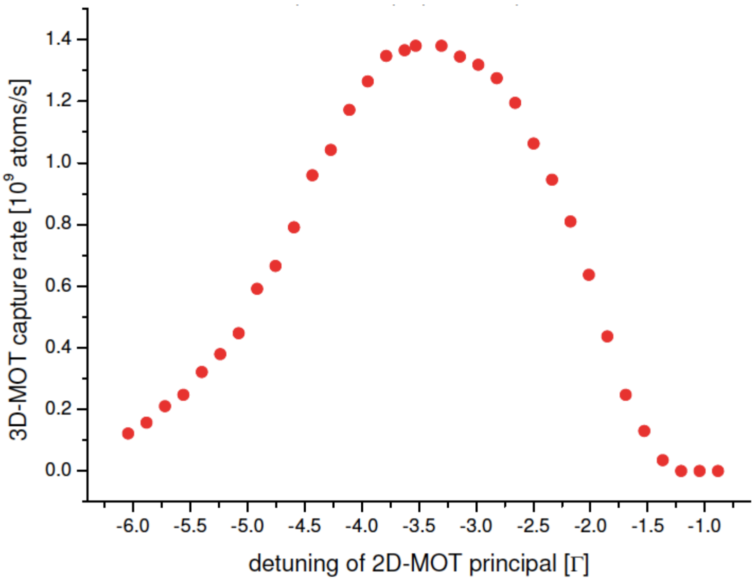

Figure 1.23: *^{40}K MOT loading rate as a function of the detuning of the cooling light.*

where m is approximated by the ^{39}K mass, since this is the more abundant isotope. Using the numbers given above, and $S \approx 9$ L.s^{-1}, due to the approximate 50 cm long DN38 tube between the pump and the cell (see equations 1.1 and 1.2), we find a lifetime of the sample of 3.2×10^7 s, which is of the order of two years of 12 hours operating days. Nevertheless, note that in principle the pumped potassium could be recycled by heating the pump.

1.4.3 Laser system

The cooling and repumping lights used for the 2D-MOT beams and the 1D molasses come from a single bichromatic beam originating from the potassium optical table (see part 1.2.1). As shown in Figure 1.7, the principal and repumping beams are recombined before a tapered amplifier in which they are amplified. After a single-pass AOM used as a switch, the beam is sent to the main table through a polarization-maintaining single-mode optical fiber. Its total power equals 450 mW, with a third of it attributed to the repumper. This optimal value is quite high and we attribute it to the small hyperfine structure of the excited state of ^{40}K. The cooling frequency is red-detuned by -2.5 Γ and the repumping one by -3.5 Γ (see Figure 1.6). We see on Figure 1.23 that there is a MOT-like trade-off behavior as far as the cooling detuning is concerned: high detunings lead to bigger capture speeds, since $v_{\mathrm{cap}} \approx -\delta/k$ due to the Doppler resonance condition (see part 2.1.7), whereas low detunings increase the cooling force.

Then, the beam is expanded with a telescope to a diameter of 27.5 mm before being divided into two parts using a polarizing beam-splitter and a half-wave plate. The first part is dedicated to the transverse cooling. It contains 75 % of the power. The second part is dedicated to the 1D imbalanced molasses.

As shown in Figure 1.24, the transverse cooling power is not sufficient to reach sat-

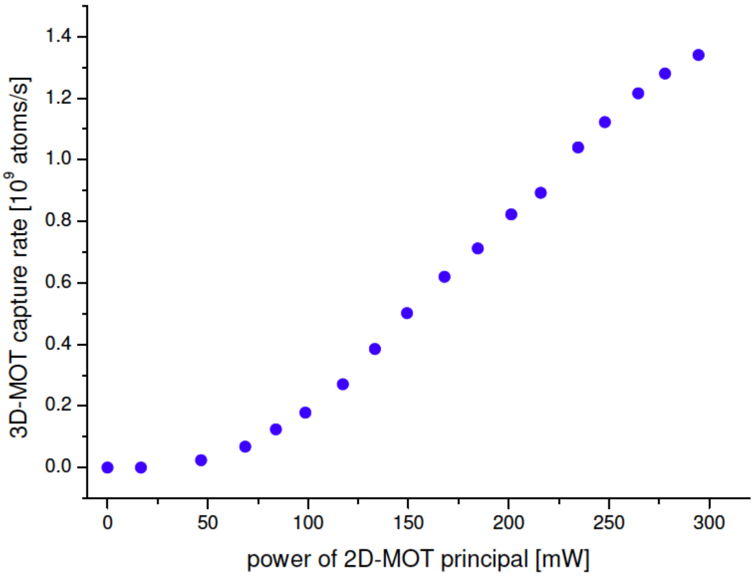

Figure 1.24: *^{40}K MOT loading rate as a function of the power of the transverse cooling light, the ratio between repumping and cooling powers being kept constant.*

uration, but gives an acceptable MOT loading rate. The transverse beam is doubled in size along the atomic jet direction, using a cylindrical telescope, before being circularly polarized through a quarter-wave plate. The counter-propagating beam of each transverse direction is obtained by a retro-reflexion on a prism, fixed on a micrometric mount (Newport M-UMR5.16) which has the property to conserve the helicity and the direction after reflexion on its 90° corner. Due to 20 % losses in the glass cell and the prism, leading to a subsequent power imbalance in a given transverse direction, the quadrupole zero line is slightly shifted by changing the individual currents of the coils (see part 1.4.1) in order to optimize the MOT loading rate.

The beam dedicated to the longitudinal 1D imbalanced molasses contains the remaining 25 % of the initial power. It remains linearly polarized, since we do not have any trapping in the longitudinal direction, and it is divided in two parts using another polarizing beam-splitter and a half-wave plate. The first ones serves as a pushing beam and contains 85 % of the molasses power, which corresponds to the optimal loading rate as shown in Figure 1.25. As a remark, this high ratio between pushing an retarding beam is due to the fact that just above the hole there is no pushing beam anymore due to the presence of a dark cylinder. Thus, the retarding beam pushes the atoms down to the mirror or to the walls of the hole, if the initial pushing acceleration is not sufficient.

1.4.4 Atomic jet

In this part, we describe the atomic jet obtained with the optimal parameters given in the previous ones. First, we could get two important pieces of information by recording the number of atoms in the ^{40}K MOT, after having switched on the 2D-MOT, and during short times in order to neglect the one and two body losses that

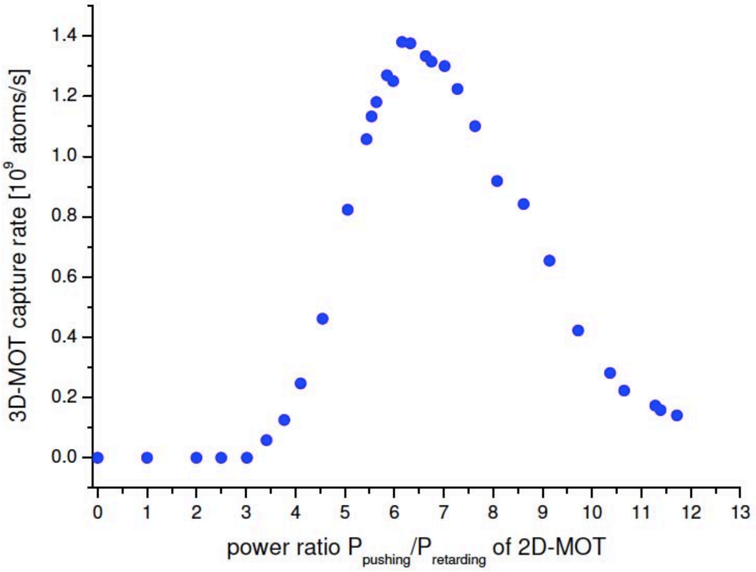

Figure 1.25: *^{40}K MOT loading rate as a function of the intensity ratio between the pushing and retarding beams of the 1D molasses.*

occur at high numbers of atoms. Results are shown in Figure 1.26. Assuming a ballistic evolution, which means neglecting the collisions, is a valid hypothesis at our 2D-MOT temperature according to [82]. In that case, the delay of 23 ms observed on the graph between the switching on of the 2D-MOT and the loading of the MOT is directly due to the time needed for the jet to reach the octagonal MOT chamber. If we divide the average length of 50 cm between the two traps (see Figure 1.22) by this delay, we get an estimate of the jet velocity. It is of the order of 22 m.s^{-1} which is close from the ^{40}K MOT capture speed that equals $\sim$ 14 m.s^{-1} (see part 2.1.7), leading to a better capture efficiency than the ^{6}Li Zeeman slower. In addition, the slope of the curve gives the loading rate. It equals 1.4×10^9 atoms.s^{-1}, which is close from the one we have for the ^{6}Li Zeeman slower (see part 1.3.5).

Another feature of the atomic jet, as for the ^{6}Li Zeeman slower (see part 1.3.4), is its divergence. Using the dimensions of the differential pumping tubes given in part 1.4.2, we see that the second tube is the one limiting the angle. The half-angle divergence is approximately 20 mrad, which means a maximal transverse displacement of 1 cm at the MOT center. This value is slightly smaller than the radial size of the MOT beams (see part 2.3.1). Therefore, in contrast with the ^{6}Li Zeeman slower, the divergence of the 2D-MOT is not critical.

In this calculation, we forgot gravity. This approximation is relevant since in $\tau =$ 23 ms the transverse displacement equals $g\tau^2/2 \approx 2.6$ mm, which is small compared to the divergence itself.

In conclusion, our 2D-MOT technique seems more efficient than our Zeeman slower, both in terms of velocity and divergence, demonstrating that this was a good choice for this expensive rare element. However, the loading rate remains very close from the one obtained for ^{6}Li, which comes from the fact that ^{40}K is only present to 4 % in the potassium ampoule, whereas ^{6}Li is nearly pure in the lithium oven. With ^{39}K, we

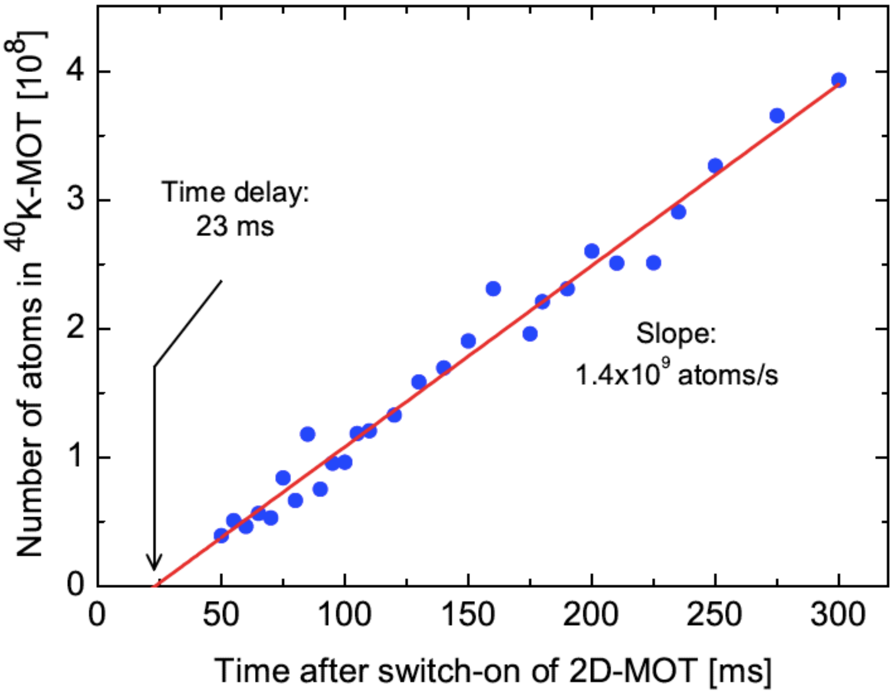

Figure 1.26: *Number of* ^{40}*K atoms in the MOT as a function of time.* $t = 0$ *corresponds to the switching on of the 2D-MOT.*

would expect a 25 times higher loading rate.

1.5 Computer control

Some particular stages in the experimental sequence require accurate timings. For instance, the ^{40}K optical pumping (see part 3.2.3) lasts 50 μs. Moreover, several tasks have to be performed simultaneously. Before magnetic trapping, we have to hide simultaneously the beam with mechanical shutters, switch off their AOM and shift their frequencies, while switching off the field and starting the optical pumping sequence. Therefore, the experiment is controlled via two computers, connected together through a dedicated network. One main National Instrument computer contains the main program as well as the analog and digital cards. One analysis Dell computer contains the imaging software (see part 2.2.2) as well as the transport program (see part 4.5.6) and stores the experimental data.

The main computer is connected to an external Digital Output/Input (DOI) board, which serves as an independent clock, with a clock rate of 20 MHz. Therefore, a computer slow down does not affect the experiment. Because of the high loading time requested by the big number of time steps, and since the typical timing of the experimental control is not below 1 ms, the clock step is increased to 500 μs. However, imaging and spin-polarization request fast sequences. Thus, for imaging, the time step is reduced to 10 μs, whereas for spin-polarization, the fast sequence is loaded into an external Stanford Research Systems (SRS) arbitrary function generator, which is triggered by the slow sequence (see part 3.2.3). In all cases, the DOI board is preloaded with the experimental sequence and then runs it through three analog cards and two digital ones. The analog cards (National Instruments PXI-6713) contain 8 BNC output ports each, delivering voltages up to 10 V with a maximal power of 2.5 W. Each digital card (National Instruments PXI-6533) contains 5 registers of 8 ports that deliver 0-5 V TTL signals.

Analog ports control either the Voltage Control Oscillators of the AOMs, or the output voltage of the power supplies. In both cases, the outputs are isolated from the command. However, this is not the case for the digital outputs, because they control the switching of the circuits involving the previous power supplies, through Metal-Oxide Semiconductor Field-Effect Transistors (MOSFET) and Insulated Gate Bipolar Transistor (IGBT). Thus, since the card can be damaged by high feedback currents passing through the gates of those transistors, we isolated the card and the experiment by optocouplers (Avago Tech ACPL-J313). The isolation box and its power supply were designed with engineer Toufik El Atmani, and assembled by Lionel Pérennès, both from the electronics workshop of Laboratoire Kastler Brossel. The principle is very similar to the isolation part of the transport logics box (see Figure 4.31).

The main program is written in C#. The interface window is divided in columns of chosen durations, each line corresponding to a port where the desired value is entered. In addition to constant values, it allows to ramp some signals from their initial values to the entered ones, during the column duration. It also allows to loop a given sequence, while scanning some parameters. After each sequence, an ASCII file containing all the values is saved on the analysis computer, which is of great help for debugging and data analysis. Symmetrically, the program can read a wave from an external ASCII file and assign it to a given port. This is the strategy we used for the transport sequence as described in part 4.5.6. Note that we recently decided to replace the main program by a similar but more versatile control software: Cicero Word Generator, which is available online and was written by Aviv Keshet, in the group of Wolfgang Ketterle at MIT. Its full implementation in our experiment will be performed soon.

1.6 Summary

In this chapter, we presented our experimental setup.

First, we assembled an ultra-high vacuum chamber allowing for a residual pressure inferior to 10^{-11} mbar in the final cell, through several differential pumping tubes. Then, using a Master Oscillator Power Amplifier (MOPA) scheme, we prepared a powerful laser system giving typical powers of 500 mW for each species, at several stabilized frequencies. The whole experiment is computer controlled.

Finally, we designed two performing atomic sources: a ^{6}Li Zeeman slower, with a loading rate in the MOT of 1.2×10^9 atoms.s^{-1}, and a ^{40}K 2D-MOT, with a loading rate in the MOT of 1.4×10^9 atoms.s^{-1}.

Using this system, we can load a large double ^{6}Li-^{40}K MOT, as developed in chapter 2.

Chapter 2

Magneto-optical trap

In chapter 1, we described the vacuum chamber as well as the two laser systems, the two atomic sources and the computer control. In the present chapter, we focus on the obtention of a large double ^{6}Li-^{40}K Magneto-Optical Trap (MOT) of respectively 5×10^9 and 8×10^9 atoms. This achievement is summarized in a dedicated publication [79]. In addition, we present the recent photoassociation of heteronuclear ^{6}Li^{40}K* molecules in the MOT chamber. This result is the main topic of a coming publication [83].

The chapter is divided as follows. First, we present the principle of magneto-optical trapping. Then, we describe the imaging diagnostics that allow us to observe and analyze the trapped atomic clouds, before presenting the experimental characterization of the single-species and double-species traps. Finally, we present the first photoassociation of cold ^{40}K^{40}K* homonuclear molecules, and cold ^{6}Li^{40}K* heteronuclear molecules.

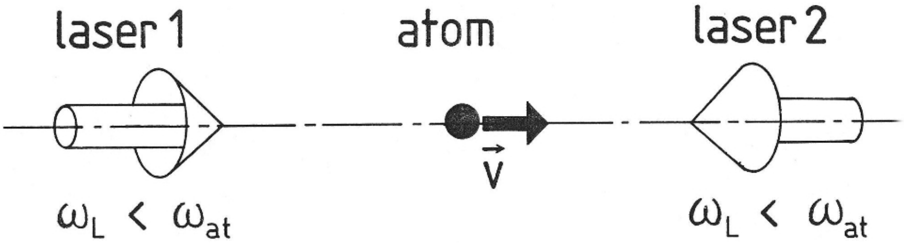

Figure 2.1: *1D principle of Doppler cooling. The counter-propagating laser beams of pulsation* ω_L *are red-detuned with respect to the atomic transition of pulsation* ω_{at}*. Then, for an atom of velocity* $\boldsymbol{v}$ *and a laser wave-vector* $\boldsymbol{k}$*, the Doppler effect* $-\boldsymbol{k}\cdot\boldsymbol{v}$ *compensates the red-detuning only for* $\boldsymbol{k}\cdot\boldsymbol{v} < 0$*. As a consequence, an atom preferentially absorbs a photon of opposite impulsion, and thus is slowed by its recoil impulsion. Picture taken from [73].*

2.1 Principle

After several attempts with direct evaporative cooling on hydrogen [84], the magneto-optical trap (MOT) was found to be a key intermediate stage in the production of the first BEC [9]. It is now commonly used in cold atoms experiments as an efficient technique to precool down alkali atoms, or atomic mixtures [85], to a few hundreds of microkelvins.

In this section, we present the general principles of the MOT, including the cooling and trapping forces, the Doppler temperature and the rescattering process. We finally estimate the phase space-densities and the trap depths of the ^{40}K and ^{6}Li single species MOTs.

2.1.1 Doppler cooling

In a first approximation, the MOT cooling principle is the Doppler cooling, which is depicted in 1D in Figure 2.1. The counter-propagating laser beams are red-detuned. Then, for an atom of velocity $\boldsymbol{v}$ and a laser wave-vector $\boldsymbol{k}$, the Doppler effect $-\boldsymbol{k}\cdot\boldsymbol{v}$ compensates the red-detuning only for $\boldsymbol{k}\cdot\boldsymbol{v} < 0$. As a consequence, an atom preferentially absorbs a photon of opposite impulsion, and thus is slowed by its recoil momentum. Since the subsequent spontaneous emission is isotropic, it does not contribute to the average velocity of the atom.

2.1.2 Zeeman trapping

The trapping principle is explained on picture 2.2. For a pedagogical purpose, we depicted a simple two level transition in 1D: from $F = 0$ to $F' = 1$, in a quadrupolar field (see part 3.1.1). Due to Zeeman effect, and since the beams are red-detuned and have opposite σ-polarizations, the beam coming from the right is more resonant with an atom placed on the right than the beam coming from the left, leading to a pushing in the left direction, and thus a restoring force.

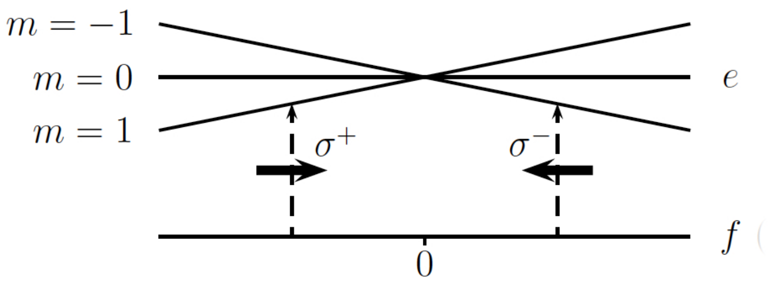

Figure 2.2: *1D principle of a magneto-optical trap. For a pedagogical purpose, we depicted a simple two level transition: from* $F=0$ *to* $F'=1$*, in a quadrupolar field chosen to be positive on the right and negative on the left. Thus, the Zeeman effect increases the energy of* $m=1$ *on the right, and decreases it on the left. Then, due to the positive helicity of both laser beams, we have a* σ^- *polarization on the right and a* σ^+ *one on the left. Since the beams are red-detuned, the beam coming from the right is more resonant with an atom placed on the right than the one coming from the left, leading to a pushing in the left direction, and thus a trapping at the center.*

Figure 2.3 shows a 3D drawing of a MOT. The principle is similar to the one introduced in 1D: in addition to the 3D quadrupolar magnetic trap generated by a pair of anti-Helmholtz coils, two counter-propagating laser beams per direction of space slow down the atoms at the center of the trap.

2.1.3 Total force

Let us now combine quantitatively the cooling and trapping principles introduced in part 2.1.1 and 2.1.2. At low intensity ($s_0 = I/I_{\text{sat}} << 1$), we can approximate the MOT force by the sum of the radiation pressures [76] of the two counter-propagating cooling beams. Thus, in 1D along z, the total MOT force $\boldsymbol{F}(z,v) = F(z,v)\boldsymbol{u_z}$ is given by:

$$F(z,v) = \hbar k \frac{\Gamma s_0}{2}\left(\frac{\Gamma^2/4}{(\delta - kv - \mu_{\mathrm{B}} bz/\hbar)^2 + \Gamma^2/4} - \frac{\Gamma^2/4}{(\delta + kv + \mu_{\mathrm{B}} bz/\hbar)^2 + \Gamma^2/4}\right), \quad (2.1)$$

where $\boldsymbol{k} = k\boldsymbol{u_z}$ ($k > 0$) is the wave-vector of the laser propagating towards increasing z, and where the magnetic gradient b is positive, by our choice of current orientation. Figure 2.4 shows a plot of $F(0,v)$. For instance, we see that for $v > 0$ the force is negative, leading to a friction effect. Moreover, around $v = 0$, this force can be developped as a linear friction. The same arguments stand for the plot of $F(z,0)$, for which we obtain a spring-like restoring force around the center.

Let us make three comments here. First, expression 2.1 is not valid anymore for intensities of the order of I_{sat}. An exact expression would take into account the total local field amplitude and the interferences, as well as the saturation of the atomic transition. Secondly, this cooling and trapping technique based on resonant light absorption contains some fundamental limits as far as the maximal achievable phase-space density is

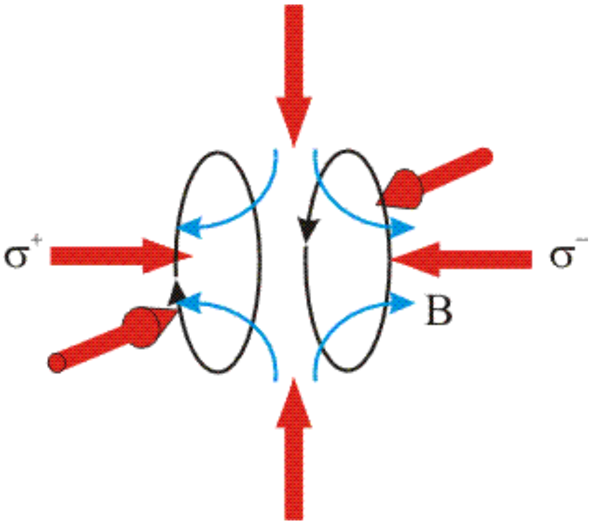

Figure 2.3: *Schematics of a magneto-optical trap. In addition to quadrupolar magnetic trapping (field lines in blue), generated by a pair of anti-Helmholtz coils (see part 3.1.1), a radiative cooling is realized through two counter-propagating laser beams per direction of space (red). Those two beams have opposite circular polarizations with respect to the chosen quantification axis.*

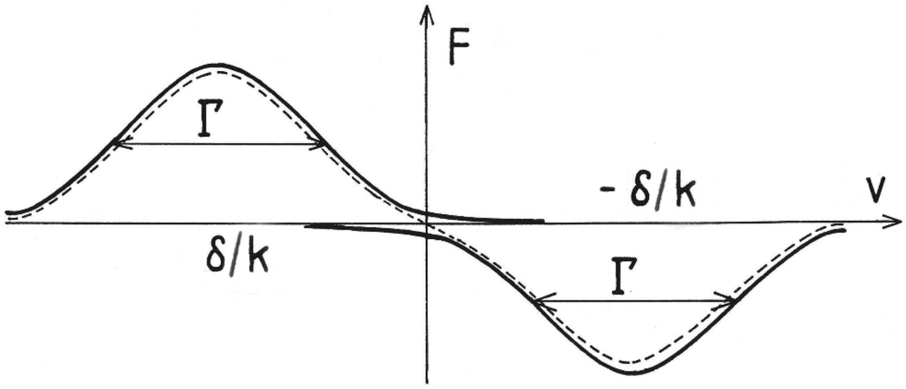

Figure 2.4: *1D total MOT cooling force (dashed line) at the center of trap as a function of velocity (see expression 2.1). The single radiation pressures of each laser beam are plotted in solid line. For* $v > 0$*, the force is negative, leading to a friction effect. Around* $v = 0$*, the force can be developped as linear friction. Picture taken from [73].*

concerned. We study this further in part 2.1.5 and 2.1.4. Thirdly, a two-level atom is needed for the resonance condition to remain identical. This can be approximated by a closed transition in presence of σ-polarized light. Nevertheless, the hyperfine structures of the excited states of ^{6}Li and ^{40}K (see Figure 1.6) are so small that such a closed transition does not exist in our case, leading to losses towards the wrong hyperfine ground-state. Thus, it is compulsory to add a repumping light in the experiment, in order to bring back the atoms in the cooling transition.

2.1.4 Doppler temperature

In this part, we recall a simple Doppler model in order to estimate the temperature in a MOT. For this purpose, we restrict ourselves to a two level atomic spectrum. During the absorption-emission cycles, since the spontaneous emission is a random process, the MOT atoms follow a random walk in momentum space with a step of the order of the photon momentum $\hbar k$. This process heats the atoms and thus limits the minimal temperature we can obtain by laser cooling. We now estimate the minimal temperature reachable in our ^{6}Li-^{40}K MOT. As for any random walk, the variance of the atomic momentum $\langle p^2 \rangle$ follows a diffusion process:

$$\frac{\mathrm{d}\langle p^2 \rangle}{\mathrm{d}t} = 2D \ ,$$

where D is the diffusion coefficient whose exact calculation can be found in [86]. Let us estimate it with simple arguments here. D should be homogenous to a momentum squared divided by a time. The typical momentum of this problem is the recoil momentum $\hbar k$, and the typical time is the inverse of the cycling rate Γs, where s is the saturation parameter. Thus, we can write:

$$D = (\hbar k)^2 \Gamma s \ . \tag{2.2}$$

For this process the fluctuation-dissipation relation is given by:

$$k_B T = \frac{D}{\gamma} \ , \tag{2.3}$$

where γ is the friction coefficient, obtained by linearizing the MOT cooling force (see equation 2.1) $\mathbf{F}_{\mathrm{cool}}$ around null velocities:

$$\mathbf{F}_{\mathrm{cool}} = -\gamma \boldsymbol{v} = 2\hbar k^2 s \frac{\Gamma \delta}{\delta^2 + \Gamma^2/4} \mathbf{v} \ .$$

Combining this expression with equations 2.2 and 2.3 leads to the equilibrium condition:

$$k_{\mathrm{B}} T = \frac{\hbar \Gamma}{2} \frac{\delta^2 + \Gamma^2/4}{\Gamma |\delta|} \ . \tag{2.4}$$

When $\delta = -\Gamma/2$, this quantity reaches a minimum given by $k_{\mathrm{B}} T_{\mathrm{D}} = \hbar\Gamma/2$. T_{D} is called the Doppler temperature and equals approximately 140 μK for ^{6}Li and ^{40}K (see appendix A.1). Putting the detunings of our double MOT (see table 2.1) in equation 2.4 gives: $T^{\mathrm{K}} = 225\ \mu$K and $T^{\mathrm{Li}} = 358\ \mu$K. Those values are slightly higher than the Doppler temperature, since the optimal detunings are different from $-\Gamma/2$ (see part 2.3.2).

One should keep in mind that other effects are not taken into account in this simple estimate. For instance, in the case of ^{40}K, the sub-Doppler mechanisms linked to the hyperfine structure of the atomic spectra can reduce the minimal temperature [87, 88, 89]. For ^{6}Li, on the contrary, due to the small hyperfine splitting of the excited state the sub-Doppler cooling is reduced.

2.1.5 Light rescattering

In a MOT, atoms are continuously absorbing and emitting resonant photons. As a consequence, the light absorbed by an atom is reemitted and can be absorbed by another one. At high densities, this generates an average repulsive force [90] that, among other effects such as oscillations [91], limits the density. Let us consider two atoms separated by a distance r and introduce the saturation parameter:

$$s = \frac{I}{I_{\text{sat}}} \frac{(\Gamma/2)^2}{\delta^2 + (\Gamma/2)^2} ,$$

In our MOT, according to table 2.1, we have $s^{\text{K}} \approx 30$ % and $s^{\text{Li}} \approx 4$ %. Thus we can suppose $s \ll 1$ as a first approximation. Then, excited by the six detuned MOT laser beams, the first atom emits $6\Gamma s/2$ photons per second. The second one absorbs a fraction $\sigma/(4\pi r^2)$ of it, where we have introduced the absorption cross-section σ defined as:

$$\sigma = \frac{3\lambda^2}{2\pi} \frac{(\Gamma/2)^2}{\delta^2 + (\Gamma/2)^2} .$$

Therefore, including the photon linear momentum $\hbar k$, we find a radiative pressure force that repels the second atom from the first one:

$$\mathbf{F}_{\text{scat}} = 3\Gamma s \hbar k \frac{\sigma}{4\pi r^3} \mathbf{r} .$$

This is a long-range, repulsive, diatomic force analogous to the Coulomb one. Note that in fact σ should be replaced by the difference between emission and absorption cross sections $\Delta\sigma = \sigma_e - \sigma_a$ [90]. Using this force we can estimate the equilibrium density inside the MOT. Let us assume a constant density n in a spherical MOT of radius R. The Gauss theorem gives a total force which is linear with $\mathbf{r}$:

$$\mathbf{F}_{\text{tot}} = n\Gamma s \hbar k \sigma \mathbf{r} .$$

Atoms are also feeling the MOT trapping force (see expression 2.1), that can be approximated around the center, for a null velocity, by a spring restoring force:

$$\mathbf{F}_{\text{trap}} = 2k\mu b s \frac{\Gamma\delta}{\delta^2 + \Gamma^2/4} \mathbf{r} ,$$

where μ is the atomic magnetic moment and b the MOT gradient. For $\delta < 0$ those two forces are opposite. They equilibrate when:

$$n = \frac{16\pi\mu b}{3\hbar\lambda^2} \frac{|\delta|}{\Gamma^2} , \tag{2.5}$$

which does not depend on light intensity. Note that we can not increase too much $|\delta|$ since it would reduce the capture efficiency. We finally estimate the maximal density for each species using our optimized parameters reported in table 2.1: $n^{\mathrm{Li}} \approx 4 \times 10^{10}$ cm^{-3} and $n^{\mathrm{K}} \approx 2 \times 10^{10}$ cm^{-3}. Nevertheless, this simple model does not take into account a shielding effect, happening at high densities, that reduces the intensity seen at the center of the cloud. This would lead to an additional compression [92].

2.1.6 Phase-space density

To estimate how close from degeneracy we can be in a MOT let us calculate the phase-space density:

$$n\lambda_{\mathrm{dB}}^3 = n(2\pi m k_{\mathrm{B}} T_{\mathrm{D}})^{-3/2} \ ,$$

where we have introduced the de Broglie wavelength λ_{dB} and the atomic mass m. This ratio is of the order of 1 when the system reaches degeneracy. Using equations 2.5, 2.4 and table 2.1, we find $n\lambda_{\mathrm{dB}}^3 \approx 10^{-7}$ for ^{40}K and $n\lambda_{\mathrm{dB}}^3 = 2 \times 10^{-6}$ for ^{6}Li. As we can see, those values are far away from $n\lambda_{\mathrm{dB}}^3 \approx 1$. Magnetic trapping and evaporative cooling, described in chapter 3, will bridge the gap.

2.1.7 Capture velocity and trap depth

Let us now give an order of magnitude of the MOT depth. We can estimate the capture velocity by considering that the cooling force is maximal at resonance, that is for the Doppler condition (see Figure 2.4):

$$v_{\mathrm{cap}} \approx \delta/k \ .$$

Using our MOT values (table 2.1) this gives: $v_{\mathrm{cap}}^{\mathrm{K}} \approx 14$ m.s^{-1} and $v_{\mathrm{cap}}^{\mathrm{Li}} \approx 20$ m.s^{-1}. Converting this into temperatures leads to $T_{\mathrm{depth}}^{\mathrm{K}} \approx 0.9$ K and $T_{\mathrm{depth}}^{\mathrm{Li}} \approx 0.3$ K. As we can see, those trap depths are hundreds time bigger than the Doppler temperature estimated in part 2.1.4.

2.2 Imaging and analysis

In this section, we describe the imaging tools, fluorescence imaging and absorption imaging, and we illustrate the latter by characterizing the numbers of atoms, the densities and the temperatures of the single ^{40}K and ^{6}Li MOTS, as well as those of the double ^{6}Li-^{40}K MOT.

2.2.1 Fluorescence imaging

In the particular case of MOT, the cloud continuously absorbs the cooling photons, and reemits them by spontaneous decay. Thus, a MOT emits light as shown in Figure 2.5. This light can be collected by a lens and focused on a photodiode. Then, the number of atoms can be deduced from the signal, as explained in the following.

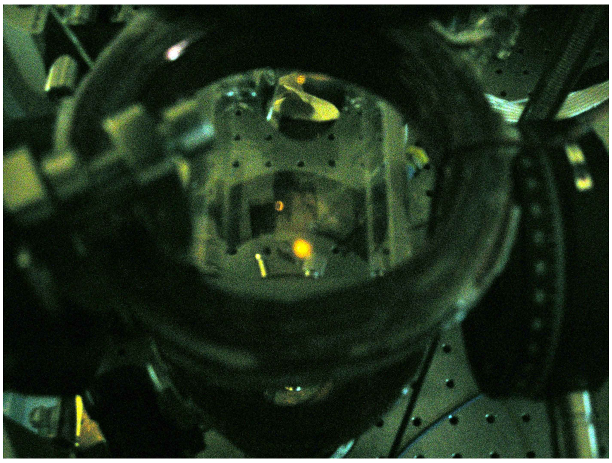

Figure 2.5: *Picture showing* ^{40}*K-MOT fluorescence in the preliminary experimental setup.*

Let us consider a cloud of N atoms. The steady-state population N_{e} of the excited state of the cooling transition is given by:

$$N_{\mathrm{e}} = \frac{1}{2}\frac{s_0}{1+s_0+(2\delta/\Gamma)^2}N \ ,$$

which corresponds to an emitted power of:

$$P = \frac{N\Gamma\hbar\omega_0}{2}\frac{s_0}{1+s_0+(2\delta/\Gamma)^2} \ . \tag{2.6}$$

The detected power P^* is then an angular fraction of P:

$$P^* = \frac{\pi r^2}{4\pi d^2}P \ , \tag{2.7}$$

where r is the radius of the collecting lens, placed at distance d from the cloud. Then combining equations 2.6 and 2.7, we obtain:

$$N = \frac{8d^2}{r^2}\frac{P^*}{\Gamma\hbar\omega_0}\frac{1+s_0+(2\delta/\Gamma)^2}{s_0} \ .$$

Note that this formula requests a calibration of the photodiode in power, and a precise calculation of the solid-angle. Furthermore, it is not valid at high numbers of atoms for which rescattering occurs (see part 2.1.5), and it contains some inhomogeneous Zeeman shift due to the presence of the quadrupolar magnetic field. Therefore, it is less precise than the absorption imaging technique (see part 2.2.2). We thus only use it, after calibration, as a diagnostic tool for optimization and control of the MOT concerning its position, shape, size, fluorescence level and loading time. Nevertheless, it has the great advantage to be a continous detection method, so that we used it for photoassociation experiments (see part 2.4), where the precise number of atoms was not of major interest.

Practically, we have two such diagnostics. One for each species. The fluorescence light is separated on a cube and sent to two identical detection systems. Each one consists of a $f = 4$ cm lens (1 inch diameter), a 10 nm interference filter centered on the desired wavelength, and a home-made amplified photodiode (Hamamatsu 1223018E) mounted on a micrometric xy-mount (Newport M-UMR5.16).

In addition, an infra-red TV-camera control system is continuously sending pictures from the fluorescence. It gives rudimentary information about the presence of clouds, its shape and its position. This information is collected in a different direction than the photodiodes one, leading to an overall 3D diagnostic.

2.2.2 Absorption imaging

This part is dedicated to the description of the absorption imaging diagnostics. First, we explain the principle of this method, by showing how we can obtain the 1D-integrated density profile of the cloud. Secondly, we present some technical aspects on the imaging beam. The imaging program Eric, written in Python, is identical to the one used in the lithium group at ENS [93].

Principle

The absorption imaging is based on the following principle. A resonant laser beam is sent on the atomic cloud, and the transmitted profile, after partial inhomogeneous absorption, is recorded on a Charge-Coupled Device (CCD) camera. For a given imaging direction x, the transverse intensity profile $I(y,z)$ on the camera equals:

$$I(y,z) = I_{\mathrm{bg}}(y,z) + T(y,z) \cdot I_0(y,z) \ . \tag{2.8}$$

In this formula, $I_{\mathrm{bg}}(y,z)$ is the background intensity on the camera, in absence of imaging beam. It includes the ambient light and the dark current of the camera. $T(y,z)$ is the transverse transmission profile due to the cloud, and $I_0(y,z)$ is the beam intensity at the camera position, in absence of atoms. The latter can be measured by taking a reference image of intensity $I_{\mathrm{ref}}(y,z)$, without atoms, and by substracting the background intensity:

$$I_0(y,z) = I_{\mathrm{ref}}(y,z) - I_{\mathrm{bg}}(y,z) \ . \tag{2.9}$$

Let us introduce the optical density $D(y,z) = -\ln[T(y,z)]$ along the beam path. At low intensity with respect to I_{sat} (see appendix A.1), $D(y,z)$ is determined by the 1D-integrated density profile through a Beer-Lambert law:

$$D(y,z) = \sigma \int_{-\infty}^{\infty} dx \ n(x,y,z) \ , \tag{2.10}$$

where $n(x,y,z)$ is the local density of the cloud, and σ the absorption cross-section at low intensity given by:

$$\sigma \approx C^2 \frac{\sigma_0}{1+(2\delta/\Gamma)^2} \ , \tag{2.11}$$

where $\sigma_0 = 3\lambda^2/(2\pi) = \Gamma\hbar\omega_0/(2I_{\mathrm{sat}})$ is the resonant cross-section, and C is the Clebsh-Gordan coefficient of the imaging transition. This coefficient equals 1 for a closed two level transition. When the atoms are not optically pumped to the cycling transition before imaging, which is our case, it is given by the average C^2 of all possible transitions, if we assume equally populated Zeeman levels. Then, it equals typically 0.5 for ^{6}Li and 0.4 for ^{40}K. Note that, at low intensity with respect to I_{sat}, σ does not depend on the imaging intensity (see equation 2.11), which is a key requirement of this imaging technique.

Finally, using equations 2.8, 2.9 and 2.10, we can summarize:

$$\int_{-\infty}^{\infty} dx\ n(x,y,z) = \frac{1}{\sigma} \ln \left[\frac{I_{\text{ref}}(y,z) - I_{\text{bg}}(y,z)}{I(y,z) - I_{\text{bg}}(y,z)} \right] . \tag{2.12}$$

We see that it requests three pictures to obtain the 1D integrated density profile: one in presence of the cloud; one reference picture without the atoms, by waiting enough time or detuning sufficiently the beam to avoid absorption; and one background picture, without atoms and beam. In part 2.2.3, we deduce some thermodynamical properties of the MOTs from this integrated density profile.

Imaging beam and camera

As described above, we need small imaging powers. Therefore, the imaging beam of each species is not reamplified through a tapered amplifier, but is directly collected from the output of the first optical fiber (see Figure 1.7). Note also that it does not contain the repumping frequency, since this makes no significant difference, as observed experimentally. However, in the particular case of Dark-MOT technique used for the MOT (see part 2.3.3), it is compulsory to perform a preliminary 500 μs hyperfine pumping before taking an image, in order to pump back the atoms from the wrong hyperfine ground-state.

On the main table, the beams of both species are combined into one single bichromatic beam using a dichroic mirror, before being expanded by a factor ten. Then, the bichromatic beam is divided into two parts using a broadband polarizing beamsplitter: one part for the MOT chamber imaging, the other one for the science cell imaging. Finally, each part is circularly polarized by a zeroth order quarter-wave plate at the potassium wavelength - which happens to work sufficiently well at the lithium wavelength. Both frequencies are resonant with the corresponding atomic transitions (see Figure 1.6), and their intensities are of the order of $s_0 = 1\%$ of I_{sat} (see appendix A.1). After the cloud, the exiting beam is focused on a CCD sensor by a 6 cm lens for the MOT chamber, and by a 7.5 cm lens for the science cell. In both cases, the magnification factor equals 0.4. The duration of each imaging pulse was chosen to be $\tau_{\text{im}} = 100\ \mu$s. This corresponds to $\Gamma \tau_{\text{im}} s_0/2 \approx 20$ photons absorbed per lithium atom during the imaging time, and thus a typical Doppler shift of typically $\Gamma/2$. Therefore, this imaging time is a maximal limit. In contrast, a smaller time would reduce the intensity-to-noise ratio, as observed experimentally.

To improve the accuracy of imaging, we can increase and fix the value of coefficient C^2 (see equation 2.11). For this purpose, we need to control the spin state of the atoms before imaging. An efficient solution is to switch on a small bias field after the magnetic trapping stage, in order to adiabatically bring the polarization of the atoms in the same orientation, without changing their internal spin state. We thus wound two

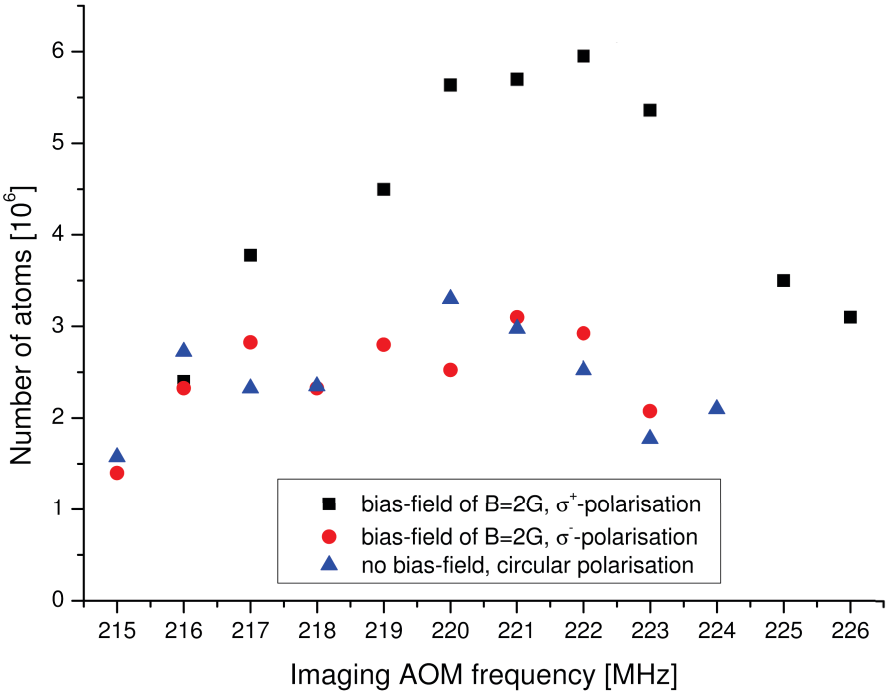

Figure 2.6: ^{40}K *Number of atoms in the science cell after 1.1 ms time-of-flight as a function of imaging frequency, for different imaging configurations. The bias field is vertical and parallel to the imaging beam.*

coils of ten turns and 5.5 cm radius in Helmholtz configuration and placed them in the same direction as the final quadrupole trap ones (vertical axis). In those coils, we pass a 5 A current which creates a bias field of the order of 2 G at the center. We checked experimentally that this could help, in combination with the σ^+ polarization of the imaging beam, to image the atoms into the closed transition: $|F = 9/2, m_F = 9/2\rangle$ to $|F' = 11/2, m'_F = 11/2\rangle$ for ^{40}K and $|F = 3/2, m_F = 3/2\rangle$ to $|F' = 5/2, m'_F = 5/2\rangle$ for ^{6}Li, and thus to ensure a $C^2 = 1$ coefficient, as for a two level transition. Figure 2.6 shows such a result. We actually find a factor 2 between the maxima.

As far as the CCD cameras are concerned, we use two Pixelfly cameras, one for each chamber. Their chip consists of 1394 × 1024 square pixels of size 6.45 μm. They can detect signals down to typically $s_0 \approx 10^{-8}$ for each species, which corresponds to the dark noise limit. The double tracks memory allows for a 5 μs delay between two single pictures, and it has a readout time of 45 ms. Thus, we could implement a fast imaging sequence, in order to limit the fluctuations between the imaging pulses: first, the main picture is taken; secondly, 2 ms after, the reference one is taken, with a $-10\ \Gamma$ detuning in order to have a transparent medium for the beam (since the cloud is still present after 2 ms); thirdly, the background picture is taken, 45 ms later. Such a normalized absorption picture is shown in Figure 3.8.

2.2.3 Analysis

As explained in part 2.2.2, the absorption imaging technique allows to get the 1D-integrated density profile. We can extract some relevant thermodynamical quantities of the cloud from this integrated profile, such as numbers of atoms, local densities and temperatures.

According to equation 2.12, the atom number is given by 2D-transversally integrating the optical density:

$$N = -\frac{1}{\sigma} \int_{-\infty}^{\infty} \int_{-\infty}^{\infty} dydz \;\; \ln[T(y,z)] \; . \tag{2.13}$$

Eric program offers to directly doubly integrate the optical density. It also displays the central optical density value. Using the optimal parameters of Table 2.1, we obtain single-species MOTs with large numbers of atoms: 8.9×10^9 for ^{40}K, and 5.4×10^9 for ^{6}Li, as plotted in Figure 2.7. Note that for the double ^{6}Li-^{40}K MOT, the numbers of atoms were slightly smaller: 8×10^9 for ^{40}K and 5.2×10^9 for ^{6}Li. This is due to inelastic interspecies collisions (see part 2.3.5). However, the optimal MOT parameters of Table 2.1 were chosen in order to minimize those losses.

Since most of the traps that we use have a cylindrical symmetry around a z-axis, the local density profile, and thus the sizes, are given by the inverse Abel transform of the optical density:

$$n(r,z) = \frac{1}{\sigma\pi} \int_{r}^{\infty} \frac{dy}{\sqrt{y^2 - r^2}} \frac{\partial \ln[T(y,z)]}{\partial y} \; , \tag{2.14}$$

where $r = \sqrt{x^2 + y^2}$. This integral can be evaluated numerically and we computed such a program. However, for the gaussian density case, it is easy to show that the optical density $D(y,z)$ is also a 2D-gaussian with the same widths. Thus, Eric program offers to directly fits the optical density by a 2D-gaussian, and displays the y and z-widths. With the parameters of Table 2.1, we find densities of 3×10^{10} atoms.cm^{-3} for ^{40}K, and 2×10^{10} atoms.cm^{-3} for ^{6}Li, which are of the same order as the ones estimated in part 2.1.5. Note that the typical diameter of the cloud is of the order of 1 cm in both cases.

Finally, we can deduce the axial temperatures of the cloud by performing a time-of-flight measurement. It consists in recording the diameter of the cloud under free expansion, for various times t after the switch-off of the trap. In fact, in a given axis x of ballistic expansion, the RMS position $\sigma(t) = \sqrt{< x(t)^2 >}$ is given by:

$$\sigma(t) = \sqrt{< [x(0) + v(0)t]^2 >} = \sqrt{\sigma(0)^2 + \frac{k_{\mathrm{B}}T}{m} t^2} \; , \tag{2.15}$$

where T is the initial temperature in the x axis, and m the atomic mass. Therefore, measuring the slope of $\sigma(t)^2$ as a function of t^2 gives the initial temperature. Using this procedure, we found $T = 290$ μK for ^{40}K, and 1.4 mK for ^{6}Li. Figure 2.8, shows a typical temperature measurement for ^{40}K. Those values are above the Doppler cooling limits calculated in part 2.1.4, mostly because of photon multiple scattering within the atomic cloud (see part 2.1.5). As a remark, using a cooling transition with a narrower

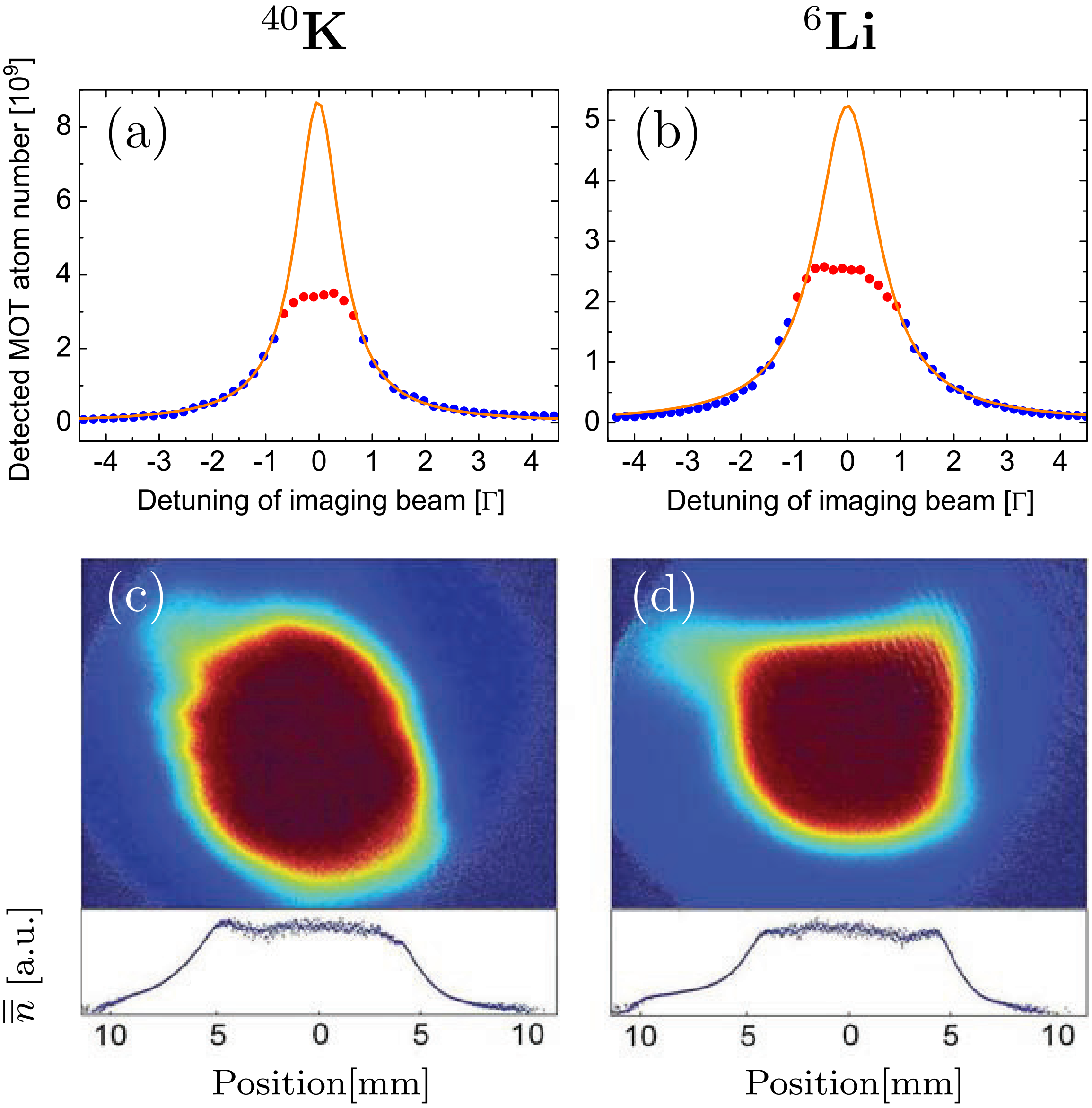

Figure 2.7: *Number of atoms in the single-species MOTs of* ^{40}K *(a) and* ^{6}Li *(b), as a function of the detuning of the imaging beam. The dots are the experimental data obtained by double integration of the optical density (see equation 2.13). Since on resonance the optical densities are too high, each graph saturates to a central plateau and thus deviates from the expected lorentzian curve. Therefore, the lorentzian fit (line) was performed on the wings only, with a fixed width that was measured independently at low numbers of atoms in the MOT. Below are shown the absorption images of* ^{40}K *(c) and* ^{6}Li *(d), as well as the 1D-integrated optical densities along the vertical direction, which are proportional to the doubly integrated atomic densities* $\bar{\bar{n}}$ *(see equation 2.10).*

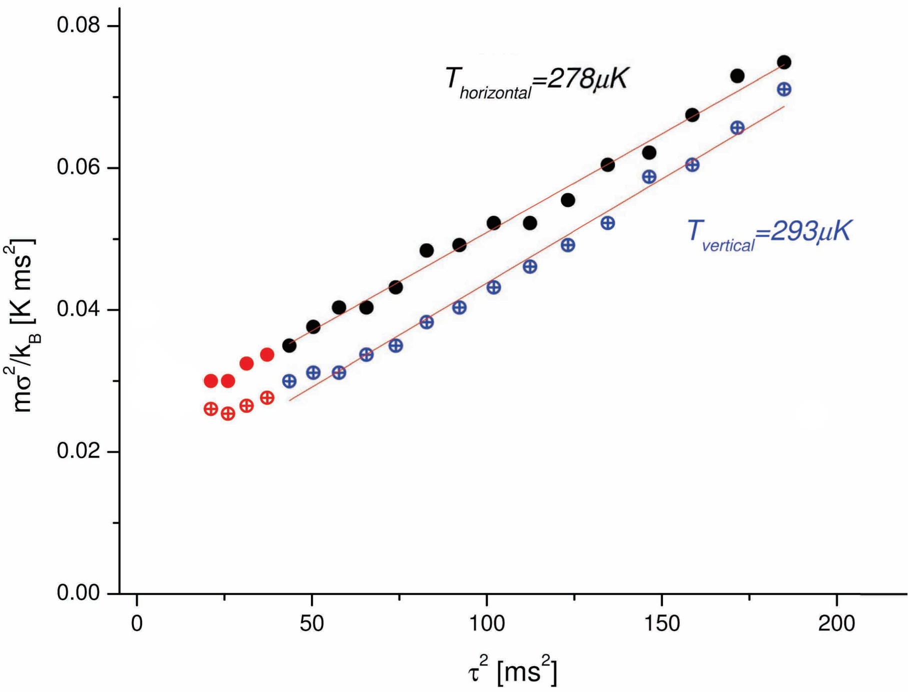

Figure 2.8: *Time-of-flight measurement of* ^{40}*K MOT temperature (see equation 2.15).*

linewidth, like the $4S_{1/2}-5P_{1/2}$ one for ^{40}K [94] or the $2S_{1/2}-3P_{3/2}$ one for ^{6}Li [95, 96], would help to decrease the Doppler temperature to a few tens of microkelvin. We plan to test this idea for ^{40}K with the 404 nm blue laser source that we built for high resolution imaging (see part 3.4.6). An alternative option would be to use sub-Doppler cooling [89, 97].

2.3 Experimental characterization

In section 2.1, we gave a simple theoretical picture of the MOT. Here, we present the experimental optimization and characterization of both single MOTs of ^{6}Li and ^{40}K, as well as the double ^{6}Li-^{40}K MOT. First, we describe the technical aspects about optics and coils and we summarize the optimal parameters. Secondly, we present the Dark-MOT scheme that allowed us to reach large numbers of atoms in the MOTs. Thirdly, we study the lifetime in the trap and the inelastic losses. Finally, we present the double species MOT and we quantify the interspecies collisions.

2.3.1 Practical aspects

Six beams are needed to generate the MOT configuration (see Figure 2.3). In addition, those beams should contain both cooling and repumping frequencies of each species (see part 2.1.3), and be σ-polarized (see Figure2.2). This configuration is achieved as explained in the following.

The bichromatic beams of each species (see part 1.2.1) are combined on the main

Physical quantity	^{40}K	^{6}Li
δ_{cool} [Γ]	-3	-5
δ_{rep} [Γ]	-5	-3
P_{tot} [mW]	220	110
$I_{\text{rep}}/I_{\text{cool}}$ [%]	5	20
$\partial B_z/\partial z$ [G.cm^{-1}]	8	8

Table 2.1: *Optimal parameters of the double ^{6}Li-^{40}K-MOT.*

table using a dichroic mirror. The resulting beam is expanded by a telescope to a 1.1 cm waist. Afterwards, using two broadband polarizing beam-splitters, and some broadband mirrors, the beam is separated into four parts. Before each cube, we use a combination of two fourth order half-wave plates: one at the lithium wavelength, the other at the potassium wavelength. In fact, a fourth order half-wave plate for the first species acts almost as a lambda-plate for the second species in our case, and thus does not change the second polarization. The four beams are attributed as follows: one of them is used for the down-up vertical beam; another one for the up-down beam; and the two others for the two horizontal directions. In each horizontal direction, there is a reflexion on a flat mirror after the chamber, in order to generate the counter-propagating beam. In addition, a $f = 10$ cm lens is placed before each retro-reflexion mirror, in order to focalize the beam before its second passing through the chamber, and to compensate the loss of intensity due to absorption in the first passing. Before entering the chamber, the MOT beams are polarized with the helicities depicted in Figure 2.3. As we can see, those helicities are identical for both beams in a given direction, leading to opposite σ-polarizations with respect to the field orientation. In addition, due to Maxwell's law $\boldsymbol{\nabla} \cdot \boldsymbol{B} = 0$, the field orientation is opposite between an horizontal direction and the vertical direction of the anti-Helmholtz pair (see equation 3.3). Thus, the helicities have to be opposite between the horizontal plan and the vertical axis.

As far as the MOT coils are concerned, we use the pair described in part 3.3.1 for the magnetic trap. It is fed by a single 45 V-140 A Delta power supply whose output is controlled in voltage (CV mode, see part 3.2.3) through the analog card of the National Instrument computer (see part 1.5). The pair resistance is $R = 0.178\ \Omega$ and it creates an axial magnetic gradient of 0.936 G.cm^{-1}.A^{-1}.

2.3.2 Optimized parameters

The optimal parameters of the double-species MOT were found to be those presented in Table 2.1. They allow us to generate the big and cold MOTs described in part 2.2.3. In this part, we present some optimization graphs on the single MOTs, about the powers and frequencies of the laser beams, as well as the dependency of the atom numbers on the magnetic field. In each of those graphs, all the constant parameters are fixed

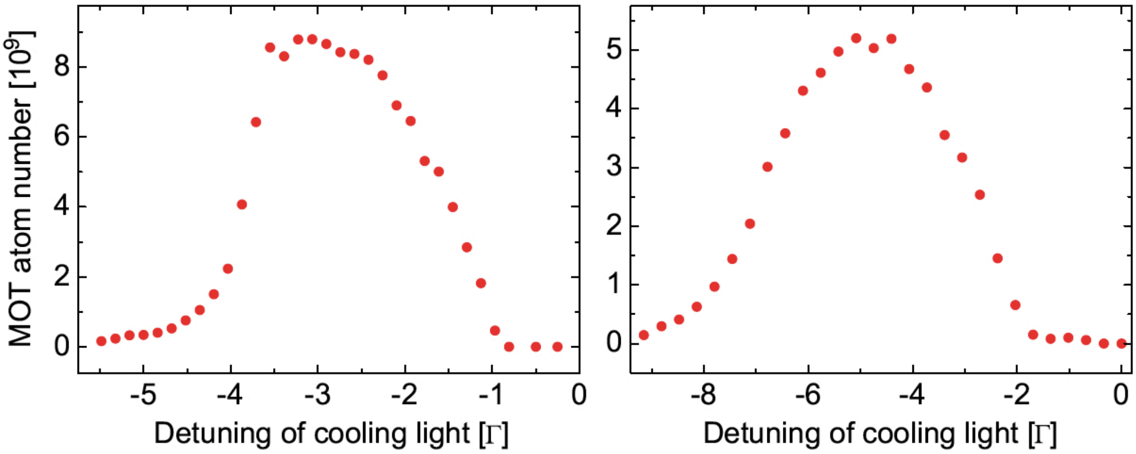

Figure 2.9: *Number of atoms in each single-species MOT:* ^{40}K *(left) and* ^{6}Li *(right), as a function of the detuning of the cooling frequency.*

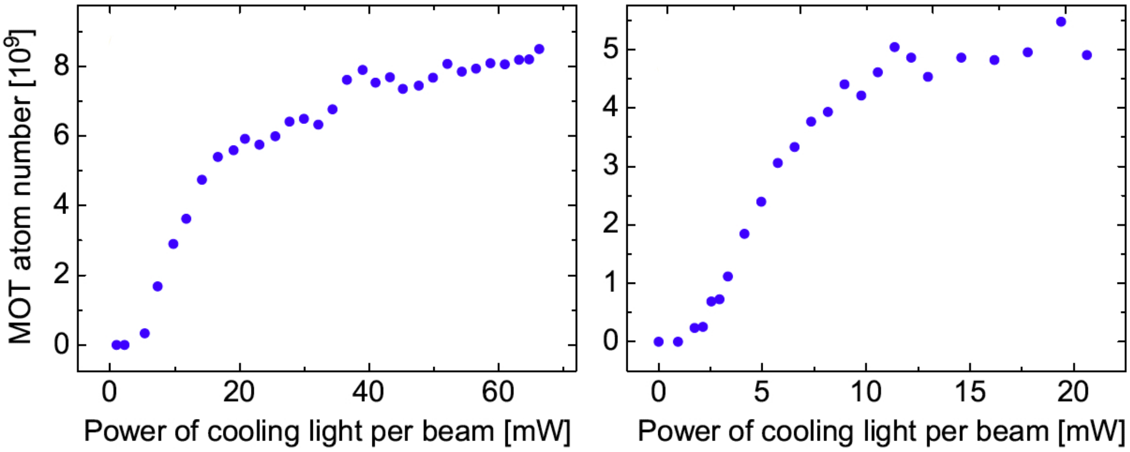

Figure 2.10: *Number of atoms in each single-species MOT:* ^{40}K *(left) and* ^{6}Li *(right), as a function of the cooling power in each of the six beams.*

to their optimal value for the double-species MOT, registered in Table 2.1. Note that, due to the high number of parameters, the optimization process required many loops over all the parameters. Here, we only present a summary of this procedure, and we restrict it to single-species MOTs.

Let us start with the principal cooling beams. Figure 2.9 shows the number of atoms in each single-species MOT as a function of the detuning of the cooling beams. In both cases, we find the typical MOT trade-off behavior between high capture velocities at high red-detunings, and high cooling efficiencies at low red-detunings. For ^{40}K the optimal detuning equals $-3\,\Gamma$, whereas it reaches $-5\,\Gamma$ for ^{6}Li. We fixed the detunings to those optimal values. Figure 2.10 shows the number of atoms in each single-species MOT as a function of the cooling power. In both cases, we observe a threshold behavior and a saturation effect : for too low intensities, the cooling is not efficient enough to reduce the atom energy notably under the trap depth; for too high intensities the

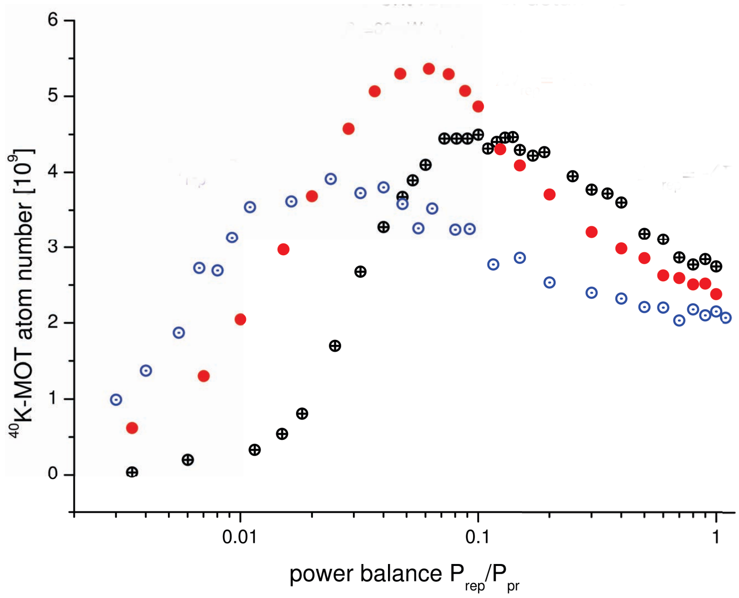

Figure 2.11: *Number of atoms in single ^{40}K-MOT as a function of the ratio between repumping and cooling powers, for different detunings of the repumper frequency: $-3\ \Gamma$ (black, cross), $-5\ \Gamma$ (red, full) and $-7\ \Gamma$ (blue, point). The cooling power is kept at 40 mW in each beam.*

cooling transition gets saturated and some additional effects, such as rescattering (see part 2.1.5) or inelastic collisions (see part 2.3.4), appear and lead to trap losses; in between the trapped numbers are quasi-proportional to the cooling intensities. For ^{40}K we have a power of approximately 40 mW per beam, focalized over a waist of 8 mm, which corresponds to a resonant saturation parameter of $s_0 = 13$. For ^{6}Li we have a typical power of 20 mW per beam, which corresponds to a resonant saturation of $s_0 = 4$.

The optimization of the repumping light is presented in Figures 2.11 and 2.12. Note that the cooling power is kept constant to its value of Table 2.1. As we can see, the behavior is slightly different for the two species. For ^{40}K, at a given detuning of the repumping light, we observe a trade-off behavior with a clear maximum: without repumping, the small hyperfine structure of the excited state (see Figure 1.6) implies a complete leak of the atoms in the dark $F = 7/2$ ground-state, whereas a lot of repumping power forces the atoms to remain in the cycling transition where the high cooling power used can induce losses through inelastic collisions (see part 2.3.4). The fact that the optimal repumping power is quite small for an atom with such a narrow hyperfine structure is explained in part 2.3.3. Besides, the displacement of the optimal ratio towards small repumping powers with increasing detuning is not clear. This could be due to the fact that the repumping light is more resonant with the jet from the 2D-MOT at high detunings, since with a jet speed of 22 m.s^{-1} (see part 1.4.4) the Doppler resonance condition occurs at a detuning of $-5.6\ \Gamma$. For ^{6}Li, on the contrary, there is no trade-off behavior at a given detuning of the repumping light. The number increases with repumping power and saturates. We attribute the absence of decrease at high repumping powers to the narrow hyperfine structure of ^{6}Li in the excited state (see

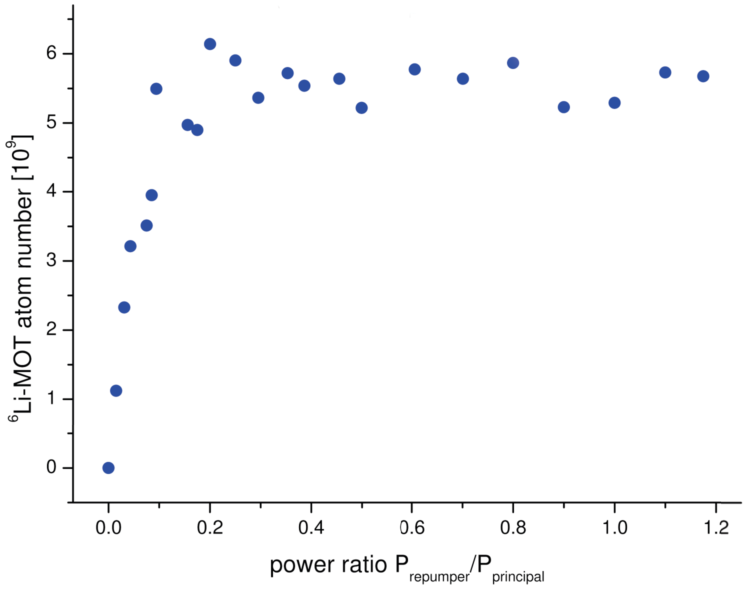

Figure 2.12: *Number of atoms in single ^{40}K-MOT as a function of the ratio between repumping and cooling powers, the cooling power being kept at 20 mW in each beam.*

Figure 1.6) that induces huge leaks towards the wrong hyperfine ground-state $F = 1/2$.

Figure 2.13 shows the number of ^{40}K atoms in the single MOT as a function of the axial magnetic gradient. The graph also shows two ^{6}Li values for reference. For ^{40}K, we observe a maximum around 7.5 G.cm^{-1}, whereas for ^{6}Li the maximum is at higher currents, the crossing value being at 10 G.cm^{-1}. Since during double MOT operation we want to attenuate the interspecies two-body losses (see part 2.3.5), we limit the common magnetic gradient to 8 G.cm^{-1}, in order to reduce those losses by reducing the densities.

2.3.3 Dark magneto-optical trap

Measuring the total number of atoms as depicted in Figure 2.7 implies to perform a preliminary hyperfine pumping just before the imaging, as explained in part 2.2.2. In fact, in the MOT steady-state regime, a fraction of the atoms is not in the cooling hyperfine ground-state but in the other one which is a dark state with respect to the imaging beam.

In order to quantify the fraction of atoms that is actually in the cooling transition during the MOT operation, we performed the following measurement for ^{40}K. 600 μs before imaging, we switch off all the MOT beams so that all the atoms decay in the two-ground-states, since the lifetime of the excited state is of the order of $2\pi/\Gamma \approx 0.2$ μs. Then, without pumping back the atoms from $F = 7/2$ to $F = 9/2$, as for an usual imaging procedure, we take a picture with an imaging beam that is resonant with the cooling transition. The number of atoms obtained represents in a good approximation the sum of the MOT populations of $F = 9/2$ and $F' = 11/2$. In fact, an atom in $F' = 11/2$ can not decay towards $F = 7/2$ due to the selection rules that forbid $\Delta F = -2$. Moreover, we can neglect the contribution of the atoms initially in $F' = 9/2$

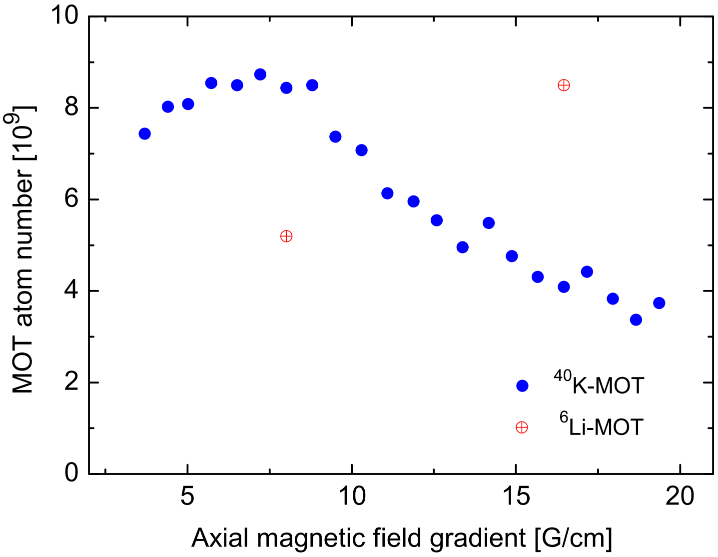

Figure 2.13: *Numbers of trapped atoms in the single-species MOTs, as a function of the axial magnetic gradient.*

to the measured number since, with our detunings (see Figure 1.6) and intensities (see Table 2.1), most of the excited atoms are in $F' = 11/2$. The experimental results are shown in Figure 2.14.

We understand the plotted behavior with a simple model. Let us consider a four level transition between two ground-states, $F_1 = 9/2$ and $F_2 = 7/2$, and two excited states, $F'_3 = 11/2$ and $F'_4 = 9/2$, with the respective populations N_1, N_2, N_3 and N_4. State F_1 is connected to F'_3 and F'_4 by spontaneous emission of rates A_{13} and A_{14}, and by stimulated emission/absorption of rates $B_{13}I_{\rm C}$ and $B_{14}I_{\rm C}$, where $I_{\rm C}$ is the cooling intensity. State F_2 is connected to state F'_4 by spontaneous emission of rate A_{24} and by stimulated emission/absorption of rates $B_{24}I_{\rm R}$, where $I_{\rm R}$ is the repumping intensity. Thus, for a constant total number of atoms, the Einstein's rate equations are:

$$\left\{ \begin{array}{l} \dot{N_1} = A_{13}N_3 + A_{14}N_4 + B_{13}I_{\rm C}(N_3 - N_1) + B_{14}I_{\rm R}(N_4 - N_1) \ , \\ \dot{N_2} = A_{24}N_4 + B_{24}I_{\rm R}(N_4 - N_2) \ , \\ \dot{N_3} = -A_{13}N_3 + B_{13}I_{\rm C}(N_1 - N_3) \ , \\ \dot{N_4} = -\dot{N_1} - \dot{N_2} - \dot{N_3} \ . \end{array} \right. \tag{2.16}$$

The steady-state of equation 2.16 leads to:

$$\frac{N_1 + N_3}{N_1 + N_2 + N_3 + N_4} = \frac{1}{1 + a + bI_{\rm C}/I_{\rm R}} \ , \tag{2.17}$$

with:

$$a = \frac{2}{\left(1 + \frac{B_{13}I_{\rm C}}{A_{13}+B_{13}I_{\rm C}}\right)\left(1 + \frac{A_{14}}{B_{14}I_{\rm C}}\right)} \ ,$$

and:

$$b = \frac{A_{24}}{B_{24}I_{\rm C}}\frac{a}{2} \ .$$

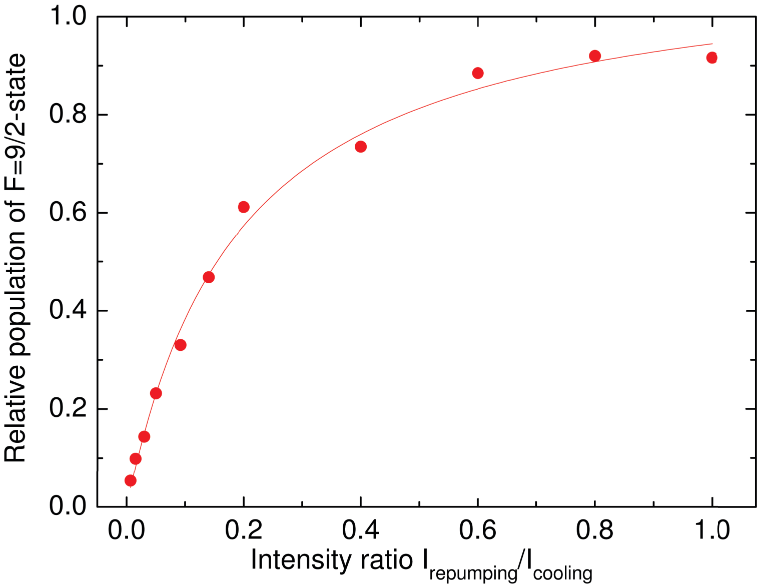

Figure 2.14: *Fraction of atoms in* $F = 9/2$ *or* $F' = 11/2$ *in the MOT steady-state, as a function of the ratio between repumping and cooling powers, the latter being kept to its value indicated in Table 2.1. The graph shows the experimental data (circles) fitted with a theoretical function (line) obtained through einstein's coefficients in a four level transition (see equation 2.17). The imaging procedure is the following: 600* μs *before imaging, all the MOT beams are switched off so that all the atoms decay in the two-ground-states before imaging. Then, a picture with an imaging beam on resonance with the cooling transition is taken. The number of atoms obtained represents in a good approximation the sum of the MOT populations of* $F = 9/2$ *and* $F' = 11/2$ *since atoms in* $F' = 11/2$ *can not decay towards* $F = 7/2$ *due to the selection rules. Moreover, the contribution of the atoms initially in* $F' = 9/2$ *(or lower* F'*) to the measured number can be neglected since, with our detunings (see Figure 1.6) and intensities (see Table 2.1), most of the excited atoms are in* $F' = 11/2$.

Fitting the experimental data with expression 2.17 gives a good agreement as shown in Figure 2.14.

Since our ratio between repumping and cooling powers equals 5 % (see Table 2.1), the fraction of atoms in the cooling transition equals only 20 %, according to Figure 2.14. Thus, a key ingredient of our big number of atoms in the MOT is the Dark-MOT configuration [98], where a majority of cooled atoms falls in the wrong ground-state, due to low repumping, and thus do not see the cooling light. In fact, this intense light leads to rescattering (see part 2.1.5), that increases volume and temperature, or to inelastic losses (see part 2.3.4). The same Dark-MOT technique is used for ^{6}Li, with a larger ratio between repumping and cooling powers of 20 % (see Table 2.1), due to the narrower hyperfine structure of ^{6}Li (see figure 1.6). Note that the use of small repumping powers is also a key ingredient to get a large double MOT, since it decreases the interspecies inelastic collisions as well (see part 2.3.5).

2.3.4 Trap losses and lifetime

To describe the single species MOT loading, as well as its lifetime and losses, let us introduce the following rate equation on the number N of atoms in the MOT:

$$\frac{\mathrm{d}N}{\mathrm{d}t} = L - \gamma N - \beta \int n^2 \, dV \ . \tag{2.18}$$

L is the loading rate, from the Zeeman slower for ^{6}Li (see part 1.3.5), and from the 2D-MOT for ^{40}K (see part 1.4.4). γ is the one-body loss rate, that is the rate of losses due to collisions with the vacuum impurities. Finally, β characterizes the two-body losses. According to parts 2.1.7 and 2.2.3, the temperatures of the trapped clouds are typically a few hundreds times smaller than the trap depths. Thus, we can neglect the losses due to elastic collisions: β describes only the light-induced inelastic collisions. For instance, let us consider a collision between two ^{6}Li atoms initially in the cooling ground-state $F = 3/2$. In presence of resonant light, this collision can form a temporary excited $^6\mathrm{Li} - ^6\mathrm{Li}^*$ state, with one excited atom inside. The principle is similar to the one of photoassociation described in part 2.4.1, apart from the fact that the formed state is not a proper bound state here. In the attractive part of the interaction potential, the excited pair can evolve to lower potential energies, before the radiative decay happens. The difference of energy will then be converted into kinetic energy for the atomic pair, which induces some trap losses. Other mechanisms, known as spin changing and hyperfine changing collisions, can also happen. They involve some exothermic transitions in the fine or hyperfine structures, which lead to trap losses as well.

Equation 2.18 can not be integrated for all regimes, due to the integral term. For instance, at low numbers, we can assume a gaussian density in the trap since around the center the potential is harmonic (see equation 2.1). Then, the volume only depends on the temperature. On the contrary, the density becomes constant at high numbers, due to the rescattering process (see part 2.1.5): the volume is proportional to the atom number in that case. However, we can still use equation 2.18 in some specific regimes, in order to obtain the loss coefficients from our experimental data.

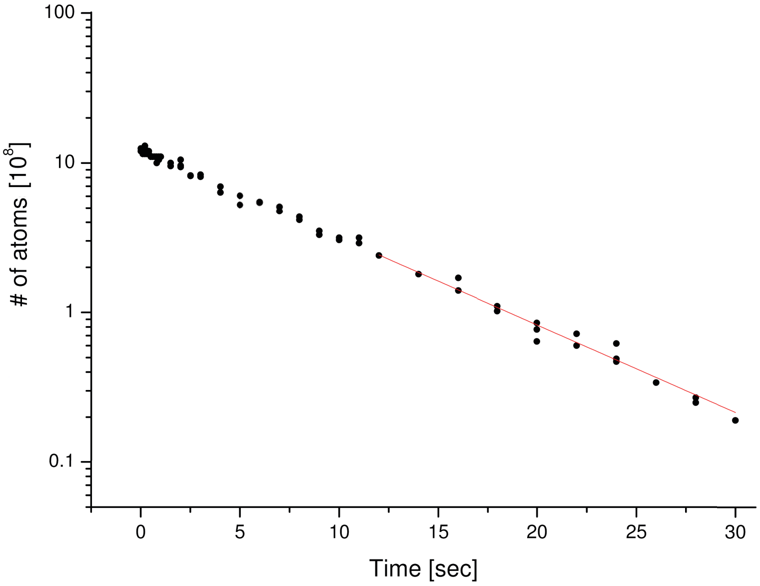

Figure 2.15: *Lifetime measurement of* ^{40}*K MOT. At* $t = 0$*, the 2D-MOT is switched off. The long-term behavior is fitted with a single exponential decay, according to equation 2.19. The long-term decay time is found to be 7.5 s.*

First, the loading rates L were measured using small loading times after having switched on the MOT magnetic field. In fact, for small trapped numbers, equation 2.18 becomes:

$$\frac{\mathrm{d}N}{\mathrm{d}t} = L \ ,$$

and thus the number of trapped atoms grows linearly with time, with a slope L. For ^{40}K, we found $L^{\mathrm{K}} = 1.4 \times 10^9$ atoms.s^{-1}, as mentioned in part 1.4.4. For ^{6}Li, we found $L^{\mathrm{Li}} = 1.2 \times 10^9$ atoms.s^{-1}, as mentioned in part 1.3.5.

Second, the one-body loss rate γ was obtained by performing a lifetime experiment, that is by recording the number of atoms after having switched off the atomic source, ^{6}Li Zeeman slower (see section 1.3) or ^{40}K 2D-MOT (see section 1.4). Then, the data was fitted by a single exponential decay, as shown in Figure 2.15 for ^{40}K. In fact, without loading ($L = 0$), and at low numbers of atoms in a deloading trap, equation 2.18 becomes:

$$\frac{\mathrm{d}N}{\mathrm{d}t} = -\gamma N \ . \tag{2.19}$$

We measured a lifetime of 7.5 s and thus $\gamma \approx 0.13$ s^{-1} for both species, which is coherent with the fact that the one-body losses are due to collisions with background impurities and do not depend much on the trapped species.

Thirdly, we extracted the inelastic collision rates β for each species, by measuring the steady-state numbers of atoms. In fact, the MOT density can be assumed to be constant at high numbers of atoms in a MOT (see part 2.1.5). Thus, the steady-state of equation 2.18 leads to:

$$\beta = \frac{1}{n}\left(\frac{L}{N} - \gamma\right) \ ,$$

where n is the steady-state density of the full loaded MOT, and N its number of atoms. Using our previous estimates of L^{K}, L^{Li} and γ, as well as the numbers and densities given in part 2.2.3, we found: $\beta^{\mathrm{K}} \approx 8.0 \times 10^{-13}$ cm^3.s^{-1} and $\beta^{\mathrm{Li}} \approx 4.4 \times 10^{-12}$ cm^3.s^{-1}. Those numbers correspond to typical times $(n\beta)^{-1}$ of respectively 42 s and 11 s, which are larger than γ^{-1} at maximal densities. This last result is coherent with the reduced inelastic losses in our Dark-MOT scheme (see part 2.3.3) and with the full loading times of the MOTs, that were measured to be of the order of 5 s and 6 s respectively, which are close to γ^{-1}. In contrast, in standard MOTs with more repumping light ($I_{\mathrm{R}}/I_{\mathrm{P}} = 20$ % for ^{40}K, and $I_{\mathrm{R}}/I_{\mathrm{P}} = 50$ % for ^{6}Li), we observed an usual double exponential decay with typical inelastic losses times of few seconds, which are smaller than γ^{-1}.

2.3.5 Double ^{6}Li-^{40}K magneto-optical trap

Using the double optical system described in part 2.3.1, as well as the parameters of Table 2.1, we could obtain a large double ^{6}Li-^{40}K MOT containing 8×10^9 atoms of ^{40}K and 5×10^9 atoms of ^{6}Li. Those numbers are respectively 10 % and 4 % smaller than the single MOT ones (see part 2.2.3). The difference is due to inelastic interspecies collisions, which can be described by an additional loss term in equation 2.18:

$$\frac{\mathrm{d}N_{\mathrm{A}}}{\mathrm{d}t} = L_{\mathrm{A}} - \gamma N_{\mathrm{A}} - \beta_{\mathrm{AA}} \int n_{\mathrm{A}}^2 \, dV - \beta_{\mathrm{AB}} \int n_{\mathrm{A}} n_{\mathrm{B}} \, dV \ , \qquad (2.20)$$

where A and B denote the two species. We reduced the interspecies inelastic collisions by reducing the densities, through the magnetic gradient, as explained in part 2.3.2. Moreover, since those collisions are induced by the cooling light, the use of low repumping light (see part 2.3.3) allowed to reduce the number of atoms in the cooling transition, and thus the colliding population.

Coefficients β_{KLi} and β_{LiK} depend on light intensities but not on the field. We estimated them in our configuration (Table 2.1) by increasing the magnetic field in order to increase the losses. In that case, the mutual influence of the two clouds was increased, as shown in Figures 2.16 and 2.17. Moreover, by decreasing L_{A} sufficiently we could make sure that the cloud A was contained inside the cloud B and that n_{B} was constant in the volume V_{A}. In this configuration, the steady-state of equation 2.20 leads to:

$$\beta_{\mathrm{AB}} = \frac{L_{\mathrm{A}} - \gamma N_{\mathrm{A}} - \beta_{\mathrm{AA}} N_{\mathrm{A}} n_{\mathrm{A}}}{N_{\mathrm{A}} n_{\mathrm{B}}} \ .$$

Thus, by measuring the reduced L_A as in part 2.3.4, as well as the densities and number of atoms, and using the value of γ obtained in part 2.3.4, we found $\beta_{\mathrm{KLi}} \approx 3 \times 10^{-12}$ cm^3.s^{-1} and $\beta_{\mathrm{LiK}} \approx 1 \times 10^{-12}$ cm^3.s^{-1}.

2.4 Molecular photoassociation

Molecular photoassociation is the formation of molecules induced by light. Since its first experimental achievement [99], molecular photoassociation of ultra-cold atoms has been being a fascinating topic for several reasons. First, it allows to perform precise molecular spectroscopy [100] and to create molecules that are unknown in nature,

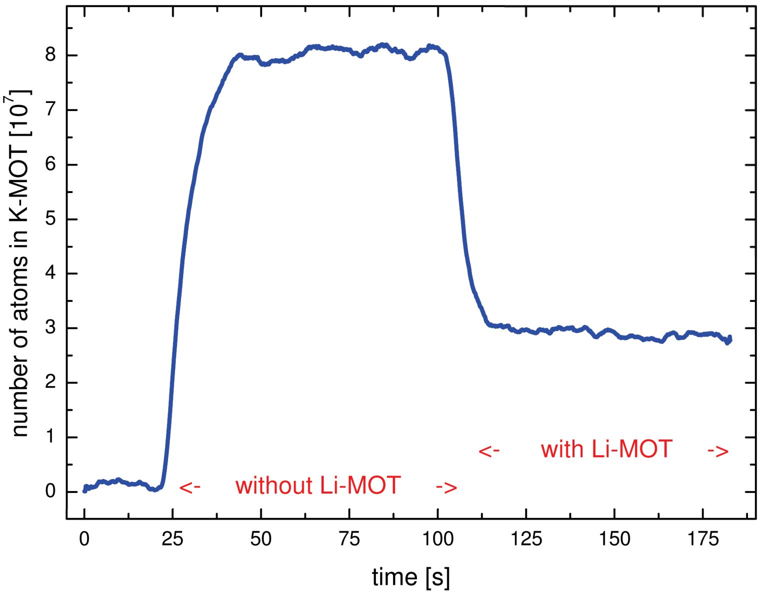

Figure 2.16: *^{40}K-MOT number of atoms in presence or not of ^{6}Li-MOT. The loading rate of ^{40}K is reduced in order to have a small ^{40}K-MOT and a constant ^{6}Li density. The axial gradient magnetic gradient is increased to 16 G.cm^{-1} in order to increase the densities and thus the inelastic losses.*

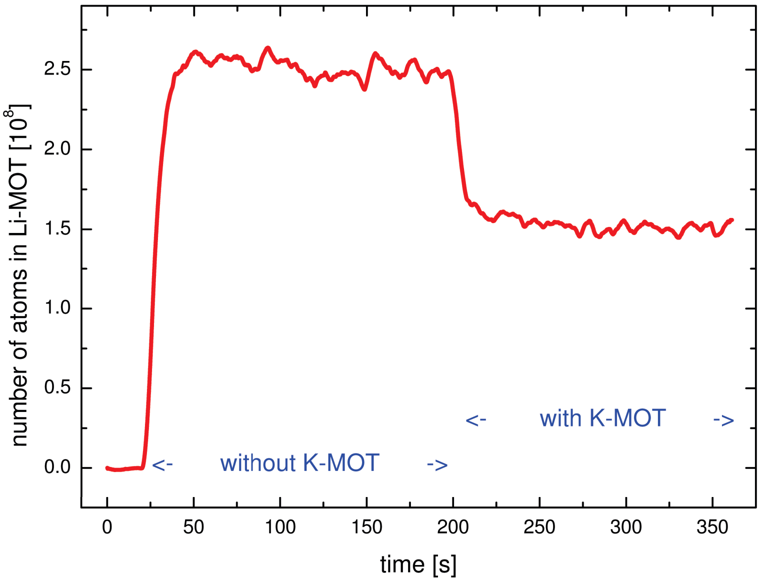

Figure 2.17: *^{6}Li-MOT number of atoms in presence or not of ^{40}K-MOT. The loading rate of ^{6}Li is reduced in order to have a small ^{6}Li-MOT and a constant ^{40}K density. The axial gradient magnetic gradient is increased to 16 G.cm^{-1} in order to increase the densities and thus the inelastic losses.*

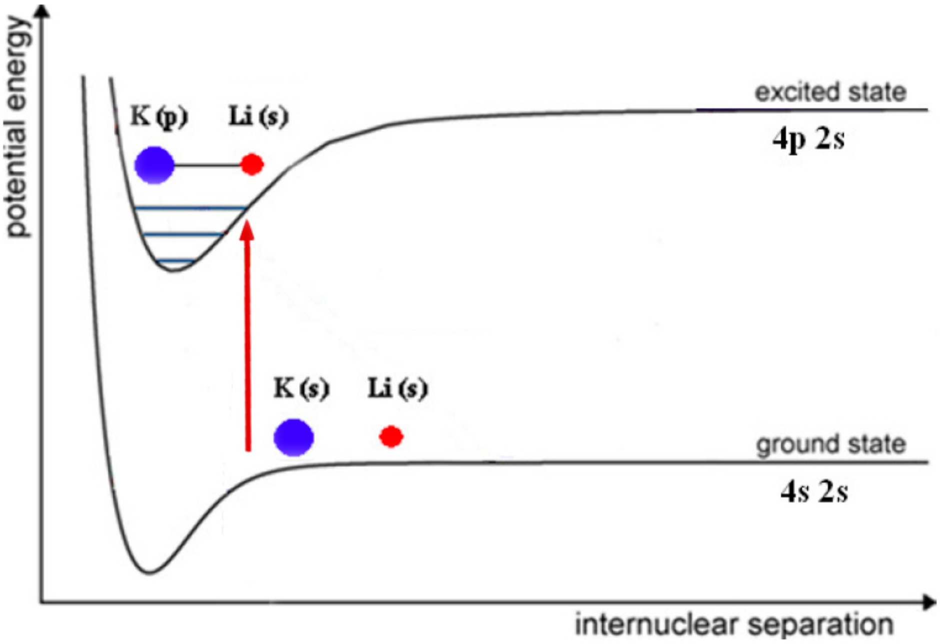

Figure 2.18: *Principle of* $^6Li^{40}K^*$ *photoassociation. A laser beam, red-detuned with respect to a* ^{40}K *atomic asymptotic transition, is resonant with a transition towards a rovibrational bound-state of one of the excited electronic states of the molecule.*

opening the way to new chemical engineering at ultra-low temperatures. Secondly, it offers to create ultracold heteroatomic molecules [101], and thus ultracold polar molecules [102], which are of interest in many-body physics and quantum information for the study of long-range interactions in dipolar gases. Finally, it offers a convenient way to measure accurately the atomic scattering properties [103].

The particular ^{6}Li^{40}K molecule is of great interest due to its large electric dipole of 3.6 D in its ground-state [54]. Magnetoassociation, through Feshbach resonances, already allowed to study its scattering properties [60], as well as its formation in a weakly bound vibrational state of the electronic ground-sate [62] .

Apart from the design and optimization of the experiment towards quantum degeneracy, we could perform the first photoassociation of ^{40}K^{40}K* and ^{6}Li^{40}K* molecules. This is described in detail in Armin Ridinger's thesis [82], as well as in a dedicated publication [83]. Therefore, we restrict ourselves to the main aspects of this result in the present section.

After a general description of the experiment, we give the basic theoretical aspects for data analysis. Then, we present the first photoassociation of ^{40}K^{40}K* homonuclear molecules and ^{6}Li^{40}K* heteronuclear molecules.

2.4.1 Principle and setup

The principle of atomic photoassociation is depicted in Figure 2.18 for the particular case of ^{6}Li^{40}K*. A laser beam, red-detuned with respect to an asymptotic atomic transition, is resonant with a transition towards a rovibrational bound-state of one of the excited electronic states of the molecule.

In the following, we describe the signature of photoassociation on the number of atoms in a MOT and we present the associated experimental setup.

Signature of photoassociation

In an MOT, the photoassociation process leads to inelastic losses since the molecule has a different spectrum than its individual atoms. Thus, for a double MOT, equation 2.20 becomes:

$$\frac{\mathrm{d}N_\mathrm{A}}{\mathrm{d}t} = L_\mathrm{A} - \gamma N_\mathrm{A} - \beta_\mathrm{AA} \int n_\mathrm{A}^2 \, dV - \beta_\mathrm{AB} \int n_\mathrm{A} n_\mathrm{B} \, dV - \beta_\mathrm{pa} \int n_\mathrm{A} n_\mathrm{B} \, dV \ , \tag{2.21}$$

where β_pa is the photoassociation rate coefficient, which depends on the frequency and intensity of the photoassociation beam, but also on the selection rules as well as the overlap between the initial and final total wave-functions via the so-called Franck-Condon factors. Assuming constant densities, which is reasonable for large MOT (see part 2.1.5), and assuming that cloud A is included in cloud B, the steady state of equation 2.21 leads to:

$$N_\mathrm{A}(\beta_\mathrm{pa}) = \frac{L_\mathrm{A}}{\gamma + \beta_\mathrm{AA} n_\mathrm{A} + (\beta_\mathrm{AB} + \beta_\mathrm{pa}) n_\mathrm{B}} \ . \tag{2.22}$$

Therefore, in principle, we can detect the photoassociation of molecules by directly observing a diminution in the steady-state atom number while scanning the photoassociation frequency (see part 2.4.1). The principle is exactly the same for homonuclear photoassociation in a single MOT, by removing the heteronuclear inelastic term β_AB in equation 2.21.

Experimental setup

The experimental setup is drawn in Figure 2.19. The photoassociation laser beam consists of a dedicated potassium laser diode (see part 1.2.2), amplified through a tapered amplifier (see part 1.2.4). After a single-mode polarization-maintaining optical fiber, the power equals 660 mW on the main table. The frequency is recorded by a wavelength-meter (High Finesse Angstrom WS-6) and scanned through the piezo-electric actuator of the laser diode (see part 1.2.2). The scanning speed is typically 15 MHz.s^{-1}, in order to allow for full reloading of the MOT between two photoassociation lines. The total scanning range is of the order of 300 GHz, below the $F = 9/2 - F' = 11/2$ transition of ^{40}K (see Figure 1.6).

As explained above, measuring the numbers of atoms in each MOT through the calibrated fluorescence (see part 2.2.1) allows to detect the photoassociation lines. However, optimizing the signal requires some care. Indeed, according to equation 2.22, we have:

$$\frac{N_\mathrm{A}(0) - N_\mathrm{A}(\beta_\mathrm{pa})}{N_\mathrm{A}(0)} = \frac{\beta_\mathrm{pa} n_\mathrm{B}}{\gamma + \beta_\mathrm{AA} n_\mathrm{A} + (\beta_\mathrm{AB} + \beta_\mathrm{pa}) n_\mathrm{B}} \ .$$

For instance, in the case of ^{6}Li^{40}K* photoassociation, we record the number of ^{6}Li atoms in the MOT in order to forget the ^{40}K^{40}K* lines. Therefore, we have to increase

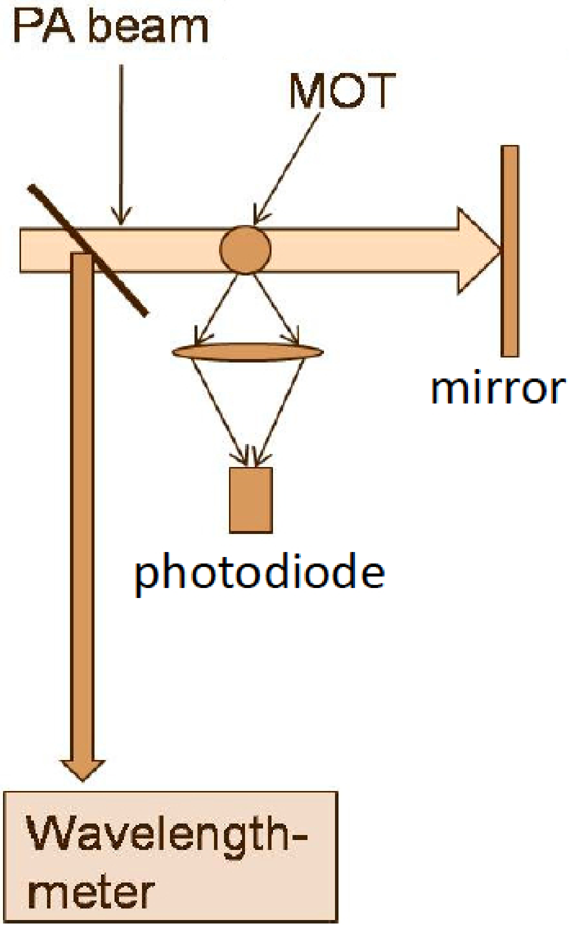

Figure 2.19: *Experimental setup of the photoassociation experiment. The photoassociation laser is sent to the MOT. While its frequency is swept, the numbers of atoms in the MOT are recorded through fluorescence (see part 2.2.1). A diminution of the number of atoms is a signature of photoassociation process, according to equation 2.22.*

the density of ^{40}K, by increasing the magnetic gradient to 20 G.cm^{-1}, while decreasing the density of ^{6}Li and the β_{LiK} coefficient, by reducing the powers of the MOT beams to $s_0^{\mathrm{Li}} = 0.5$ and $s_0^{\mathrm{K}} = 10$, as well as the lithium loading rate L_{Li}. In addition, we make sure that we have a steady-state stability of a few percents in fluorescence, and that the ^{6}Li-MOT is contained inside the ^{40}K one.

2.4.2 Theoretical aspects

In this part, we present the main theoretical aspects that were used to analyze the experimental data. First, we give the Leroy-Bernstein formula for the long-range vibrational spectrum. Secondly, we characterize the rotational substructure.

Vibrational spectrum

Let us assume an interaction potential $V(r) = -C_\alpha r^{-\alpha}$, with a hard core repulsive barrier in $r = R_0$, and let us consider the weakly bound states. For $\alpha > 2$, the associated energies $E(n)$, labelled by the integer $n \geq 1$, can be approximated by the Leroy-Bernstein formula [104]:

$$E(n) = -A_\alpha (n_\alpha - n)^{2\alpha/(\alpha-2)} \ , \tag{2.23}$$

with:

$$A_\alpha = C_\alpha \left(\frac{\Gamma(1/\alpha+1)\pi\hbar(\alpha-2)}{\Gamma(1/\alpha+1/2)\Gamma(1/2)\sqrt{2\mu C_\alpha}} \right)^{2\alpha/(\alpha-2)} \ ,$$

where we have introduced the gamma function $\Gamma(x)$ and the reduced mass μ. The reference in energy is chosen to be at the dissociation limit, where $n = n_\alpha$, with n_α a given number between 0 and 1.

The interaction in the electronic ground-state is a van der Waals interaction in R^{-6}, thus $\alpha = 6$. However, the interaction potential in the excited state depends on the molecule. In the case of homonuclear $^{40}\mathrm{K}^{40}\mathrm{K}^*$, the resonant dipole interaction gives $\alpha = 3$, whereas in the heteronuclear case $^{6}\mathrm{Li}^{40}\mathrm{K}^*$, the van der Waals interaction gives $\alpha = 6$.

Rotational barrier

For a symmetrically spherical potential $V(\boldsymbol{r})$, the wave-function can be developed in the spherical harmonic basis, and the variables can be separated. In addition to the potential $V(r)$, a repulsive term thus appears in the radial problem:

$$V^*(r) = V(r) + \frac{\hbar^2 l(l+1)}{2\mu r^2} \ ,$$

where l is the rotational angular momentum quantum number, and μ the reduced mass. In the case of collisions in the electronic ground-state, we have a van der Waals interaction $V(r) = -C_6^{\mathrm{gs}} r^{-6}$, as mentioned above. By differentiating $V^*(r)$, we obtain the height of the rotational barrier:

$$V^*_{\max}(l) = \left(\frac{\hbar^2 l(l+1)}{3\mu (2C_6^{\mathrm{gs}})^{1/3}} \right)^{3/2} \ . \tag{2.24}$$

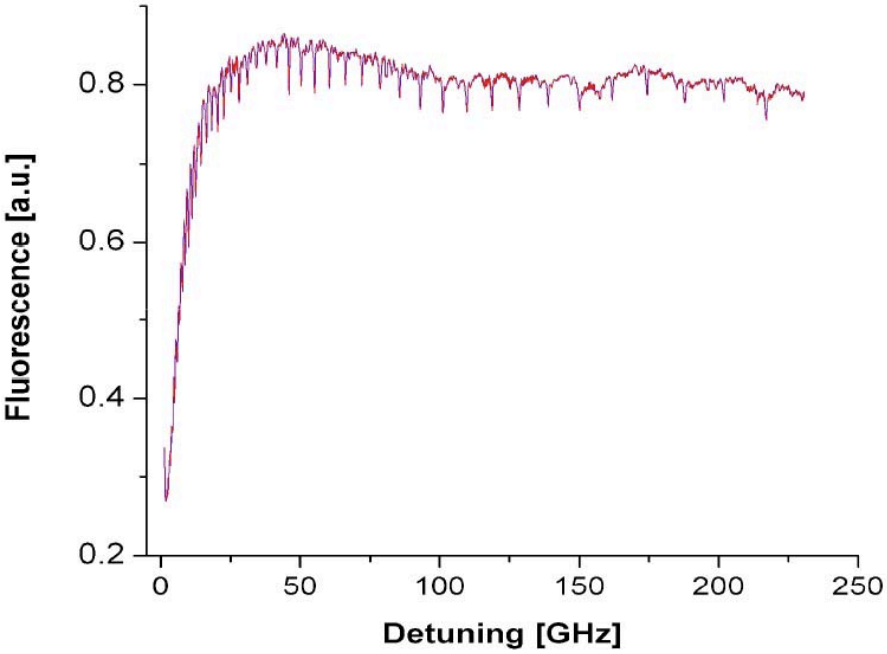

Figure 2.20: *Fluorescence of single ^{40}K MOT as a function of the photoassociation detuning ($-\delta$) with respect to the cooling transition. Note that close from resonance the photoassociation beam is harmful for the MOT, as expected. Note also that the atom density is maximal at intermediate detunings due to the attractive optical dipole forces (see part 3.4.4) created by the intense photoassociation beam. The experimental setup is described in Figure 2.19.*

Putting numbers, we find $V^*_{\text{max}}(0) = 0.3$ mK and $V^*_{\text{max}}(1) = 1.5$ mK for $^{40}\text{K}^{40}\text{K}^*$, and $V^*_{\text{max}}(0) = 2.6$ mK and $V^*_{\text{max}}(1) = 13.4$ mK for $^6\text{Li}^{40}\text{K}^*$. Since the barrier grows like $\sim l^3$, we can neglect collisions with $l \geq 2$ according to our MOT temperatures (see part 2.2.3). Thus, taking into account the spins of the two colliding atoms, the maximal spin-orbit momentum J equals 2. The selection rule $\Delta J = 0, -1, +1$ allows to reach $J' = 3$ for the excited molecule, which means 4 rotational line per vibrational line at maximum.

2.4.3 Results

In this part, we present the first photoassociation of $^{40}\text{K}^{40}\text{K}^*$ homonuclear molecules and $^6\text{Li}^{40}\text{K}^*$ heteronuclear molecules.

Homonuclear molecules : $^{40}\mathbf{K}^{40}\mathbf{K}^*$

With the setup described in part 2.4.1, we first observed the homonuclear $^{40}\text{K}^{40}\text{K}^*$ lines, as plotted in Figure 2.20. Using Leroy-Bernstein formula 2.23 for $\alpha = 3$ (see part 2.4.1), we could fit the experimental data by a sixth order power. As plotted in Figure 2.21, the agreement is good and gives $C_3 = 14.20 \pm 0.02$ a.u. which is very close from Wang et al. experimental value for the 0_u^+ excited potential of $^{39}\text{K}^{39}\text{K}^*$: $C_3(0_u^+) = 14.14 \pm$

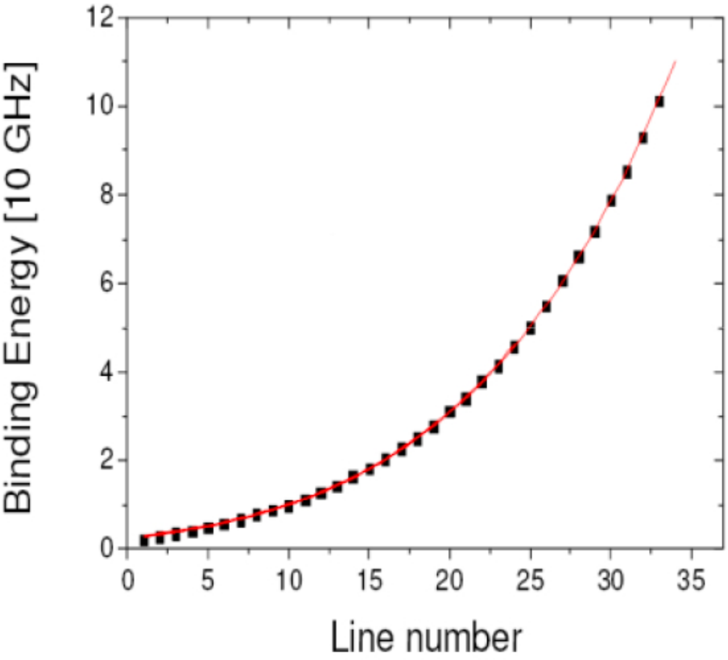

Figure 2.21: *Leroy-Bernstein fit (see formula 2.23 with $\alpha = 3$) of the $^{40}K^{40}K^{*}$ photoassociation binding energies found in Figure 2.20.*

0.05 a.u. [105], where 0_u^+ is the spectroscopic notation of the considered excited state. In addition, we found another series, with peaks of smaller amplitude in Figure 2.20, corresponding to another excited potential. There also, the Leroy-Bernstein fit is good, leading to $C_3 = 13.37 \pm 0.05$ a.u., which is very close from Wang et al. experimental value for the 1_g excited potential of $^{39}\mathrm{K}^{39}\mathrm{K}^*$: $C_3(1_\mathrm{g}) = 13.54 \pm 0.1$ a.u. [105]. Note that in both cases, due to the large reduced mass μ of $^{40}\mathrm{K}^{40}\mathrm{K}^*$, and its large typical radius, the rotational substructure (see equation 2.24) remains unresolved.

Finally, using those results, we could determine the linewidth Γ of the $4p$ atomic state of $^{40}\mathrm{K}$ [106]:

$$\frac{\Gamma}{2\pi} = \frac{d^2\omega^3}{3\pi\epsilon_0 c^3 h} ,$$

where ω is the pulsation of the atomic transition, and d the matrix element $\langle 4S|\mu|4P\rangle$, connected to the C_3 values by the theoretical prediction $C_3(0_\mathrm{u}^+) = 5d^2/3$ and $C_3(1_\mathrm{g}) = (2+\sqrt{7})d^2/3$ [107]. Putting numbers, we find $\Gamma/(2\pi) = 6.136 \pm 0.017$ MHz, which is close to the experimental value of Wang et al., $\Gamma/(2\pi) = 6.042 \pm 0.011$ MHz [106], used all along this thesis (see appendix A.1).

Heteronuclear molecules : $^6\mathrm{Li}^{40}\mathrm{K}^*$

As far as $^6\mathrm{Li}^{40}\mathrm{K}^*$ heteronuclear photoassociation is concerned, the experimental data was more complex than in the homonuclear $^{40}\mathrm{K}^{40}\mathrm{K}^*$ case. Figure 2.22 shows the experimental binding energies, put in an increasing order. As we can see, in contrast with $^{40}\mathrm{K}^{40}\mathrm{K}^*$ (see Figure 2.21), the single heteronuclear Leroy Bernstein fit (see formula 2.23

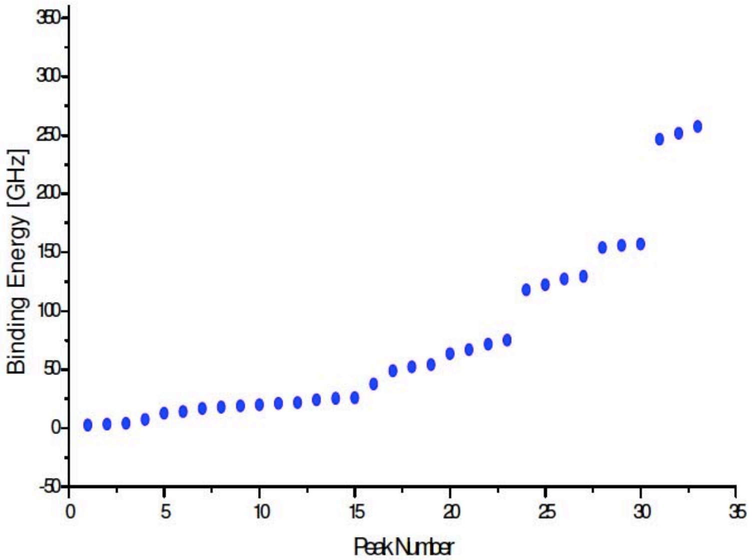

Figure 2.22: $^6Li^{40}K^*$ *photoassociation binding energies by increasing order.*

with $\alpha = 6$) does not work. The assignment of the resonances is more complex. First, heteronuclear molecules have less restrictive selection rules, leading here to five accessible excited potentials: $\Omega = 0^+$, $\Omega = 0^-$, $\Omega = 1^{\mathrm{down}}$, $\Omega = 1^{\mathrm{up}}$ and $\Omega = 2$, in spectroscopic notation. Secondly, due to the smaller reduced mass and the smaller typical radius, the rotational substructure (see equation 2.24) is now comparable to the vibrational spacing. Thirdly, the Leroy-Bernstein formula 2.23 is less precise due to the smaller internuclear distances, where other terms in the potential start to play a role, and where chemical bonding becomes important. We do not explain the complete resolution of this spectrum, since it was the object of [82], but we recall the main results: the five excited vibrational series were identified, and their rotational substructure as well. The rotationless binding energies were fitted by the heteronuclear Leroy-Bernstein formula 2.23, as shown in Figure 2.23. The C_6 coefficients obtained from the fits give $C_6^2 = 9170$ a.u., $C_6^{1\mathrm{up}} = 9240$ a.u., $C_6^{1\mathrm{down}} = 25220$ a.u., $C_6^{0-} = 22800$ a.u., $C_6^{0+} = 25454$ a.u., which are in a good agreement with the theoretical predictions [108].

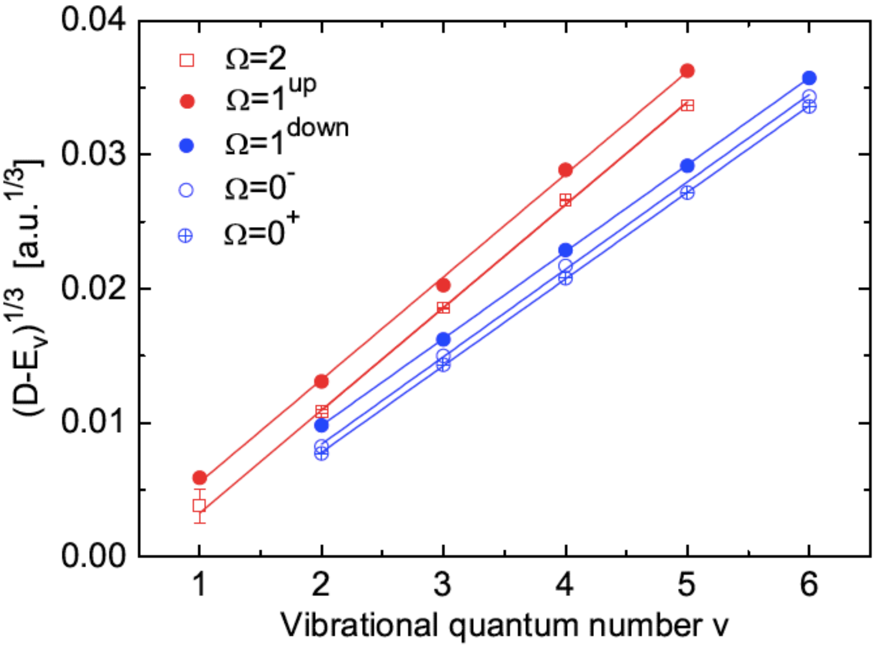

Figure 2.23: *Leroy-Bernstein fits (see formula 2.23 with* $\alpha = 6$*) of the* $^6Li^{40}K^*$ *photoassociation binding energies found in Figure 2.22, for five excited potentials.*

2.5 Summary

In this chapter, we presented our performing double ^{6}Li-^{40}K MOT and its optimization, as well as the first photoassociation of homonuclear ^{40}K^{40}K* and heteronuclear ^{6}Li^{40}K* molecules.

First, we recalled the principles of a MOT and we described our imaging diagnostics, from which we measured the thermodynamical properties of the trapped cloud. For ^{40}K, we obtained 8.9×10^9 atoms at a temperature of 290 μK and a central density of 3×10^{10} atoms.cm^{-3}. For ^{6}Li, we obtained 5.4×10^9 atoms at a temperature of 1.4 mK and a central density of 2×10^{10} atoms.cm^{-3}. In the double MOT configuration, we obtained 8×10^9 atoms of ^{40}K and 5×10^9 atoms of ^{6}Li. Those values were optimized by reducing the inelastic losses through a Dark MOT scheme with low repumping light, as shown through the measured loss rates and hyperfine populations.

Using this double MOT, we produced the first homonuclear ^{40}K^{40}K* and heteronuclear ^{6}Li^{40}K* molecules. In the first case, this allowed to measure the linewidth of the $4p$ atomic state of ^{40}K, that was found to be $\Gamma/(2\pi) = 6.136 \pm 0.017$ MHz, which is close from the value obtained by Wang et *al.* [106]. In the second case, it allowed to assign precisely five series of rovibrational lines, which opens the way to future photoassociation of polar ^{6}Li^{40}K molecules in their electronic ground-sate. This is of interest for the study of dipolar gases.

Due to the continuous absorption-emission process that occurs in a MOT, the phase-space density can not exceed 10^{-6}. Therefore, in order to get closer from quantum degeneracy, we then transfer the mixture in a quadrupolar magnetic trap, as developed in chapter 3.

Chapter 3

Magnetic trap

In chapters 1 and 2, we described our system and showed how we could reach a double MOT with high numbers for ^{40}K and ^{6}Li. However, event if a MOT is a necessary step towards quantum degeneracy, it contains some fundamental limits linked to its dissipative character as far as density (see part 2.1.5) and temperature (see part 2.1.4) are concerned. They limit from reaching higher phase-space densities than typically 10^{-6}, as shown in part 2.1.6, which is still far from the quantum degenerate regime. Then, to obtain quantum degeneracy, we transfer the mixture into a conservative trap where evaporative cooling will be performed.

A possible solution is to directly use a red-detuned optical dipole trap [109]. However, creating such a trap with a depth of the order of 1 mK and a capture volume close to the MOT volume would require an unrealistic laser power. Therefore, it is more efficient to load the atoms first in a magnetic trap and to start evaporation there, before transferring the obtained dense mixture in an optical trap, as already performed by the group of Amsterdam [56].

In the present chapter we describe such a magnetic trap. After a theoretical description of magnetic trapping and loss mechanisms, we explain how to prepare the sample before loading it into the trap. Then, we characterize experimentally our trap. We finally present the optically plugged magnetic trap, where evaporative cooling will be performed, and we describe the forthcoming optical dipole trap as well as the high resolution imaging and the design of the Feshbach coils. The magnetic transport between the MOT chamber and the science cell is described in chapters 4 and 5 that are dedicated to this purpose.

3.1 Principle

As already explained in the introduction of this chapter, in order to increase the phase-space density we transfer the atoms in a conservative trap. In this section, we describe the theoretical principle of such a trap: the quadrupolar magnetic trap. We first describe its potential energy manifold. Then, we present the so-called Majorana losses mechanism and estimate an associated lifetime. Finally, we present the issue of spin-relaxation.

3.1.1 Trapping potential

Let us consider an atom, described by a total magnetic moment operator $\hat{\boldsymbol{\mu}}$, inside a magnetic field $\boldsymbol{B}$. The coupling hamiltonian $\hat{H}$ is given by the minimal coupling:

$$\hat{H} = -\hat{\boldsymbol{\mu}} \cdot \boldsymbol{B} \ . \tag{3.1}$$

For an atom whose magnetic moment is adiabatically following the magnetic field $\boldsymbol{B}$ during its movement, the magnetic energy E is given by the perturbation theory of hamiltonian 3.1 in the hyperfine basis [110]:

$$E = \mu_{\mathrm{B}} g_F m_F B \ , \tag{3.2}$$

where B is the modulus of the magnetic field, μ_{B} the Bohr magneton, g_F the hyperfine Landé factor, and m_F the hyperfine magnetic quantum number. Here, we have assumed that the hyperfine Zeeman effect remains linear, which in not necessarily true but valid in our case as discussed at the end of this part. We see that finally only the modulus of the field matters and not the vectorial quantity.

By applying a current to a pair of coils in anti-Helmholtz configuration, one can generate a field whose expression is given by the Taylor expansion in the neighborhood of the center of the pair:

$$\boldsymbol{B}(\boldsymbol{r}) = \boldsymbol{B}(\boldsymbol{0}) + (\boldsymbol{r} \cdot \boldsymbol{\nabla})_{r=\boldsymbol{0}} \boldsymbol{B} + \ldots$$

Since by antisymmetry $\boldsymbol{B}(\boldsymbol{0}) = \boldsymbol{0}$, this leads to a quadrupolar field:

$$\boldsymbol{B}(\boldsymbol{r}) \approx (\boldsymbol{r} \cdot \boldsymbol{\nabla})_{r=\boldsymbol{0}} \boldsymbol{B} = (b_x x, b_y y, b_z z) \ ,$$

where $b_i = \partial B_i / \partial r_i$. Using cylindrical symmetry and Maxwell-Thomson's equation $\boldsymbol{\nabla} \cdot \boldsymbol{B} = 0$, we finally find:

$$\boldsymbol{B} = b(-x, -y, 2z) \ , \tag{3.3}$$

where z is the axial coordinate and $-b = b_x = b_y$ the magnetic gradient in the orthogonal plan. b happens to be positive in our experiment, by our choice of current orientation. Note that this approximative expression also satisfies the static Maxwell-Ampère equation $\boldsymbol{\nabla} \times \boldsymbol{B} = 0$, as expected, and that it is valid until a distance of the order of the coils radius. After this distance, the non-linear terms of the Taylor development above can not be neglected anymore. However, the radius of the MOT coils being of the order of 6 cm, which is more than ten times bigger than the cloud radius (see part 3.3.2), the quadrupolar approximation is valid to describe our magnetic trap.

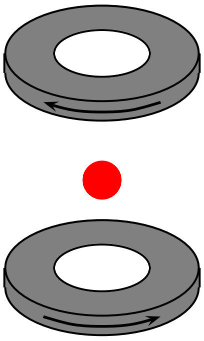

Figure 3.1: *Atomic cloud trapped in a quadrupole potential created at the center of an anti-Helmholtz pair of coils.*

Using expression 3.3, the magnetic energy of equation 3.2 becomes:

$$E = \mu_{\mathrm{B}} g_F m_F b \sqrt{x^2 + y^2 + 4z^2}\ . \tag{3.4}$$

A minimum of magnetic potential energy is then created at the center of the pair of coils for the anti-parallel (low field seeking) Zeeman states, *i.e.* with $m_F > 0$ when $g_F > 0$. Thus, it is possible to trap a spin-polarized atomic cloud (see Figure 3.1) [111].

We just saw that, prior to the trapping, it is important to optically pump the atoms into a $m_F > 0$ state. Moreover it is of interest to maximize m_F in order to confine more efficiently the atoms, especially regarding the forthcoming magnetic transport in the DN10 differential pumping tube (see chapter 4), and to avoid spin-relaxation (see part 3.1.3). Figure 3.2 shows the Zeeman effect on the two hyperfine ground sates of both ^{40}K and ^{6}Li, obtained from the Breit-Rabi formula [112], the ground-states of the cooling transitions being respectively $F = 9/2$ and $F = 3/2$. We thus wish to polarize ^{40}K in the stretched $m_F = 9/2$ state and ^{6}Li in the stretched $m_F = 3/2$ one. However, since an option for evaporative cooling is to cool down ^{40}K first and then sympathetically cool down ^{6}Li (see part 3.4.3), we may want to have an incomplete spin-polarization of ^{40}K, in order to keep also some atoms into the unstretched $m_F = 7/2$ state for collisions.

Note finally that, according to Figure 3.2, the Zeeman effect is linear even at high field for the two chosen stretched states. Moreover, until typically 357 G (see arrow for ^{40}K on Figure 3.2) our assumption of linear Zeeman effect is valid also for the unstretched $m_F = 7/2$ state. Situation would have been different with ^{6}Li because the linear Zeeman effect stands only until typically 27 G (see arrow for ^{6}Li on Figure 3.2). In conclusion, linear Zeeman effect can be assumed and equation 3.2 can be used to describe precisely magnetic trapping and magnetic transport, if we restrict ourselves to the three mentioned states and to magnetic fields lower than 357 G, which is the case.

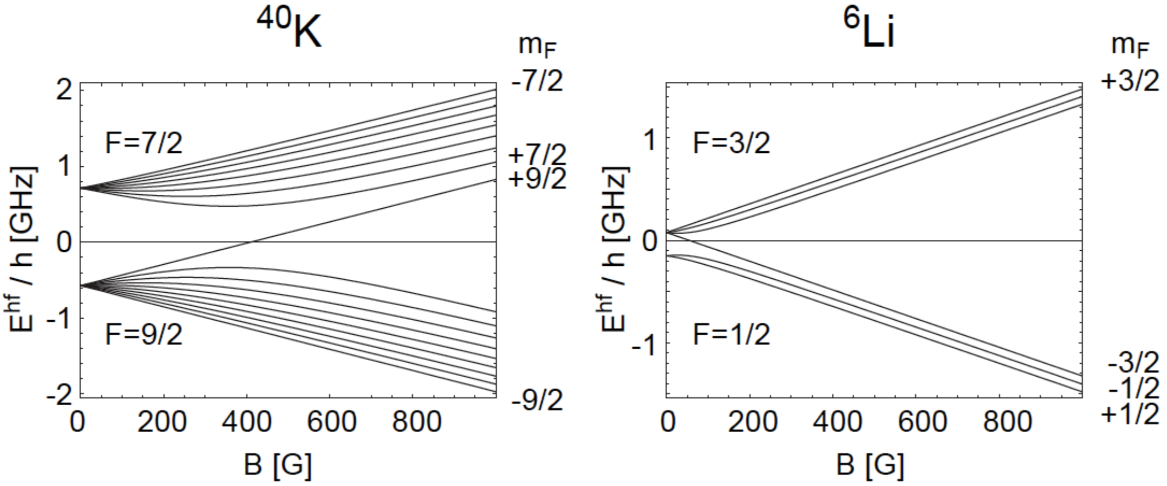

Figure 3.2: *Zeeman effect of the two hyperfine ground-states of ^{40}K and ^6Li obtained from the Breit-Rabi formula [112]. Note the inverted structure for ^{40}K.*

3.1.2 Majorana losses

If one wishes an atom of mass m to remain in such a trapped state, its magnetic moment μ has to follow adiabatically the magnetic field. This implies, for an atom with velocity v at distance r from the center, that the Larmor period $\hbar/\mu b r$, where b is the gradient, remains small in comparison with the typical flipping time r/v of the field seen by the atom. If this condition is not satisfied, the atomic spin eventually flips to an untrapped magnetic state. This loss mechanism is called Majorana loss. A direct consequence is the existence of a minimal safety distance $r_{\min}(v)$ for each class of velocity:

$$r_{\min}(v) = \sqrt{\frac{v\hbar}{\mu b}} \ . \tag{3.5}$$

Let us now estimate the Majorana loss rate of each species by considering its RMS velocity v^*, instead of each class of velocity. In addition, we assume that the trap is spherical, since we are only interested in obtaining an order of magnitude of the loss rate. During an infinitesimal time dt, the average volume dV of gas entering the spin-flip region is given by:

$$dV = 4\pi r_{\min}^2(v^*)v^* dt \ .$$

The rate $\dot{N}$ of atoms entering the spin-flip region is then obtained by multiplying dV/dt by the typical density in the trap:

$$\dot{N} = \frac{4\pi r_{\min}^2(v^*)v^*}{4\pi R^3/3} N \ , \tag{3.6}$$

where R is the average cloud radius. The loss rate is then simply given by:

$$\frac{1}{\tau_{\mathrm{M}}} = \frac{3r_{\min}^2(v^*)v^*}{R^3} \ . \tag{3.7}$$

Now let us invoke the virial theorem for a linear trap, in order to connect the average quantities R and v^*:

$$mv^{*2} = \mu b R \ . \tag{3.8}$$

Finally, using equations 3.5, 3.6 and 3.8, one can rewrite equation 3.7 as:

$$\tau_{\mathrm{M}} = \frac{m}{3\hbar} R^2 \ . \tag{3.9}$$

This simple estimate in spherical geometry gives a similar result as [113]:

$$\tau_{\mathrm{M}} = \kappa \frac{m}{\hbar} R^2 \ ,$$

where $\kappa \approx 0.36$ was obtained experimentally.

In the worst case, R is of the order of a millimeter. We deduce that $\tau_{\mathrm{M}}^{\mathrm{K}} \approx 200$ s and $\tau_{\mathrm{M}}^{\mathrm{Li}} \approx 30$ s, which will be useful numbers for the choice of the magnetic transport dynamics, as explained in part 4.3.3.

3.1.3 Spin-relaxation

Another mechanism can induce harmful trap losses in a magnetic trap. Let us have a closer look at the hyperfine spectra of both species shown in Figure 1.6. The hyperfine structure of ^{6}Li reveals that the cooling ground sate $F = 3/2$ is above $F = 1/2$ in energy. Thus, for $F = 3/2$, if the magnetic traps contains atoms in both $m_F = 3/2$ and $m_F = 1/2$ Zeeman states, a collision may occur between them that ends up in $F = 1/2$ sublevels [65]. The difference of hyperfine energy is converted into 230 MHz kinetic energy, that is 11 mK, which is of the order of the trap depth (see parts 3.3.4 and 3.4.1). This is the reason why the ^{6}Li spin-polarization should be realized perfectly and why this isotope can not be cooled down alone in a magnetic trap [22]. The case of ^{40}K is quite different. As shown in Figure 1.6, its structure is inverted: $F = 9/2$ is below $F = 7/2$. As a consequence the spin-relaxation mechanism is suppressed in the case of ^{40}K. This is the reason why evaporative cooling of ^{40}K by sympathetic cooling between $m_F = 9/2$ and $m_F = 7/2$ is working in $F = 9/2$ [56].

3.2 Preliminary stages

Before loading atoms into the magnetic trap described above, we need first to prepare the cloud in order to optimize the transfer. As already explained before, we have to spin-polarize the cloud, that is to optically pump the atoms into their highest m_F state. Since this optical pumping has to take place in a constant and low field environment, it is compulsory to switch off completely and quickly the quadrupole (see part 3.3.1 for technical details on switches). Then, the atoms are not trapped anymore and shall experience a free expansion that creates some additional potential energy, and thus temperature, after the forthcoming magnetic trap is switched on.

This implies two things. First the spin-polarization step has to be the shortest possible as explained in part 3.2.3. Secondly, it may be interesting to compress the MOT (at constant temperature) before the spin-polarization time-of-flight, in order to minimize the additional potential energy. In addition, this compression allows for high

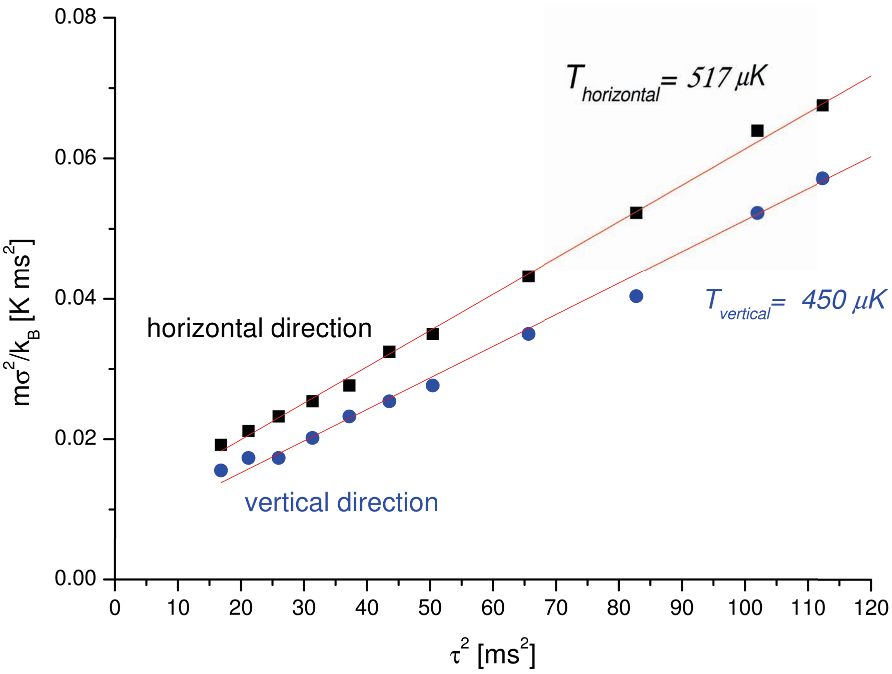

Figure 3.3: *Temperature of the* ^{40}*K compressed MOT (CMOT) measured by time-of-flight method (see part 2.2.3).*

interspecies collision rate which is helpful for thermalization and evaporative cooling. We tried this idea of compressed MOT for both species, as described in part 3.2.1, and we found out a better method for ^{40}K: the Cold MOT, as explained in part 3.2.2).

3.2.1 Compressed magneto-optical trap

In order to reduce the initial size of the cloud before the spin-polarization phase and to ensure a high interspecies collision rate in the magnetic trap, we tried to add a compressed MOT (CMOT) phase [114] for potassium and lithium. Results are reported here.

Potassium

In the case of ^{40}K, our best results were obtained by using a three steps process: a first one, lasting 15 ms, where the MOT current is ramped linearly to $I_M = 50$ A in order to increase the density; a second one, lasting 2 ms, where the current is brought back linearly to its standard MOT value $I_M = 9$ A, while the cooling frequency is detuned by additional $-1.5\,\Gamma$ in order to cool down the cloud; a third one, lasting 3.5 ms, where the MOT current is ramped down to zero while the cooling frequency is detuned even more by additional $-2\,\Gamma$, and where the repumping light is tuned to resonance in order to bring back all the atoms hidden in $F = 7/2$ towards $F = 9/2$ (hyperfine pumping) before the spin-polarization starts.

With those optimized parameters, we could increase the ^{40}K atomic density to $\sim 1 \times 10^{11}$ cm^{-3}. However this induced some heating as shown in Figure 3.3. The

^{40}K MOT temperature of 290 μK increased by compression to approximately 500 μK. With such a CMOT, the number of atoms was reduced by a factor 2. Then, since we were loosing in temperature and number in the magnetic trap, we decided to implement another method for potassium: the Cold MOT (see part 3.2.2), more adapted to achieve efficient magnetic trapping, transport and to ensure high phase-space densities in the final cell.

Lithium

In the case of ^{6}Li, our best results were obtained by using a similar CMOT protocol as the one described in [115]. In our experiment, the optimal CMOT phase lasts 5.5 ms and the cooling frequency is brought back closer from resonance by 2 Γ leading to a total detuning of -3 Γ, while its intensity is ramped down to zero in order to reduce the rescattering process (see part 2.1.5) and thus the temperature. In parallel, the repumper intensity is simply reduced by 30 %. This leads to a final temperature of 1 mK instead of 1.4 mK in the standard MOT, and a doubling of the atomic density that reaches 3.5×10^{10} cm^{-3}.

3.2.2 Cold magneto-optical trap

The CMOT phase described in part 3.2.1 heats the for ^{40}K cloud as shown in Figure 3.3. We then found a better way to increase the density while reducing the temperature, without loosing atoms: the Cold MOT.

Its philosophy is quite different from the CMOT one. In fact our Cold MOT is comparable to an optical molasses. There is no magnetic field and the cooling frequency is detuned furthermore to diminish the heating induced by radiation pressure. The Cold MOT consists of a 3.5 ms step where the magnetic field is linearly ramped down to zero whereas the cooling frequency is detuned by additional -2.5 Γ, resulting in a total detuning of -5.5 Γ. What is particular to our system is that the repumping frequency is brought from -5 Γ to only $-\Gamma$, that is closer to resonance. This allows for a strong hyperfine repumping of the atoms hidden in $F = 7/2$ towards $F = 9/2$ before the spin-polarization starts, as explained for the CMOT in part 3.2.1.

With this method, the MOT temperature could be reduced from 290 μK to 200 μK and the atomic density could reach 5×10^{10} cm^{-3}, which is equal to almost twice the MOT density. Moreover we did not see any consequent loss in atom number which confirmed us that the Cold MOT is more relevant in our system for ^{40}K. However, this may not be appropriated for ^{6}Li, and an optimized compression stage has to be find for the ^{6}Li-^{40}K mixture.

3.2.3 Optical pumping

As explained above, before loading the atoms into the magnetic trap we need to optically pump them into the stretched state, that is the one maximizing m_F for the cooling ground-states: $F = 9/2$ for ^{40}K and $F = 3/2$ for ^{6}Li.

To achieve this, after the end of Cold MOT, where all the atoms hidden in the repumper states have been brought back into their cooling ground-state by hyperfine pumping, we shine a vertical resonant laser beam with circular σ^{+} polarization on the

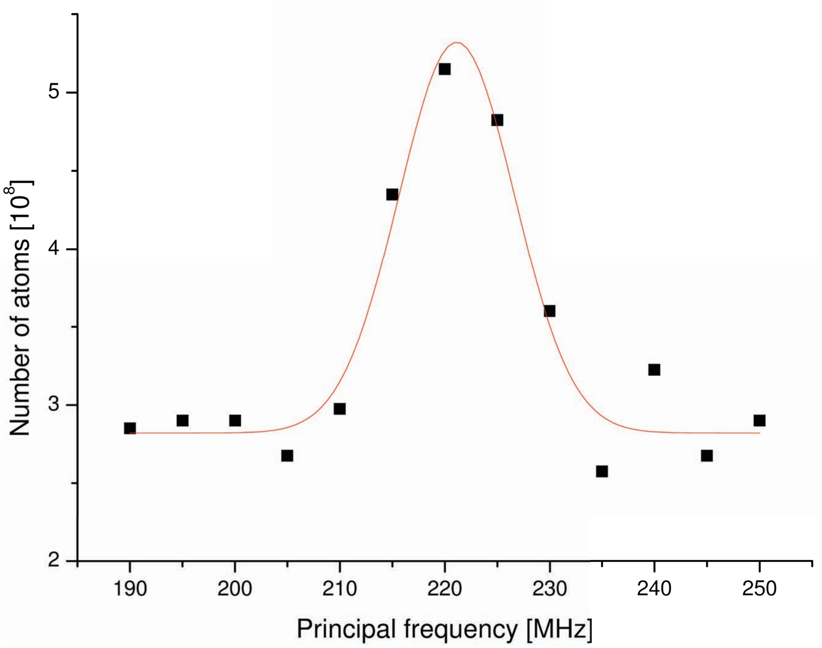

Figure 3.4: *Dependency of ^{40}K atom number on the spin-polarization principal AOM frequency. The maximum corresponds to the atomic resonance. The picture has been taken after 54 ms in the magnetic trap and 2.1 ms of time-of-flight (see part 2.2.3).*

atomic sample. In parallel, we add a 2 G vertical bias magnetic field along the beam, in order to have a vertical guiding field for the σ-polarizations. As usual, this resonant beam induces a transition towards the levels: $F' = 11/2$ for ^{40}K and $F' = 5/2$ for ^{6}Li, but with conservation of angular momentum comes the additional selection rule: $\Delta m_F = +1$. Therefore, after the pumping light is off, the atoms tend to accumulate in their cooling ground-state with $m_F = 9/2$ for ^{40}K and $m_F = 3/2$ for ^{6}Li, as expected. In the following, we give precise details regarding our experimental achievement of spin-polarization. Note that the optimization of the ^{6}Li optical pumping is still in progress, following the one already implemented in the lithium group at ENS [22].

First of all, the pumping beam originates from the MOT MOPAs. Actually, for each atomic species, there is a single-pass switch AOM after the MOT MOPA as shown in Figure 1.7. The diffraction order used for the MOT beam is the first one. Since the MOT beam and the spin-polarization beam are never used simultaneously, we decided to derivate the zeroth order of this AOM for the spin-polarization beam. This beam contains both principal and repumping light, in a controlled ratio, and passes through an additional shift AOM, in order to have the desired resonant frequency before injecting an independent polarization-maintaining single-mode fiber. Figure 3.4 shows the spin-polarization efficiency as a function of the AOM frequency. The curve is a standard lorentzian resonance function. Its full width at half maximum is of the order of 2 Γ instead of the expected Γ, which we attribute to the Zeeman broadening of the bias magnetic field. In fact, 2 G correspond to 2.8 MHz, i.e. approximately $\Gamma/2$. Note that the circularly polarized imaging beam is horizontal, and thus not σ^+ in this configuration.

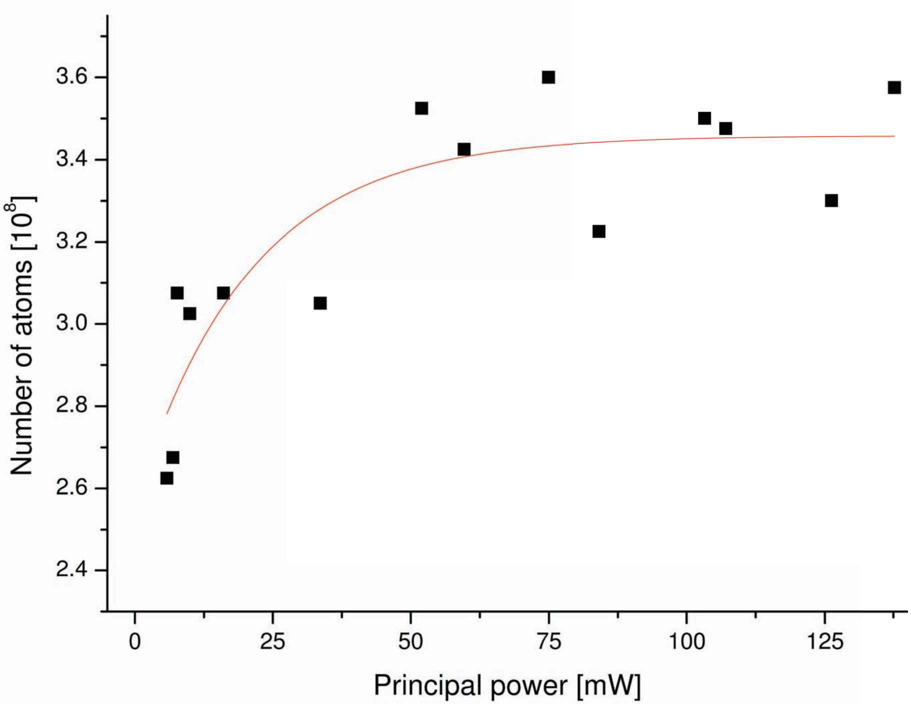

Figure 3.5: *Dependency of the ^{40}K atom number on the power of the spin-polarization principal beam. As far as it is concerned, repumping power equals 30 mW. The picture has been taken after 54 ms in the magnetic trap and 2.1 ms of time-of-flight (see part 2.2.3).*

The output of the spin-polarization fiber is located on the main table. There, the beams of each species are joined together using a dichroic mirror that passes one wavelength and reflects the other. The obtained beam is expanded to a 1.3 cm waist using a telescope, so that it is slightly bigger than the MOT size (see part 2.3.1). Then, using a broadband cube, it splits into two beams of equal intensities. One is joining the down-up MOT beam, on a cube, while the other is joining the up-down beam in a similar way. The idea here is, with a constant total intensity, to avoid the vertical acceleration created by the radiation pressure of a strong single spin-polarization beam. In fact, the intensities are the following: $I^{\mathrm{K}} \approx 63\ I^{\mathrm{K}}_{\mathrm{sat}}$ and $I^{\mathrm{Li}} \approx 10\ I^{\mathrm{Li}}_{\mathrm{sat}}$, where the I_{sat} are given in appendix A.1. Figure 3.5 shows the dependency of the number of ^{40}K atoms with the principal power of the beams. We see that we are in the saturation regime with the chosen intensities.

As far as the timings are concerned, the pumping stage lasts 500 μs, which is the minimal time step available in our actual computer sequence. Then the magnetic trap is ramped up in 3 ms, with a corresponding 150 A overshoot in the constant voltage (CV) analog command. Note that using the constant current (CC) mode or the CV mode without overshoot would have required a too high ramp up time, of the order of 10 ms. Another point is that the pumping beam is not always on during those 500 μs, otherwise it would heat and expel all the atoms from the trap region. It is actually on only during 50 μs in the case of ^{40}K and 250 μs in the case of ^{6}Li. To achieve this we use a Stanford Research Systems (SRS) function generator where we program the

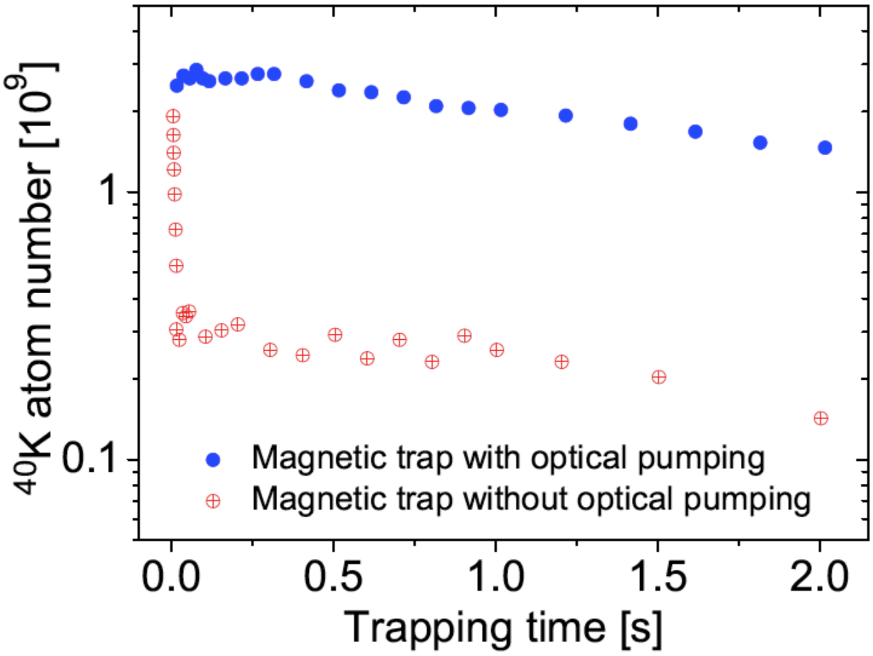

Figure 3.6: *Number of ^{40}K atoms in the magnetic trap, with and without the optical pumping stage after the Cold MOT. The pumping efficiency is close to 100 % since there is no short-time loss when the beam is on (dots). In absence of optical pumping (crosses), we notice a fast initial decay due to expulsion of atoms in high-field seeking states (occurring on a 5 ms time scale) and spin-relaxation among trapped magnetic states. The fact that the initial atom number seems to be different from the Cold MOT atom number is an artifact: there is a different Clebsh-Gordan coefficient in the imaging diagnostic (see equation 2.11) due to spin-polarization of the cloud. Note also that both curves show a long-term one-body decay due to collisions with residual background gas (see part 3.3.5).*

short pulse that feeds the amplitude port of the VCO of the spin-polarization AOM. This pulse ends 150 μs before the end of the 500 μs pumping stage and it is trigged by the digital control of the AOM.

Finally, note that the AOM amplitude of the repumping beam is kept at 100 %, in order to have a lot of repumper light in the spin-polarization beam to bring back again the atoms from the ground-state $F = 7/2$.

With these parameters, we could get almost 100 % of pumping efficiency for ^{40}K, as shown in Figure 3.6, and 30 % for ^{6}Li for which optimization is still in progress. Note that, despite the different imaging Clebsh-Gordan coefficient in a fully polarized cloud that can lead to errors in the evaluation of the numbers of atoms (see equation 2.11), we can assume that the initial number of atoms in Figure 3.6 corresponds to the number measured in the Cold MOT. Indeed, we do not observe any initial loss on a 5 ms time scale, which demonstrates the absence of high-field seeking states and spin-relaxation.

The long-term decay of both curves on the graph is due to the vacuum quality. It is studied in part 3.3.5. We conclude from the short-term data that the pumping is compulsory if we do not want to loose 90 % of the atoms due to spin-relaxation or high field seeking states.

Unfortunately, this process is still not perfect since it induces a consequent heating. In fact, due to the pumping beam intensity the potassium horizontal temperature reaches 344 μK in the cooler case, and the vertical one 423 μK. We could avoid this effect by attenuating the pumping beam but the transfer efficiency then also decreased. Thus, there is a trade-off between high numbers and low temperatures. The final fine tuning of this intensity will be achieved during the evaporation stage, where we will try to maximize the phase-space density, knowing that we may need an imperfect pumping for ^{40}K, since we may use both $m_F = 7/2$ and $m_F = 9/2$ for thermalization (see part 3.4.3).

Let us finally mention that we want to remove any possible source of stray light during magnetic trapping. Thus we shut down all the AOM with the VCO attenuators and detune strongly their frequencies. AOM have a short switch-off time of less than a microsecond. However their attenuation is limited to 10^{-4}, thus we need to add some mechanical shutters. Those have a full attenuation but are quite slow in comparison to AOM, since they need 100 μs to mask the beam once they start to move. They are of two kinds, home-made ones with razor blades glued on electromagnets (Tyco Electronics, T90N1D12-12), or commercial iris-type from Uniblitz. In both cases, they have a delay in response time of the order of 5 ms that we had to calibrate precisely and incorporate in our computer time sequence. Note that this delay is only a calibrated offset in the response time, before the shutter moves, which is independent from the 100 μs switching time.

3.3 Experimental characterization

After the previous preliminary steps, ^{6}Li CMOT, ^{40}K Cold MOT and spin-polarization, we load the atomic mixture into the magnetic trap. In this section we present its main experimental characteristics, such as temperatures, numbers of atoms, sizes and lifetimes, after a brief overview about some technical aspects on power, switches and security.

3.3.1 Technical overview

The pair of coil of the magnetic trap is the MOT pair. It is fed by a single 45 V-140 A Delta power supply whose output is controlled in voltage (CV mode, see part 3.2.3) through the analog card of the National Instrument computer (see part 1.5). The pair resistance is $R = 0.178\ \Omega$ and it creates an axial magnetic gradient of 0.936 G.cm^{-1}.A^{-1}.

We need to take pictures in order to get information about the trapped cloud. Because of the inhomogeneous Zeeman effect it is necessary to switch off completely the magnetic field to get homogenous detunings as far as the imaging frequency is concerned (see part 2.2.2). However, the current in the magnetic quadrupole pair can reach $I_M = 150$ A. With such a high current, a standard MOSFET switch (such as the one used for transport, described in part 4.5.2) was shown to be too slow, as it would require approximately 10 ms to switch off, which is the duration after which the size of the ^{40}K cloud reaches the imaging limits. Instead we decided to use an Insulated

Gate Bipolar Transistor (IGBT) from Mitsubichi Electric (CM600HA-24H), for which the closing time at high currents is of the order of 1 ms.

Besides, to protect the IGBT during switch-off phases, we put a varistor on the drain-source channel to limit the overloads created by electromotive forces. We also installed flyback diodes (Vishay 400U120D) on the power supply, in order to prevent strong negative Lenz currents from flowing back inside the power supply. In addition, the gate-source digital command is isolated from the computer by the optocoupling box described in part 1.5.

Finally, note that the coil M is home-made. We used an Ertacetal mount and hollow wire (4 mm outside diameter, 2.5 mm inside diameter) in order to pass water directly inside for cooling. For safety reasons, we placed a 10 kΩ thermistance to control the temperature of the pair, as well as a water flux-meter. Both thermistance and flux-meter are coupled to the interlock circuit of the power supply to turn it off in case of problem.

3.3.2 Atomic cloud properties

Using the ^{6}Li CMOT (part 3.2.1), the ^{40}K Cold MOT (part 3.2.2), the optical pumping (part 3.2.3) and the technical aspects (part 3.3.1) described before we could get single magnetic traps of typically 1×10^9 atoms for each species. With our biggest MOT we could even reach the value of 3×10^9 for ^{40}K (see Figure 3.6). Note that, due to the 1 ms switching time of the coils, it was not possible to get *in-situ* pictures so we had to wait usually 2 ms before taking an image.

As far as they are concerned, the temperatures of the two single-trapped atoms are quite different: $T^{\mathrm{K}} \approx 400\ \mu$K (see Figure 3.7) and $T^{\mathrm{Li}} \approx 1.3$ mK.

From these temperatures we can deduce sizes. By definition of the RMS velocity in 1D, we have:

$$\frac{1}{2} m v^{*2} = \frac{1}{2} k_{\mathrm{B}} T \ . \tag{3.10}$$

This result, combined with virial relation 3.8, leads to:

$$R = \frac{k_{\mathrm{B}} T}{\mu_{\mathrm{B}} b} \ . \tag{3.11}$$

Thus, with a vertical gradient $b = b_z = 85$ G.cm^{-1} (corresponding to $I_M = 90.5$ A) we get $R^{\mathrm{K}} = 0.7$ mm and $R^{\mathrm{Li}} = 2.3$ mm in the vertical direction, which is also in accordance with the sizes that we extract directly from the 2 ms time of-flight pictures, a snapshot of which is given in Figure 3.8. For the shallower horizontal direction, that has half the vertical gradient, we just have to multiply those numbers by a factor 2, according to equation 3.11.

Using the sizes of the clouds and the numbers of atoms we can obtain the average densities. We find $n \approx 2 \times 10^{11}$ atoms.cm^{-3} for ^{40}K, and $n \approx 5 \times 10^9$ atoms.cm^{-3} for ^{6}Li.

The results presented above concern only single species traps. The study of the double magnetic trap is still in progress and should give some useful data about the mutual influence of polarized ^{6}Li and ^{40}K soon. In particular, we expect to get some quantitative information about thermalization and inter-species collisions.

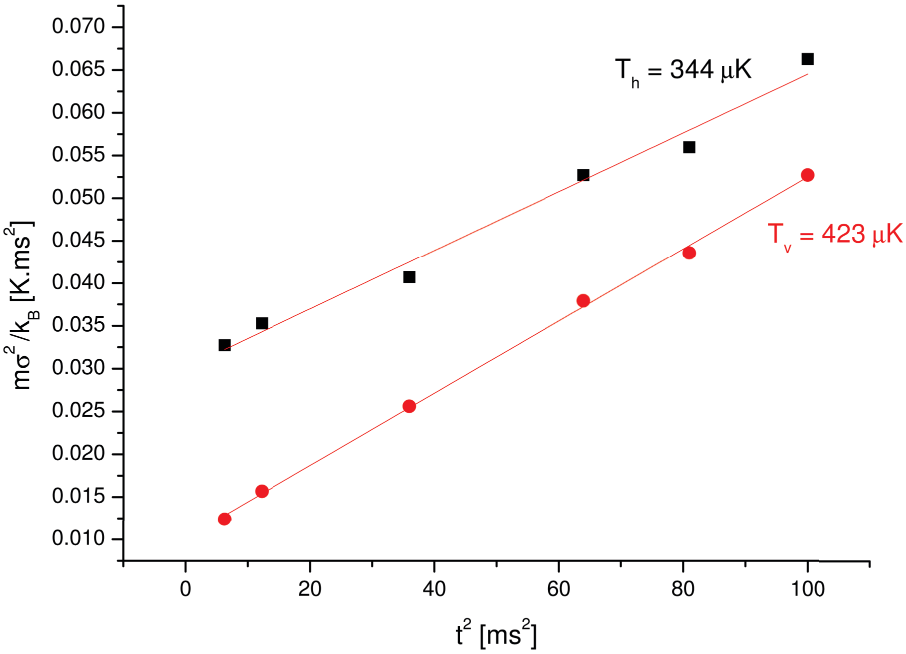

Figure 3.7: *Vertical and horizontal temperatures of* ^{40}K *atoms in the magnetic trap measured by time-of-flight method (see part 2.2.3).*

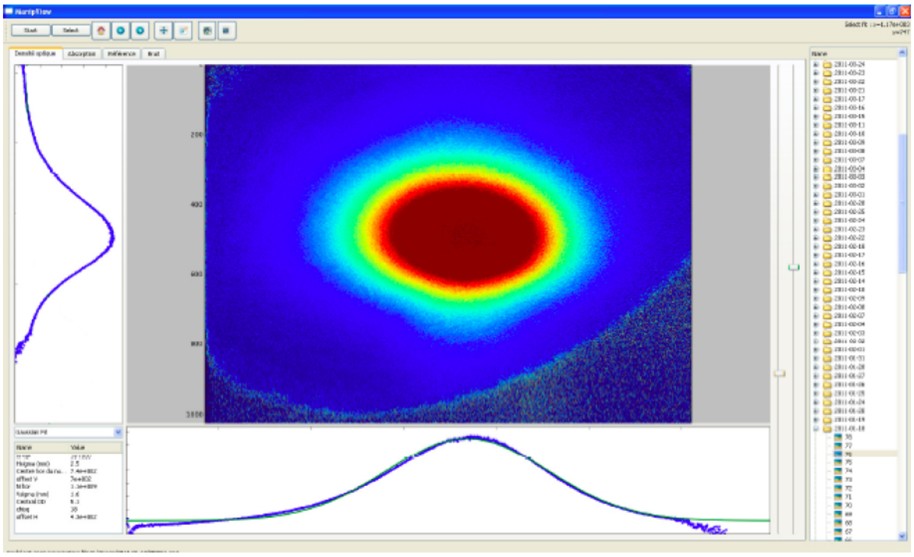

Figure 3.8: *Screen capture of a 2.1 ms time-of-flight picture (see part 2.2.3) of the* ^{40}K *magnetic trap, using Eric software.*

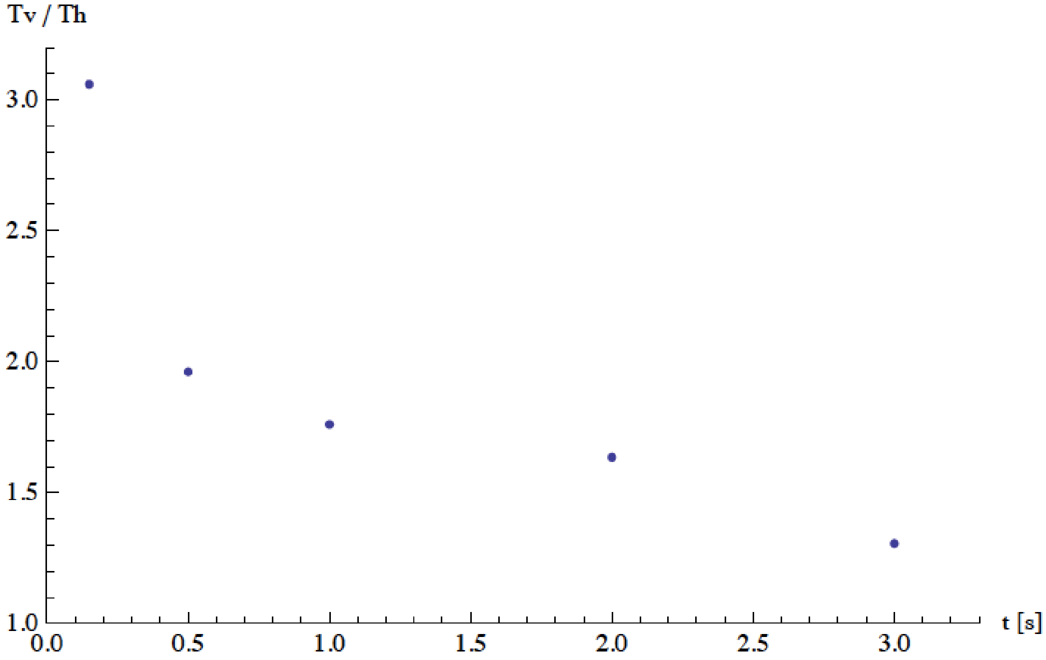

Figure 3.9: *Evolution with time of the ratio between vertical and horizontal temperatures, in a* ^{40}K *magnetic trap.*

3.3.3 ^{40}K p-wave cross-section

Due to Pauli exclusion principle, s-wave intraspecies collisions are suppressed for fermions in a single spin state. Nevertheless, for a temperature greater than a threshold temperature of 100 μK in the case of ^{40}K, p-wave collisions can occur [116]. Those collisions are characterized by an elastic cross-section of approximately 2×10^{-11} cm^2.

While measuring the temperature in the ^{40}K magnetic trap, we noticed that the vertical and horizontal temperatures were actually different just after the loading of the trap. We attribute this to the spin-polarization phase that heats the cloud vertically. Moreover, the two temperatures equilibrate to a same value after a few seconds, as shown in Figure 3.9, and the thermalization time τ is of the order of a second. From this measurement we estimate the ^{40}K p-wave elastic cross-section, through its definition:

$$\sigma = \frac{1}{\tau v^* n} , \tag{3.12}$$

where $v^* = \sqrt{3k_\mathrm{B}T/m}$ is the 3D RMS velocity, and n is the average ^{40}K density in the magnetic trap. Using the numbers given in part 3.3.2, we obtain $\sigma_\mathrm{KK} \approx 1.2 \times 10^{-11}$ cm^2, which is in good agreement with the value from JILA [116]. Note that this estimate relies on the fact that spin-polarization in a single spin state is perfect, since the s-wave elastic cross-section is of the same order as the p-wave elastic cross-section at the temperature of the magnetic trap.

This result is important. It demonstrates that, above a few tens of microkelvins, collisions still occur in a ^{40}K cloud polarized in a single spin state. Therefore, it offers an additional strategy for evaporative cooling above a few tens of microkelvins (see part 3.4.3), which consists of cooling down the purely polarized ^{40}K atoms only. With this technique, it is not necessary to transfer some atoms in another spin state before evaporation. This measurement will be implemented as well for the double cloud, in order to probe the interspecies elastic collisions.

3.3.4 Trap depth and gravity

Using equation 3.11 and including a $D = 3$ cm minimal distance from the center to the walls (see Figure 4.7), one can obtain the trap depth in temperature units:

$$T_{\text{depth}} = \frac{\mu_{\text{B}} b D}{k_{\text{B}}} \ , \tag{3.13}$$

independently of the atomic mass. Putting numbers, and using $b = -b_x = 0.5\ b_z$, leads to $T_{\text{depth}} \approx 8.5$ mK, which is six times greater than the critical T^{Li}: we do not loose atoms by evaporation on the MOT chamber walls. Finally we can verify that gravity can be forgotten in such a trap. Let us compare the gravitational force mg to the typical vertical magnetic force $\mu_{\text{B}} b_z$, in the case of the heavy ^{40}K:

$$\frac{m^{\text{K}} g}{\mu_{\text{B}} b_z} \approx 8\% \ ,$$

which does not affect strongly the trap depth. We can neglect losses due to the gravity tilt in the magnetic trap.

3.3.5 Lifetime

We notice on Figure 3.6 that, apart from the quick losses due to ^{40}K in untrappable states, there is a long term decay. Actually, in the vacuum chamber where the trapping takes place there is a background gas thermalized with the room temperature walls. It is composed of impurities due to partial baking out as well as atoms from the vapor of ^{6}Li and ^{40}K. Because of the finite depth of the trap calculated in part 3.3.4, collisions between the trapped atoms and the background gas can lead to losses. Neglecting other loss mechanisms, such as Majorana losses or spin-relaxation, the number of trapped atoms N in a magnetic trap evolves with the rate equation:

$$\frac{\mathrm{d}N}{\mathrm{d}t} = -\frac{N}{\tau} \ ,$$

where τ is the lifetime associated to those one-body losses. We measured this exponential decay for both ^{6}Li and ^{40}K magnetic traps and found out $\tau \approx 3$ s in both cases. A typical experimental curve for ^{40}K is given in Figure 3.10. The absorption pictures has been taken after various durations in the magnetic trap and an additional 2.6 ms delay in order to ensure the complete switch off of the coils (see part 3.3.1). We can make three comments about this lifetime.

First, it is disconnected from Majorana losses since we found in part 3.1.2 that $\tau_{\text{M}}^{\text{K}} \approx 200$ s and $\tau_{\text{M}}^{\text{Li}} \approx 30$ s, and from spin-relaxation and high field seeking states losses that happen in the first 100 ms (see Figure 3.6).

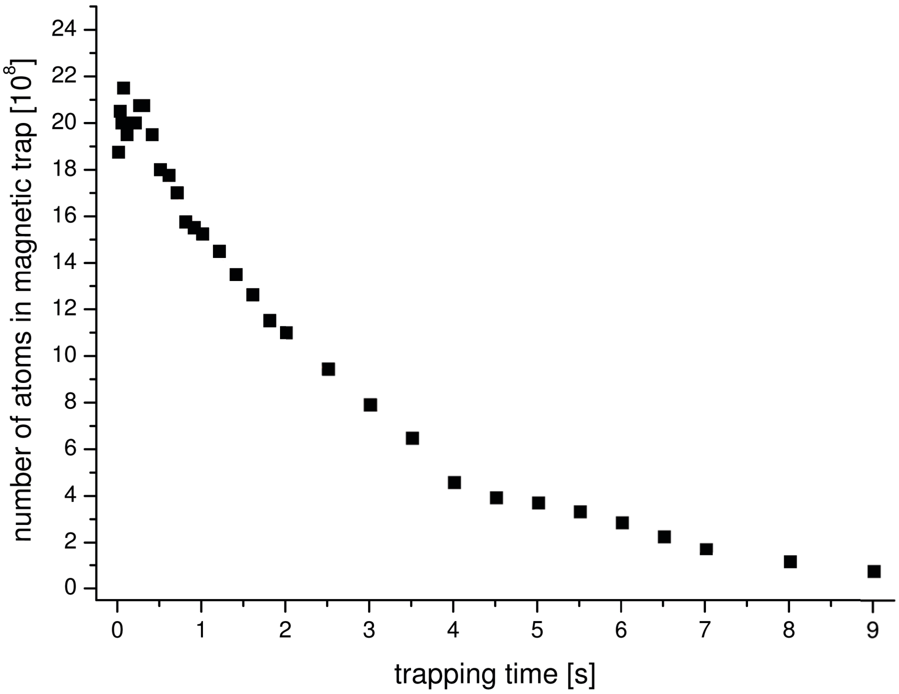

Figure 3.10: *Number of* ^{40}K *atoms in the magnetic trap* ($I_M = 90.5$ *A*) *as a function of time.*

Secondly, it is almost half smaller than the MOT lifetime which is 7.5 s for both species. This is not surprising if we compare the depth of both traps. For the magnetic trap, we found in part 3.3.4: $T_{\mathrm{depth}} \approx 8.5$ mK. For the MOT, we found in part 2.1.7: $T^{\mathrm{K}}_{\mathrm{depth}} \approx 0.9$ K and $T^{\mathrm{Li}}_{\mathrm{depth}} \approx 0.3$ K, which are respectively 100 and 30 times bigger than the magnetic trap depth. According to [117] the lifetime is proportional to $T^{1/6}_{\mathrm{depth}}$: this is consistent with the approximate factor 2 that we observe.

Thirdly, those lifetimes, both for MOT and magnetic traps, are quite low. We thus performed an helium leak-test on the vacuum chamber showing no major leak. We also side-checked that separating the atomic sources by closing the valves during 24 hours would not change these lifetimes, removing the hypothesis of pollution by the source regions. We finally think that incomplete outgassing could be the reason of such a low lifetime. Nevertheless, the science cell is separated from this region by a differential pumping tube (part 1.1.3), and it is pumped out by a Varian 40 L.s^{-1} ionic pump and a titanium sublimation pump. Therefore, we reach a vacuum with 30 s lifetime in the final magnetic trap, as measured in Figure 5.20, which is reasonable for evaporative cooling of the mixture.

3.4 Next stages

As explained above we measured the one-body lifetime of the magnetic trap (see Figure 3.10) to be 3 s, which is too small to allow for evaporative cooling of the atomic sample. Moreover, the optical access is not optimal in the MOT chamber, due to numerous 2 inches MOT optics. We then transfer the mixture from the MOT octagonal chamber to a glass science cell, 60 cm and an elbow away, where the lifetime was measured to be of the order of 30 s. This transfer is exhaustively described in chapter 4 and 5.

Once the atoms reach this final cell, they are kept in the transported magnetic trap. However, if one cools down the sample by evaporation, the Majorana lifetime τ_{M} reduces with temperature T. In fact, combining equation 3.9 with equation 3.11 leads to: $\tau_{\mathrm{M}} \propto T^2$. Thus, efficient evaporative cooling is impossible in a simple quadrupole trap.

Various solutions to this issue exist, three of them being in magnetic traps. The first one is the Ioffe-Pritchard configuration [118], also-called QUadrupole-Ioffe Configuration (QUIC). In such a trap, the harmful minimum of magnetic magnitude is shifted from zero to a finite value by adding a single coil orthogonally to the pair axis. The second method is the so-called Time-average Orbiting Potential (TOP) [113], which was historically used for the observation of the first BEC in 1995 [9]. Its principle is to add a rotating magnetic field in the transverse plan of the quadrupole, with a frequency small in comparison with Larmor frequency (otherwise additional Majorana spin-flips may occur), but higher than the typical oscillation frequency in the quadrupole potential (see equation 4.16). The time-averaged potential acts on the atoms as an effective harmonic potential with a finite minimum in field magnitude seen by the atoms. We decided to implement a third method: the optically plugged trap which led to the first Na BEC in 1995 [11], and which was proven to be efficient for ^{6}Li-^{40}K [56]. This trap is a combination of a standard magnetic quadrupole and a repulsive blue-detuned laser beam passing through its center and thus blocking the region where Majorana losses occur. We describe it further in part 3.4.2 and we present the evaporative cooling schemes in part 3.4.3.

Once evaporative cooling in the optically plugged magnetic trap has sufficiently reduced the temperature, and thus the size of the cloud, we can transfer the mixture into an optical dipole trap, where the evaporation process can be continued. We describe its principle in part 3.4.4.

Then, in part 3.4.5, we present the design of the Feshbach coils allowing for Feshbach resonances [18], and thus for control of the interatomic interactions. Finally, we present our high resolution imaging device in part 3.4.6.

3.4.1 Final quadrupole trap

At the end of the transport sequence, the mixture is kept in the quadrupole trap created by the penultimate pair of transport coils: the quadrupole pair. Its total resistance is $R = 0.11\ \Omega$ and it creates an axial magnetic gradient of 3.75 G.cm^{-1}.A^{-1}. The power supply, the coil winding, the switch details and the safety operations are the same as the ones described in part 3.3.1 for the initial magnetic trap coils. We can reach under these conditions an axial gradient of 560 G.cm^{-1} at 150 A during a minute, without major heating. The Helma science cell having a minimal horizontal half-size of 1.1 cm, the associated trap depth estimated through equation 3.13 is of the order of 20 mK.

3.4.2 Optically plugged magnetic trap

The principle of the Plugged Magnetic Trap [11, 119] is to add a repulsive blue-detuned dipole barrier (see part 3.4.4) at the center of the trap, in order to repel the atoms from the dangerous low field region. The waist of the laser creating the dipole barrier should be bigger than the Majorana radius given at equation 3.5 and estimated for the RMS velocity of the sample. For 560 G.cm^{-1} (see part 3.4.1), and in the worst case of ^{6}Li at 1 mK, this gives a RMS Majorana size of 3 μm. Thus, a typical laser waist of 20-30 μm s is acceptable for the plugged barrier.

In addition, simulations of Majorana losses have been performed. They showed that a 660 nm MOPA of 500 mW focused on 30 μm was not creating a high enough repulsive barrier (770 μK for ^{40}K and 140 μK for ^{6}Li) whereas a 532 nm Verdi laser of 10 W was satisfactory (1 mK for both species).

We decided to install the latter in the vertical direction, using the imaging Pixel Fly CCD camera for fine pointing. The Verdi consists of an intracavity-doubled Nd:YVO4 laser with 12 W maximal output power(Coherent, Verdi V12). We focus 7 W of its power over a waist of 20 μm using high power optics. Those are placed in a Thorlabs cage system to avoid the presence of dust on the beam path and to ensure pointing stability. In addition, to control this pointing, the penultimate mirror on the beam path is electronically controlled by a Thorlabs circuit (TST001 and ZST13). Finally, the switch-off of the Verdi is realized with a 110 MHz AOM (AA optoelectronic, MCQ110-A2). This modulator is controlled by an home-made VCO amplified through a Minicircuits RF-amplifier (ZHL-5W-1) and it is air-cooled.

3.4.3 Evaporative cooling

Since we are working with fermions, it is compulsory to perform the ultimate evaporative cooling stage through sympathetic cooling between two distinguishable fermions or spin states [20]. In fact, s-wave collisions are forbidden for undistinguishable fermions, due to Pauli's exclusion principle, whereas p-wave collisions are suppressed under 100 μK for ^{40}K [116] and 6 mK for ^{6}Li [120], by Pauli blocking [21].

As explained in part 3.1.3, using two different hyperfine states of ^{6}Li would not work in a magnetic trap because of spin-relaxation. One solution consists in evaporatively cooling ^{40}K, using a mixture of $|F = 9/2, m_F = 9/2\rangle$ and $|F = 9/2, m_F = 7/2\rangle$ states in an optically plugged magnetic trap. In this protocol, ^{6}Li is sympathetically cooled by ^{40}K. The associated potassium intraspecies s-wave scattering length equals $a = 170\ a_0$ [121], which is larger than the interspecies one of 64 a_0 [122], leading to higher cross-section $\sigma = 4\pi a^2$, and thus to better rethermalization and cooling efficiency.

According to the result summarized in part 3.3.3, above a few tens of microkelvins another possible strategy is to cool down by evaporation the purely polarized ^{40}K atoms in $|F = 9/2, m_F = 9/2\rangle$. In this protocol also, ^{6}Li is sympathetically cooled by ^{40}K. Then, around 50 μK, the mixture can be transferred into an optical dipole trap, and the evaporative cooling can be continued using an intraspecies Feshbach resonance, in order to increase the elastic collision rate.

Nevertheless, other strategies of evaporative cooling are possible with our design, and we could choose another one depending on the initial conditions. For instance, the following procedures have already been tested in other ^{6}Li-^{40}K experiments. In

Singapore [55], the bosonic ^{87}Rb is cooled down by evaporation, leading to sympathetic cooling of the fermionic ^{6}Li and ^{40}K. In Amsterdam [56], ^{40}K in three spin states is evaporatively cooled down, leading to sympathetic cooling of ^{6}Li. In Innsbruck [57], ^{6}Li in two spin states is evaporatively cooled down in an optical trap, leading to sympathetic cooling of ^{40}K. In Boston [58], evaporative cooling is performed on the bosonic ^{41}K, leading to sympathetic cooling of the fermionic ^{6}Li and ^{40}K.

Evaporative cooling is performed using microwaves signals that couple a trapped and an untrapped state at a certain distance of the trap center. We have already installed and tested the radio-frequency synthesizer (Agilent Technologies MXG ATE N5161A) and the associated antennas in the final quadrupole trap, by blasting out all the atoms from the science cell. In addition, a simulation of evaporation efficiency in a plugged trap, created with a 10 W Verdi laser, has been performed and confirms its feasibility. Finally, we measured the lifetime in the final cell and compared the associated loss rate to the elastic collision rate, as developed in part 5.4.2.

3.4.4 Optical dipole trap

Once the evaporation process is sufficiently advanced in the optically plugged magnetic trap, we plan to transfer the mixture in another conservative trap, the optical dipole trap [109, 123], in order to cool down further the cloud before studying it or transferring it into optical lattices [124]. Note that the optical dipole forces have also several applications in biology and micromechanics [125, 126]. In this part, we present the general principle of the optical dipole trap, as well as our first low-power experimental realization of dipolar trapping for ^{40}K in the MOT chamber. Then, we characterize the trap that we plan to get with a Coherent high-power laser, before presenting our simulations of parametric heating induced by the noise in this high-power laser.

General principle

In the theory of linear response, the classical polarizability of an atom is described by a complex number. In presence of an electrical field, such as the one carried by a laser beam, its imaginary part is maximal at resonance and it is linked to dissipation and radiation pressure that are used in laser cooling. On the contrary, the real part of the polarizability is linked to non-dissipative processes. It is null at resonance and it induces a potential that can be written far off-resonance as [86, 127, 128, 123]:

$$U_{\mathrm{dip}}(\boldsymbol{r}) = \frac{3\pi c^2 \Gamma}{2\omega_0^3} \frac{I(\boldsymbol{r})}{\Delta} \ , \tag{3.14}$$

where Δ is the detuning, $I(\boldsymbol{r})$ the beam intensity profile and ω_0 the transition pulsation. For a red detuning ($\Delta < 0$), this potential is attractive: atoms seek high intensities and thus are trapped at the focus point. On the contrary, far off-resonance blue-detuned light ($\Delta > 0$) can be used to generate some repulsive potentials around the cloud [129, 130]. This is a possible way to confine the cloud in a plan, or even on a line, and thus to reduce the effective dimension of the problem.

Even if the detuning of the laser is large, its intensity is large also so that absorption of photons can still occur and heat the cloud. Therefore, another important number

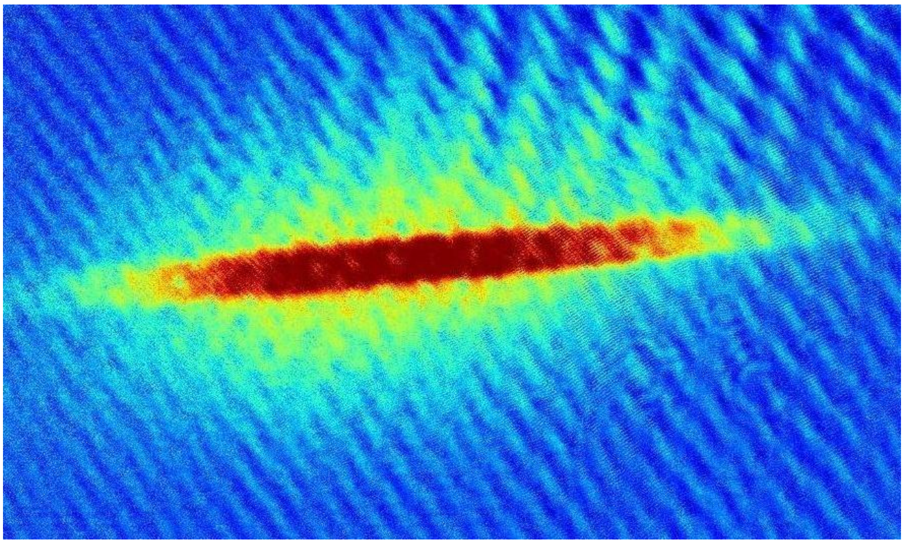

Figure 3.11: ^{40}*K dipole trap picture.*

to characterize an optical dipole trap is the scattering rate of photons $\Gamma_{\mathrm{scat}}(\boldsymbol{r})$. Its expression is given by [123]:

$$\Gamma_{\mathrm{scat}}(\boldsymbol{r}) = \frac{U_{\mathrm{dip}}(\boldsymbol{r})}{\hbar\Delta}\Gamma \ . \tag{3.15}$$

Experimental realization with low-power laser

We did not install yet a strong far off-resonance dipole trap in the science cell, but we tested its principle in the MOT chamber, using a low-power low-detuned focalized laser beam. An absorption picture is given in Figure 3.11. It consists of 5×10^7 ^{40}K atoms in an optical dipole trap of 3.5 mK depth. The trapping beam was generated by the additional diode and MOPA (see part 1.2.4) that we used for the photoassociation experiment (see part 2.4.1). Its fiber output power equals 660 mW. The beam is extended to a waist of $w = 2.2$ mm using a telescope, before being focalized over a waist of $w' = f\lambda/\pi w = 110$ μm (gaussian focal-to-focal magnification) using a lens with focal length $f = 1$ m, and its frequency is red-detuned by 10^4 $\Gamma/2\pi \approx 60$ GHz. The resulting maximal scattering rate equals $\Gamma_{\mathrm{scat}} \approx 10^{-3}$ Γ. The horizontal size equals 1.8 mm and the vertical one equals 420 μm.

Preliminary estimations with high-power laser

We decided to purchase a 25 W Coherent infra-red laser at 1064 nm. Then, it is feasible to focalize at least 10 W of power over a waist of 30 μm. From equations 3.14 and 3.15, we can estimate the associated trap depth for ^{40}K to be of the order of ~ 400 μK, and the scattering rate to be of the order of $\sim 8 \times 10^{-8}$ Γ, which is reasonable to trap efficiently a cloud at ~ 50 μK. For ^{6}Li, the trap depth equals ~ 180 μK and the scattering rate is of the order of $\sim 2 \times 10^{-8}$ Γ.

Simulation of parametric heating with high-power laser

Before purchasing the expensive Coherent high-power laser, we simulated the effect of the intensity noise of the laser on the energy distribution of the atoms. Actually, due to the direct dependencies on intensity in equation 3.14 and to the inherent intensity noise of the lasers, parametric heating may occur in the trap and induce consequent losses.

First, according to [131], at a given trap frequency f we can connect the parametric heating rate $\Gamma_{\mathrm{p}}(f)$ to the relative intensity noise spectrum $S(f)$ by the relation:

$$\Gamma_{\mathrm{p}}(f) = \pi^2 f^2 S(2f) \ .$$

The parametric heating time T_{p} is then simply given by $T_{\mathrm{p}} = 1/\Gamma_{\mathrm{p}}$. Since we could not get the noise data of the desired Coherent infra-red laser at 1064 nm, we used instead the data of another Coherent laser: the 10 W Verdi laser (V10) at 532 nm. Its noise spectra was obtained from the measurements of Scott Diddams at NIST (see Figure 3.12 (a)). Afterwards, Zoran Hazdibabic from Cambridge sent us the noise spectrum of the Coherent infra-red laser which happens to be similar to the Verdi one. Figure 3.12 (b) shows the calculated parametric heating time as function of trap frequency. We see that under 24 kHz the parametric heating time is above 5×10^4 s, which is reasonable for experiments that last less than a minute. For higher trap frequencies up to 70 kHz, it remains greater than 500 s, apart from a narrow spike (certainly due to the noise in the internal power supply that drives the pump diodes) where it reaches 190 s. This value is still acceptable.

Secondly, we obtained the lifetime in such a noisy trap through a numerical simulation. The evolution of the energy distribution $n(E,t)$ with time t follows a Fokker-Planck equation [132]:

$$\frac{\partial n(E,t)}{\partial t} = \frac{\Gamma_{\mathrm{p}}}{4} E^2 \frac{\partial n(E,t)}{\partial E^2} - \frac{\Gamma_{\mathrm{p}}}{2} n(E,t) \ ,$$

where the total number $N(t)$ of trapped atoms is given by:

$$N(t) = \int_{U_0}^{0} dE \ n(E,t) \ ,$$

with $U_0 = U_{\mathrm{dip}}(\mathbf{0})$. A typical result for $\Gamma_{\mathrm{p}} = 1000$ s and an initial temperature such as $T/U_0 = 1\%$ is given in Figure 3.13. The initial trap loss rate depends on the initial temperature of the trapped atomic cloud, however the asymptotic form of the solution of the Fokker-Planck equation [133], gives a trap loss rate of $9\Gamma_{\mathrm{p}}/16 \approx \Gamma_{\mathrm{p}}/2$, which is of the same order of magnitude as Γ_{p}.

Let us estimate now the trap frequency. For a single beam of waist w, the stronger confinement is in the radial direction with a trap frequency of [123]:

$$f_{\mathrm{r}} = \frac{1}{2\pi} \sqrt{\frac{4U_0}{mw^2}} \ ,$$

where m is the atomic mass. For the light ^{6}Li, with a laser of 10 W at 1064 nm, focused on a waist of 30 μm, we find a trap frequency of $f_{\mathrm{r}} \approx 5$ kHz, for which the

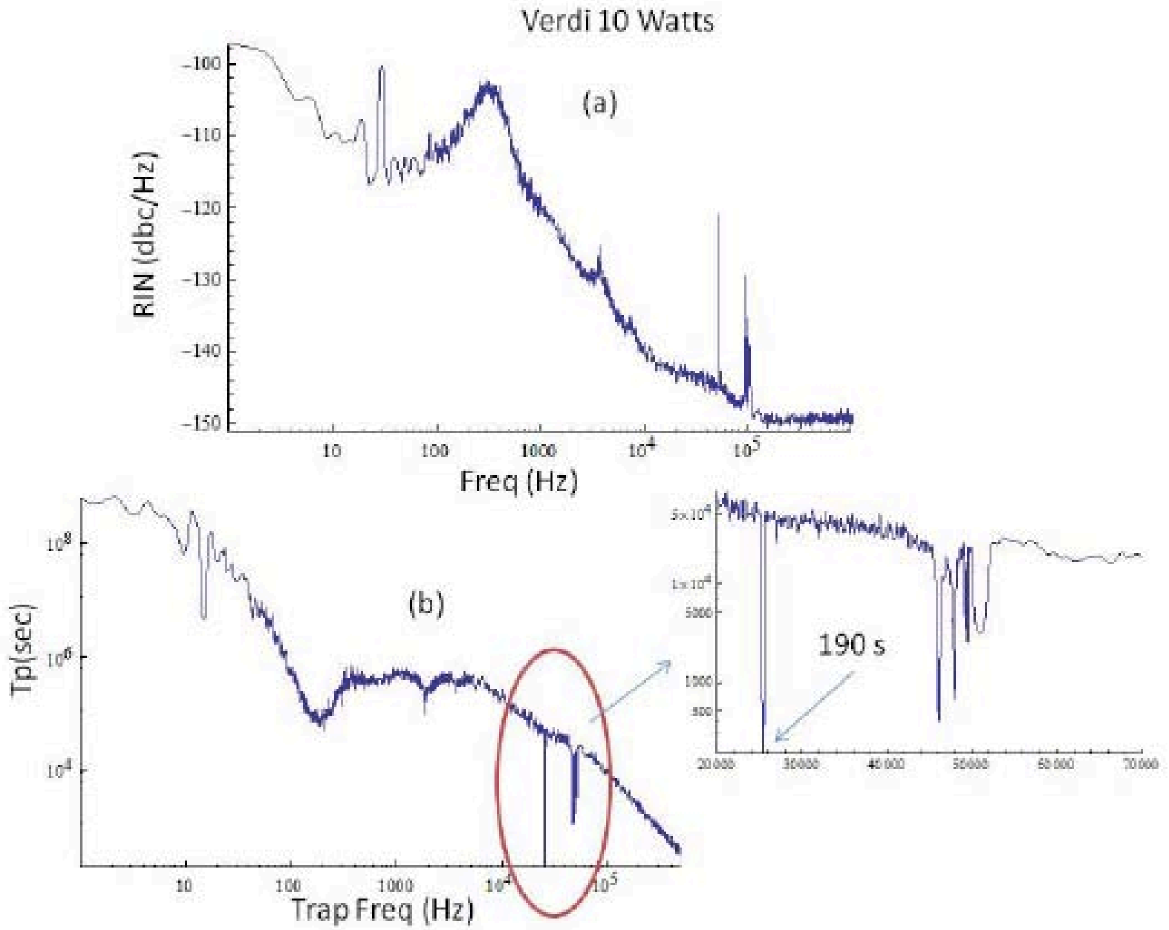

Figure 3.12: *Parametric heating time for Verdi 10 W laser of 532 nm. (a) Relative Intensity Noise (RIN) as a function of frequency. (b) Parametric heating time as a function of trap frequency.*

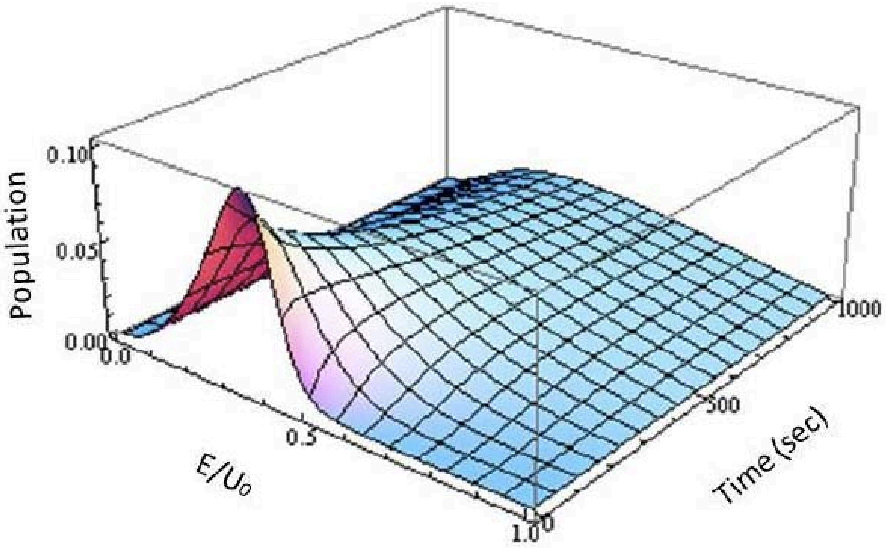

Figure 3.13: *Time evolution of the energy distribution in an optical trap. The parametric heating time is chosen to be 1000 s. The initial temperature is chosen such as* $T/U_0 = 1\%$.

parametric heating time is largely bigger than 1000 s (see Figure 3.12). The Coherent infra-red laser is thus acceptable regarding noise issues in optical dipole traps.

However, one should keep in mind that with optical lattices higher trap frequencies are reached. In 1D, along the lattice direction we have for instance:

$$f_{\mathrm{z}} = \frac{1}{2\pi}\sqrt{\frac{8U_0k^2}{m}}\ ,$$

which gives $f_{\mathrm{z}} \approx 300$ kHz for a 10 μK lattice depth. Thus, in future, the high frequency noise spectrum should be studied carefully as well.

3.4.5 Feshbach coils

Finally, during optical trapping, we will use one more time the quadrupole coils of the final magnetic trap (see part 3.4.1), but they will be switched into Helmholtz configuration in order to generate high and uniform bias magnetic fields. This will allow for interspecies Feshbach resonances between ^{6}Li and ^{40}K [60, 61], as well as for intraspecies resonances, and thus for a general control of the interactions.

For this purpose, we designed a new set of coils with stable mounts in order to replace the home-made quadrupole pair. Each coil of this new pair contains actually two coils: one big internal coil of 4 by 11 turns to generate strong bias fields of 10 G.A^{-1}, and one small coil of 4 by 4 turns giving a field of 2.64 G.A^{-1} in order to sweep quickly the field around a Feshbach resonance. We calculated that their theoretical overall inhomogeneity in magnetic field is of the order of a ppm over a cloud size of 100 μm. This inhomogeneity is acceptable to address physics at unitarity, since for a resonance of 155 G we need a precision of 43 mG according to [56], which means an inhomogeneity

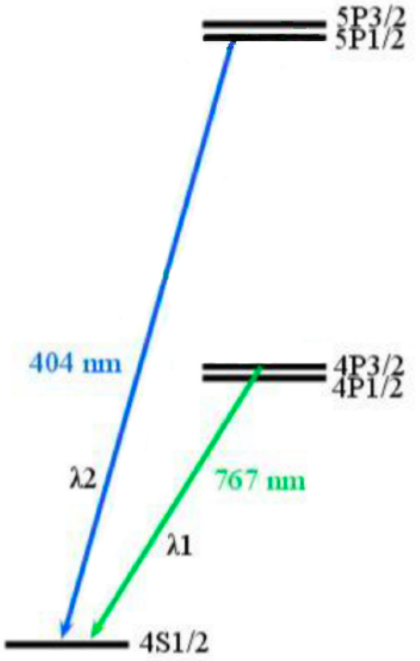

Figure 3.14: *Partial* ^{40}K *fine spectrum.* $\lambda 1$ *is the wavelength used for cooling and standard imaging.* $\lambda 2$ *is the wavelength used for high-resolution imaging.*

of 3×10^{-4}. The winding of this new pair is being performed at the moment by Oswald company and the coils will be installed as soon as we receive them.

3.4.6 High resolution imaging

High resolution imaging of single atoms in optical lattices is one of the hot topics in cold atoms physics nowadays [134, 135]. If one tries to image a single atom at a wavelength λ, by using a lens of focal length f and diametral aperture d, the Airy diffraction pattern obtained from Huygens principle has a radius of:

$$r = 1.22\frac{\lambda f}{d} \ .$$

Therefore, following Rayleigh's criterium, in order to distinguish two atoms they have to be typically separated by r. Since the best numerical aperture d/f we can obtain for a spherical lens is of the order of unity, the spatial resolution of such a lens is of the order of λ. As we wish to study atoms in optical lattices that have a periodicity of $\lambda^*/2$, where λ^* is the wavelength used to generate the lattice, we see that we need to have $\lambda \leq \lambda^*/2$. Since we plan to use a $\lambda^* = 1064$ nm Coherent infrared laser to generate the lattice (see part 3.4.4), we designed a high-resolution imaging system using the $\lambda = 404.414$ nm blue transition of ^{40}K shown in Figure 3.14 [136]. The diode used is a Sharp chip (GH02040A2GE). The design is a similar extended cavity Littrow configuration as the one described in part 1.2.2. As shown in Figure 3.15, we could observe the saturated absorption profile of this transition, using an absorption

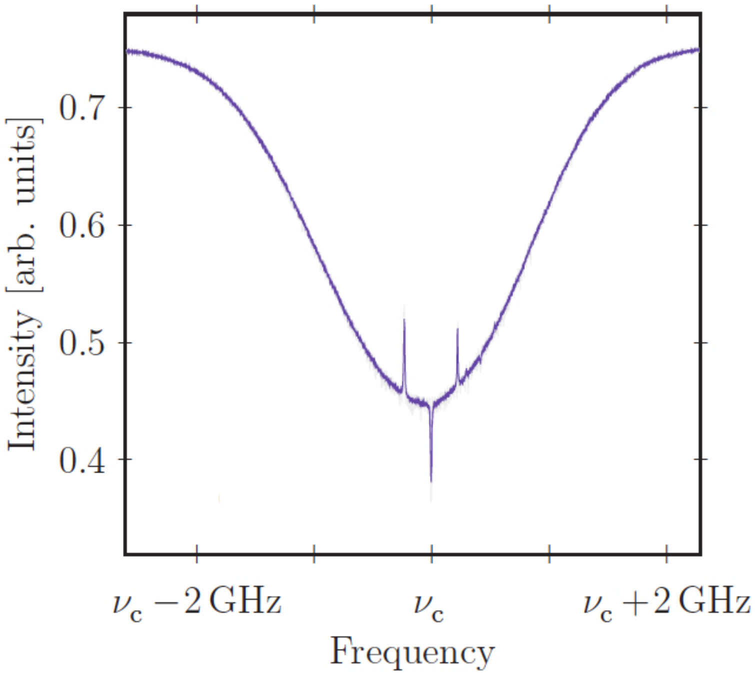

Figure 3.15: *Saturated absorption lines of the* $4S_{1/2}$*–*$5P_{3/2}$ *transition of* ^{39}K*. The middle peak is the crossover between the two others peaks that correspond to the transitions from the two hyperfine ground-states to the upper unresolved multiplet.*

cell heated to 150°C. We then locked the laser on the cross-over line, with a similar synchronous detection as the one introduced in part 1.2.3.

3.5 Summary

In this chapter, we presented our magnetic trap for ^{6}Li and ^{40}K, as well as the preliminary and forthcoming stages.

First, we described the general principle of magnetic trapping, as well as the losses mechanisms. In particular, we estimated the Majorana loss rates, that will be useful for the design of the magnetic transport.

Secondly, we characterized the preliminary stages for efficient magnetic trapping: compression and spin-polarization. For ^{40}K, using a quick Cold MOT scheme, we could compress the cloud to a density of 5×10^{10} atoms.cm^{-3}, and cool it further to 200 μK, with 100 % efficiency. Then, we could optically pump it into the $|F = 9/2, m_F = 9/2\rangle$ state, with 100 % efficiency. For ^{6}Li, using a quick CMOT scheme, we could compress the cloud to a density of 3.5×10^{10} atoms.cm^{-3}, and cool it further to 1 mK, with a 100 % efficiency. Then, we could optically pump it into the $|F = 3/2, m_F = 3/2\rangle$ state, with 30 % efficiency.

After those preliminary stages, we could load single-species magnetic traps with an axial magnetic gradient of 85 G.cm^{-1}, and we obtained typically 10^9 atoms in each case, after 1 s of trapping. With our biggest MOT we could even reach the value of 3×10^9 for ^{40}K. The temperatures were measured to be 400 μK for ^{40}K, and 1.3 mK for ^{6}Li. The thermalization time of ^{40}K was found to be of the order of 1 s, leading to an estimated p-wave cross-section, $\sigma_{\mathrm{KK}} = 1.2 \times 10^{-11}$ cm^2, close to the value obtained at JILA [116]. This offers an interesting strategy for evaporative cooling in an optically plugged magnetic trap above a few tens of microkelvin, by allowing for the cooling of ^{40}K in a single spin-state $|F = 9/2, m_F = 9/2\rangle$.

Finally, the forthcoming stages have been described. We designed the optically plugged magnetic trap in the science cell, where evaporative cooling will be initiated, as well as the optical dipole trap, where quantum degeneracy will be reached. Besides, we presented our high resolution imaging scheme, based on a 404 nm transition of ^{40}K, as well as the design of the Feshbach coils.

In order to perform evaporative cooling, and to study degenerate Fermi mixtures in optical traps, it is crucial to ensure a ultra-high vacuum environment and a good optical access. Therefore, we transfer the magnetic trap from the octagonal chamber to a final science cell. The design and engineering of this magnetic transport are described in chapter 4.

Chapter 4

Magnetic transport: design

During my thesis I designed, set up and studied a magnetic transport system for a cold ^{6}Li -^{40}K mixture. Starting from the magnetic trap described in chapter 3, we first ramp up the gradients in order to confine more the cloud and to avoid future losses by evaporation on the walls during transfer. Then we move the trap center over a total distance $L_4 = 64.7$ cm so that the atomic cloud is transferred into the science cell where vacuum and optical access are better than in the octagonal chamber of the MOT. Thus evaporative cooling becomes possible and, furthermore, different trap types can be achieved: optically plugged magnetic trap, optical trap or optical lattices of various dimensions and geometries. In addition, the final quadrupole pair being closer from the cloud than the MOT pair is, one can reach steeper confinement.

In this chapter, we present the theoretical aspects and the design of such a transport device. A following chapter is dedicated to its experimental implementation. Note that on one hand the displacement velocity should be high enough to prevent Majorana losses (see part 3.1.2) but on the other it should be low enough to ensure adiabaticity and protect the transport against losses due to heating. Two versions of this transport technics have been implemented. The first one, developed in the group of T. Hänsch and I. Bloch in Munich [137] relies on time-varying currents in a static ensemble of pairs of coils. The second one, invented in the group of E. Cornell in Boulder [138], is based on a physical displacement of the trap coils. We have chosen the first method, more complex but excluding mechanical vibrations of the system and more reliable after optimization of the various currents has been performed.

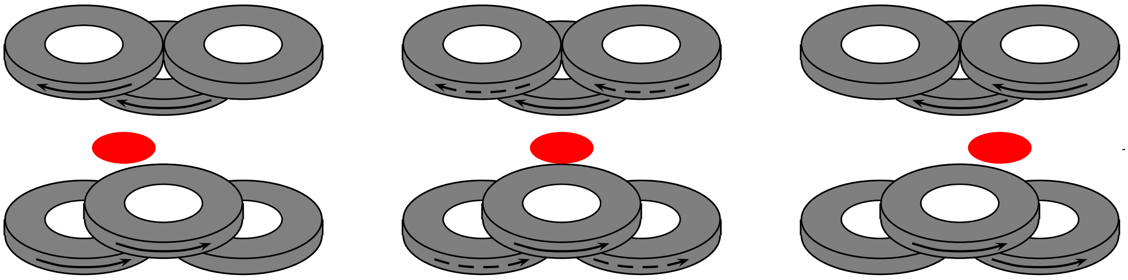

Figure 4.1: *Changing the currents in three consecutive anti-Helmholtz pairs of coils moves the center of the trap: if we decrease the current in the first pair of coils as we increase the current in the third one (see arrows), the center of the trap moves toward this third pair.*

4.1 Statics

In this section, we present the principle of the algorithm that calculates the current in each coil for a a given position of the trap, with gradients equal to the constraints at this point. We also describe the three critical points in the transfer: injection from magnetic trap, turning at the elbow and transfer into the final quadrupole trap.

4.1.1 Algorithm

The principle of the magnetic transport is described below. As explained in part 3.1.1 about the magnetic trap, the linear Zeeman shift (equation 3.2) is valid in our case and the quadrupolar development (equation 3.3) of the field created by the MOT coils as well. We note Ox the direction of the transport, even after the elbow, and Oz the vertical one. We want to impose and control the shape and the position of the trap. Thus we need to control four parameters: the trap position in the x axis, and the three gradients. However the gradients are not independent, since they are linked through the Maxwell equation:

$$\nabla \cdot \boldsymbol{B} = 0 \ .$$

We can then restrict ourselves to three control parameters. For instance: centre position x^*, gradient component $b_y = dB_y/dy$, and aspect ratio $A = b_x/b_z$. Note, that the latter necessarily varies if the trap evolves from a MOT configuration to a transport one, where the cylindrical symmetry is broken since several pairs of coils contribute at the same time. Three control parameters means three independent variables: the currents in three consecutive pairs of coils. Moreover one can show [139] that the optimal situation corresponds to the intuitive case where the distance between pairs is equal to the external radius of a single pair. A larger distance induce a sharp movement during transfer, whereas a smaller one implies a bigger total number of coils for a similar transfer. With such a triplet configuration, one easily understands that if we switch off the first pair of coils as we switch on the third one, the center of the trap moves toward this third pair (see Figure 4.1). When the first current reaches zero, we switch on a fourth pair of coils and then simply repeat the process. We first have to write an algorithm that calculates the currents in all the coils as a function of the position of the center of the trap. Then we can easily add the temporal dynamics by assigning a time at each position of the center of the trap. The principle of this algorithm relies on a resolution of the following system of equations:

$$\begin{cases} \boldsymbol{B}(\boldsymbol{r^*}) = \boldsymbol{0} \ , \\ b_y(\boldsymbol{r^*}) = b_y^*(\boldsymbol{r^*}) \ , \\ A(\boldsymbol{r^*}) = A^*(\boldsymbol{r^*}) \ , \end{cases}$$

where $\boldsymbol{r^*} = (x^*, y^*, 0)$ is the chosen position of the center, A^* the chosen aspect ratio function and b_y^* the chosen gradient function. For three consecutive pairs indexed by i=0, 1, 2, with three currents I_0, I_1, I_2, and the associated fields and gradients by unit of current $\tilde{B}_i$ and $\tilde{b}_i$, the system of equations becomes:

$$\begin{cases} \sum_{i=0}^{2} \tilde{B}_{i,x}(\boldsymbol{r^*}) I_i = 0 \ , \\ \sum_{i=0}^{2} (\tilde{b}_{i,x}(\boldsymbol{r^*}) + \tilde{b}_{i,z}(\boldsymbol{r^*})) I_i = -b_y^*(\boldsymbol{r^*}) \ , \\ A(\boldsymbol{r^*}) = A^*(\boldsymbol{r^*}) \ . \end{cases} \tag{4.1}$$

We solve this 3D system using Mathematica and exact formulas for the magnetic field created by a single loop of current (see appendix A.2 and A.3). We start from three pairs and when $I_0 = 0$ we increment the pair index. The chosen sampling precision is the millimeter which means a total number of points of the order of 647 since $L_4 = 64.7$ cm.

4.1.2 Injection

The initialization of the transport raises two main issues. First, in the method of transport described here we switch from a simple quadrupole trap situation, with a single pair of coils, to a transport situation with three pairs simultaneously working. As a consequence the chosen aspect ratio and gradient have to follow some ramps from their initial values to their transport values. Secondly, the first coils of the transport are the MOT ones (M). Due to size of the octagonal chamber, and especially the vertical view port flange, those coils have a small possible overlap with other coils. Thus it is compulsory to add a pushing coil (P) behind the MOT and a pulling pair (T1/2) between the MOT and the transport in order to allow the transfer of the cloud toward the transport coils. A schematics of the transport is given in Figure 4.2. We separate the initialization phase in two steps. A first pushing step where the pushing coil, the MOT coils and the first pair of transport coils are switched on. This step ends when the pushing current reaches zero after a pushing length $L_1 = 6.8$ cm, which is a parameter of the program: we can change its value, once the geometry has been fixed, to optimize the transport. Then, between the positions $x = L_1$ and $x = L_2 = 12$ cm, comes a ramp step where the y-gradient and the aspect ratio finish to reach their transport values. The transport then starts with constant gradient and aspect ratio. Note that the current of the pushing coil is not a variable like the others. It is actually imposed in our design, in order to allow for a finite pushing step and reasonable variations of currents with time. At the beginning of the algorithm the variable are simply the three next pairs of coils: MOT, T1/2 and T1 (see Figure 4.2) and the second member of system 4.1 is slightly modified by including the contribution of the pushing coil.

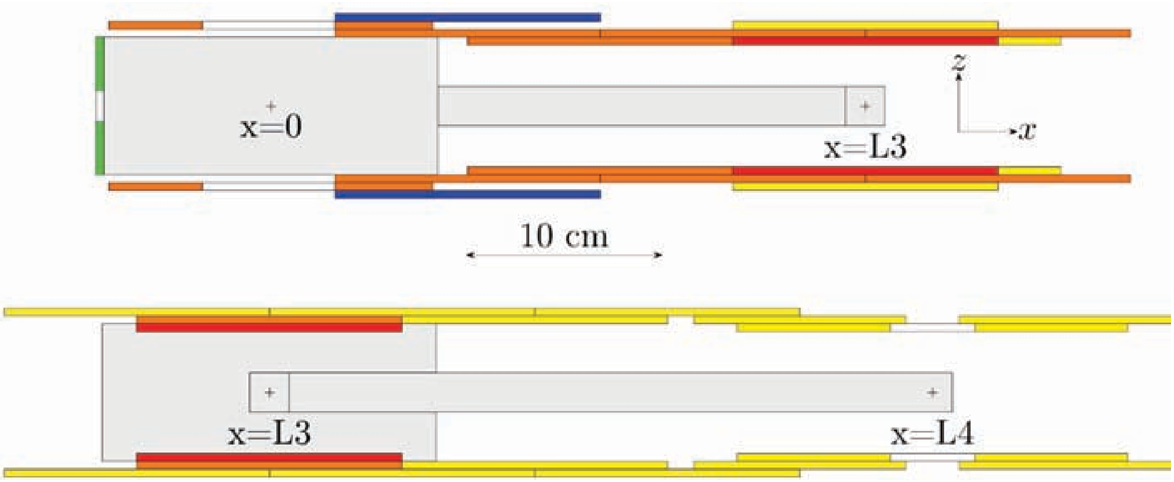

Figure 4.2: *Schematics of the two arms of the transport. By convention, x is the position in the transport direction, even after the elbow.The MOT octagonal cell is centered on $x = 0$. The pushing coil (P) is in green. The pulling pair (T1/2) is in blue. The other coils in the first arm of the transport are in orange, those in the second one are in yellow and the red ones belongs to both arms. $x = L_3 = 30.95$ cm is the position of the elbow. $x = L_4 = 64.7$ cm is the position of the final quadrupolar trap, in the science cell.*

4.1.3 Elbow

If we perform a single axis transport we loose the transport axis for imaging or laser manipulation. Moreover the vacuum can be polluted by atoms in ballistic flight coming from the MOT chamber. A trick introduced by the group of Munich [137] is to add a 90 ° elbow (see Figure 4.2) on the transport way. We also applied this idea to our design. The principle is the following. Let us call $L_3 = 30.95$ cm the distance from the initial octagonal cell to the elbow. When the transport reaches this point, the only pair which is on is the fourth transport pair (see Figure 4.2). We are back to a cylindrical symmetry, and the aspect ratio has been ramped progressively to -0.5. Then we switch on the coils in the second arm and ramp one more time the aspect ratio to its transport value -0.3. The principle is then identical to the first arm. Note that, due to the fact that only a single pair is switched on at the elbow, the angle of the elbow does not matter and we can keep x as the transport direction.

An engineering drawing of the elbow cross is shown in appendix A.6. Apart from the two connexions for the transport tubing, the three others allow to pump the chamber, to observe the atomic fluorescence (see part 2.2.1), and to have a laser beam in the direction of the second arm.

4.1.4 Outcoupling

After a total transport distance $L_4 = 64.7$ cm, the cloud is finally transferred into a standard quadrupolar trap, generated by the penultimate pair of transport coils. The constraints on aspect ratio and y-gradient have been ramped to their final values during the end of the transport. Note that those coils are different from the standard transport ones. After a future transfer in an optical trap, they will be converted into Feshbach coils. They are one millimeter away from the science cell walls and their inner diameter is 3.1 cm in order to allow for optical access for the high resolution imaging. This implies by the way, that the two adjacent pairs, the so called "neighbor pairs" (see Figure 4.2), are smaller than the transport pairs by 1.55 cm in radius.

4.2 Atomic cloud properties

We would like to study now the evolution of size and temperature of the cloud as a function of our magnetic constraints. Moreover, an additional differential pumping stage has been introduced in the transport tube in order to improve the vacuum quality in the final cell. We thus want to quantify the losses due to this pumping tube of 10 mm diameter. As explained above, in order to prevent the cloud from being heated, the sequence must be adiabatic. We can look for an adiabatic invariant in our quadrupolar geometry. Then, knowing the initial conditions, we can use this quantity to express the temperature and the size of the cloud as a function of the gradients only. In particular, it is relevant to compare the size with the tube dimensions, in order to control the chosen ramps on the gradients. The transport coils have an average diameter of the order of 6.5 cm and are located 3.5 cm away from the tube axis (DN16 or DN10). Thus, the typical length on which non-linearities appear in the energy is bigger than the tube size. We can then neglect them and assume that we remain in a quadrupolar trap truncated on the transport walls.

4.2.1 Adiabatic evolution

For a Boltzmann ideal gas in a quadrupole trap, we have the following adiabatic invariant (see appendix A.4):

$$\frac{T}{\left|b_x b_y b_z\right|^{2/9}} = \mathrm{cte} = \frac{T^0}{\left|b_x^0 b_y^0 b_z^0\right|^{2/9}} \,, \tag{4.2}$$

where the b_i are the three components of the gradient and T is the temperature of the cloud. In addition, since we assume independent particles, we can write in each direction:

$$(\Delta r_i)^2 \equiv < r_i^2 >= \frac{1}{z} \int\int \frac{d\boldsymbol{r} d\boldsymbol{p}}{h^3} r_i^2 e^{-\beta\left(\frac{\boldsymbol{p}^2}{2m} + \mu\sqrt{\sum_i b_i^2 r_i^2}\right)} = \left(\frac{2k_\mathrm{B}T}{\mu b_i}\right)^2 \,, \tag{4.3}$$

with m the atomic mass, μ the magnetic moment and z the monoatomic partition function (see appendix A.4). Then, combining equations 4.2 and 4.3, the RMS positions in the trap are given by:

$$\Delta r_i = \frac{2k_\mathrm{B}}{\mu} \frac{T^0}{\left|b_x^0 b_y^0 b_z^0\right|^{2/9}} \frac{\left|b_x b_y b_z\right|^{2/9}}{b_i} = \alpha \frac{\left|b_x b_y b_z\right|^{2/9}}{b_i} \,,$$

where we have introduced the parameter α. Note that the factor 2 comes from the algebraic definition of r_i, whereas in equation 3.11 the square root was taken before the statistical averaging. In the program, the constraints are fixed on b_y and $A = b_x/b_z$, where x is the transport direction and the z the vertical one. One can rewrite the RMS positions in each direction and the temperature as functions of those two constraints only:

$$\Delta x = \alpha \frac{|A+1|^{5/9}}{|A|^{7/9}} \frac{1}{|b_y|^{1/3}} , \tag{4.4}$$

$$\Delta y = \alpha \frac{|A|^{2/9}}{|A+1|^{4/9}} \frac{1}{|b_y|^{1/3}} , \tag{4.5}$$

$$\Delta z = \alpha \, |A|^{2/9} \, |A+1|^{5/9} \, \frac{1}{|b_y|^{1/3}} , \tag{4.6}$$

$$T = \frac{T^0}{\left|b_x^0 b_y^0 b_z^0\right|^{2/9}} \frac{|A|^{2/9}}{|A+1|^{4/9}} \, |b_y|^{2/3} \ . \tag{4.7}$$

As a remark, those quantities do not depend on the atomic mass: they are identical for both species, at fixed temperature. Let us finally calculate the fraction R_σ of atoms in the volume $\Omega = 2^3 \Delta x \Delta y \Delta z$, the fraction $R_{2\sigma}$ in the volume $2^3\Omega$, and the fraction $R_{3\sigma}$ in the volume $3^3\Omega$:

$$R_\sigma = \frac{1}{z} \int\int_{\Omega} \frac{d\boldsymbol{p} d\boldsymbol{r}}{h^3} e^{-\left(\frac{\boldsymbol{p}^2}{2m} + \mu\sqrt{\sum_i b_i^2 r_i^2}\right)/k_\mathrm{B}T} \approx 44\% , \tag{4.8}$$

$$R_{2\sigma} = \frac{1}{z} \int\int_{8\Omega} \frac{d\boldsymbol{p} d\boldsymbol{r}}{h^3} e^{-\left(\frac{\boldsymbol{p}^2}{2m} + \mu\sqrt{\sum_i b_i^2 r_i^2}\right)/k_\mathrm{B}T} \approx 86\% , \tag{4.9}$$

$$R_{3\sigma} = \frac{1}{z} \int\int_{27\Omega} \frac{d\boldsymbol{p} d\boldsymbol{r}}{h^3} e^{-\left(\frac{\boldsymbol{p}^2}{2m} + \mu\sqrt{\sum_i b_i^2 r_i^2}\right)/k_\mathrm{B}T} \approx 97\% . \tag{4.10}$$

4.2.2 Size and temperature

The ramps on b_y and A are given on Figure 4.3 and 4.4. Let us consider that we initiate the transport with a $T^0 = 1$ mK cloud, which is reasonable for ^{6}Li, and slightly over-estimated and safe for ^{40}K. The cylindrical symmetry in the initial magnetic trap implies $A^0 = -0.5$. We choose an initial gradient of $b_y^0 = -67$ G.cm^{-1}, which corresponds to the limit of the first power supply. Then during the pushing and ramp steps the constraints evolve until they reach their transport values $A = -0.3$ and $b_y = -155$ G.cm^{-1}. The gradient b_y is fixed at this last value whereas the aspect ratio is brought back to $A = -0.5$ during the two pulling steps: at the elbow ($x = L_3 = 30.95$ cm) and at the end of the transport ($x = L_4 = 64.7$ cm).

Thanks to formulas 4.4, 4.5, 4.6 and 4.7, we can plot the RMS sizes and the temperature during the whole transport. Results are shown on Figures 4.5 and 4.6. We notice that temperature remains reasonably low, under 2 mK.

We then compare the sizes to the tube dimensions as shown in Figure 4.7 and 4.8. It seems that in the worst case the efficiency is close to $R_{2\sigma} \approx 86\%$ (see equation 4.9) with our choice of constraints. Note that on Figure 4.7 we can recognize the MOT chamber walls, the DN10 differential pumping tube, and the main DN16 tube. To define the tube size in the transport direction we have taken the minimal distance

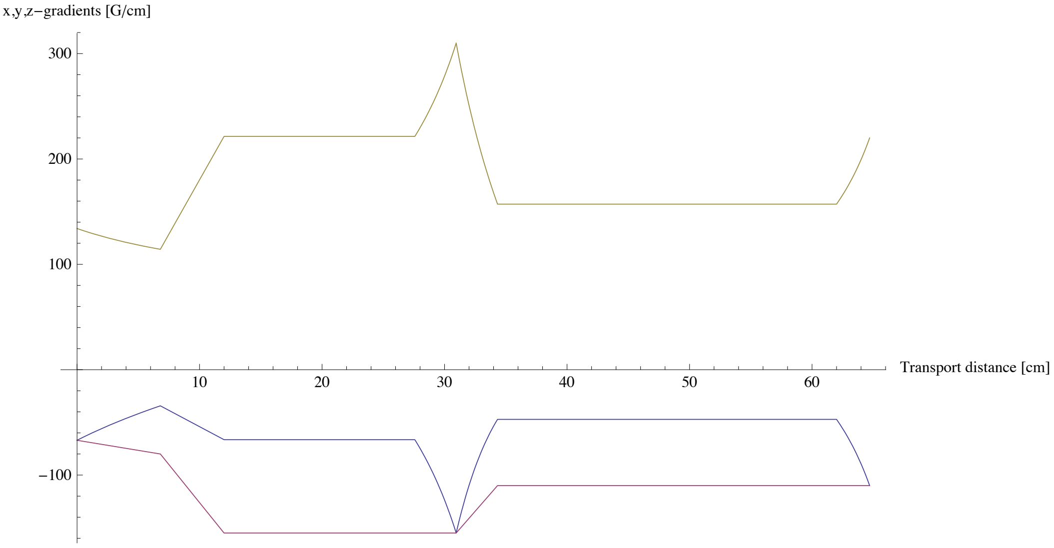

Figure 4.3: *Constraints on magnetic gradients: x-gradient (blue), y-gradient (pink), and z-gradient (yellow).*

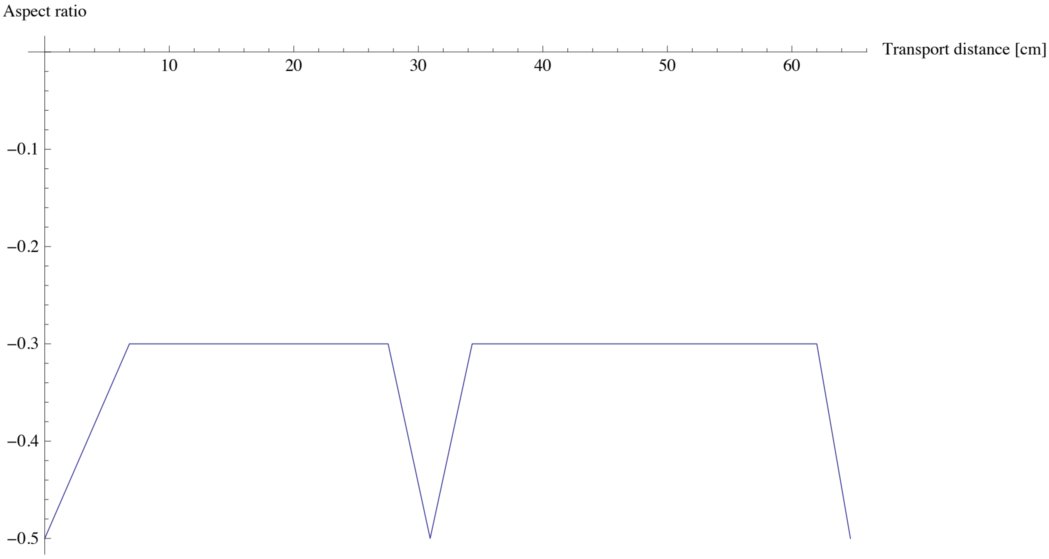

Figure 4.4: *Constraint on magnetic aspect ratio* $A = b_x/b_z$.

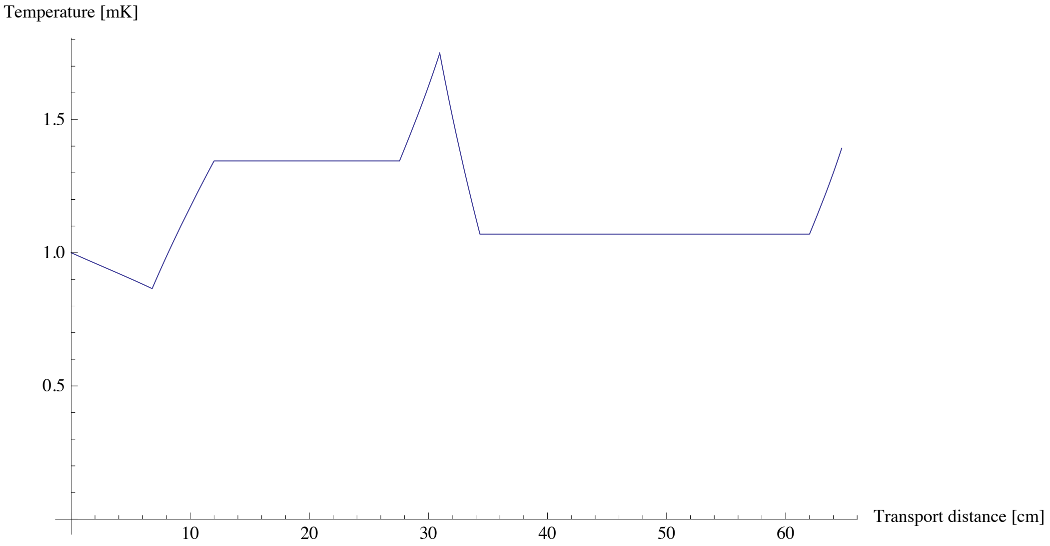

Figure 4.5: *Theoretical cloud temperature during the adiabatic transport. The initial temperature is chosen to be 1 mK. Since the cloud temperature is proportional to the initial temperature according to equation 4.7, the graph can be used for any initial temperature by adding the initial factor.*

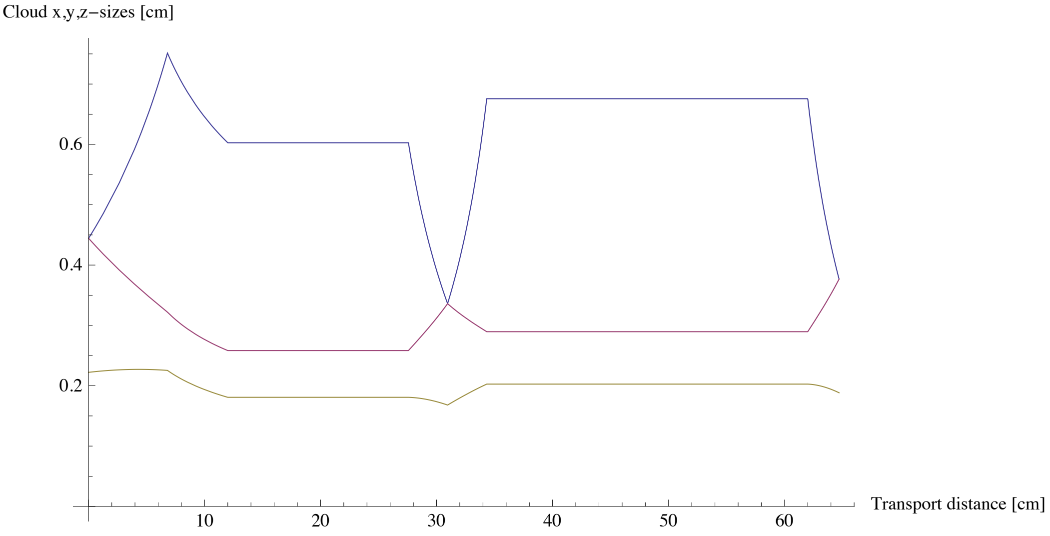

Figure 4.6: *Theoretical RMS sizes of the cloud during adiabatic transport (see equations 4.4, 4.5 and 4.6). x-size in blue, y-size in pink and z in yellow. The confinement is weaker in the second arm because the coils are farther from the cloud, since they are mounted on top of the first arm.*

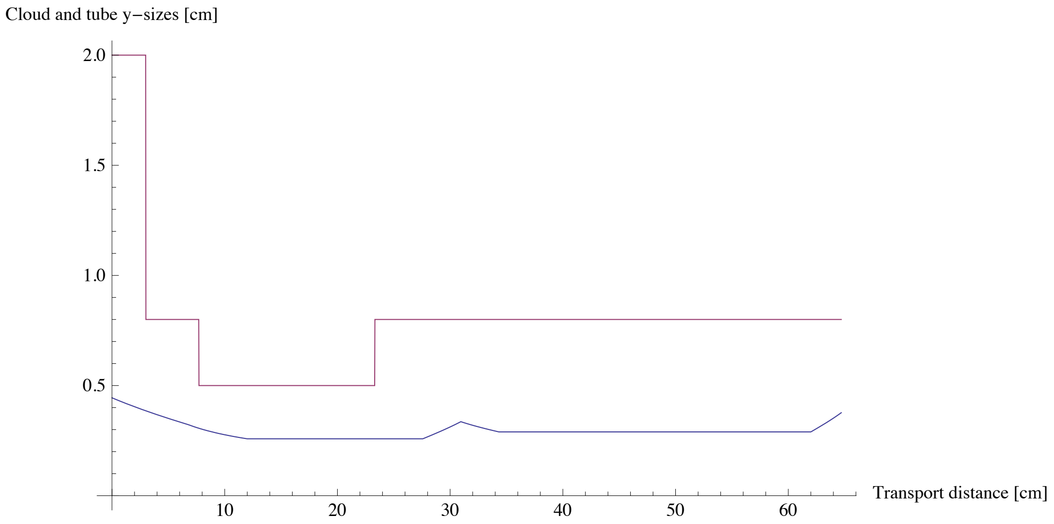

Figure 4.7: *Theoretical RMS size (see equation 4.5) of the transported cloud (blue), and radius of the tube (pink) along y.*

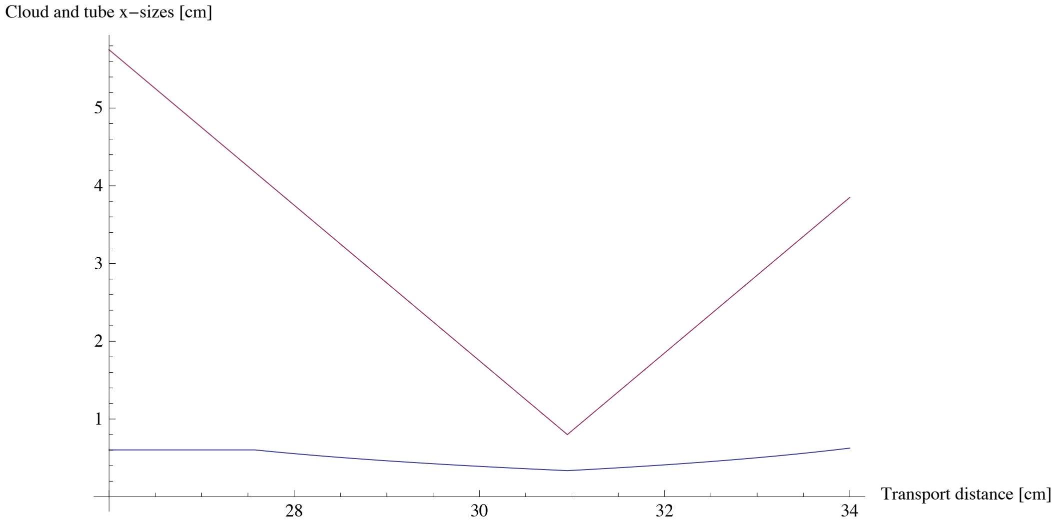

Figure 4.8: *Theoretical RMS size (see equation 4.4) of the transported cloud (blue), and radius of the tube (pink) along x. Zoom around the elbow. To define the tube size in the transport direction we have taken the minimal distance to the walls.*

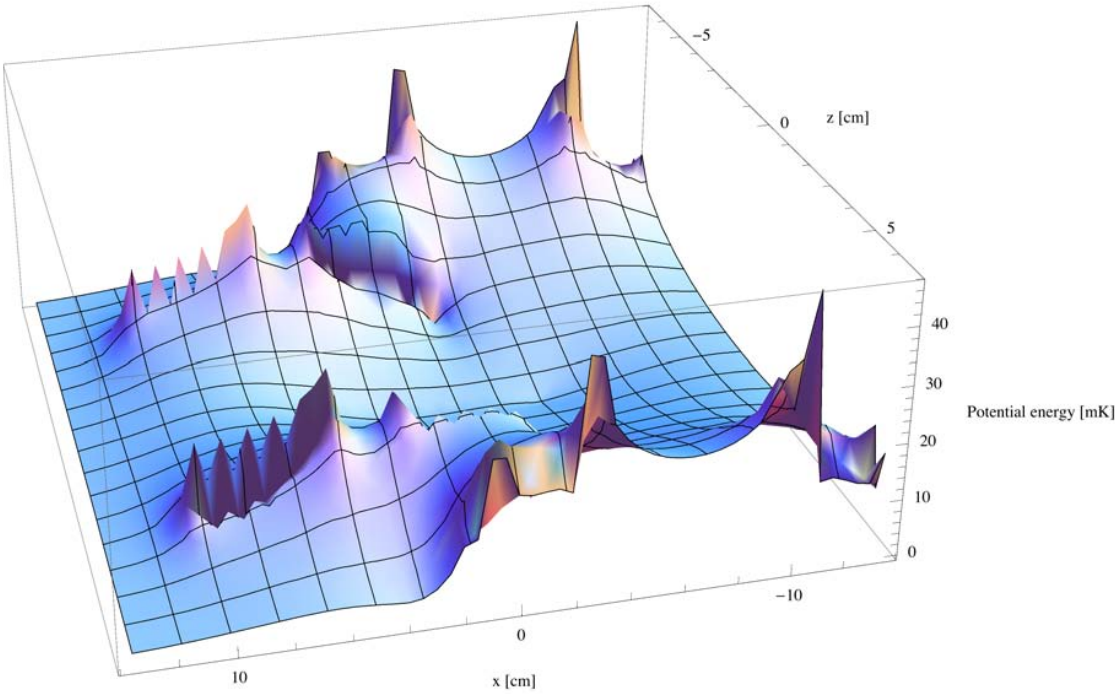

Figure 4.9: *Profile of the trap in the $x - z$ plan. The height of the box corresponds to 50 mK. Center corresponds to $x = y = z = 0$, start of the transport.*

to the walls (which is the relevant definition at the elbow). However let us keep in mind that the linear approximation in the energy is only valid until a length of the order of the coil size (roughly 6.5 cm in radius): if the x-distance to the walls is bigger than the coil size, we have to find the real dimensions of the trap by plotting the exact magnetic field profile. As an illustration, we computed this at the beginning of transport on Figure 4.9. There, the distance along x between the edge and the center of the potential equals approximately 10 cm. This implies that the x-size of the cloud around the $x = 6$ cm transport position (the worst case, cf peak in Figure 4.6) is smaller than the trap size.

Finally, it seems that the efficiency is still close to $R_{2\sigma} \approx 86\%$ (see equation 4.9). However, one should keep in mind that this study was performed for $T^0 = 1$ mK, which is over-estimated for potassium where we rather have $T^0 = 500$ μK. Thus we should have a better efficiency. In addition, we use the 3D quantity R_σ, even if only one or two directions are critical but this is justified if we assume ergodicity, which is experimentally relevant as explained in chapter 5.

4.3 Dynamics

In the previous parts we saw how the currents at each position are calculated and we established the adiabatic evolution of size and temperature. But a transfer is a dynamical process. Thus we need to add time in our program in order to move the trap and then we need to send this complete information to the National Instrument cards. Adding time is a simple task, we only need to make a bijective correspondence between position and time. Nevertheless the overall timing has to be chosen carefully in order to prevent losses during transfer: neither too fast in order to smoothen the acceleration of inertia nor too long to keep Majorana losses negligible. The same care should be taken during ramp phases, where trap geometry varies, in order to ensure adiabaticity. In fact, since gradients vary with time, the transported quadrupole is not a conservative trap anymore: energy can be transferred to the cloud if one does not transport with care.

4.3.1 Inertia

When one drives a car, if the acceleration is too strong, the body is pushed back. This common phenomenon is an illustration of the inertia forces that take place in an accelerated frame. For atoms in a magnetic trap the effect is the same: if the trap center accelerates too much, the center of mass of the atomic cloud is pushed away from it and since the trap has a finite height, this shift can induce a consequent loss of atoms. Therefore it is compulsory not to exceed a maximal acceleration that we estimate now. Let us first propose a rough estimate of this quantity. The typical acceleration that we can associate to a quadrupole trap contains the Bohr magneton μ_B, the gradient b and the atomic mass m. The only acceleration we can build dimensionally with those quantities is:

$$a_\mathrm{max} = \frac{\mu_\mathrm{B} b}{m} \ . \tag{4.11}$$

In the case of potassium, the heaviest atom, and if we consider the minimal x-gradient $b_x = -34$ G.cm^{-1} (see Figure 4.3), this acceleration is approximately equal to 47 m.s^{-2}, *i.e.* roughly five times the gravity. To get a clearer picture we can differentiate the magnetic energy given at equation 3.4, and consider the equation of motion on the transport axis x for a single atom:

$$\ddot{x}' = -a^* - \frac{\mu_\mathrm{B} b_x}{m} \mathrm{sign}[x'] \ , \tag{4.12}$$

where x' is the distance to the trap center position and a^* the transport acceleration. We see here that the acceleration found in equation 4.11 corresponds actually to the vanishing of the trapping force. In other words, with such a transport acceleration the linear trap is tilted so much by inertia that the trapping potential becomes constant and null for $x' < 0$. But we should not forget that that the trap is not a perfect quadrupole. As we already mentioned, non-linearities appear on a distance R_trap (of the order of the coils size) and limit the trap depth. So, even if the the acceleration remains smaller than a_max, if the center of mass is shifted by a distance comparable to R_trap from the trap center atoms can leave the trap. One more time, using equation 3.1 we can write a 1D potential energy E including the inertia tilt due to a^*:

$$E = m[a^* x' + a_\mathrm{max} \left| x' \right|] \ ,$$

which means for $x' < 0$:

$$E = m(a_\mathrm{max} - a^*) \left| x' \right| \ . \tag{4.13}$$

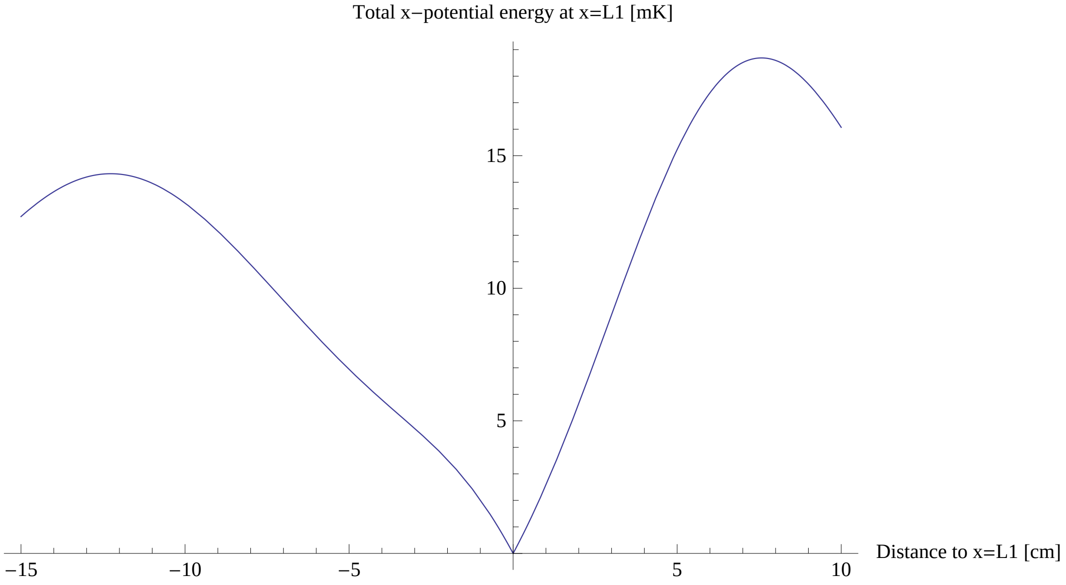

Figure 4.10: *Static trap profile in the transport direction at* $x = L_1$. *The small asymmetry is due to the coils asymmetry since* $x = L_1$ *is between the MOT pair (M) and the first transport pair (T1).*

Now let us assume that the atoms are lost if the trap depth is of the order of the cloud temperature, *i.e.* $T \approx 1$ mK in the worst case. If we plot the static trap profile in the transport direction at $x = L_1$ (Figure 4.10), which is the position of the trap with the smaller trap depth, we see that for negative x' the trap ends after $|x'| = R_{\mathrm{trap}} \approx 12$ cm. Thus, using equation 4.13, a^* should not exceed:

$$a^*_{\mathrm{max}} \approx a_{\mathrm{max}} - \frac{k_{\mathrm{B}}T}{mR_{\mathrm{trap}}} \ .$$

In the worst case of potassium, this acceleration approximately equals 45 m.s^{-2} which is close to a_{max}. Note that due to non-linearities in the trap, the maximal acceleration is in fact slightly smaller, as we can guess in Figure 4.10 by noticing the finite curvature at $x' = -2$ cm. We calculate it by computing the exact trap profile for a given acceleration a^* and find the acceleration value a^*_{max} that leads to a trap depth of 1 mK. The result is $a^*_{\mathrm{max}} = 28$ m.s^{-2} and the associated dynamical trap profile is shown on Figure 4.11. From a^*_{max} we can estimate a minimal time for the transport, assuming constant acceleration. Since we have two arms, there is, in the simplest sequence, a succession of four steps of constant acceleration. In fact each arm can be separated into two equal phases, the first with acceleration a^*_{max} and the second with deceleration $-a^*_{\mathrm{max}}$. The total time τ^{in} is then given by the free fall formula:

$$\tau^{\mathrm{in}} = 4\sqrt{\frac{2d}{a^*_{\mathrm{max}}}} \ ,$$

where we have taken into account four half-arms of length $d \approx 15$ cm. Thus the transport should last more than $\tau^{\mathrm{in}} \approx 400$ ms:

$$t^{\mathrm{tot}} \gg \tau^{\mathrm{in}} \ . \tag{4.14}$$

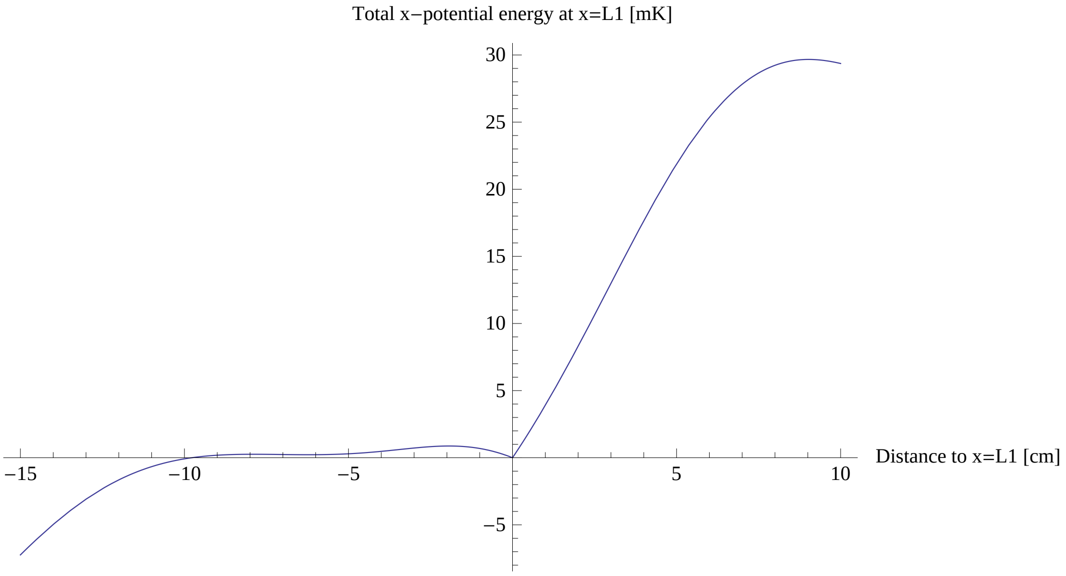

Figure 4.11: *Dynamical trap profile in the transport direction at* $x = L_1$*, including a critical inertia tilt of* $a^*_{max} = 28\ m.s^{-2}$*. Due to non-linearities, the dynamical capture region in the transport axis is reduced to approximately 2 cm.*

4.3.2 Adiabaticity

In addition to the limits on acceleration and total transport time found above, we have to look carefully at the ramp phases, where the trap shape changes. In fact, to prevent the sample from heating, the typical variation time of the trap geometry τ^{var} has to be greater than the characteristic evolution times in the trap: T^{Li} and T^{K}. The worst case being the one of the heaviest atom, we want:

$$\tau^{\mathrm{var}} \gg T^{\mathrm{K}} \,. \tag{4.15}$$

This is the adiabaticity criterium. However, since the quadrupole trap is a linear trap we can obviously not define a unique period. One can nevertheless estimate a maximal time for an atom to cross the full cloud, which is the important information regarding adiabaticity. With R the size of the cloud, b the gradient, m the mass of the atom and μ_{B} the Bohr magneton, we can dimensionally build only one quantity homogeneous to a time:

$$T = \sqrt{\frac{mR}{\mu_{\mathrm{B}} b}} \,, \tag{4.16}$$

In the case of potassium, this leads to $T^{\mathrm{K}} \approx 15$ ms for an atom $R = 1$ cm away from the center, if $b = 34$ G.cm^{-1}. In fact those numbers correspond to the actual lowest gradient in our transport sequence (it happens in the x direction, at $x = L_1$), which is the worst case as far as the adiabaticity criterium is concerned. In conclusion the transport, and furthermore the ramp phases, should last more than T^{K}. Further more, we can deduce from this a maximal transport velocity. Let us admit the intuitive statement that we do not want an atom to move over a distance of the order of the

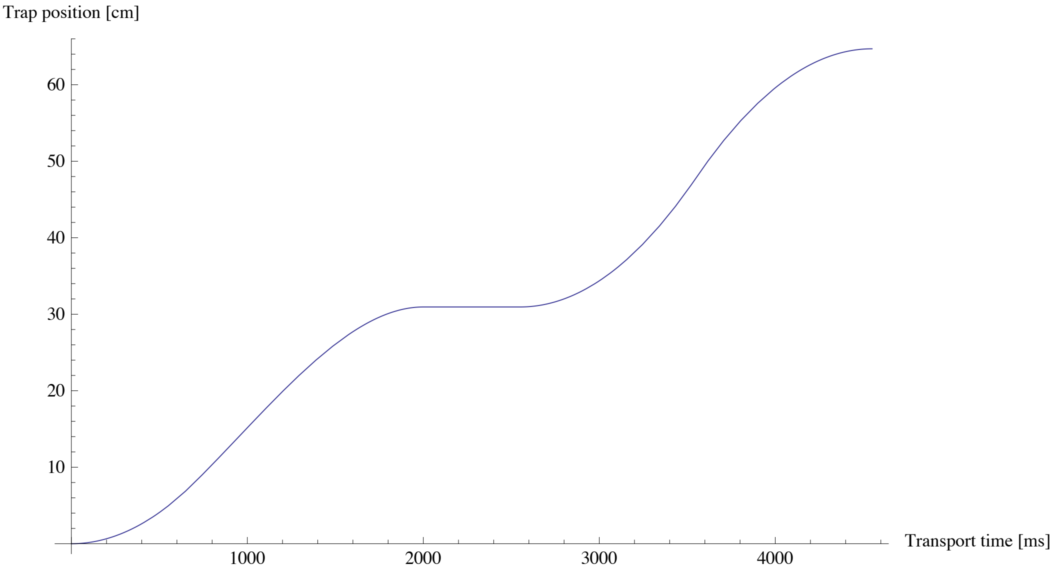

Figure 4.12: *Position of the center of the trap.*

cloud size in a time smaller than T^{K}. For typical x-size $R = 0.6$ cm (see Figure 4.6) it leads to:

$$v_{\max} = 0.4 \text{ m.s}^{-1} \ .$$

4.3.3 Trap trajectory

In chapter 3, we deduced with formula 3.9 that the Majorana lifetimes of both species are $\tau_{\mathrm{M}}^{\mathrm{K}} \approx 200$ s and $\tau_{\mathrm{M}}^{\mathrm{Li}} \approx 30$ s, for a cloud of typical size $R = 1$ mm. As a consequence the total transport duration t^{tot} must follow:

$$t^{\mathrm{tot}} \ll \tau_{\mathrm{M}}^{\mathrm{Li}} \ . \tag{4.17}$$

Using equations 4.14, 4.15 and 4.17, we can write finally:

$$T^{\mathrm{K}} \ll \tau^{\mathrm{in}} \ll t^{\mathrm{tot}} \ll \tau_{\mathrm{M}}^{\mathrm{Li}} \ . \tag{4.18}$$

In summary, since $T^{\mathrm{K}} \approx 15$ ms, $\tau^{\mathrm{in}} \approx 400$ ms, and $\tau_{\mathrm{M}}^{\mathrm{Li}} \approx 30$ s, a transport duration of the order of a few seconds seems reasonable. Knowing this we could build a proper position-to-time correspondence. We also made sure that the typical velocities are smaller than $v_{\max}$. Our final transport trajectory is described on Figures 4.12, 4.13 and 4.14. We cut the transport in five stages of independent timings: injection until the tube, transport in the first arm, stop at the elbow, first half of the second arm and second half. We used second order polynomials in position, to ensure constant acceleration, except during the second step where we used a third order polynomial because of the number of continuity constraints, and the elbow stop where the center of the trap is stationary. On Figure 4.14 we can note that our total time is around $t^{\mathrm{tot}} = 4.6$ s and that our maximal acceleration is of the order of 0.3 m.s^{-2}, which is a hundred times weaker than $a^{*}_{\max}$ (see part 4.3.1). In addition, on Figure 4.13 we notice than $v < v_{\max}$. To sum up, we fulfill all our requirements.

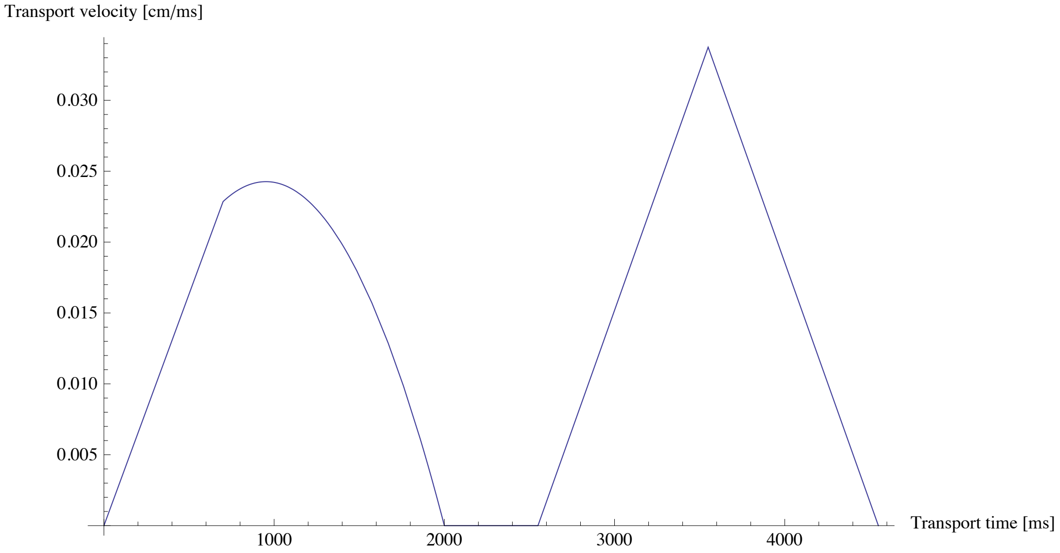

Figure 4.13: *Velocity of the center of the trap.*

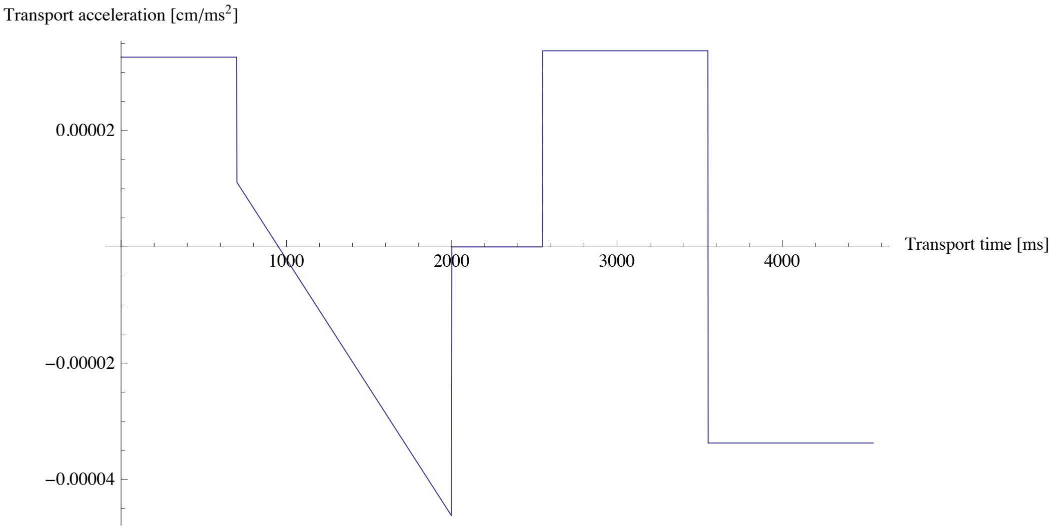

Figure 4.14: *Acceleration of the center of the trap.*

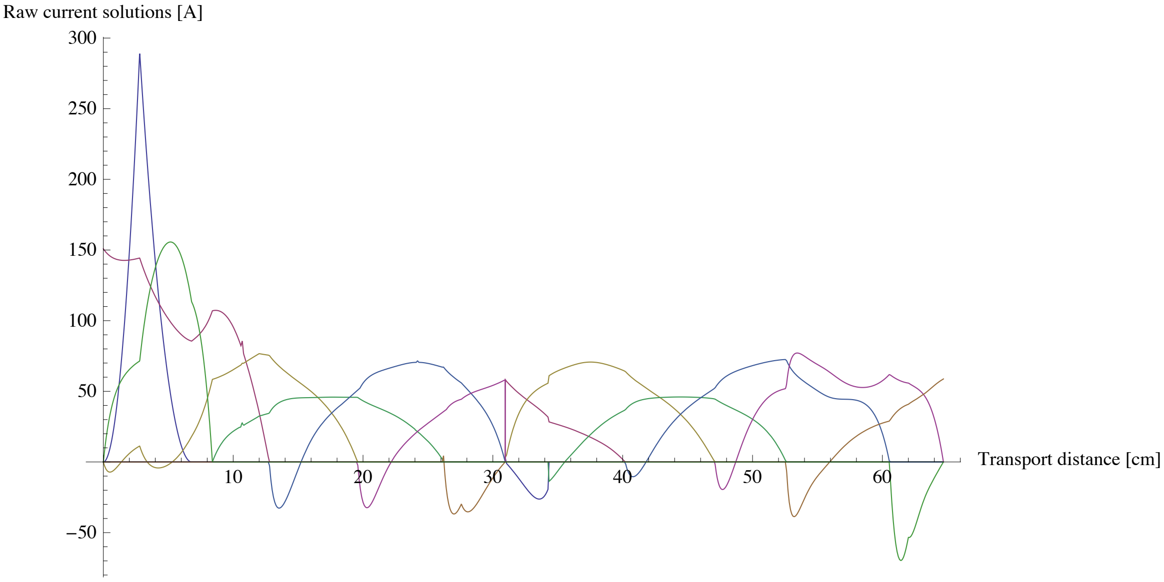

Figure 4.15: *Raw current solutions of the transport.*

4.4 Results and checking

After having reported how the static transport program works and having characterized the regime where the dynamics would not be harmful for the cloud, let us have a closer look at the evolution of the currents during the transport sequence. Furthermore we explain how we double checked the obtained values and the effect of negative currents.

4.4.1 Currents

First of all, after an optimization of the mechanical and physical parameters of the design, essentially in order to improve the injection and transfer steps, we finally obtained some reasonable curves for the currents regarding their shape and their maximal values. The raw results are shown on Figure 4.15. However, as one can notice on the curves, the results include some negative currents. This is an issue if the currents are not of constant sign: commercial power supplies for such high currents are polarized and can not afford alternative currents. A first solution to this problem would have been to reverse the current sign by using switches circuits based on Insulated Gate Bipolar Transistors (IGBT). But this method costs a lot of digital commands to control all the IGBTs gates. A simpler solution consists on putting to zero the negative part of the currents that are not of constant sign, which means replacing those currents $I_i(x)$ by the functions $I_i' = \mathrm{Max}\,[I_i(x), 0]$ as shown on Figure 4.16. Nevertheless this idea imposed to side-check that the modification of currents did not affect too strongly the gradients. We describe this procedure in the next two sub-sections. Note that, as described in the engineering section, we have only five power supplies for all the coils, and thus the currents controlled by a same power supply are now joined together (same color on the graphs).

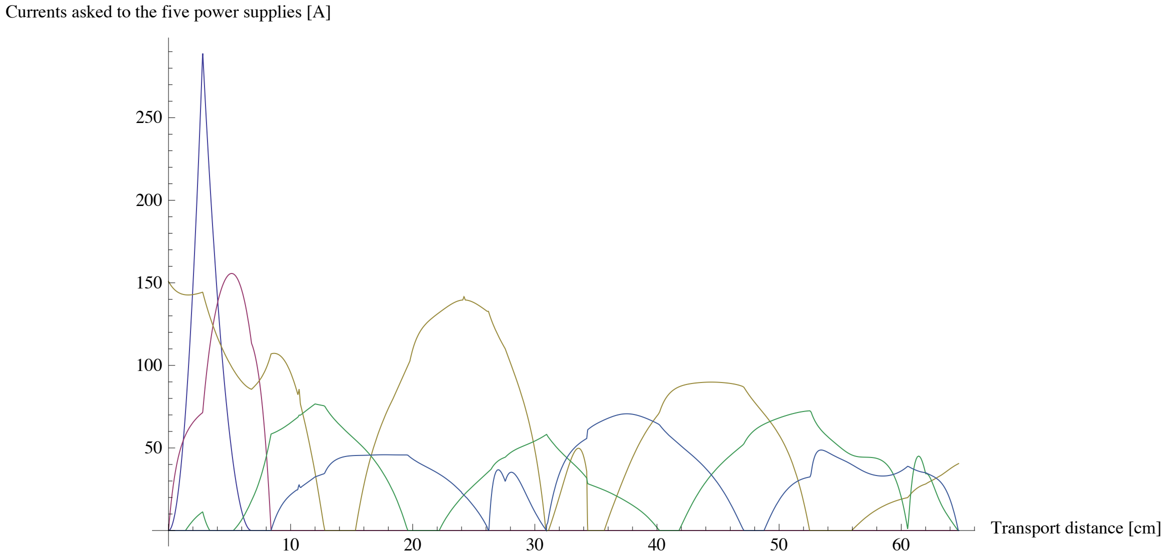

Figure 4.16: *Positive currents asked to the five power supplies.*

4.4.2 Checking the constraints

In addition to the control of the error induced by removing the negative currents, it was compulsory to check that the currents we obtained by solving the system 4.1 were really corresponding to the desired gradients for the atoms. Thus, using currents from Figure 4.16 we recalculated all the gradients at each position of the trap centre and we compared them to the initial constraints. Results are plotted on Figures 4.17, 4.18 and 4.19. As we see, there is a perfect agreement except for the regions where we nullify the negative currents. In the second arm the difference can even reach 50 % at $x = 54$ cm for the gradient along the transport direction. But this is not be dangerous if we pass through those regions sufficiently slowly, since those variations are actually equivalent to some kind of new ramps for the trap geometry and that they increase the size of the cloud only in the transport axis where there is no wall. Nevertheless, for safety reasons, we decided to quantify the heating induced by those unnecessary ramps, as described below.

4.4.3 Numerical simulation of a default

In order to test the effect of the forced cancellation of negative currents we simulated numerically a magnetic bump. More precisely this involved a resolution of the 1D equation 4.12 where the trap center position x^* follows a uniform movement, with velocity $\dot{x}^* = 10$ cm.s^{-1}, and where the defect is 4 cm long and corresponds to a relative variation of 50 % on the gradient. The simulation has been performed in Fortran 90, using a fourth order Runge-Kutta routine [140]. The initial assignation of velocities and position into the trap is done accordingly to the associated phase-space distributions in such a trap for a 1.5 mK lithium cloud and a 500 μK potassium cloud. Results for 10000 independent atoms of each species are shown in Figure 4.20. According to this simulation, it seems that for small velocities the variation of total

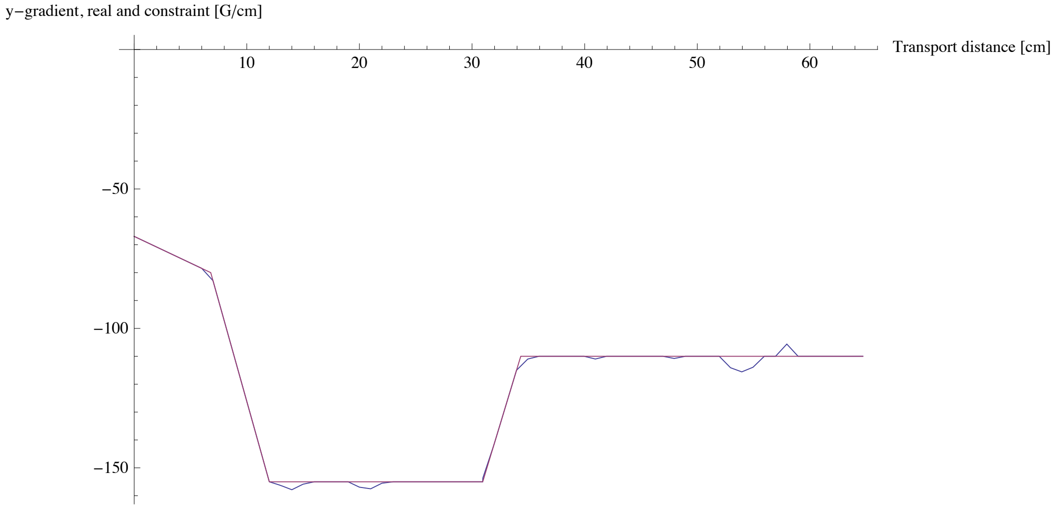

Figure 4.17: *y-gradient: constraint (pink) and recalculated with the positive currents (blue).*

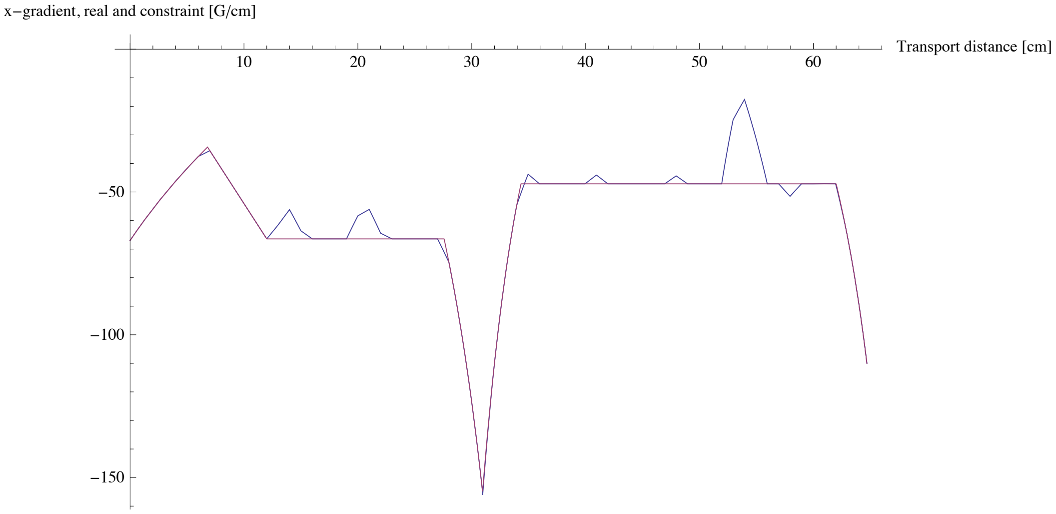

Figure 4.18: *x-gradient: constraint (pink) and recalculated with the positive currents (blue).*

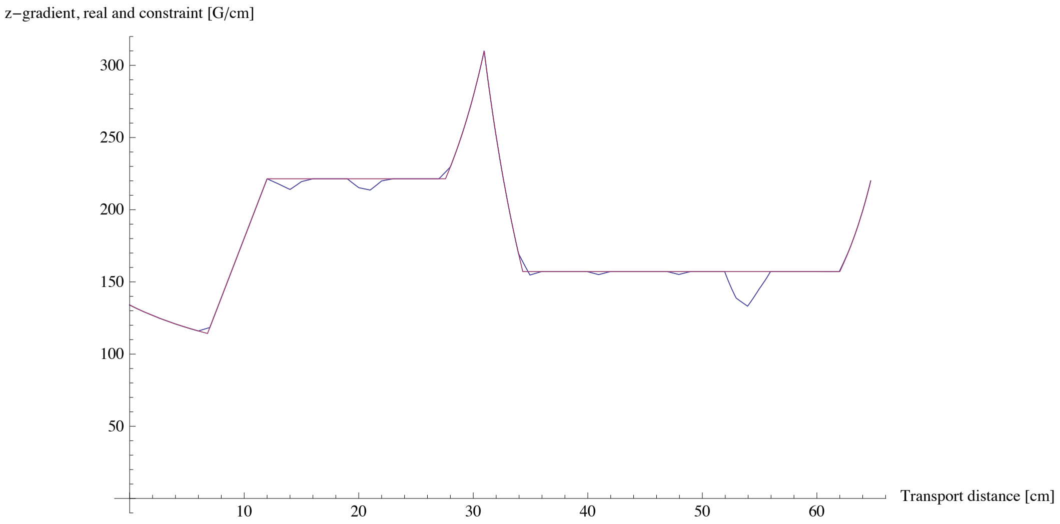

Figure 4.19: *z-gradient: constraint (pink) and recalculated with the positive currents (blue).*

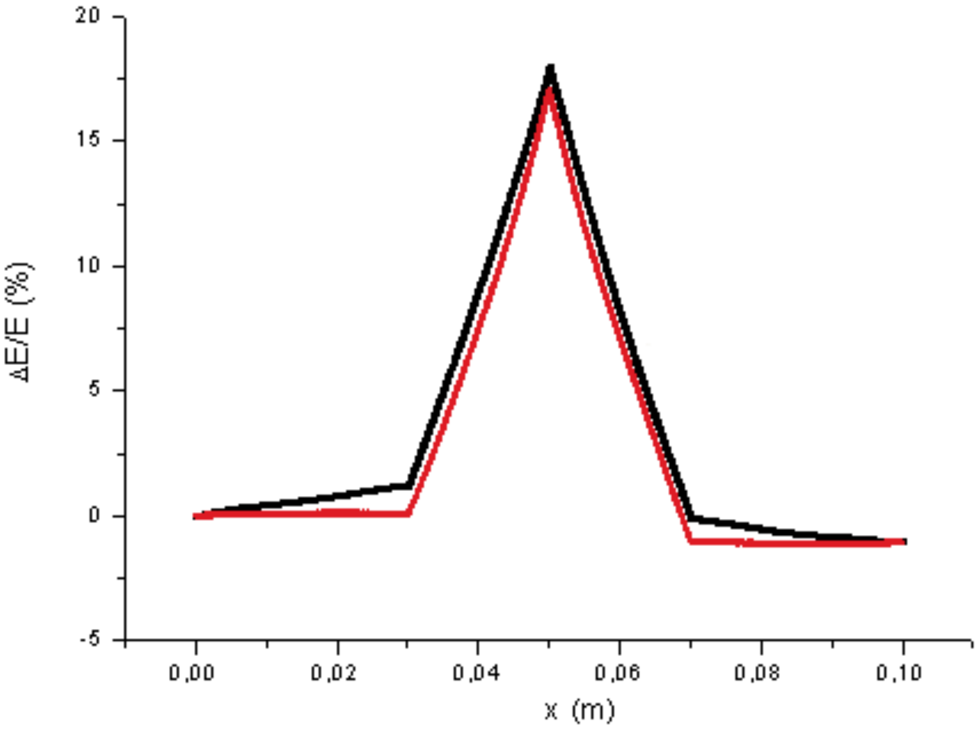

Figure 4.20: *Numerically simulated relative variation of energy for 10000 ^{40}K atoms (black) and 10000 ^{6}Li atoms (red), due to a local magnetic defect in the sequence. The defect is 4 cm long and corresponds to a relative variation of 50 % on the gradients. The simulation has been performed in Fortran 90, using a fourth order Runge-Kutta routine [140].*

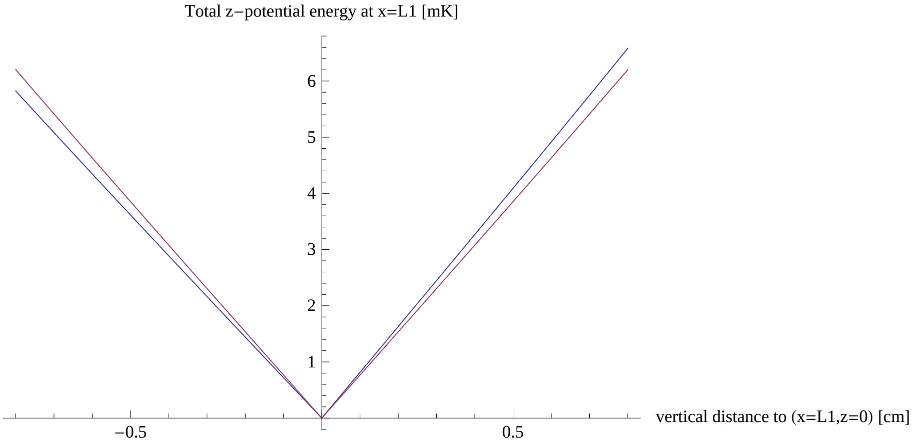

Figure 4.21: *Vertical trap profile at $x = L_1$, with (blue) and without (pink) the gravitational tilt. There the vacuum tube has a DN16 size (0.8 cm radius), and the position $x = L_1$ is 9 mm away from the DN10 transport tube (0.5 cm radius).*

energy does not exceed 20 %, which is acceptable compared to the worst trap depth shown in Figure 4.21 .

4.4.4 Trap depth and gravity

A complementary check of our sequence, was to use the solutions for currents to calculate the exact trap profile at every position of the trap center, in order to avoid too small trap depths. In addition, we included the gravity tilt mgz in the vertical direction, since this could have a strong effect in the DN10 transport tube. Figure 4.21 shows the vertical trap depth of the trap, in presence of gravity or not, at $x = L_1$, which is the point of weakest gradients in our sequence. There the vacuum tube has a DN16 size (0.8 cm radius), and the position $x = L_1$ is 9 mm away from the DN10 transport tube (0.5 cm radius). As we can see, the gravity tilt is small in such a trap. Moreover there is no risk of loosing atoms on the tube walls, even in a DN10 (radius of 5 mm) tube since $x - L_1 = 5$ mm corresponds almost to a 4 mK vertical depth. The x direction is also not harmful since there is no walls in this axis. On the contrary, the y direction is the critical one regarding trap depth, because of the tube limit and a smaller gradient compared to the vertical one. However, in this region the y-gradient equals 70 % of the vertical one, which still gives a reasonable 3 mK trap depth for a DN10 tube, in the worst point. During the experimental implementation of magnetic transport (see chapter 5), we deeply investigated this possible issue of losses on the walls in the transverse direction. This is developed in part 5.3.2.

4.5 Engineering

The previous part exposed the theoretical aspects of the transport design. This last section is dedicated to actual engineering and construction of the transport system. We intend here to give details about technical aspects such as mechanics and winding,

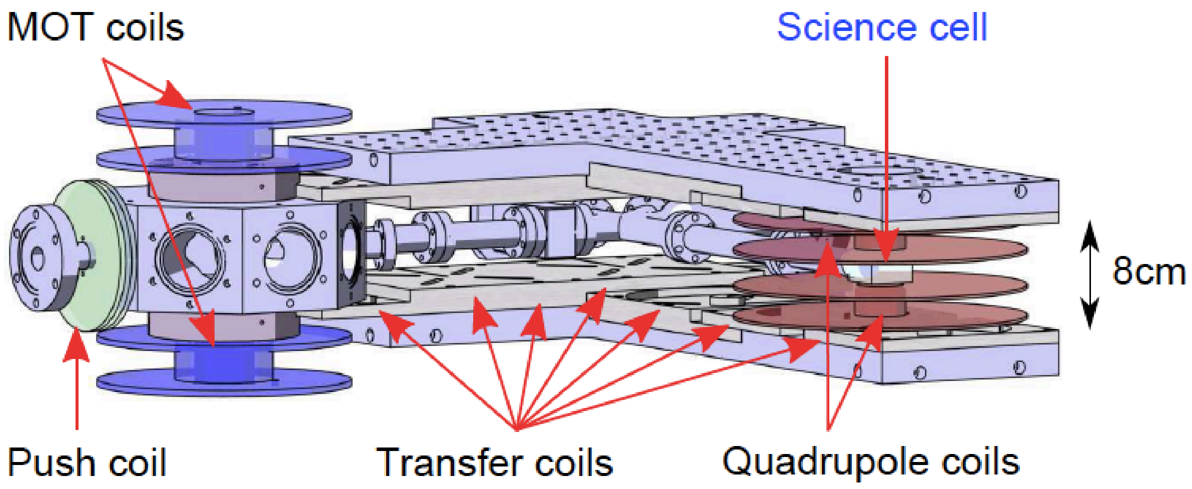

Figure 4.22: *Scaled Catia transport drawing with 1 pushing coil (green), 2 MOT coils (blue), 2 quadrupole coils (red), 18 transport coils and 4 neighbor coils (white). On top of the transport coils is the cooling plate. This drawing does not show the additional pulling coil T1/2, placed over the cooling in between the MOT and first transport coils (see Figure 4.24). See engineering drawings in appendix A.6.*

power issues, cooling of the coils, security, electronics and logics, as well as computer interface.

4.5.1 Mechanics and winding

The theoretical parameters in the program were chosen in order to ensure the lowest positive currents and to fit with standard sizes (thread diameters for instance). The main values are shown in appendix A.5. Using this data we could design a complete mounting system under Catia with engineer Jean-Michel Isac from Laboratoire Kastler Brossel's workshop. A view of the design is shown in Figure 4.22. The assembly contains a single pushing coil (P) of resistance $R = 0.06\ \Omega$ creating an axial field of 0.25 $\mathrm{G.A^{-1}}$ at the MOT center; a pair of MOT coils (M) of resistance $R = 0.178\ \Omega$ creating an axial magnetic gradient of 0.936 $\mathrm{G.cm^{-1}.A^{-1}}$; nine pairs of transport coils (T1 to T9, see picture in Figure 4.23 and engineering drawing in appendix A.6) of resistance $R = 0.36\ \Omega$ creating an axial magnetic gradient of 3.2 $\mathrm{G.cm^{-1}.A^{-1}}$; a pair of quadrupole coils (Q) of resistance $R = 0.11\ \Omega$ creating an axial magnetic gradient of 3.75 $\mathrm{G.cm^{-1}.A^{-1}}$. In addition, a pair of pulling coil (T1/2, see Figure 4.24) is placed in between the MOT and the first transport ones. This pair is actually made with four standard transport coils. In addition, a fifth single one is placed on top in order to generate a small bias field, if necessary during injection. Finally, note that just before and after the final quadrupole pair, we do not have standard transport coils, because they would obstruct the vertical optical access. Instead we have two so-called neighbor pairs (V1 and V2, see engineering drawing in appendix A.6), which are simply slightly smaller transport coils. Note that the transport coils are flat discs in order to allow for small changes of the distance to the transport axis. All the pairs are roughly in

Figure 4.23: *Single transport coil. See engineering drawing in appendix A.6.*

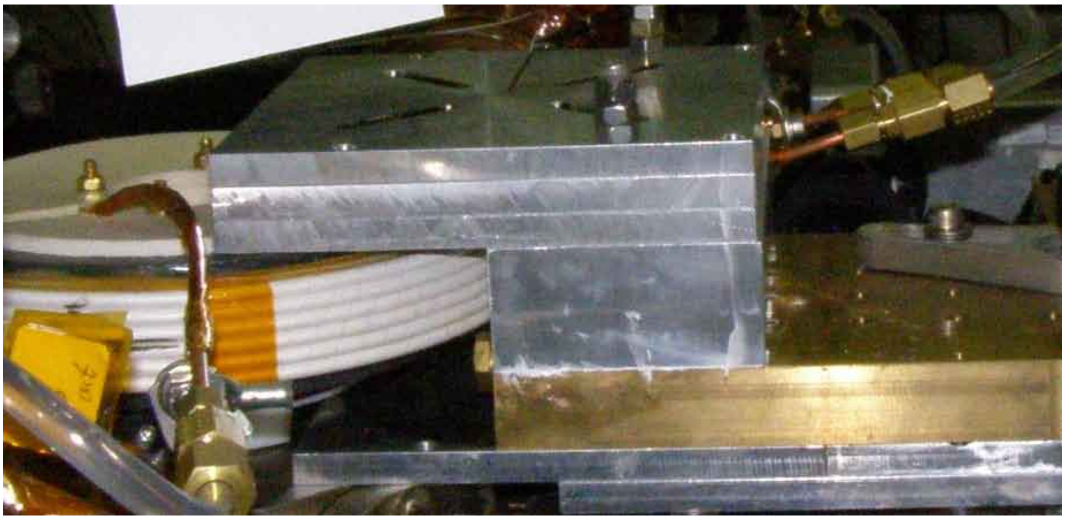

Figure 4.24: *Pulling coil (T1/2) placed in between the MOT pair (M) and the first transport pair (T1). In addition, a fifth single one is placed on top in order to generate a small bias field, if necessary during injection. See engineering drawings in appendix A.6.*

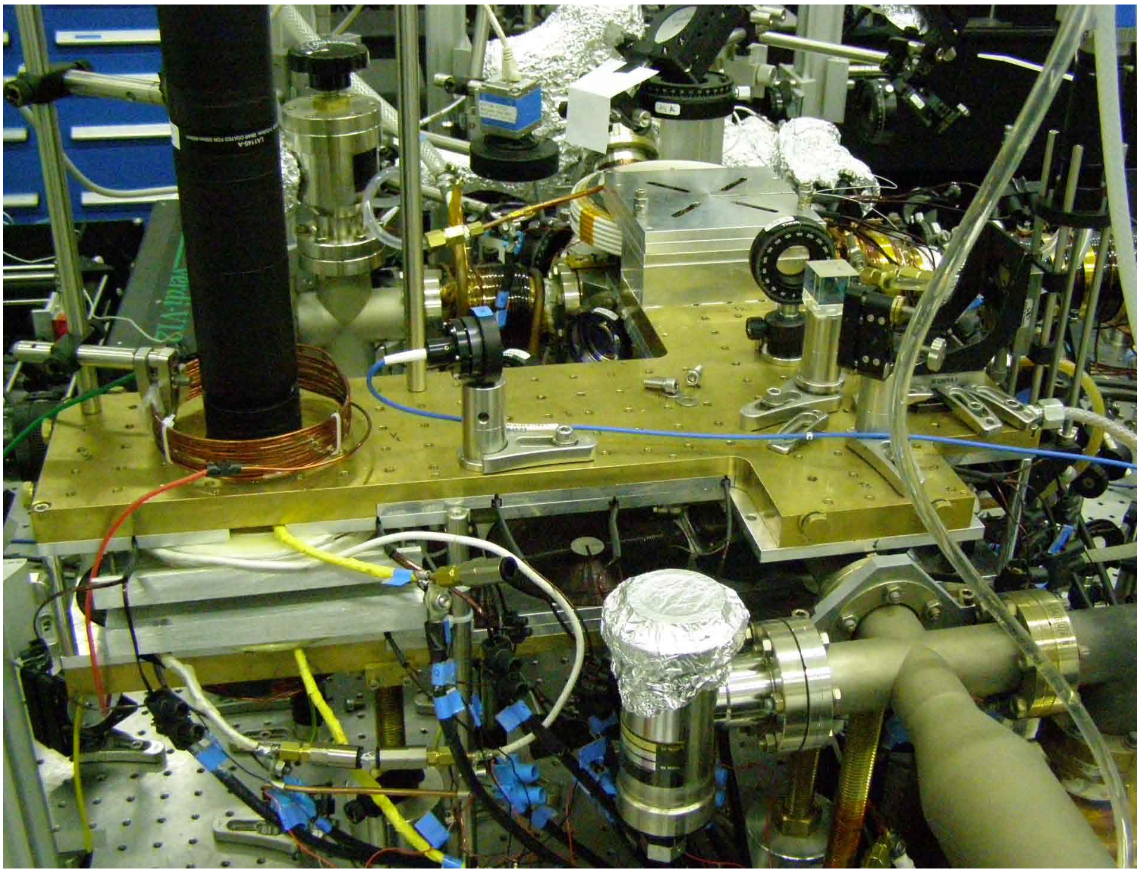

Figure 4.25: *Full transport setup. See engineering drawings in appendix A.6.*

anti-Helmoltz configuration, for efficiency, except Q which is close to the science cell to allow for curvature and strong confinement. Figure 4.25 shows a real side-view of the complete transport assembly. The system is mostly in Dural aluminum, due to the lightness of this metal, except for the cooling plate described in Part 4.5.3 which is in brass, due to its higher thermal conductivity. All the mechanics has been performed by the workshop team. The winding of the transport and quadrupole coils has been performed by Oswald company directly in our mountings. The other coils were winded by us using copper cables insulated with Nomex tape, a material that can sustain high temperatures of the order of 200 $°C$. Finally, Eddy currents are reduced by inserting holes inside the mount, orthogonally to the current flow.

4.5.2 Power supplies

As far as the power supplies are concerned we decided to work with only five independent sets of power supplies since they are quite expensive. Moreover, they are controlled by the main computer through National Instrument analog cards (see part 1.5) and since we have only 24 analog ports, it would have been impossible to dedicate 15 of them to command 15 supplies. We then preferred to use only five sets of power supplies, and switch from one coil to another using transistor switches and some adapted logics as described in part 4.5.5. Each power supply is a Delta power supply whose ground is floating, with a power of 3 kW or 6 kW and an response time smaller than a millisecond. It is programmable using analog or GPIB ports, and the grounds of command and load are decoupled by a galvanic isolation, which protects the analog cards from high currents. The assignation is as follows:

- an ensemble of two 15 V-400 A power supplies in series for P coil,
- an ensemble of two 30 V-200 A in series for T1/2 coils,
- a single 45 V-140 A for M, T3, T6, T8 and Q coils,
- a single 45 V-140 A for T1, T4, T9 and V2 coils,
- a single 45 V-140 A for T2, T5, T7 and V1.

Regarding the analog programming, we saw experimentally that it is important to drive all the power supplies in control voltage mode (CV) rather than control current mode (CC). In fact, the response time of the power supply to quick changes of the command is smaller in CV mode: we could actually reduce in such a way the delay between loads and command signals from 10 ms in CC mode to less than 1 ms in CV (see part 5.1.2). However, as far as the magnetic field is concerned, the relevant quantity remains the current in the coils. Thus we needed to calibrate the commands, by measuring precisely the resistances of the coils, including the connections. Note that this is slightly more complicated than it seems since the resistances of the coils driven by a same power supply are not necessary identical (see for instance M and T1 coils): the solution is just to use once again the resistance calibrations in order to add a corrective factor on each coil directly inside the Mathematica waves. This is the reason why currents seem different between Figures 4.15 and 4.16.

To optimize the switching of the coil circuits great care has been taken. First we used metal-oxide semiconductor field-effect transistors (MOSFET). More precisely we used negative power MOSFETS from IXYS (ref: IXFN 200N10) controlled by TTL signals coming out of the logics (see part 4.5.5). Those transistors can sustain 200 A. They are all put in the same isolated box shown in picture 4.26. For coil P, whose current reaches 300 A, we put two in parallel and in all cases we put varistances to limit the voltage both on the drain-source (100 V max) and the gate-source channels (20 V max), the latter being the critical one. Without these protections, the components happened to die frequently because of overloads created by counter-electromotive forces LdI/dt during switch off phases, where L is the self-inductance of the pair. In addition to those varistances, note that we put flyback diodes (Vishay 400U120D) on each power supply, in order to prevent strong negative Lenz currents from flowing back inside the power supply.

4.5.3 Cooling system

The MOSFETs described before are all fixed on a metallic mount in order to radiate their heat. Joints are ensured by the use of thermal paste.

As far as the coils are concerned, as already plotted in Figure 4.15, the currents in this assembly can reach quite high values. More precisely, the dissipated Joule

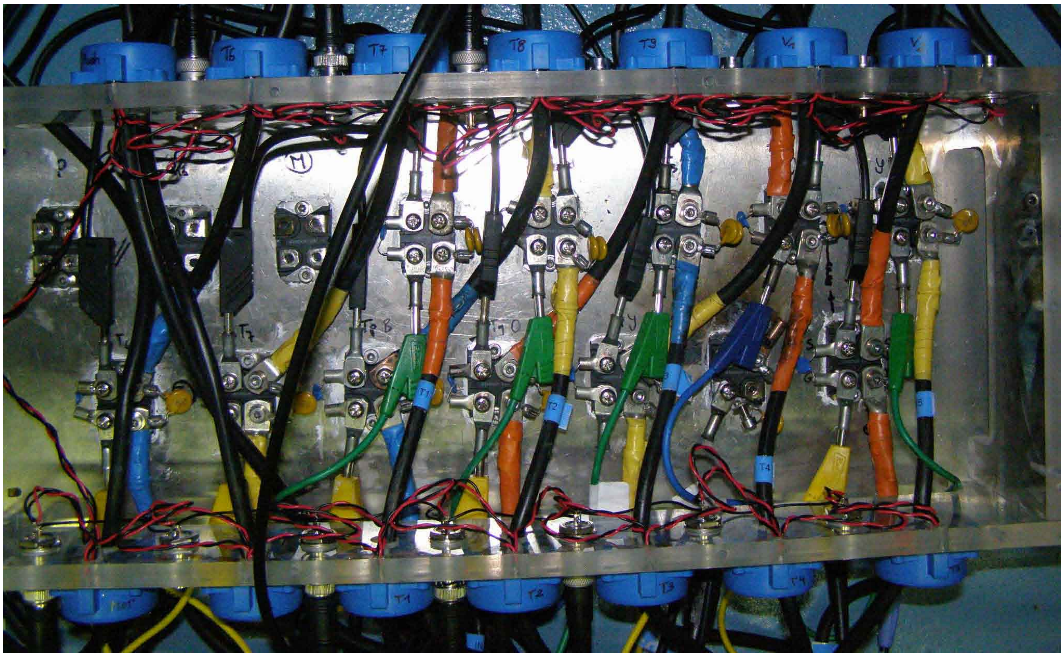

Figure 4.26: *The transport switch box with MOSFETs. The blue circles are the current transducer probes (LEM).*

power can reach $P_{\text{Joule}} = RI^2 \approx 2$ kW during typically 0.5 s. Thus an energy of $E_{\text{Joule}} = 1$ kJ per transport cycle is dissipated in the mount. We now evaluate the increase of temperature ΔT linked to this energy. Let us consider that a coil is a block of copper of mass $m = 1$ kg. Thus the heat Q^{coil} of the coil is given by the formula:

$$Q^{\text{coil}} = mc_p\Delta T \ ,$$

where $c_p = 385$ J.K^{-1}.kg^{-1} is the specific heat at atmospheric pressure per unit of mass. Then, assuming that the whole Joule energy heats the copper we find:

$$\Delta T \approx 2.5 \text{ K} \ .$$

This value is not harmful for the transport coils or the vacuum chamber. However, it can modify the resistance calibration used in CV mode, since the resistance depends on the temperature. Moreover, a transport sequence is repeated a lot in a normal experimental day (typically a cycle per minute). In addition, problems may occur, or longer sequences could be tested, so that it is compulsory to have a cooling system and some diagnostics and security tools (see part 4.5.4). Therefore, we designed a brass cooling plate covering all the transport coils (see Figure 1.2 and engineering drawing in appendix A.6). Note that this cooling plate serves also as a mounting support for the transport assembly and has M6 holes drilled on it for optics fixation purposes. In addition, as explained in chapter 3, we used hollow wire (4 mm outside, 2.5 mm inside) for M and Q coils in order to pass water directly inside since they are working during longer times. For instance, during evaporative cooling, the Q coil can be on at high currents (~ 150 A) during half a minute.

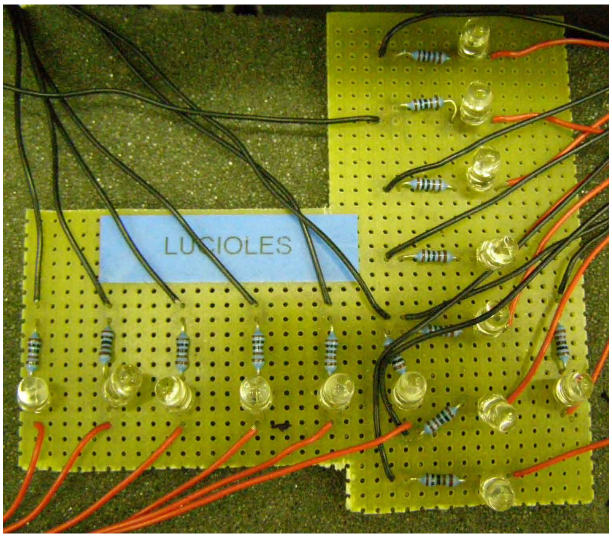

Figure 4.27: *In parallel with each coil a LED is placed in series with a 1 kΩ resistance, in order to control where the current is flowing.*

4.5.4 Diagnostics and security

The transport system is a complicated device involving high currents and numerous fragile components such as MOSFETs. Thus it is compulsory for security and debugging to have some feedback tools about the system. Firstly, some 10 kΩ thermistances are measuring continuously the temperature of each coil. Moreover, we have installed water flux-meters on each cooling tube. If one of the associated signals is not as expected, a coupling to the interlock circuit of the power supplies makes them turn off immediately. Secondly, a current transducer probe (LEM HTFS800-P) is placed around each coil line to check the currents flowing inside (see Figure 4.26). Thus, if one MOSFET fails, the measured current will be different from the asked one, or even zero: it is thus straightforward to detect the defective component without disconnecting and testing them one by one. In addition, in parallel with each coil a LED is placed in series with a 1 kΩ resistance, as shown in Figure 4.27. The LED has a threshold voltage of 1.6 V. If some current is flowing inside the coil, a little part of it (given by the ratio of the coil resistance over 1 kΩ) flows in the LED which thus emits light. This group of LED was of great help to debug the transport.

4.5.5 Logics

An organization chart of the transport control is given in Figure 4.28. As explained in part 4.5.2, to control the coils we chose to use five sets of power supplies and to create a logic circuit that switches on and off the currents through MOSFETs at desired timings. This box is called “caterpillar” for reasons that will be clear below. It has been designed at ENS with engineer Bernard Trégon and assembled by Lionel Pérennès, both from the electronics workshop of Laboratoire Kastler Brossel. It consists of a third order shift-register (NXP 74HC4017) with a leg per MOSFET. This counter moves leg by leg a triplet of 5V signals each time an incoming clock signal is received. Thus only

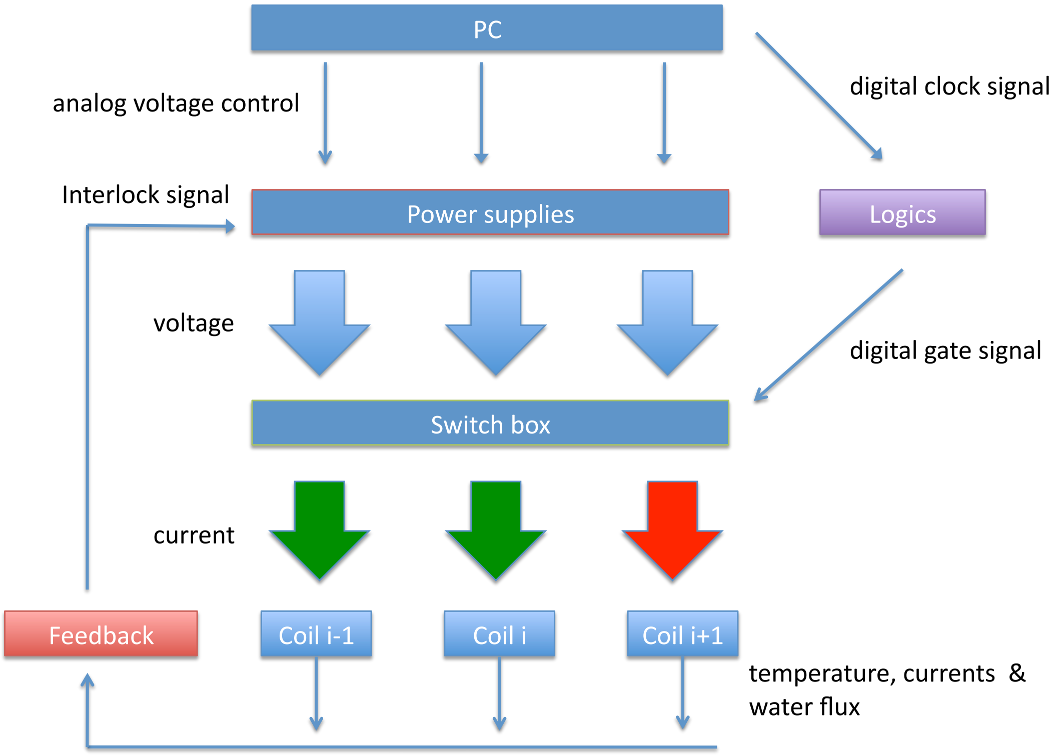

Figure 4.28: *Organization chart of the transport control.*

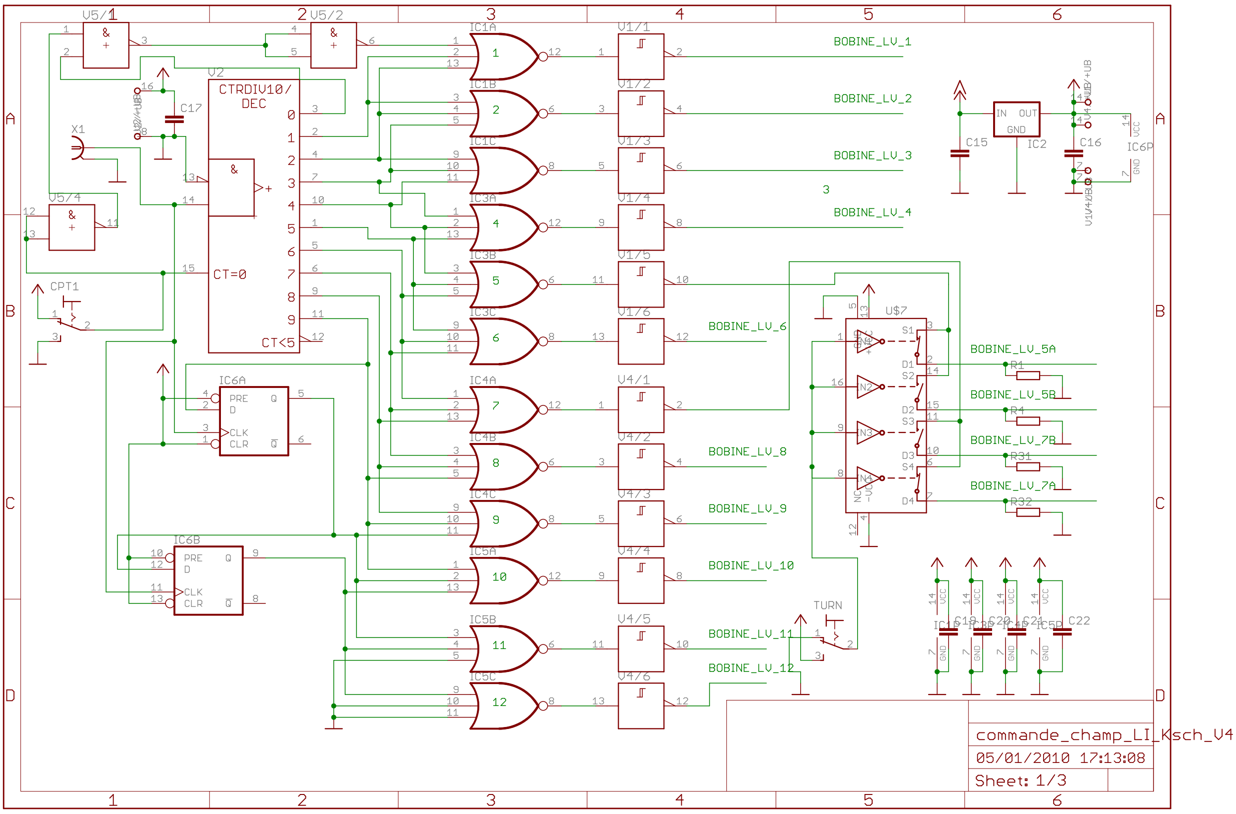

Figure 4.29: *Shift register circuit for the transport command.*

three pairs of consecutive coils can be on simultaneously, according to the principle explained in part 4.1.1. The design software used was Eagle. The circuit is shown on figure 4.29.

To control this logic stage the National Instrument digital card (see part 1.5) sends to the shift register an increment TTL signal at each shifting time in the sequence. This clock signal is called “intops” and is shown on Figure 4.30. Its profile is calculated in the Mathematica transport program in order to make a correspondence between 5 V fronts and annulations of currents in the transport sequence (see part 4.1.1 for details). In addition to this clock digital command, the caterpillar has two other entries: one which acts as an on/off or reset knob, and another one controlling for a simultaneous switch between T3 and T6, and T5 and T7, in order to manage the elbow rotation (see Figure 4.30).

Besides, MOSFETs have a common source (the “ground” for a negative transistor) for drain-source and gate-source channels. As a direct consequence some high currents could possibly flow inside the command cables and reach the logics or even the National Instrument cards. In order to avoid this, an optocoupling stage has been placed in between the logics and the MOSFETs. Each MOSFET command has its own optocoupler (Avago Tech ACPL-J313). It is contained inside the caterpillar box and it is similar to the other one which is placed just after the National Instrument digital cards (see part 1.5). Its Eagle map is given on Figure 4.31.

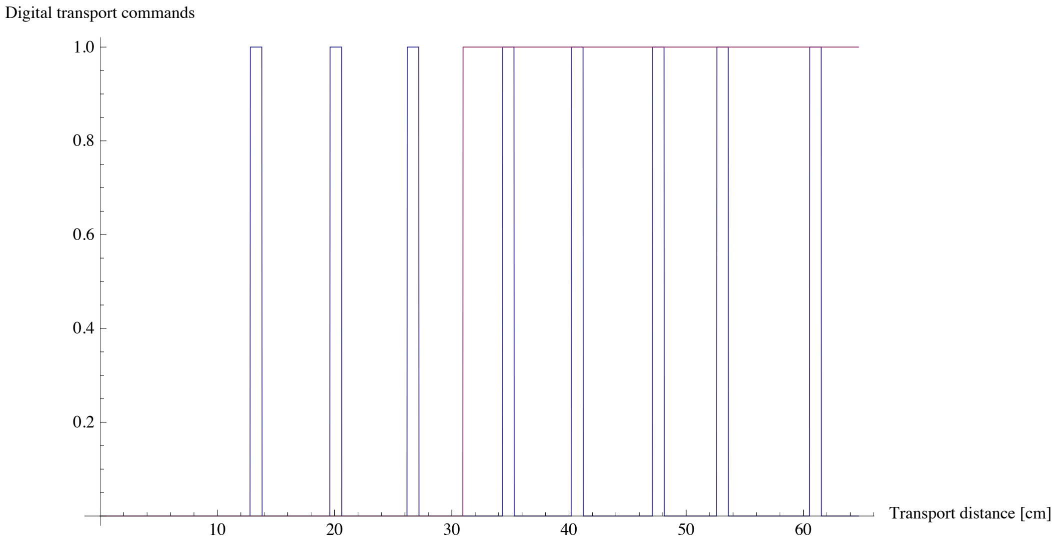

Figure 4.30: *Digital clock sequence to drive the transport shift logics (blue), and switch at the elbow (pink).*

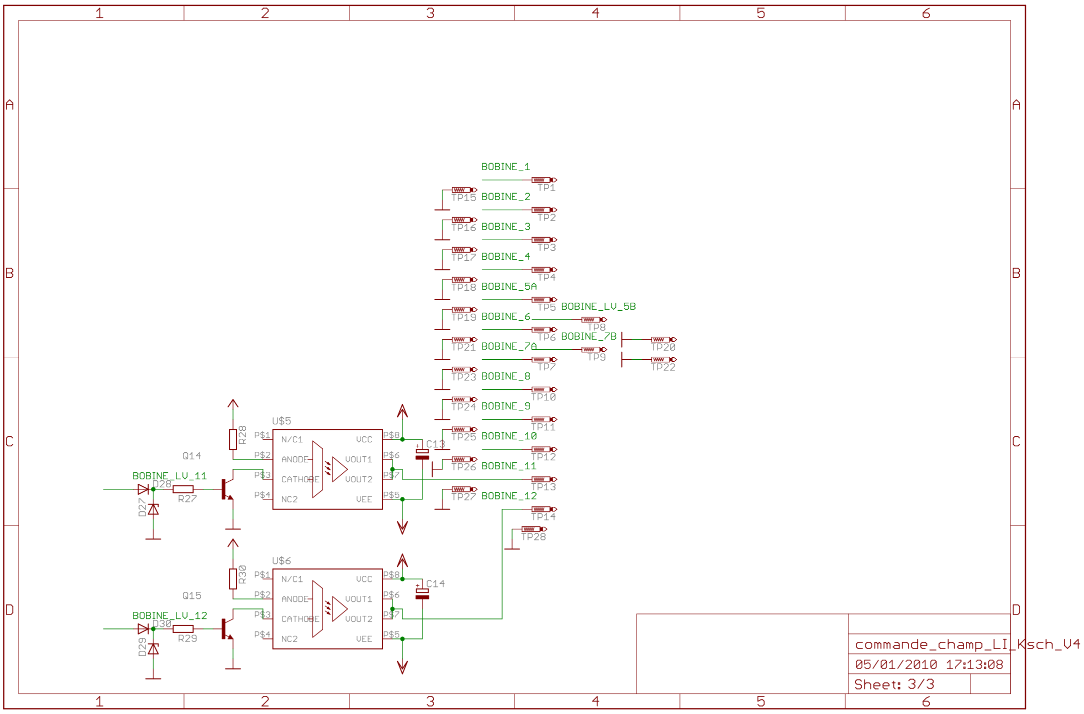

Figure 4.31: *Optocoupling stage between the logics and the MOSFETs.*

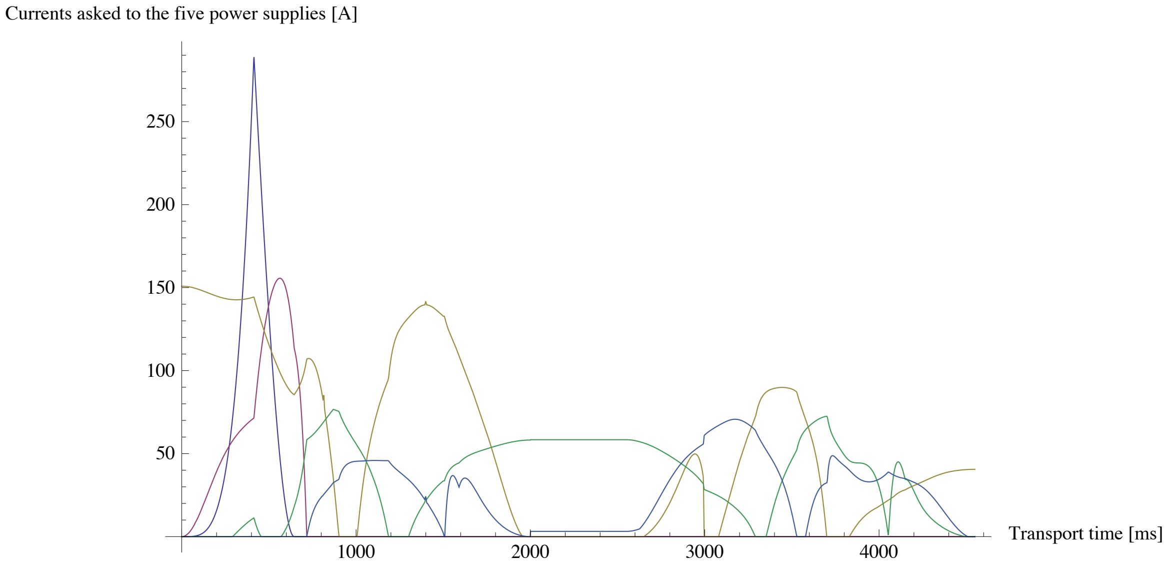

Figure 4.32: *Effective currents asked to the five power supplies.*

4.5.6 Computer control

As far as engineering is concerned, we presented in previous parts, the mechanics, the power and the logics of transport. Let us turn now to computer control. We already mentioned that the Mathematica program creates a clock signal for the shifting logics (see Figure 4.30). Combining static positive currents (Figure 4.16) and dynamics (Figure 4.12) it also creates a time-wave for each current as shown in Figure 4.32. Those two pieces of information are joined and exported into a CSV file and sent via ethernet connection from the analysis computer to the main computer. Then the main program reads this file and sends its values to the National Instrument analog and digital cards (see part 1.5) during the transport phase.

4.6 Summary

In this chapter, we presented the design of the magnetic transport, as well as its engineering.

First, we explained the main algorithm of the program that calculates the currents in all the coils, in order to control the trap geometry and its position. We also calculated an adiabatic invariant, that allowed us to obtain the sizes and temperatures of the transported clouds as functions of the ramps on the gradients. We then compared those theoretical sizes to the tube dimensions, which was useful to validate the chosen ramps. The transport horizontal transverse gradient equals 160 G.cm^{-1} and the magnetic aspect ratio between the transport and the vertical directions equals $b_x/b_z = -0.3$.

Secondly, we presented the transport dynamics. The sequence should be quick enough to reduce the Majorana losses, and slow enough to ensure adiabaticity and to reduce the inertia forces. We estimated that Majorana losses occur on a time scale of 10 s, whereas the inertia forces become harmful below a total transport time of 400 ms. Therefore, a transport time of a few seconds was estimated to be a relevant tradeoff. Using the limit conditions, we could built a proper trajectory for the trap.

Then, we presented the currents calculated by the program and we checked that they correspond to the chosen ramps on the gradients, apart from a few regions of negative currents, where we replaced the currents by zero. In order to check the effect of those corrections, we performed a numerical simulation an checked that the defects were not increasing the average energy of the cloud by more than 20 %. We also calculated the 3D trap depth along the transport, and showed that it never goes below 3 mK in our sequence.

Finally, we presented the engineering of the transport system, including mechanics, differential pumping, winding, logics, power, cooling, security and computer control.

With this design, we expect $\sim$ 80 % of transport efficiency. The experimental characterization of the system is developed in chapter 5.

Chapter 5

Magnetic transport : characterization

In chapter 4, we introduced the magnetic transport of ^{6}Li-^{40}K through its theoretical aspects, before describing the engineering of the system. After completing the design, we installed the transport assembly in the experiment and performed its experimental characterization.

In the present chapter, we present those experimental aspects and we particularly focus on the optimization of the transport efficiency. The main problem we encountered and solved was the trap depth at the most critical point of the transport: the entrance of the DN10 differential pumping tube. Actually, this particular region happens to be also the point of weakest gradients, since it is located in between the MOT center and the transport assembly, where the overlap is small.

The chapter is divided in four parts. In the first one, we present the experimental characterization of the hardware: currents, fields and computer control. In the second one, we study the dynamics of the transport that has to be chosen carefully in order to ensure adiabaticity and to avoid heating issues linked with the acceleration. The third part investigates the statics of the transport through the problem of trap depth. Finally, we summarize the results obtained after optimization, and we show that they are reasonable to start evaporative cooling of ^{40}K in one single spin state, and sympathetic cooling of ^{6}Li.

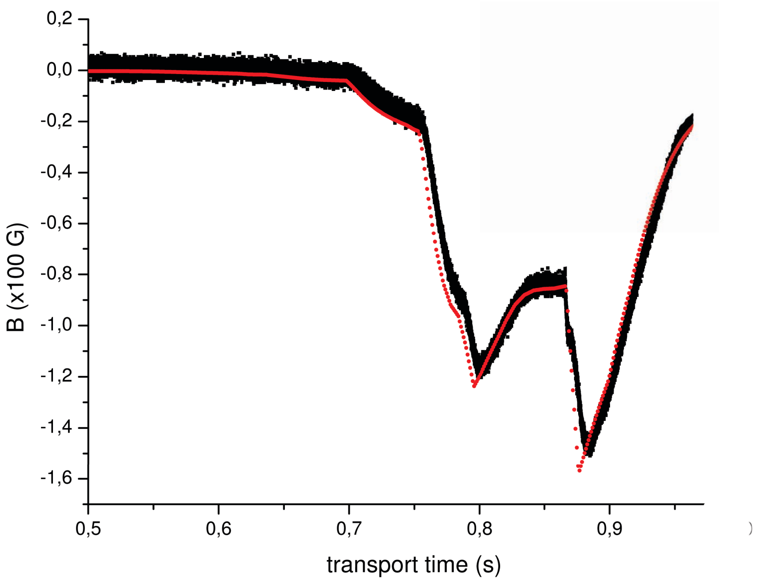

Figure 5.1: *Measurement (black) of the x-field at the center of the final quadrupole pair as a function of the transport time. Theoretical calculation (red) obtained with the transport program. The total transport sequence lasts 1 s here. The measurement was performed before assembling the transport system on the experiment, with a homemade Hall probe mounted on a xyz-translation mount.*

5.1 Hardware and software

Before launching the transport sequence in presence of atoms, we checked the reliability of the transport system. This was done by comparing the map of the magnetic field with the theoretical one and by checking the matching of the actual currents measured in each pair of coils with the asked one. Therefore, we could check the fidelity of the computer control and the commutation logics, as well as the absence of delays, shortcuts and electrical defects. In addition, we could validate the field calculation of the software, since any error in the field definition would have led to a difference with the measurements.

5.1.1 Magnetic field

The mechanical and electrical parts of the transport setup are presented in part 4.5. Prior to their final installation, we assembled them beside the vacuum chamber. There, we recorded the 3D magnetic field at the center of each pair as a function of time, apart from the MOT pair and the pushing coil, since they were already assembled. An example of result is shown in Figure 5.1 where we plotted the x-field at the center of the final quadrupole pair. The measurement was performed with a homemade amplified Hall probe (UGM3503U) mounted on a Newport xyz-translation mount and connected to an oscilloscope in single trace mode. The field detection was triggered by a digital signal (see part 1.5) sent at the beginning of the transport sequence. For each coil of the assembly, starting from the third transport pair (since before the field is wrong in absence of MOT coils), we compared the measurements to the values calculated by the transport program from the currents of Figure 4.32. There was no major deviation (see Figure 5.1 for instance), which validates the hardware after the third transport pair, as well as the field expression in the program. However, in order to control the timings on the millisecond scale, we then recorded the real currents with current transducer probes, and we compared the results to the theoretical values.

5.1.2 Currents

As explained in part 4.5.4, a current transducer probe (LEM HTFS800-P) is placed around each coil circuit in order to monitor continuously the current passing through it (see Figure 4.26). This allowed us to compare the actual currents in all coils with the ones asked by the transport program (see Figure 4.32). By zooming around the switching times, we observed systematic 10 ms delays between commands and loads in Constant Current (CC) mode. This may be harmful for the cloud. In fact, looking at Figure 4.13, the maximal speed of the cloud in the sequence is of the order of 35 cm.s^{-1}. Thus, if we tolerate a maximal error on the cloud position of the order of 1 mm, we can not accept more than approximately 3 ms in timing precision. As explained in part 4.5.2, the delay could be reduced to less than 1 ms by switching to Constant Voltage (CV) mode in the power supplies, which increased the overall transport efficiency by approximately 10 %.

An example of final results is shown in Figure 5.2, where we plot the theoretical currents asked to four pairs of coils (before the conversion into voltages for the CV mode operation) as well as the real currents passing in those pairs. As we can see, the agreement is perfect. In conclusion, the chain between the transport program and the current is reliable, and there is no shortcut or electrical defect since, in CV mode, any change of resistance would imply a change of current. Moreover, we checked that the result is identical while repeating the sequence over several minutes, showing that the change of resistance due to heating is negligible.

5.2 Dynamics

After having tested the technical aspects of the transport system, as presented in section 5.1, we characterized and optimized the physical aspects of the transport by running the sequence in presence of atoms. The transport sequence starts after a 50 ms magnetic trapping stage (see chapter 3). As explained in chapter 4, the transport program is divided in two independent parts: first, a routine defining the static trap geometry at each given position, and calculating the associated currents; secondly, a routine fixing the time evolution of the trap center. In this section, we focus on the dynamics. Section 5.3 is dedicated to the study of the statics.

As far as the dynamics is concerned, we first optimized the transport efficiency by changing the timings in each of the four parts: injection, first arm of the transport, elbow and second arm. We could thus obtain a preliminary efficiency of transfer of 15 % for ^{40}K and 7 % for ^{6}Li, including the vacuum losses. The associated trajectory is the one shown in Figure 4.12, with the acceleration profile of Figure 4.14. Besides,

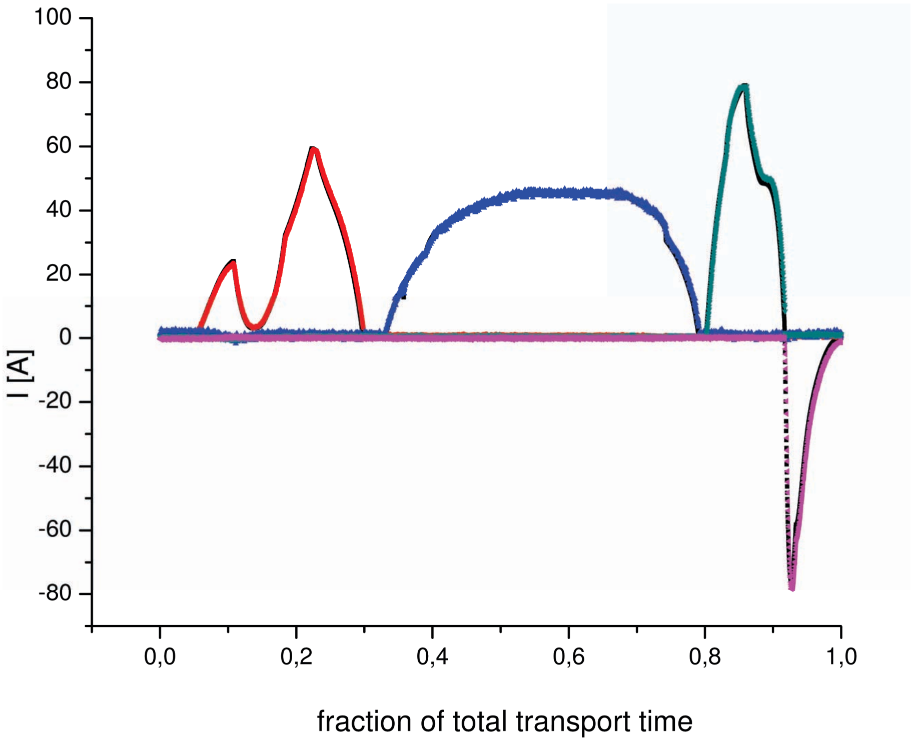

Figure 5.2: *Measurement of the currents passing through four pairs of coils connected to a same power supply (see parts 4.5.1 and 4.5.2) as a function of transport time. The coils are T1 (red), T4 (blue), T9 (green), V2 (pink). The graph shows also the theoretical current asked by the transport program (black). The measurements were performed using the current transducer probes described in part 4.5.4, and for a total transport duration of 4.6 s. The fact that the V2 current does not match with its value on the green curve of Figure 4.32 is due to two reasons: first, the opposite sign is a consequence of the chosen orientation of currents in this pair to account for its negative current in Figure 4.15; secondly, in Figure 4.32 there is a scaling calibration factor depending on the pair, which is due to the CV operation where a single voltage is asked to a power supply that drives four pairs of different resistances.*

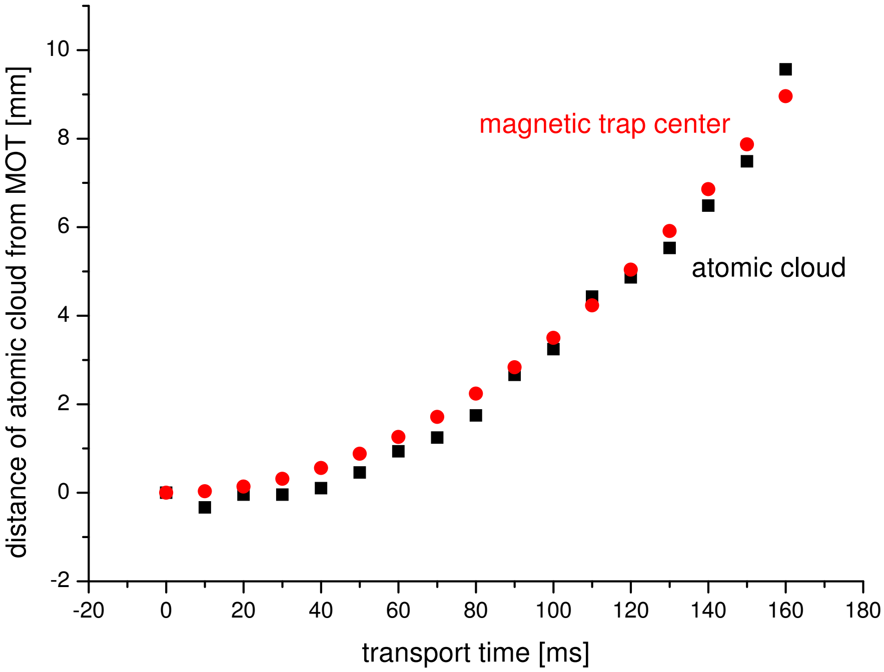

Figure 5.3: *Position of the ^{40}K cloud and the theoretical trap center as a function of transport time, for a constant acceleration of 0.7 m.s^{-2}. The cloud position is obtained by absorption imaging (see part 2.2.2).*

we also tried to have smoother acceleration profiles, such as higher orders polynomials, sinusoidal or gaussian profiles, but it appeared not to be critical.

Here, we study successively the dynamics of the injection stage, the acceleration, and the temperature of the transported cloud over a round-trip experiment.

5.2.1 Injection

After the preliminary optimization of the timings mentioned above, we checked the injection in the transport by recording the real position of the cloud as a function of the transport time and by comparing it to the expected trap position. The position was measured by absorption imaging (see part 2.2.2), the imaging being limited by the optical access in the MOT chamber to 1 cm in the transport direction. The result is shown in Figure 5.3 for ^{40}K with a constant acceleration of 0.7 m.s^{-2}. As we can see, the injection is nicely working at this acceleration which corresponds approximately to twice the maximal acceleration of the chosen profile shown in Figure 4.14. Moreover, no major losses were observed during this injection stage.

5.2.2 Inertia

The effect of the acceleration of inertia was presented in part 4.3.1. We found a maximal acceleration of $a^*_{\mathrm{max}} = 28$ m.s^{-2}, above which atoms are theoretically lost due to the force of inertia. In order to check this, we recorded the real cloud position when the trap center reaches $x = 8$ mm, for several accelerations of the transported trap.The

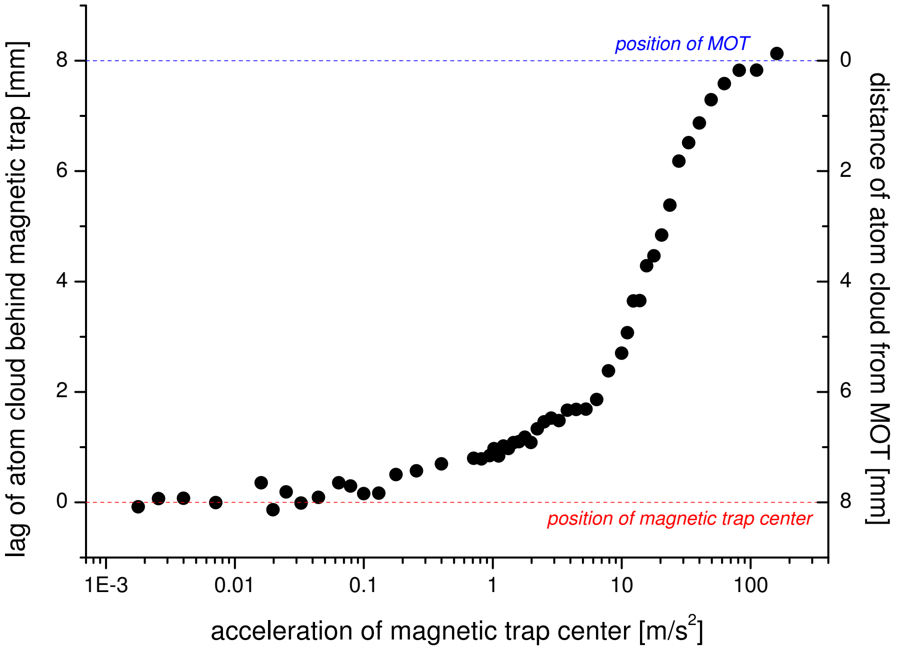

Figure 5.4: *Lag of ^{40}K cloud with respect to a theoretical trap center position (8 mm) as a function of the trap acceleration.*

result is shown in Figure 5.4, for ^{40}K. As expected, a lag between the trap center and the cloud appears at high acceleration. On the contrary, at low acceleration, the two positions match. The threshold is approximately 0.1 m.s^{-2}. With $a^*_{\mathrm{max}} = 28$ m.s^{-2}, the lag equals 7 mm. At $x = L_1 = 6.8$ cm, where the gradients are the smallest, the RMS size of the cloud reaches 7.5 mm (see Figure 4.6). This means a total 1.5 cm typical radial deviation from the theoretical trap center, which is of the same order as the trap extension in presence of inertia, as shown in Figure 4.11. Therefore, our estimate of a^*_{max} was correct, and with the chosen acceleration $a = 0.3$ m.s^{-2} (see Figure 4.14), there is no risk of loosing atoms by inertia.

5.2.3 Adiabaticity

Even in absence of inertia forces, a bump in the sequence or a local misalignment can be harmful, since it may lead to a violation of the adiabaticity criterium presented in part 4.3.2. As a consequence, the cloud can be heated. This is undesirable as far as the forthcoming evaporative cooling stage is concerned, since it reduces the elastic collision rate and thus the cooling efficiency. Furthermore, it may also induce some consequent trap losses during transport. Therefore, we checked the temperature of the cloud after a round-trip in the transport. An example of result is shown in Figure 5.5, for a ^{40}K round-trip to 1 cm in 200 ms. Compared to the initial $T_{\mathrm{h}} = 344$ μK and $T_{\mathrm{v}} = 423$ μK in the ^{40}K magnetic trap (see Figure 3.7), there is only a slight increase of temperature. It is in accordance with the adiabatic compression (see formula 4.7) from the gradient of the magnetic trap, $b_y = -42.5$ G.cm^{-1}, to the initial transport value, $b_y = -67$ G.cm^{-1}. In addition, no significant loss in number of atoms was observed.

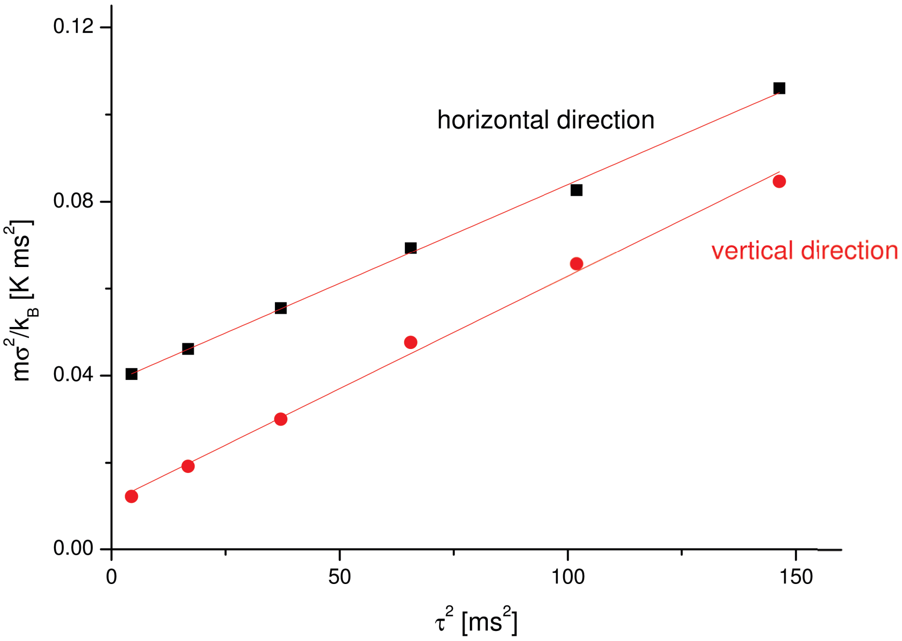

Figure 5.5: *Time-of-flight (see part 2.2.3) of the* ^{40}K *cloud after a transport round-trip to 1 cm in 200 ms. The linear fits give a vertical temperature of 517 µK and an horizontal one of 455 µK.*

As a conclusion concerning the transport dynamics, there is no problem of inertia and adiabaticity with the chosen trajectory of Figure 4.12. To optimize the sequence we then had to study the static trap depth.

5.3 Trap depth

In this part, we present the static transport optimization through the issue of trap depth. We first show the main diagnostics, the round-trip experiment that allows us to localize the main losses of atoms. Then, we present our investigation of the causes of those losses, by analyzing the sources of truncation of the atomic distribution on the transport walls. Besides, we check the hypothesis of evaporative cooling due to this truncation. Finally, we study the trap depth along the transport direction.

5.3.1 Round-trip experiment

The main diagnostics that we use while optimizing the transport system is the round-trip experiment mentioned in part 5.2.3. It consists of probing each position of the transport by moving the trap to this point before going back to the octagonal chamber, where absorption imaging is performed (see part 2.2.2). However, it is important to normalize the obtained number of atoms by the vacuum losses measured in the fixed magnetic trap (see part 3.3.5) for a duration identical to the transport time, in order to measure the absolute efficiency of the transport independently of the vacuum losses.

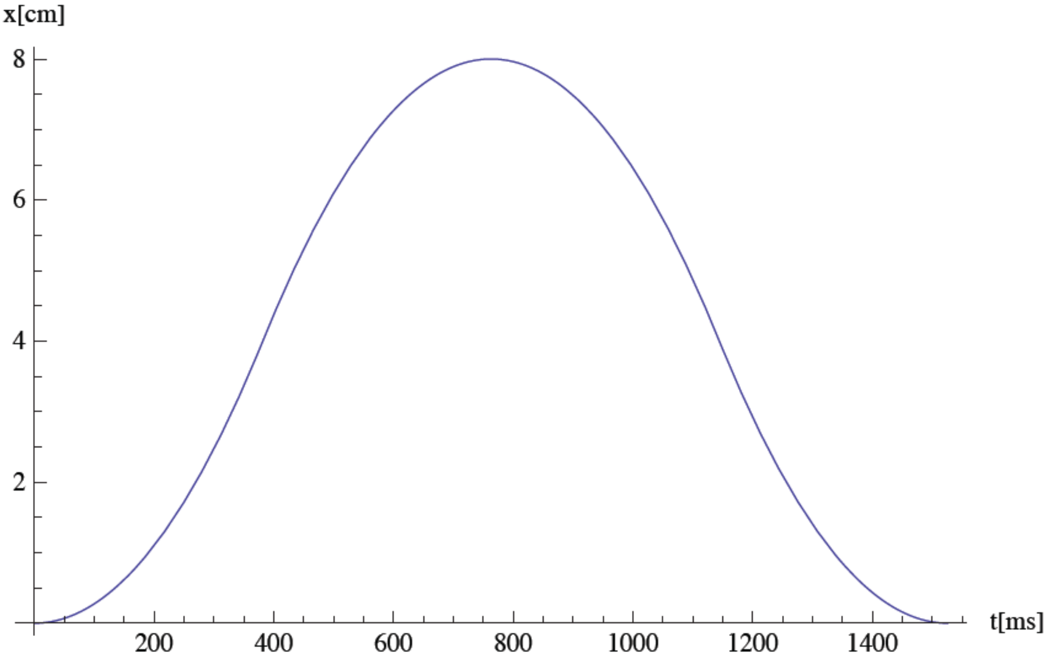

Figure 5.6: *Trajectory of the center of the trap in a round-trip transport experiment to* $x = 8$ *cm.*

This diagnostics is more precise than imaging directly the atoms in the final cell, for two reasons: it gives a local information along the transport direction, and the imaging setup of the transported cloud is identical to the initial imaging. Note that the transport efficiency should not depend on the initial number of atoms. In fact, at 500 μK, we are still far from a Fermi-Dirac distribution for which the maximal energy increases with the number of atoms. In addition, there is almost no collision in the magnetic trap (see part 3.3.3). Thus, the truncation of the distribution remains a quasi one-body problem.

Nevertheless, one should keep in mind that this diagnostics introduces some dynamical artifacts. First, the trajectory profile is different from the real one (see Figure 4.12), as shown in Figure 5.6. In fact, even if we adapt the overall timings so that the maximal acceleration is close to the one of Figure 4.14, we introduce some differences in the sequence. For instance, with the round-trip at $x = 8$ cm shown in Figure 5.6, we have a null velocity at $x = 8$ cm, which is completely different from the full transport case, where the velocity is nearly maximal and equals 25 cm.s^{-1}. However, since we do not exceed the maximal acceleration of 0.3 m.s^{-2}, we can assume than the inertia does not play a significant role, according to part 5.2.2. As far as ergodicity is concerned, we could argue that staying at a given point or passing twice through it is quite different from passing once and quickly through it. However, as demonstrated in the following, the typical time of ergodization equals a few tens of milliseconds which remains small in comparison with the typical transport times.

Secondly, the number of atoms at a given point is not independent from the number of atoms at a point placed before in the sequence. As an example, if a defect occurs somewhere in the sequence, leading to swinging of the cloud (and thus heating), the

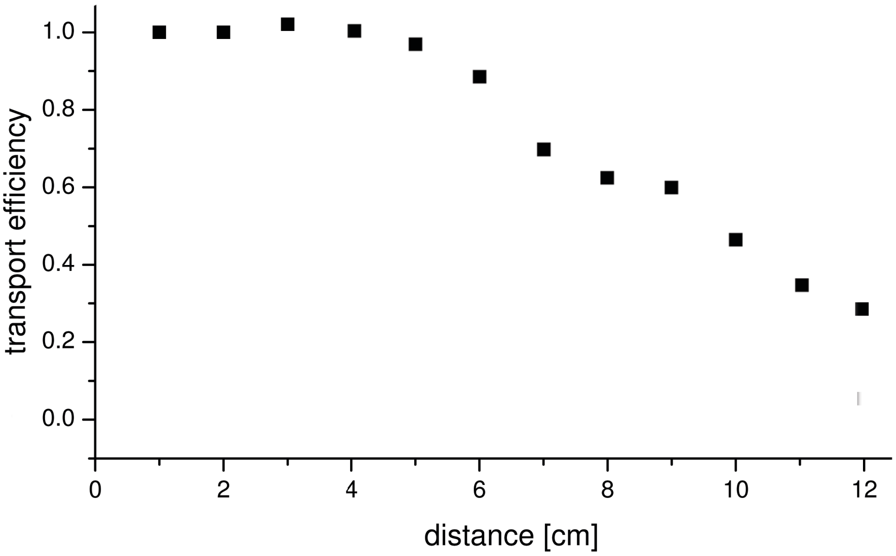

Figure 5.7: *Initial transport efficiency of* ^{40}K *as a function of transport distance. Each point is an average over 6 measurements. The efficiency at a given point is defined as the ratio between the number of atoms measured after a round-trip to this point and the number of atoms in a fixed magnetic trap during the same duration. The initial number is* 5×10^8 *in the magnetic trap.*

efficiency at further points will be reduced. Once again, the dynamical check described part 5.2.3, ensures that no major heating occurs during the round-trip experiment, which allow us to be confident in the round-trip diagnostics.

Finally, one should keep in mind that we are actually interested in the absolute number of atoms and not the transport efficiency. In fact, in case of a bump in the magnetic trajectory, moving slowly can reduce the losses due to transport but it increases the losses due to vacuum (see part 3.3.5), especially in the region of the octagonal chamber where the vacuum quality is not as good as the one in the final science cell. Thus, after understanding and optimizing the key parameters of the transport through the round-trip diagnostics, it will be important to change the overall timing in order to find the trade-off between transport efficiency and lifetime in the trap.

Practically speaking, the round-trip experiment implies to calculate a new trajectory for each distance travelled in the transport, as the one shown in Figure 5.6. Moreover it requires to disconnect the switch box of the transport (see part 4.5.5) since it does not allow to come back in the sequence. Instead, we directly control the MOSFETs described in part 4.5.2, through the digital outputs of the main computer (see part 1.5). Finally, we performed the measurement with ^{40}K first since it is cooler, and thus less sensitive to losses.

After turning to CV control of the power supplies, as described in part 5.1.2, and for maximal accelerations of the order of 0.3 m.s^{-2}, according to part 5.2.2, we could record the round-trip curve depicted in Figure 5.7 for ^{40}K. The efficiency is close to 100 % before $x = 6$ cm where is starts to reduce until 30 % at $x = 12$ *cm*.

After $x = 13$ cm, the raw number of transported ^{40}K atoms equals approximately

7×10^7 atoms and remains constant until the elbow located at $x = 30.95$ cm (see Figure 4.2). We attribute this to the differential pumping tube which starts at $x = 7.7$ cm (see part 1.1.3), and which already divides by two the background pressure at $x = 13$ cm. Therefore, after $x = 13$ cm, we normalize the transported number of atoms by the number of atoms remaining in a fixed magnetic trap, for a duration equal to the one needed to transport the trap to $x = 13\ cm$. The transport efficiency is thus estimated to be of the order of 30 % at the elbow. The total round-trip until the elbow lasts 4 s.

In addition, as already mentioned in section 5.2, we performed a first test of full transport that gave 15 % for ^{40}K and 7 % for ^{6}Li of transfer efficiency, including the vacuum losses.

In the following, we investigate the possible causes of those losses, in order to optimize the transport.

5.3.2 Truncation on the tube

In part 5.3.1, we presented our initial results from the round trip diagnostics. Figure 5.7 reveals the existence of a critical region in between 6 cm and 12 cm. This region can be harmful for several reasons.

First, the differential DN10 pumping tube, starting at $x = 7.7$ cm and ending at $x = 24\ cm$, reduces the inner diameter from 1.6 cm to 1.0 cm, which can truncate the wings of the atomic distribution.

Secondly, according to Figure 4.3, $x = L_1 = 6.8$ cm corresponds to the minimal gradient in x and z directions, and to a gradient close to its minimal value in the y direction. This is due to the fact that $x = L_1$ is in the region of weak overlapping between MOT and transport coils. This implies that the atoms are close from the walls in this region (see Figure 4.7). Note also that the MOT pair goes off at $x = 12.8$ cm (see Figure 4.16).

Thirdly, this region is the place of smallest trap depth in x direction, where it equals 3.4 mK. This particular point is studied in part 5.3.4.

Fourthly, according to Figures 4.3 and 4.4, the ramps on the gradients last until $x = L_2 = 12$ cm. However, we checked that reducing L_2 to 8 cm had no major effect.

In this part, we focus on the transverse trap depth. We present successively our theoretical and numerical models of ergodic truncation, the role of the initial temperature, the effect of a misalignment, and the dependency of the trap depth on the gradient and the size of the tube.

Theoretical model

To understand the losses in the transport tube, we assume a truncation of the distribution in the transverse directions y and z (see Figure 5.8). We also assume ergodicity, which means that atoms have enough time to explore the whole available phase space. Thus, they are removed if their energy is greater than the trap depth (see equation 3.4):

$$E_{\mathrm{depth}} = \frac{\mu_{\mathrm{B}} b r}{k_{\mathrm{B}} T} , \tag{5.1}$$

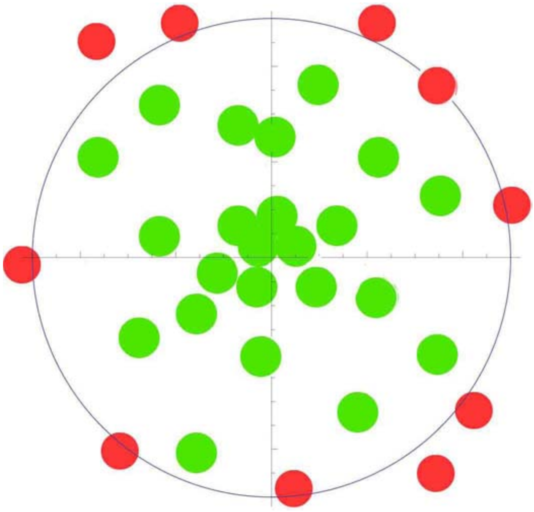

Figure 5.8: *Cartoon of the analytical (see equation 5.2) and numerical models for the truncation of the atomic distribution: each time an atom have enough energy to reach the walls of the differential pumping tube, it is lost (red).*

where r is the radius of the tube, $-b$ is the y-gradient, and T is the temperature of the cloud. This hypothesis is reasonable since the typical time for an atom to cross the trap is of the order of 15 ms for potassium (see equation 4.16). Moreover, we found numerically a typical ergodization time of 20 ms for ^{40}K, as explained below.

Therefore, using the density of energy in a linear trap (see appendix A.4), the transport efficiency $\epsilon(x)$ can be defined as:

$$\epsilon(x) = \frac{\int_0^{a(x)r(x)} du\ u^{7/2} e^{-u}}{\int_0^{\infty} du\ u^{7/2} e^{-u}} \ , \tag{5.2}$$

where $r(x)$ is the effective radius of the tube at transport position x, and:

$$a(x) = \frac{\mu_{\mathrm{B}} b(x)}{k_{\mathrm{B}} T(x)} \ , \tag{5.3}$$

whith $-b(x)$ the y-gradient, and $T(x)$ the cloud temperature.

According to parts 4.3.2 and 5.2.3, we assume that the transport is adiabatic. Therefore, equations 4.7 and 5.3 lead to:

$$a(x) = \frac{\mu_{\mathrm{B}} b(x)^{1/3} (b^0)^{2/3}}{k_{\mathrm{B}} T^0} \left[\frac{2|1 + A(x)|^2}{|A(x)|} \right]^{2/9} \ , \tag{5.4}$$

with an initial cylindrical trap of aspect ratio $A = -0.5$, y-gradient $b_y^0 = -b^0$ and temperature T^0. Thus, $a(x)$ is completely determined by the initial temperature in the magnetic trap T^0, and by the ramps on y-gradient $b_y(x) = -b(x)$, and aspect ratio $A(x)$, given in Figures 4.3 and 4.4.

Using this model, we calculate in the following the influence of the initial temperature, an hypothetic misalignment and the gradients. We also fit the experimental data in various conditions.

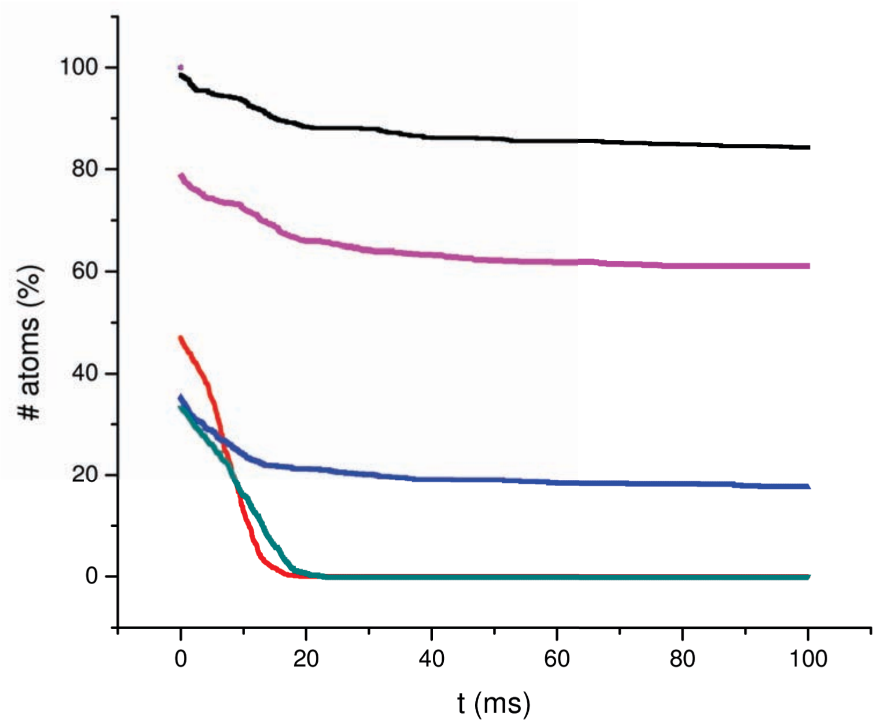

Figure 5.9: *Numerical simulation of the percentage of* ^{40}K *atoms remaining in a static quadrupole trap with* $b_y = -100$ *G.cm*$^{-1}$ *as a function of time, for various conditions:* $T = 0.5$ *mK and DN10 tube (black),* $T = 1$ *mK and DN16 tube (pink),* $T = 1$ *mK and DN10 tube (blue),* $T = 0.5$ *mK and DN10 tube misaligned by 5 mm (red),* $T = 1$ *mK and DN10 tube misaligned by 5 mm (green).*

Ergodicity

In addition to the analytical model of equations 5.2 and 5.4, we performed a numerical simulation containing the same ingredients, in order to validate the hypothesis of ergodicity and to double check our results. Similarly to one described in part 4.4.3 and [140], the program has been written in Fortran 90, using a fourth order Runge-Kutta routine. The initial assignation of velocities and position of 10000 ^{40}K atoms into the trap is done accordingly to the initial phase-space distribution. The magnetic force is calculated with the ramps given in Figures 4.3 and 4.4, as well as the trap trajectory of Figure 4.12. Finally, each time an atom comes outside the tube defined in Figure 4.7, it is removed from the cloud. Thus, the efficiency is given by the ratio between the final and initial numbers of atoms.

Figure 5.9 shows the numerical simulation of the percentage of ^{40}K atoms remaining in a static magnetic trap as a function of time, for several conditions. We see that it requires between 10 and 20 ms, after the initial cut in distribution, to fulfill the ergodicity criterium, that is for a ^{40}K atom of energy greater than the trap depth to be removed from the trap. This time is small compared to the typical time of variation of the trap, as explained in part 4.3.2. Therefore, our model of equation 5.2 is valid.

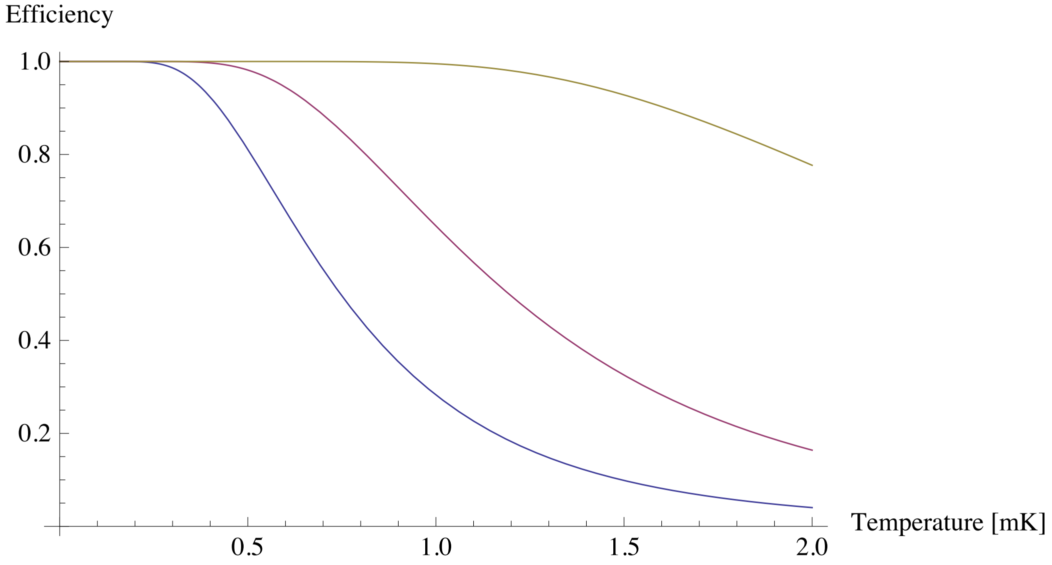

Figure 5.10: *Theoretical efficiency of trapping* ^{6}*Li and* ^{40}*K atoms in a static magnetic trap of gradient 93 G.cm*$^{-1}$ *as a function of temperature, for three different tubes: DN10 (blue), DN16 (pink), and DN38 (yellow). The model used is given in equations 5.2 and 5.4.*

Temperature

Using equations 5.2 and 5.4, as well as the numerical simulation described above, we studied the effect of temperature on the losses.

We saw in Figure 5.9 that the temperature is very critical in a DN10 tube, since the efficiency goes from approximately 90 % to 20 % by heating the cloud from 0.5 mK to 1 mK.

To confirm this, using our analytical model of equations 5.2 and 5.4, we studied the percentage of atoms remaining in a static magnetic trap as a function of temperature, in various tubes. The y-gradient is fixed to $b_y = -b = -93$ G.cm^{-1}, since it is the value at the entrance of the differential pumping tube ($x = 7.7$ cm), as shown in Figure 4.3, which corresponds to the weakest distance to the tube (see Figure 4.7). The result is plotted in Figure 5.10. There is a good agreement with the results of the numerical simulation shown in Figure 5.9. Furthermore, the graph confirms that the temperature is critical above 0.5 mK in a DN10 tube. On the contrary, the situation is safe below this value. According to the round-trip experiment (see Figure 5.7), the transfer efficiency for ^{40}K equals approximately 60 % at $x = 7.7$ cm, which corresponds to an initial temperature of 700 μK. We checked the initial temperature in the compressed magnetic trap before the transport and we actually found a temperature of 700 μK. The difference between this high value and the temperature measured in the magnetic trap $T^{\mathrm{K}} \approx$ 400 μK (see part 3.3.2) means that our ramping to the initial transport value is not adiabatic. In fact, starting from $T^{\mathrm{K}} \approx 400$ μK in a magnetic trap of y-gradient 42.5 G.cm^{-1} and ramping it up adiabatically to 67 G.cm^{-1}, which is the transport initial value (see Figure 4.3), one should get approximately 540 μK, according to equation 4.7.

We then optimized the ramping of the magnetic trap after the spin-polarization

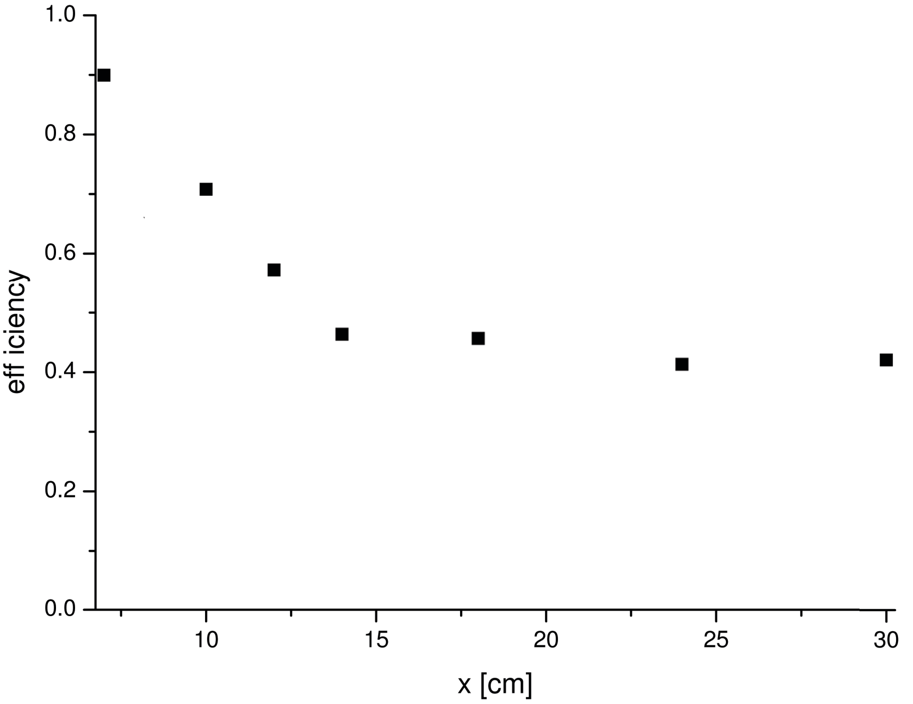

Figure 5.11: *Transport efficiency of* ^{40}K *as a function of transport distance. Each point is an average over 6 measurements. The efficiency at a given point is defined as the ratio between the number of atoms measured after a round-trip to this point and the number of atoms in a fixed magnetic trap during the same duration, in order to account for vacuum losses (see part 3.3.5). After* $x = 13$ *cm, the raw number of* ^{40}K *atoms stabilizes to approximately* 1.3×10^8 *atoms until the elbow located at* $x = 30.95$ *cm (see Figure 4.2). Therefore, after* $x = 13$ *cm, we normalize the transported number of atoms by the number of atoms remaining in a fixed magnetic trap, for a duration identical to the one needed to transport the trap to* $x = 13$ *cm. The total round-trip until the elbow lasts 4 s.*

stage (see part 3.2.3), by directly reaching the transport gradient of 67 G.cm^{-1} in 3 ms. The initial temperature could be reduced to 500 μK, as already shown in Figure 5.5. The associated round-trip experiment is shown in Figure 5.11. The efficiency before the entrance of the DN10 tube became greater than 90 %. The efficiency at $x = 8$ cm could be increased from 60 % to 80 %, as expected in Figure 5.10 with an initial temperature of 500 μK. In fact, note that according to Figure 5.10 the real temperature is close to the initial one at $x = 7.7$ cm.

After the entrance of the DN10 tube, the efficiency reduces until 40 % at $x = 13$ *cm*. After $x = 13$ cm, the raw number of transported ^{40}K atoms equals approximately 1.3×10^8 atoms, and remains constant until the elbow located at $x = 30.95$ cm (see Figure 4.2). The new transport efficiency is estimated to be of the order of 40 % at the elbow.

We improved the efficiency before the entrance of the DN10 tube. However, the losses in the tube depicted in Figure 5.7 are still present and can not be explained by the temperature since the efficiency decreases whereas we ramp up the gradient. Indeed,

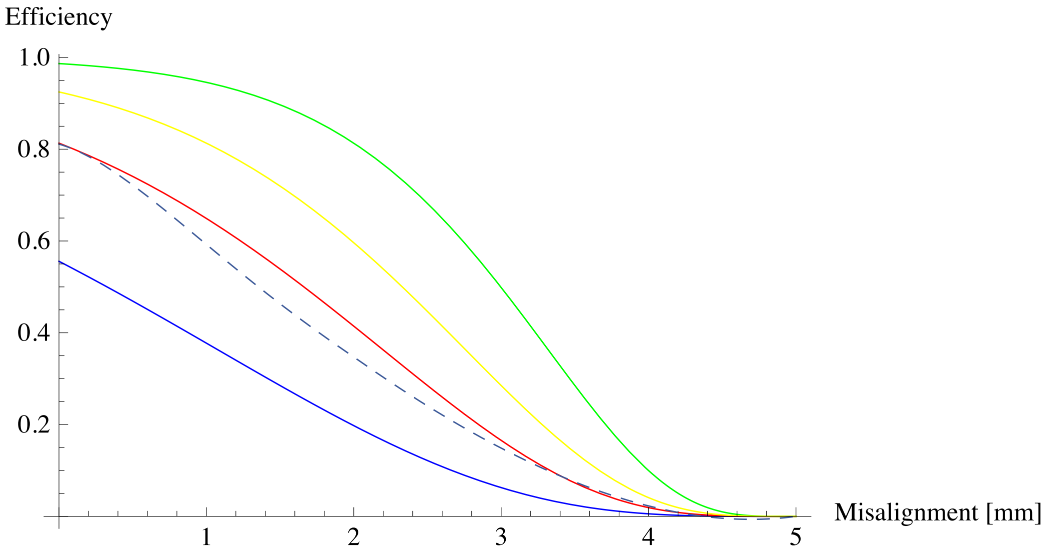

Figure 5.12: *Theoretical efficiency of trapping* ^{6}*Li and* ^{40}*K atoms in a static magnetic trap of gradient 93 G.cm*$^{-1}$ *in a DN10 tube as a function of misalignment, for four temperatures: 0.3 mK (green), 0.4 mK (yellow), 0.5 mK (red), and 0.7 mK (blue). The model used is given in equations 5.2 and 5.4. In addition, a numerical simulation at 0.5 mK in an identical magnetic trap is shown (dashed line).*

according to equation 5.2 and Figure 4.4, the efficiency should increase adiabatically with the gradient, independently of the real temperature of the cloud. We thus study an hypothetic misalignment, as well as the trap depth, in the following.

As a remark, $T^{\mathrm{Li}} \approx 1.3$ mK in the magnetic trap (see part 3.3.2). Thus, the transfer efficiency of ^{6}Li equals 20 %. Therefore, we have to reduce its temperature by improving the CMOT (see part 3.2.1) and spin-polarization stages (see part 3.2.3) for ^{6}Li.

Misalignement

With the same procedure as for the temperature, we studied the effect of an hypothetic misalignment of the DN10 differential pumping tube with respect to the center of the magnetic trap. The study was performed at the entrance of the tube where the cloud is the closest from the walls (see Figure 4.7). The y-gradient is fixed to its value at the entrance of the DN10 tube: $b_y = -b = -93$ G.cm^{-1}. The results of numerical simulations and analytical calculations based on equations 5.2 and 5.4 are summarized in Figure 5.12. Once again they are in good agreement. In addition, the graph shows that a misalignment of 1 mm could explain the 40 % efficiency obtained in Figure 5.11 at $x = 13$ cm. In fact, for an initial temperature of 500 μK, the real temperature at this point equals approximately 700 μK (see Figure 4.5). Therefore, we decided to move the transport assembly by a few millimeters in several directions. In addition, we installed a single coil on top of one coil of the T1/2 pair (see Figure 4.24) in order to shift vertically the position of the trap. In both cases it did not help.

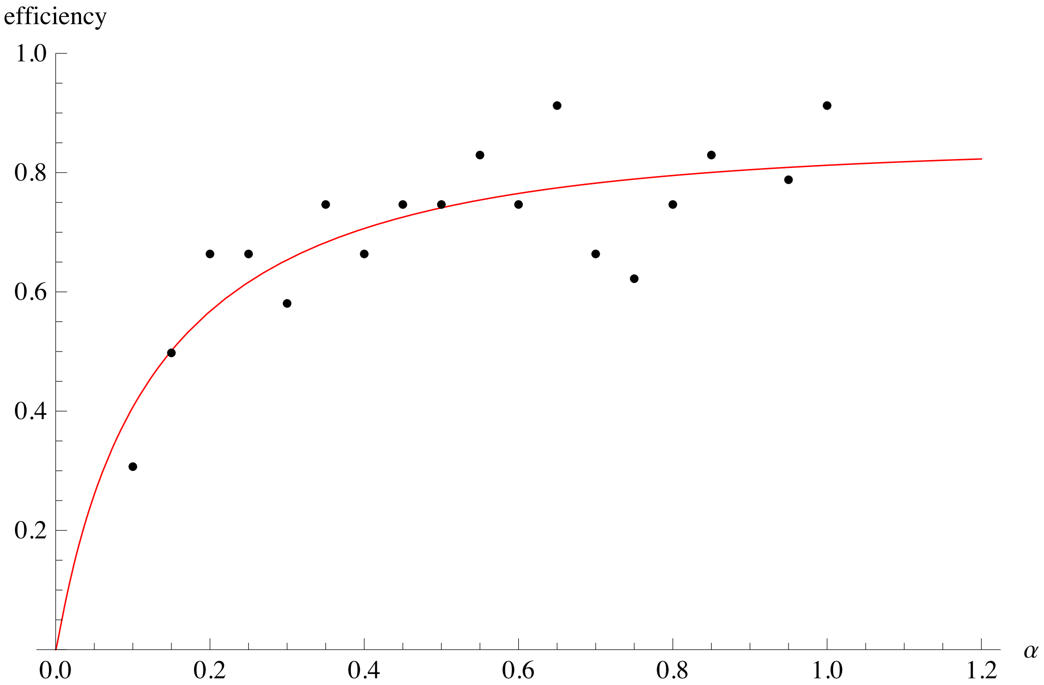

Figure 5.13: ^{40}*K transfer efficiency at* $x = 9$ *cm as a function of the gradient at* $x = 9$ *cm.* α *is the ratio between the y-gradient and the y-gradient of the normal sequence (see Figure 4.3). The initial number of atoms is* 5×10^8 *and the initial temperature is* 500 μ*K. The fit is based on equations 5.2 and 5.4, normalized by the vacuum losses in 1.6 s. Its outputs are a radius of the tube of 6 mm and an initial number of atoms of* 4×10^8.

Transverse trap depth

In order to check the effect of the gradient on the transverse trap depth in the DN10 tube, we performed two studies.

First, we measured the ^{40}K transfer efficiency in a round trip experiment at $x = 9$ cm, which is 1cm inside the DN10 tube where the losses occur (see Figure5.11), as a function of the gradient at this point. The sequence is the following. We first move normally to $x = 9.cm$, then we stay at this point, while reducing adiabatically the current by a factor α. Afterwards, we ramp up again the currents and the cloud is brought backwards to the octagonal chamber. Therefore, we can precisely probe the truncation on the DN10 tube. Results are shown in Figure 5.13. The initial number of atoms is 5×10^8 and the initial temperature is 500 μK. We then performed a fit using equations 5.2 and 5.4, normalized by the vacuum losses in the sequence time. The free parameters of the fit are the radius of the tube, $r = 6\ mm$ and the initial number of atoms, $N_0 = 4 \times 10^8$. As we can see, those numbers are close to the real values, $r = 5$ mm and $N_0 = 5 \times 10^8$. The slight difference may be due to the fluctuations in number of atoms. Therefore, we can conclude that we are close from saturation with our value $\alpha = 1$. This means that we are not limited by the gradient.

Secondly, we plotted the full theoretical transfer efficiency of ^{6}Li and ^{40}K, as a

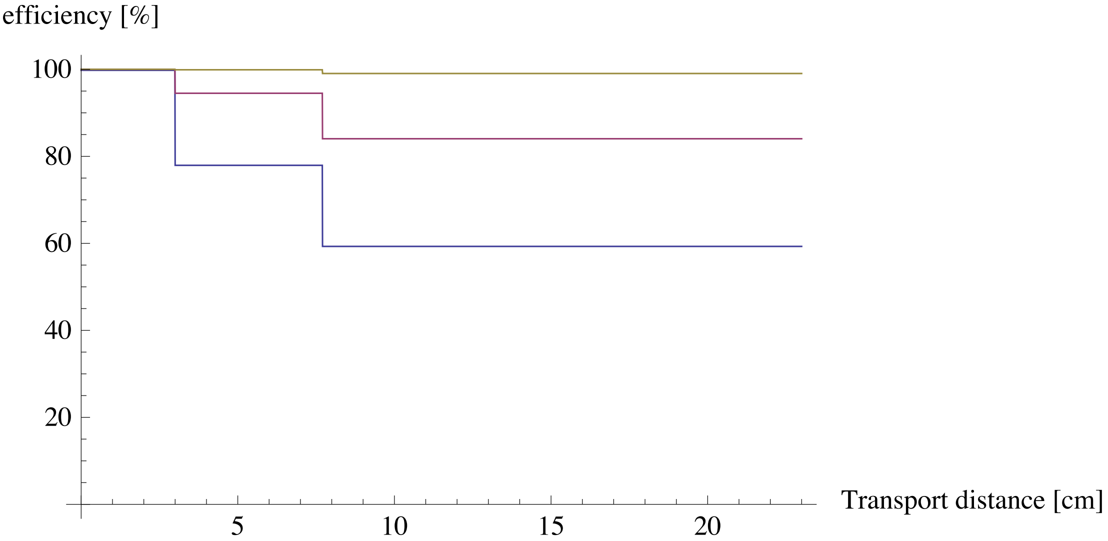

Figure 5.14: *Theoretical transfer efficiency of* ^{6}*Li and* ^{40}*K as a function of transport distance, for three temperatures: 0.3 mK (yellow), 0.5 mK (pink), and 0.7 mK (blue). The model used is given in equations 5.2 and 5.4, and takes into account the full ramps on the gradients (see Figure 4.3).*

function of transport distance. The model is once again based on equations 5.2 and 5.4 and takes into account the real ramps on the gradients described in Figures 4.3 and 4.4. Results are shown in Figure 5.14, for three initial temperatures. We conclude that, with a minimal y-gradient of 93 G.cm^{-1} in the tube, and with an initial temperature in the compressed magnetic trap of 500 μK, we should have a full transport efficiency of ~ 85 %, as already demonstrated in Figure 5.10 and measured in Figure 5.11.

In conclusion of this part dedicated to the truncation on the transport tube, we could suppress the losses occurring after $x = 6$ cm in Figure 5.7, by reducing the initial temperature, as depicted in Figure 5.11. However, the efficiency after $x = 8$ cm decreases until 40 %, where it stabilizes. The problem seems no to be linked to the transverse trap depth, since, according to Figure 5.14, we should have a transfer efficiency of 80 % with our initial ^{40}K temperature of 500 μK. In the following, we thus study the longitudinal trap depth. Before, since we expect 20 % losses on the transport walls, we present an estimate of evaporative cooling in the tube.

5.3.3 Evaporative cooling in the tube

In part 3.3.3, we calculated the ^{40}K p-wave elastic cross-section to be close from the value obtained at JILA [116], $\sigma = 2 \times 10^{-11}$ cm^{-2}. Using, this value in equation 3.12, we can estimate the collision time τ in the ^{40}K transported magnetic trap, for an initial temperature in the transport of $T = 500$ μK, and a number of atoms of 5×10^8. The calculation leads to $\tau_{\rm K} \approx 280$ ms, using the transport gradients (see Figure 4.3) and equation 3.11 to calculate the atomic density in the tube, and noticing that the temperature in the tube is nearly 1.3 higher than the initial one (see Figure 4.5).

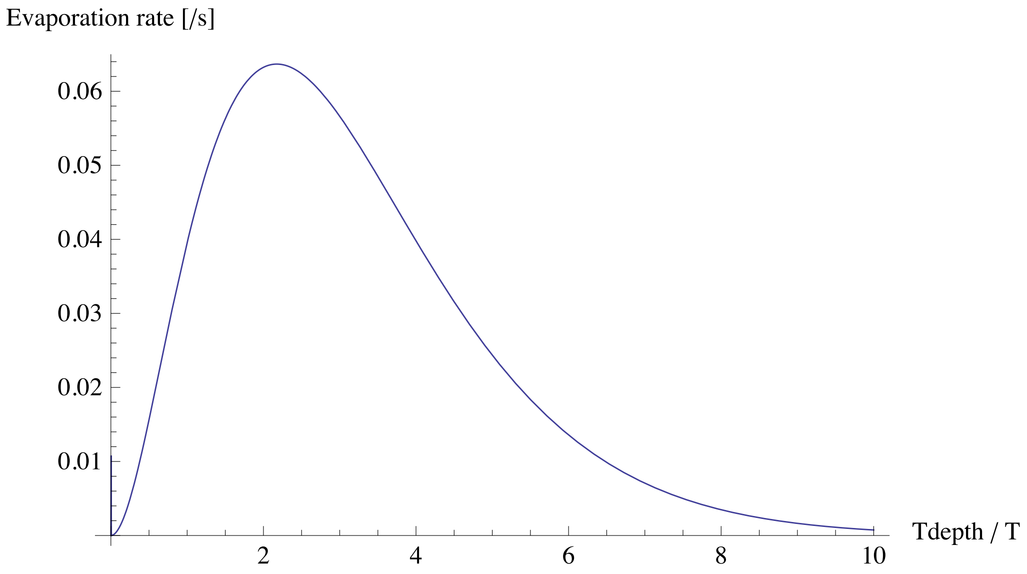

Figure 5.15: ^{40}K *evaporation rate in the transported magnetic trap as a function of the evaporation parameter* $\eta = T_{depth}/T$ *(see equation 5.5). The evaporation rate is defined as the rate of atoms that reach an energy higher than the trap depth after an elastic collision.*

Using this collision time, we calculate the evaporation rate Γ_{evap} in a linear trap as a function of the evaporation parameter $\eta = T_{\text{depth}}/T$. The evaporation rate is defined as the rate of atoms that reach an energy higher than the trap depth after an elastic collision. According to [141], we can write:

$$\Gamma_{\text{evap}}(\eta) = \frac{1}{\tau} e^{-\eta} \left[\eta - \frac{11}{2} \frac{P(11/2, \eta)}{P(9/2, \eta)} \right] , \tag{5.5}$$

with:

$$P(x, y) = \frac{\int_0^y du\ u^{x-1} e^{-u}}{\int_0^\infty du\ u^{x-1} e^{-u}} .$$

$\Gamma_{\text{evap}}(\eta)$ is plotted for ^{40}K in Figure 5.15. In the most critical position of the transport, the entrance of the DN10 tube at $x = 7.7$ cm where $b_y = -93$ G.cm^{-1}, the transverse trap depth equals 3.1 mK (see equation 5.1), for a temperature of the cloud of 500 μK, which means $\eta = 6$. With this value, we find $\Gamma_{\text{evap}}(6) \approx 14 \times 10^{-3}$ s^{-1}, according to equation 5.5, which corresponds to a typical evaporation time of ~ 70 s. This is large compared to the transport duration. Therefore, we can neglect the evaporation process in the transport tube for ^{40}K. The same conclusion stands for ^{6}Li, since p-wave collisions are suppressed under 6 mK for this fermionic atom [120].

5.3.4 Longitudinal trap depth

In this part, we study the trap depth in the transport direction. Using the auxiliary pulling pair of coils T1/2 (see Figure 4.24), we previously increased it to more than 6 mK at the most critical point $x = L_1$, as shown in Figure 5.16.

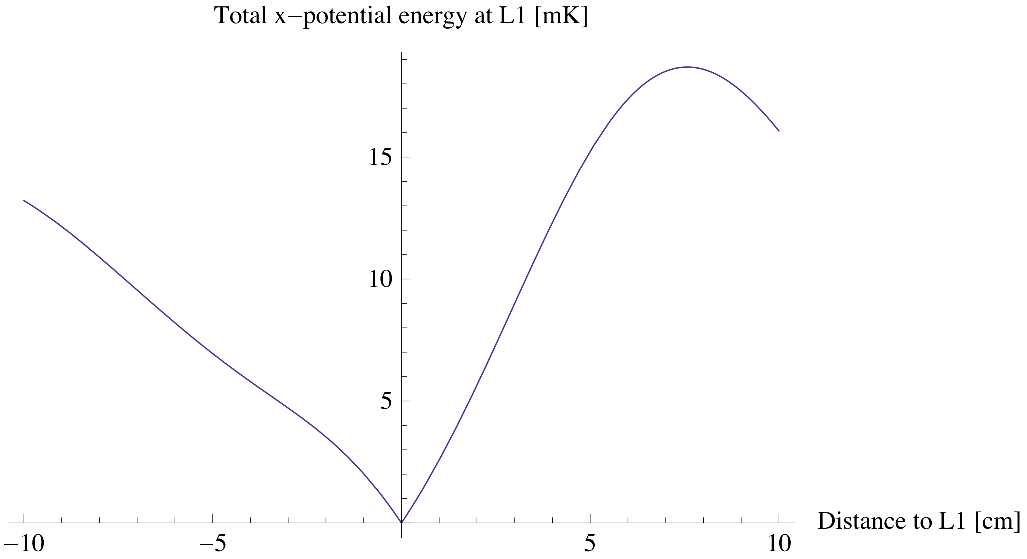

Figure 5.16: *Trap profile along the transport direction at* $x = L_1 = 6.8$ *cm.*

However, we finally understood that due to the new overlapping geometry, the most critical point was actually displaced from $x = L_1 = 6.8$ cm to $x = 8\ cm$. Indeed, with an independent program calculating the field profile at each position in the transport we could generate a movie of the transported trap. A snapshot at the most critical point $x = 8$ cm is given in Figure 5.17. As we can see, the maximal field reaches 50 G, which is equivalent to 3.4 mK in temperature units. Therefore, the longitudinal static trap depth is comparable to the 3.1 mK one in the transverse direction, which leads to losses, as developed in part 5.3.2. Moreover, dynamical effects can appear in the transport direction, which make this small depth even more dangerous, especially at the entrance of the DN10 tube. Note that we saw another dangerous region at the end of the transport, where once again the overlapping is reduced since we leave the transport region (transport coils) to enter the science cell (final quadrupole coils), by passing through the metal-to-glass adapter of the science cell, of 5 mm radius.

We thus decided to increase the trap depth, by changing the aspect ratio ramp $A(x)$ of Figure 4.4 around $x = 8$ cm. The result for $A(x = 8\text{ cm}) = -0.5$ is shown in Figure 5.18. With this new ramp, the linear trap is doubled. This could finally solve the problem of efficiency in the differential pumping tube, between $x = 8$ cm and $x = 12$ cm. Actually, the two loss regions initially observed in Figure 5.7 were due to a combination of two simultaneous effects: a truncation on the walls of the transport, and a reduced trap depth along the transport, which is not directly controlled by the transport program (see part 4.1.1). We present the final results in following section 5.4.

5.4 Final results and evaporative cooling

In this section, we present the optimized results on transport efficiency, we characterize the lifetime in the final cell, and we show that the obtained numbers are reasonable to start evaporative cooling in the optically plugged magnetic trap for ^{40}K in one single

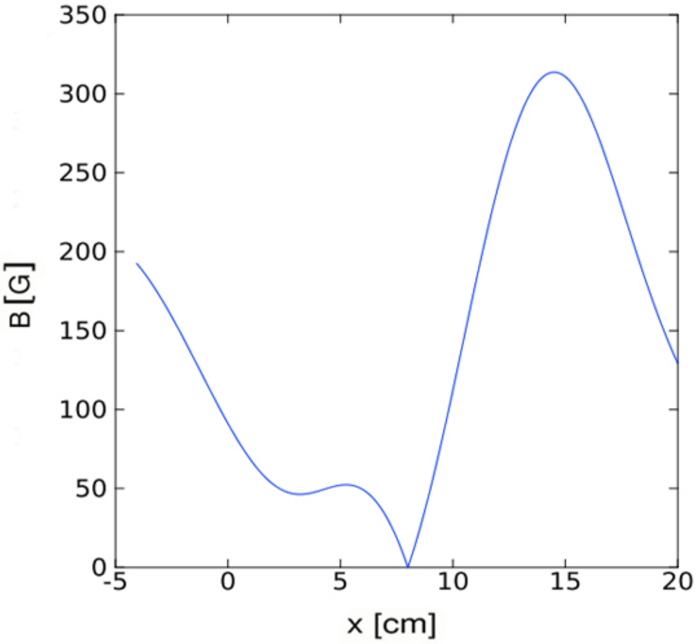

Figure 5.17: *Magnetic profile in the transport direction at $x = 8$ cm (old sequence).*

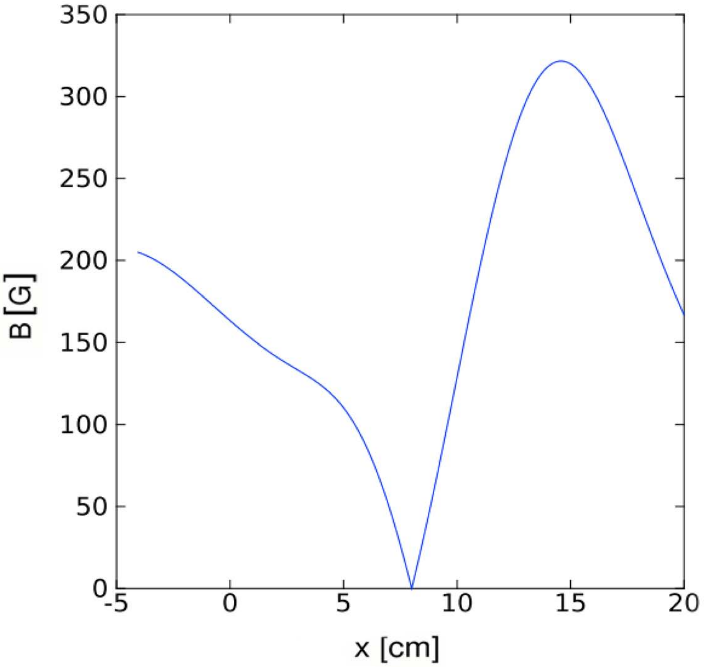

Figure 5.18: *Magnetic profile in the transport direction at $x = 8$ cm (new sequence).*

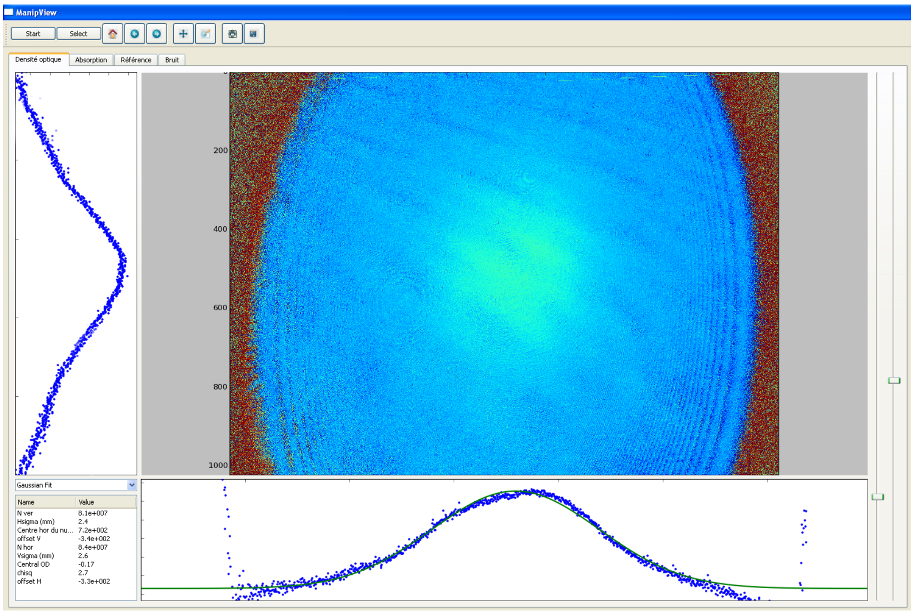

Name	Value
N ver	8.1e+007
Hsigma (mm)	2.4
Centre hor du nu...	7.2e+002
offset V	-3.4e+002
N hor	8.4e+007
Vsigma (mm)	2.6
Central OD	-0.17
chisq	2.7
offset H	-3.3e+002

Figure 5.19: *Screen capture of an absorption image (see part 2.2.2) of the first transported* ^{6}*Li cloud. The number of atoms equals* 8.3×10^7 *here.*

spin state, with sympathetic cooling of ^{6}Li.

5.4.1 Final results

We understood the losses in the tube (see Figure 5.11), and we reduced them by increasing the longitudinal trap depth (see part 5.3.4). In addition, we could magnetically trap and transport a double mixture of ^{6}Li-^{40}K.

For ^{40}K, we obtained a full efficiency (normalized with vacuum losses) of 80 %, as expected with our theoretical model for an initial temperature of 500 μK (see Figure 5.14). For the hotter ^{6}Li, we obtained a full efficiency (normalized with vacuum losses) of 30 %. An absorption picture of ^{6}Li in the science cell is shown in figure 5.19. Some improvement could be performed by reducing the initial temperature. However, in our scenario of evaporative cooling (see parts 3.4.3 and 5.4.2), the atom number of ^{6}Li is not critical since we plan to evaporate ^{40}K only.

The horizontal and vertical temperatures of the mixture in the science cell were measured to be $T_\mathrm{h} = 567$ μK and $T_\mathrm{v} = 500$ μK, and the lifetime was measured to be 30 s, as shown in Figure 5.20.

5.4.2 Starting evaporative cooling

The results presented in part 5.4.1 are reasonable to start evaporative cooling in the optically plugged quadrupole trap (see parts 3.4.2 and 3.4.3). In fact, let us consider $\sim 10^8$ atoms of each species, at ~ 500 μK, in the final quadrupole trap with an horizontal gradient of 110 G.cm^{-1}. According to part 3.4.3, we consider evaporative cooling of ^{40}K in one single spin state $|F = 9/2, m_F = 9/2\rangle$, through p-wave elastic

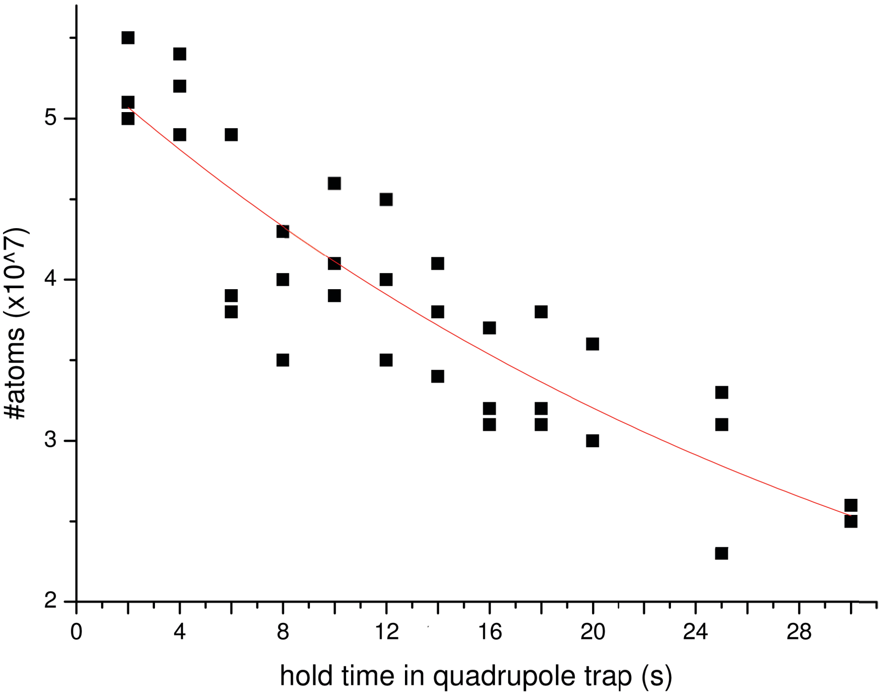

Figure 5.20: *Lifetime of* ^{6}*Li atoms in the final magnetic trap. The exponential fit (see part 2.3.4) gives a characteristic time of* ~ 30 *s.*

collisions.

Using equations 3.11 and 3.12, with $\sigma \approx 1.2 \times 10^{-11}$ cm^2 as obtained in part 3.3.3, we find an elastic collision rate of $\Gamma_{\rm el}^{\rm K} \approx 100$ s^{-1}. This is ~ 3000 times larger than the inelastic loss rate $\Gamma_{\rm in} = 1/30 \approx 0.03$ s^{-1}, measured in Figure 5.20. Thus, we can reasonably start the evaporative cooling of ^{40}K. According to equation 5.5, we find the evaporation rate shown in Figure 5.21. For a typical evaporation parameter $\eta = 4$, this gives an evaporation rate of $\Gamma_{\rm evap}(4) \approx 1.2$ s^{-1}.

The ^{6}Li atoms will be cooled done as well, through sympathetic cooling. In fact, the interspecies scattering length equals $a = 64\ a_0$ [122]. Then, using a similar calculation where $\sigma = 4\pi a^2$, we find an interspecies elastic collision rate of $\Gamma_{\rm el}^{\rm LiK} \approx 12$ s^{-1}, which is approximately ~ 400 times larger than $\Gamma_{\rm in}$.

Therefore, in principle, we could cool down typically 10^7 atoms of each species to a temperature of 50 μK, since for $\eta = 4$ we have $\delta N/N \sim \delta T/T$ [141]. Finally, this would be sufficient to load the high-power optical dipole trap presented in part 3.4.4.

We then started the evaporative cooling procedure and the alignment of the optical plug.

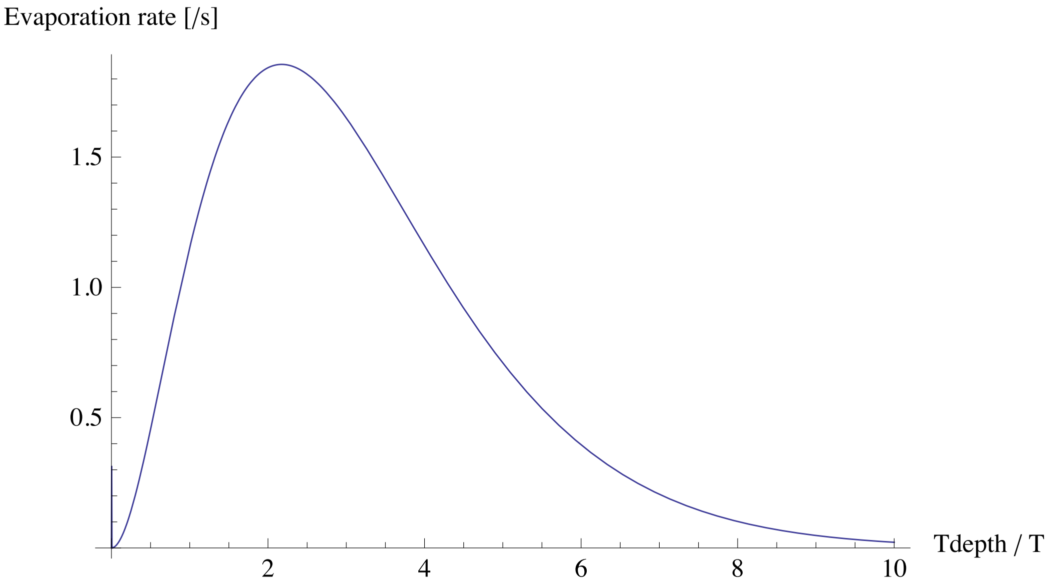

Figure 5.21: ^{40}K *evaporation rate in the final magnetic trap as a function of the evaporation parameter* $\eta = T_{depth}/T$ *(see equation 5.5). The evaporation rate is defined as the rate of atoms that reach an energy higher than the trap depth after an elastic collision. We consider* $\sim 10^8$ *atoms of* ^{40}K *in a single spin state* $|F = 9/2, mF = 9/2\rangle$*, at a temperature of* $\sim 500\ \mu K$*, in the final quadrupole with an horizontal gradient of* $110\ G.cm^{-1}$.

5.5 Summary

In this chapter, we presented the experimental characterization of our magnetic transport system, as well as its optimization based on an analytical model and a numerical simulation. With our results, we could start evaporative cooling of ^{40}K in one single spin state, and sympathetic cooling of ^{6}Li.

First, we checked that the currents and fields measured as functions of time were identical to the theoretical ones. After the hardware optimization, we could improve the overall efficiency by 10 %.

Then, we performed a round-trip experiment in order to probe the harmful regions of the transport, and we observed two critical regions: one after $x = 6$ cm and another one after $x = 8$ cm, leading to a ^{40}K transfer efficiency of 60 % at $x = 8$ cm, and 30 % at the elbow.

Using an analytical model of truncation of the atomic distribution on the transport tube, as well as a numerical simulation, we understood the experimental dependencies of the transfer efficiency on temperature, misalignment, and size of the tube. These studies allowed us to understand that the initial temperature in the transport was critical. We thus managed to reduce it to 500 μK in the initial transport trap of 67 G.cm^{-1} horizontal gradient, and we obtained the improved efficiencies of 90 % before $x = 8$ cm, and 40 % at the elbow. Then, we could fit the behavior of the efficiency inside the tube for different trap depths, with a good agreement. This showed that increasing the gradients would not help anymore. We then understood that some losses after $x = 8$ cm were due to the longitudinal trap depth of 3.4 mK. We could increase this trap depth by changing the magnetic aspect ratio to $b_x/b_z = -0.5$ at this point.

After optimization, we transported efficiently the double mixture of ^{6}Li-^{40}K. For ^{40}K, we obtained a full efficiency (normalized with vacuum losses) of 80 %, as expected with our theoretical model for an initial temperature of 500 μK. For the hotter ^{6}Li, we obtained a full efficiency (normalized with vacuum losses) of 30 %, which is large enough since we evaporate only ^{40}K in our evaporative cooling scenario.

Finally, the lifetime in the science cell was measured to be 30 s. Therefore, we started evaporative cooling of ^{40}K in one single spin state, since the associated elastic collision rate $\Gamma_{\mathrm{el}}^{\mathrm{K}} \approx 100\ \mathrm{s}^{-1}$ is ~ 3000 times larger than the inelastic loss rate due to vacuum losses. The ^{6}Li atoms can be cooled down as well by sympathetic cooling, since the interspecies collision rate is ~ 400 times larger than the inelastic loss rate.

Conclusion

During this thesis work, we designed and assembled from scratch a complete experimental setup allowing to produce, control and study ultracold imbalanced atomic Fermi mixtures of ^{6}Li and ^{40}K.

We built an ultra-high vacuum chamber, with a residual pressure inferior to 10^{-11} mbar in the final cell. We prepared a powerful laser system giving typical powers of 500 mW for each species, at several stabilized frequencies, and we designed two performing atomic sources: a ^{6}Li Zeeman slower, with a loading rate in the MOT of 1.2×10^9 atoms.s^{-1}, and a ^{40}K 2D-MOT, with a large loading rate in the MOT of 1.4×10^9 atoms.s^{-1}.

Using this system, we could load a performing double MOT of ^{6}Li-^{40}K. We obtained 8.9×10^9 ^{40}K atoms at a temperature of 290 μK with a central density of 3×10^{10} atoms.cm^{-3}, and 5.4×10^9 ^{6}Li atoms at a temperature of 1.4 mK with a central density of 2×10^{10} atoms.cm^{-3}. In the double MOT configuration, we obtained 8×10^9 atoms of ^{40}K and 5×10^9 atoms of ^{6}Li. Those values were optimized by reducing the inelastic losses through a Dark MOT scheme.

In this MOT, we produced the first homonuclear ^{40}K^{40}K* and heteronuclear ^{6}Li^{40}K* molecules. This allowed to measure the linewidth of the $4p$ atomic state of ^{40}K, that was found to be $\Gamma/(2\pi) = 6.136 \pm 0.017$ MHz, which is close from the value obtained by Wang et al. [106]. It also allowed to assign precisely five series of ^{6}Li^{40}K* rovibrational lines, which opens the way to future photoassociation of polar ^{6}Li^{40}K molecules in their electronic ground-sate. This is of strong interest in the study of dipolar gases.

Using a Cold MOT scheme, we could compress the ^{40}K MOT cloud to a density of 5×10^{10} atoms.cm^{-3}, and cool it further to 200 μK, with 100 % efficiency. Then, we optically pumped it into the $|F = 9/2, m_F = 9/2\rangle$ state, with 100 % efficiency. Using a CMOT scheme, we could compress the ^{6}Li MOT cloud to a density of 3.5×10^{10} atoms.cm^{-3}, and cool it further to 1 mK, with a 100 % efficiency. Then, we optically pumped it into the $|F = 3/2, m_F = 3/2\rangle$ state, with 30 % efficiency. After those preliminary stages, we loaded the single-species magnetic traps, with an axial magnetic gradient of 85 G.cm^{-1}, and we obtained typically 10^9 atoms in each case, after 1 s of trapping. With our biggest MOT we could even reach the value of 3×10^9 for ^{40}K. The temperatures were measured to be 400 μK for ^{40}K, and 1.3 mK for ^{6}Li. The thermalization time of ^{40}K was found to be of the order of 1 s, leading to an estimated p-wave cross-section, $\sigma_{\mathrm{KK}} = 1.2 \times 10^{-11}$ cm^2, close to the value obtained at JILA [116].

In parallel, we designed, assembled an studied a complete magnetic transport system allowing to move the magnetically trapped cloud to a region of ultra-high vacuum, and large optical access. Its efficiency could be calculated, measured and optimized, leading to a performing simultaneous transfer of the mixture in the science cell. For ^{40}K, we obtained a full efficiency (normalized with vacuum losses) of 80 %, as expected with our theoretical model for an initial temperature of 500 μK. For the hotter ^{6}Li, we obtained a full efficiency (normalized with vacuum losses) of 30 %, which is large enough since we evaporate only ^{40}K in our evaporative cooling scenario. In the final trap, the lifetime equals 30 s, which is sufficient to enable evaporative cooling in an optically plugged magnetic trap for ^{40}K in one single spin state, and sympathetic cooling of ^{6}Li.

The forthcoming stages have been prepared as well. They consist of an optically plugged magnetic trap in the science cell and an optical dipole trap, where quantum degeneracy will be reached. In addition, we developed a high-resolution imaging scheme involving a 404 nm ^{40}K transition, and we designed the Feshbach coils.

At the end of my PhD, everything is ready to perform an efficient evaporative cooling of the mixture. Actually, the evaporation has been initiated in the final quadrupole trap and the fine alignment of the optical plug is in progress. Therefore, our group shall cool down soon a ^{6}Li-^{40}K mixture with large numbers of atoms to quantum degeneracy in an optical dipole trap, and study further ultracold Fermi mixtures in bulk or in optical lattices.

In close future, the Cooper pairing mechanism [25] and the BEC-BCS cross-over [36, 38] could be studied in presence of mass imbalance, the thermodynamics [42, 43] of the ultracold Fermi mixture could be explored as well, and we could investigate the universal properties of a Fermi mixture in low and mixed dimensions [51].

Appendix A

A.1 Atomic data

Physical quantity	^{40}K	^{6}Li
m [u]	39.96	6.02
λ_{sp} [nm]	767	671
$\Gamma/(2\pi)$ [MHz]	6.04	5.87
I_{sat} [mW.cm^{-2}]	1.75	2.54

Potassium has one stable fermionic isotope ^{40}K (0.012 %), and two stable bosonic isotopes ^{39}K (93.258 %) and ^{41}K (6.730 %). Lithium has one stable fermionic isotope ^{6}Li (7.42 %), and one stable bosonic isotope ^{7}Li (92.58 %).

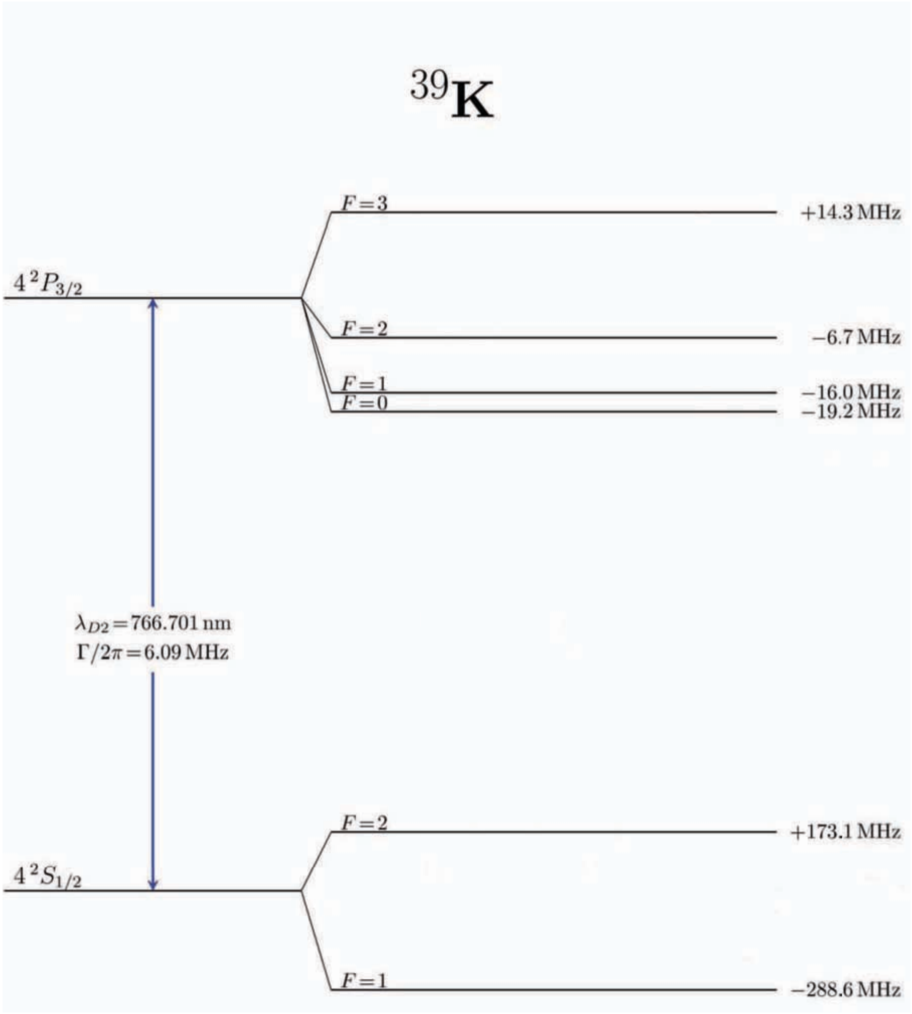

Figure A.1: *Hyperfine structure of the* ^{39}K *D2 line.*

A.2 Magnetic field of a current loop

Let us consider a single current loop with axis z, radius a and current I. By cylindical symetry the orthoradial field is null. The axial and radial ones are given everywhere by the first and second order elliptical functions, K and E:

$$\begin{cases} B_r = \frac{\gamma B_0}{\pi\sqrt{Q}}\left[\frac{1+\alpha^2+\beta^2}{Q-4\alpha}\mathrm{E}(k) - \mathrm{K}(k)\right] \ , \\ B_z = \frac{B_0}{\pi\sqrt{Q}}\left[\frac{1-\alpha^2-\beta^2}{Q-4\alpha}\mathrm{E}(k) + \mathrm{K}(k)\right] \ , \end{cases}$$

with the following definitions:

$$\begin{cases} B_0 = \frac{\mu_0 I}{2a} \ , \\ \alpha = \frac{r}{a} \ , \\ \beta = \frac{z}{a} \ , \\ \gamma = \frac{z}{r} \ , \\ Q = \left[(1+\alpha)^2 + \beta^2\right] \ , \\ k = \sqrt{\frac{4\alpha}{Q}} \ . \end{cases}$$

A.3 Transport routine

This appendix shows a sample of the Mathematica transport code. It is in fact the matrix inversion of the system 4.1 that calculates the currents from the constraints. All the mechanical information on the coils (thread diameter, number of turns, number of layers, inner and outer radius...) is saved in the *bob*$[i, j]$ matrix, where i is the pair index and j the data index. This data can be found in appendix A.5. *br*, *gbr* and *gbz* are the x-field, x-gradient and z-gradient per unit of current. They follow the formulas given in appendix A.2. *gby* and *asp* are the y-gradient and aspect ratio constraints. And the IF loop is the incrementation procedure when a current reaches zero.

```
Do[mat = {Table[Sum[br[xm - bob[[j, 1]],
      0 - bob[[j, 2]] - (k - 1) * bob[[j, 7]], bob[[j, 6]] + bob[[j, 3]] / 2 + i * bob[[j, 3]]],
     {i, 0, bob[[j, 4]] - 1}, {k, 1, bob[[j, 5]]}], {j, l - 2, l}],
   (Table[Sum[gbr[xm - bob[[j, 1]], 0 - bob[[j, 2]] - (k - 1) * bob[[j, 7]],
        bob[[j, 6]] + bob[[j, 3]] / 2 + i * bob[[j, 3]]],
       {i, 0, bob[[j, 4]] - 1}, {k, 1, bob[[j, 5]]}], {j, l - 2, l}]) -
    asp[xm] (Table[Sum[gbz[xm - bob[[j, 1]], 0 - bob[[j, 2]] - (k - 1) * bob[[j, 7]],
         bob[[j, 6]] + bob[[j, 3]] / 2 + i * bob[[j, 3]]],
        {i, 0, bob[[j, 4]] - 1}, {k, 1, bob[[j, 5]]}], {j, l - 2, l}]),
   -Table[Sum[gbr[xm - bob[[j, 1]], 0 - bob[[j, 2]] - (k - 1) * bob[[j, 7]],
        bob[[j, 6]] + bob[[j, 3]] / 2 + i * bob[[j, 3]]],
       {i, 0, bob[[j, 4]] - 1}, {k, 1, bob[[j, 5]]}], {j, l - 2, l}] -
    Table[Sum[gbz[xm - bob[[j, 1]], 0. - bob[[j, 2]] - (k - 1) * bob[[j, 7]],
       bob[[j, 6]] + bob[[j, 3]] / 2 + i * bob[[j, 3]]],
      {i, 0, bob[[j, 4]] - 1}, {k, 1, bob[[j, 5]]}], {j, l - 2, l}]};
 courantco =  Inverse[mat].{0, 0, gby[xm]};
 If[courantco[[1]] < 0.5, l = l + 1;
  mat = {Table[Sum[br[xm - bob[[j, 1]], 0 - bob[[j, 2]] - (k - 1) * bob[[j, 7]],
       bob[[j, 6]] + bob[[j, 3]] / 2 + i * bob[[j, 3]]],
      {i, 0, bob[[j, 4]] - 1}, {k, 1, bob[[j, 5]]}], {j, l - 2, l}],
    (Table[Sum[gbr[xm - bob[[j, 1]], 0 - bob[[j, 2]] - (k - 1) * bob[[j, 7]],
         bob[[j, 6]] + bob[[j, 3]] / 2 + i * bob[[j, 3]]],
        {i, 0, bob[[j, 4]] - 1}, {k, 1, bob[[j, 5]]}], {j, l - 2, l}]) -
     asp[xm] (Table[Sum[gbz[xm - bob[[j, 1]], 0 - bob[[j, 2]] - (k - 1) * bob[[j, 7]],
          bob[[j, 6]] + bob[[j, 3]] / 2 + i * bob[[j, 3]]],
         {i, 0, bob[[j, 4]] - 1}, {k, 1, bob[[j, 5]]}], {j, l - 2, l}]),
    -Table[Sum[gbr[xm - bob[[j, 1]], 0 - bob[[j, 2]] - (k - 1) * bob[[j, 7]],
         bob[[j, 6]] + bob[[j, 3]] / 2 + i * bob[[j, 3]]],
        {i, 0, bob[[j, 4]] - 1}, {k, 1, bob[[j, 5]]}], {j, l - 2, l}] -
     Table[Sum[gbz[xm - bob[[j, 1]], 0. - bob[[j, 2]] - (k - 1) * bob[[j, 7]],
        bob[[j, 6]] + bob[[j, 3]] / 2 + i * bob[[j, 3]]],
       {i, 0, bob[[j, 4]] - 1}, {k, 1, bob[[j, 5]]}], {j, l - 2, l}]};
  courantco =  Inverse[mat].{0, 0, gby[xm]}];
 vect = {0, 0, 0, 0, 0, 0, 0, 0};
 vect[[l - 1]] = courantco[[1]];
 vect[[l]] = courantco[[2]];
 vect[[l + 1]] = courantco[[3]];
 courant = Join[courant, {Join[{xm}, vect]}],
 {xm, Lt1 + 0.0000001, La1, pas}]
```

Figure A.2: *Sample of Mathematica transport code.*

A.4 Adiabatic invariant of the quadrupole trap

For a single atom with mass m and magnetic moment μ, in a magnetic quadrupole trap of gradient $\boldsymbol{b}$, the density of energy ρ is given by:

$$\rho(\epsilon) = \int\int \frac{d\boldsymbol{p}d\boldsymbol{r}}{h^3}\, \delta\left(\epsilon - \frac{\boldsymbol{p}^2}{2m} - \mu\sqrt{\sum_i b_i^2 r_i^2}\right) = B\frac{\epsilon^{7/2}}{|b_x b_y b_z|} \ ,$$

where the b_i are the three components of the gradient and B a constant number. At temperature T, the monoatomic partition function z can be written as:

$$z = \int d\epsilon \rho(\epsilon) e^{-\epsilon/k_{\mathrm{B}}T} = C\frac{T^{9/2}}{|b_x b_y b_z|} \ ,$$

where C is another constant number. For N atoms of an ideal gas, and for a low enough phase-space density, one can approximate the total partition function Z as:

$$Z \approx \frac{z^N}{N!} \ .$$

We can then deduce the free energy F:

$$F(N, T, \{b_i\}) = -k_{\mathrm{B}}T \ln Z = -Nk_{\mathrm{B}}T \ln\left(\frac{CT^{9/2}}{|b_x b_y b_z|}\right) + k_{\mathrm{B}}T \ln(N!) \ ,$$

and the entropy S:

$$\frac{S}{Nk_{\mathrm{B}}} = -\frac{1}{Nk_{\mathrm{B}}}\left(\frac{\partial F}{\partial T}\right)_{N,\{b_i\}} = \frac{9}{2} + \ln C - \frac{1}{N}\ln(N!) + \ln\left(\frac{T^{9/2}}{|b_x b_y b_z|}\right) \ .$$

Assuming $S = \mathrm{cte}$ and $N = \mathrm{cte}$, we obtain the adiabatic invariant:

$$\frac{T}{|b_x b_y b_z|^{2/9}} = \mathrm{cte} = \frac{T^0}{|b_x^0 b_y^0 b_z^0|^{2/9}} \ .$$

A.5 Mechanical parameters of the transport

Parameter	Value
number of layers pushing coils	8
number of layers MOT coils	6
number of layers transport and neighbour coils	2
number of layers quadrupole coils	4
number of turns per layer pushing coil	4
number of turns per layer MOT coils	14
number of turns per layer transport coils	47
number of turns per layer neighbour coils	34
number of turns per layer quadrupole coils	19
thread diameter pushing coil	0.21 cm
thread diameter MOT and quadrupole coils	0.42 cm
thread section transport and neighbour coils	0.27×0.12 cm^2
MOT chamber radius	8.70 cm
MOT chamber height	7.00 cm
Pushing coil inner radius	4.59 cm
Pushing coil outer radius	5.44 cm
MOT coils inner radius	3.25 cm
MOT coils outer radius	9.29 cm
transport and neighbour coils inner radius	1.14 cm
transport coils outer radius	6.63 cm
neighbour coils outer radius	5.08 cm
quadrupole coils inner radius	6.75 cm
quadrupole coils outer radius	9.75 cm
distance between edge of MOT chamber and center of transport coils	2.00 cm
distance between edge of MOT chamber and first pushing loop	1.05 cm
L_1	6.80 cm
L_2	12.00 cm
L_3	30.95 cm
L_4	64.70 cm

A.6 Engineering drawings

The Catia files of the mountings are kept by engineer Jean-Michel Isac, from the workshop of Laboratoire Kastler Brossel at ENS. Here are the most useful plans.

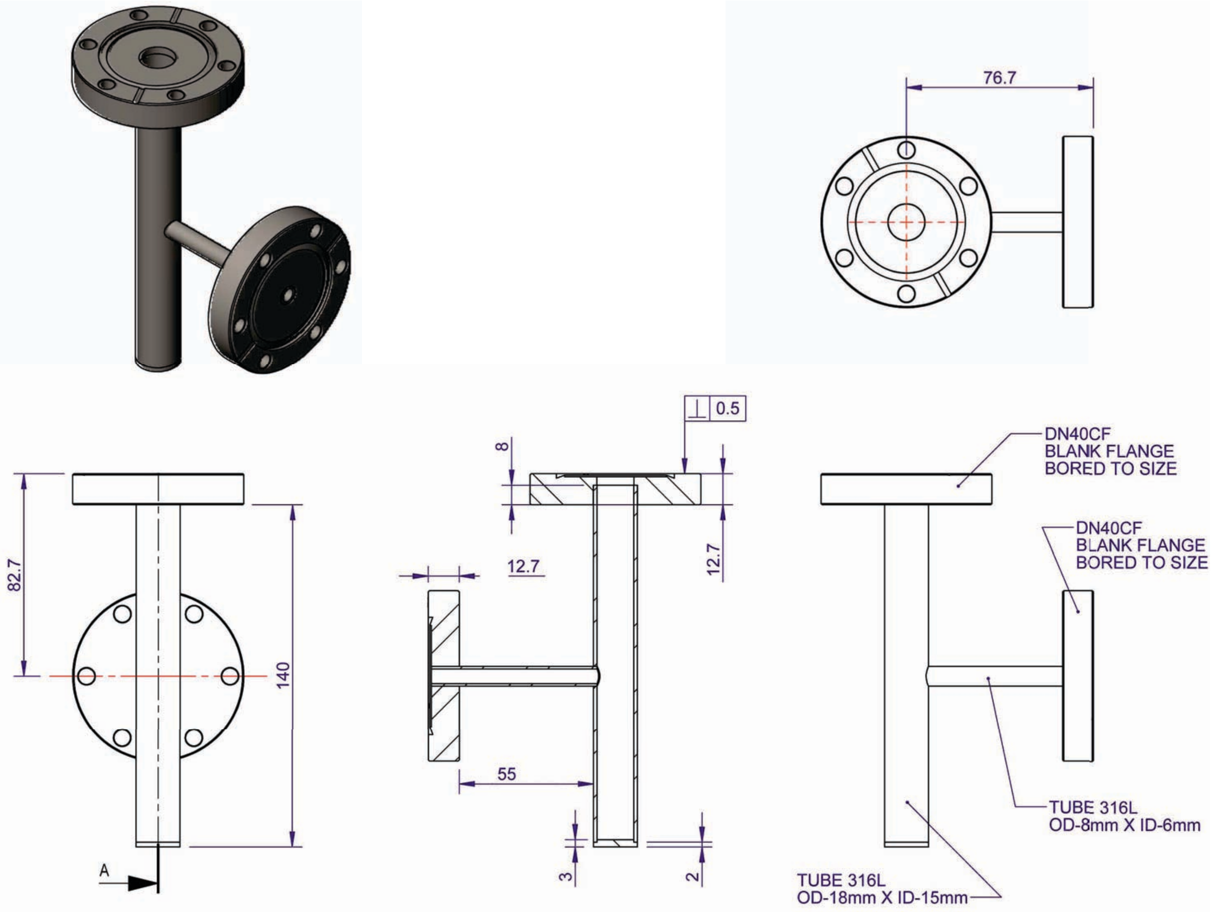

Figure A.3: ^{6}*Li oven (dimensions in millimeters).*

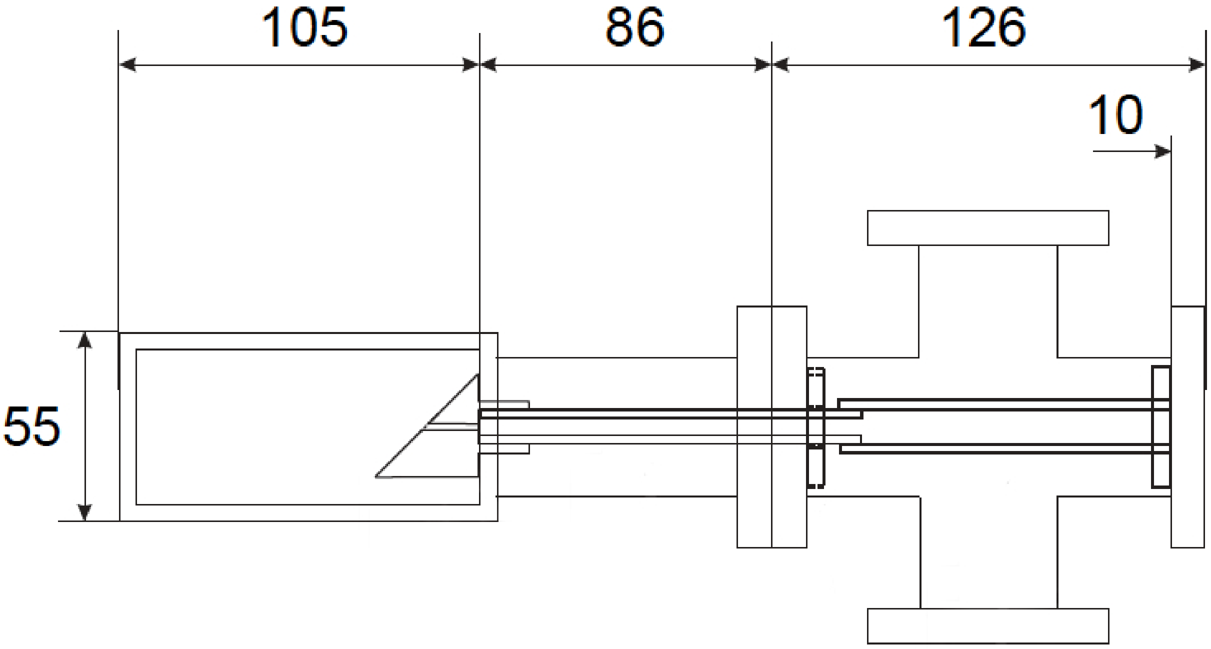

Figure A.4: *2D-MOT chamber with differential pumping tube inside (dimensions in millimeters). The differential pumping tube consists of three joined pipes: the cylinder hole in the mirror of 2 mm diameter and 20 mm length, a tube of 5 mm diameter and 116 mm length, and a tube of 10 mm diameter and 86 mm length.*

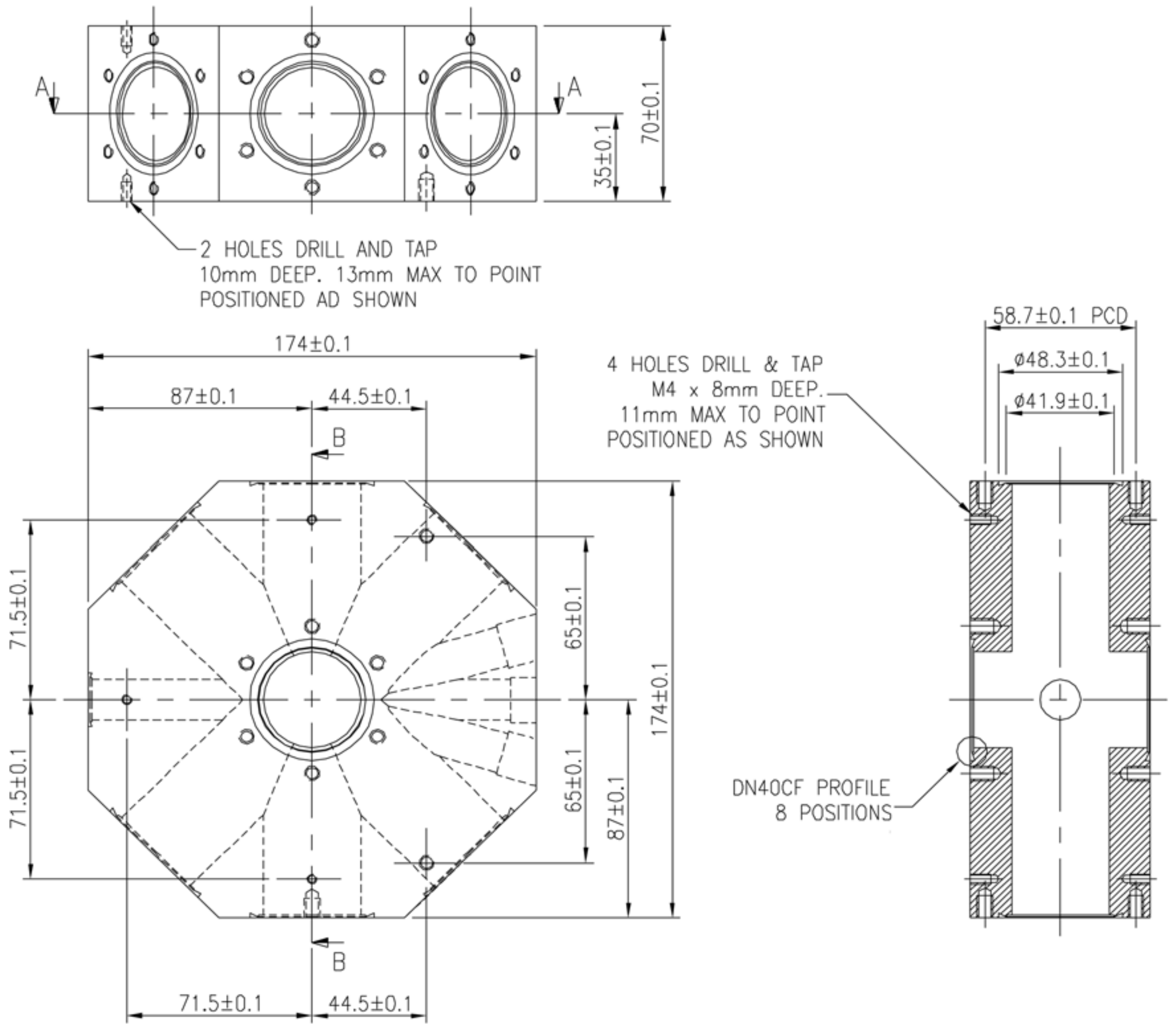

Figure A.5: *Octagonal MOT chamber (dimensions in millimeters).*

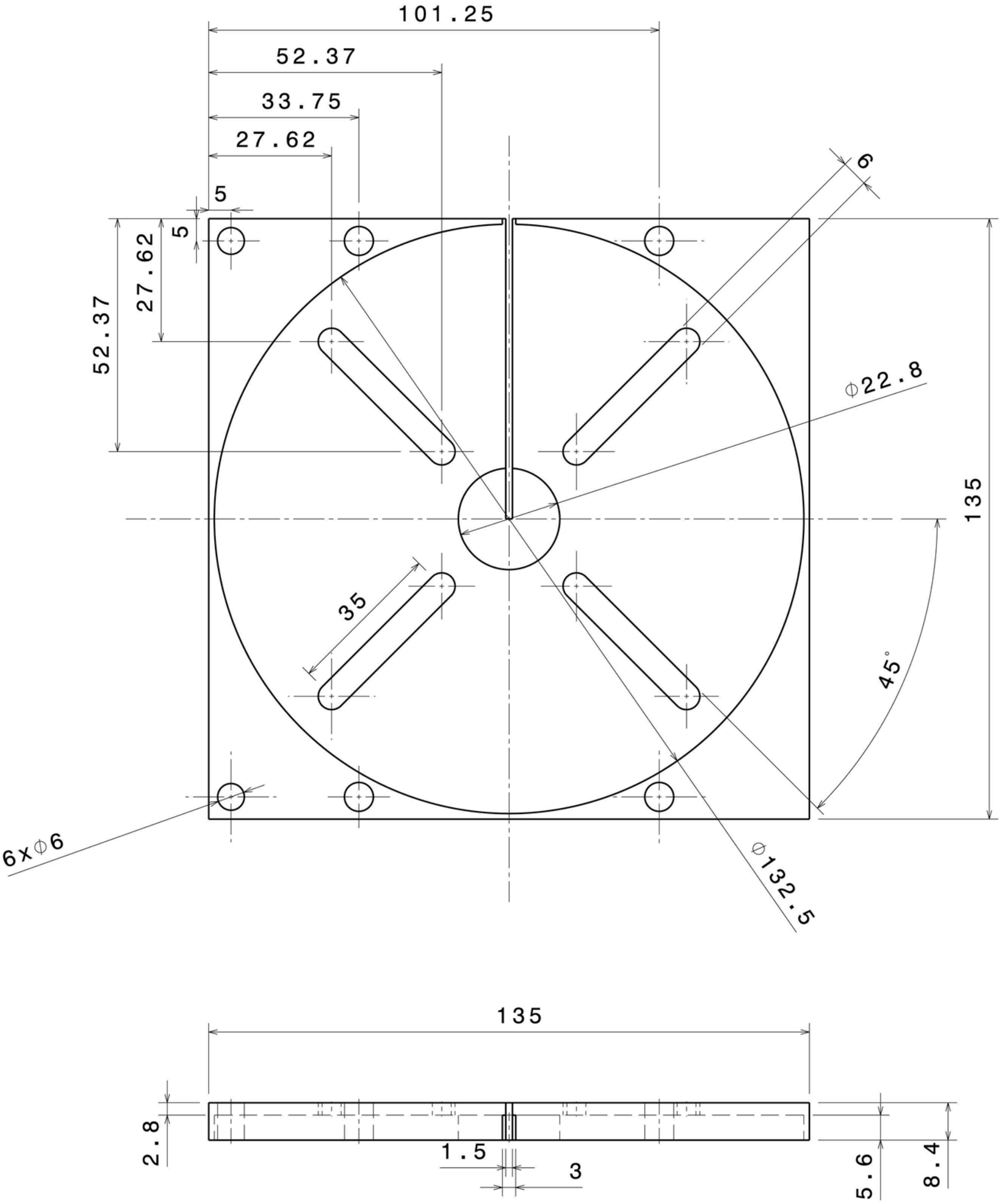

Figure A.6: *Mount of a transport coil (dimensions in millimeters).*

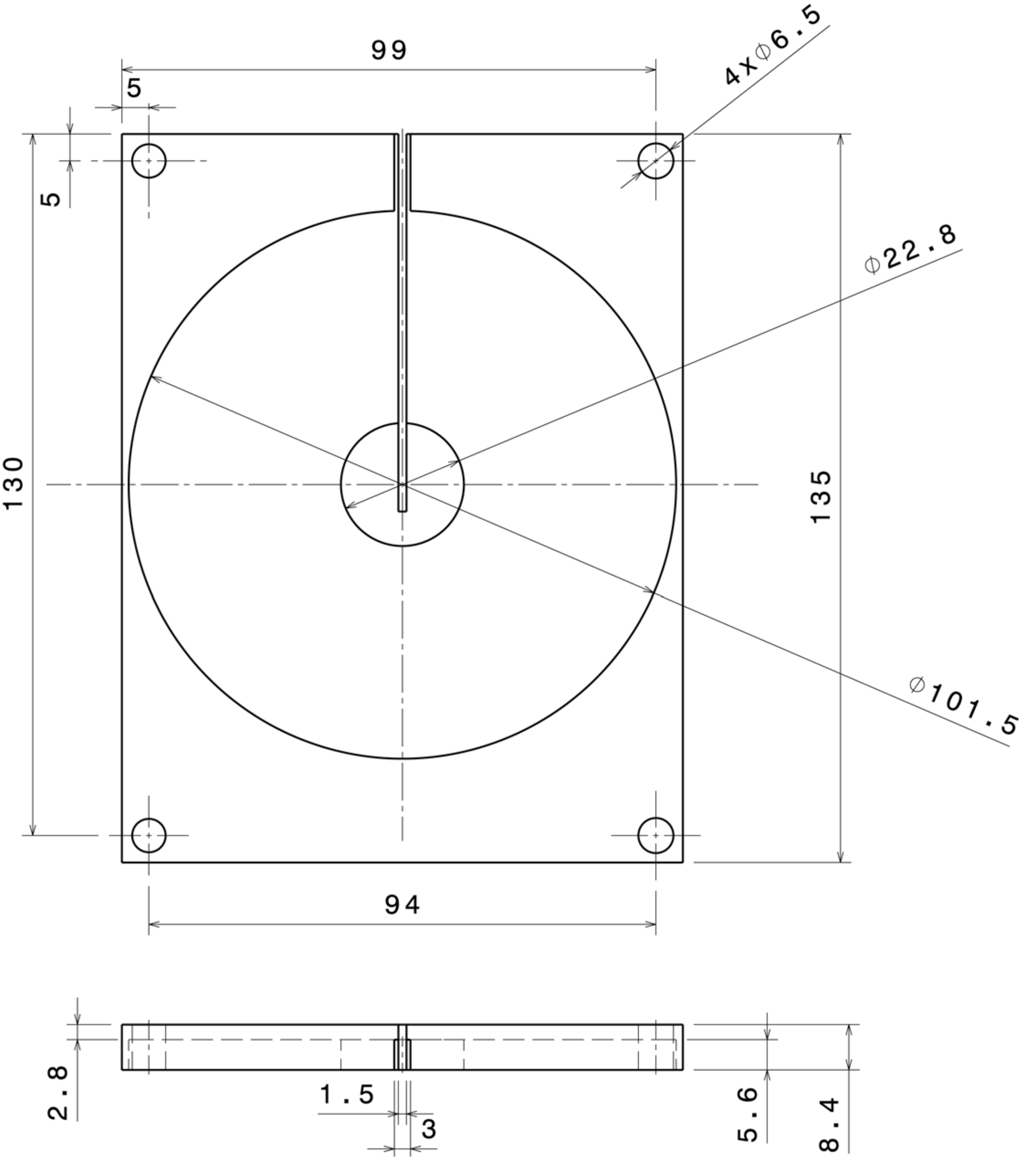

Figure A.7: *Mount of a neighbor coil (dimensions in millimeters).*

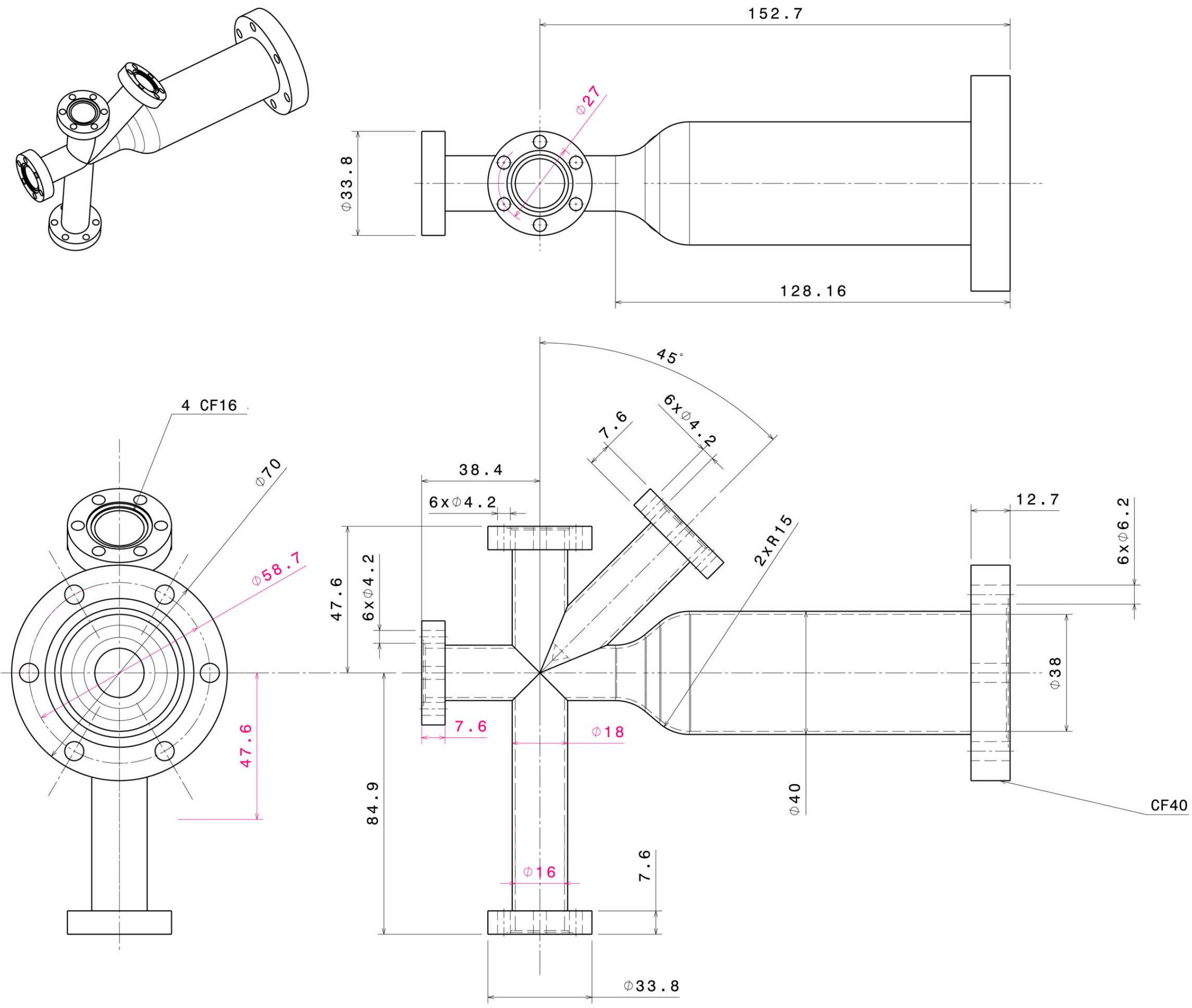

Figure A.8: *Transport elbow cross (dimensions in millimeters).*

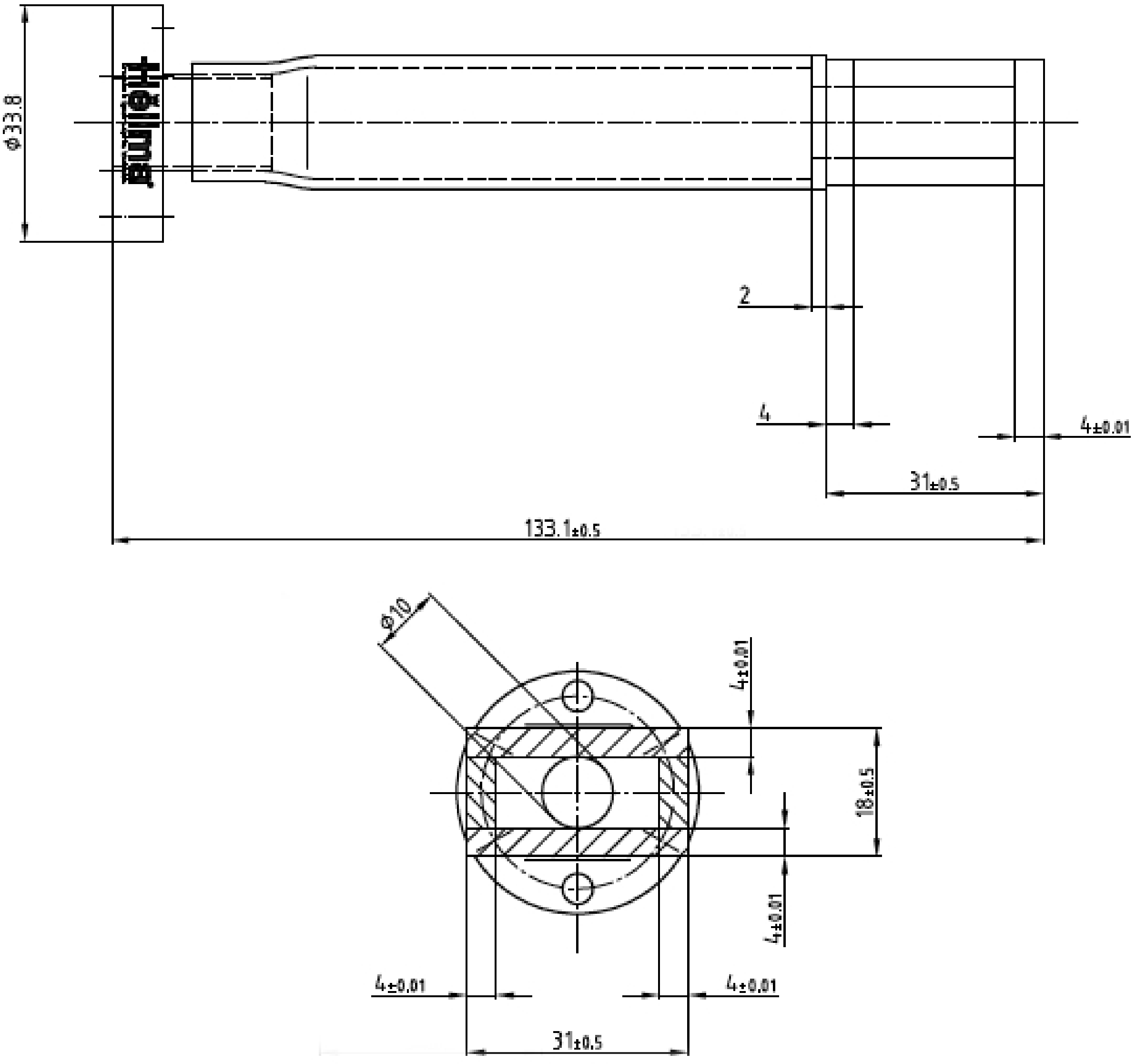

Figure A.9: *Hellma science cell (dimensions in millimeters).*

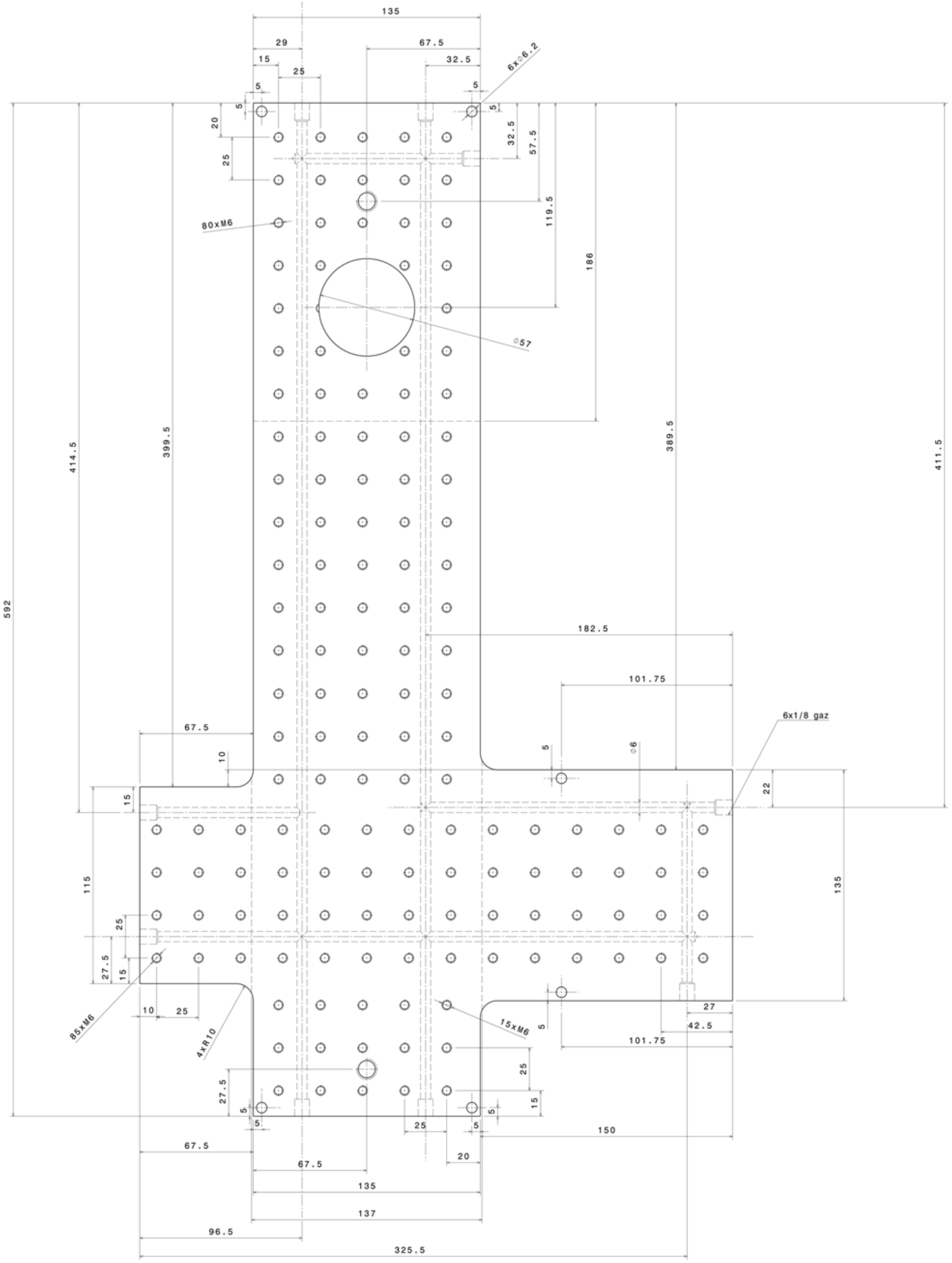

Figure A.10: *Transport cooling plate (dimensions in millimeters).*

Bibliography

[1] R. P. Feynman. Simulating physics with computers. *Int. Jour. Theo. Phys.*, **21** 467, 1982. 3, 17

[2] PHENIX Collaboration. Flow measurements via two-particle azimuthal correlations in Au+Au collisions at $\sqrt{S_{NN}} = 130$ GeV. *Phys. Rev. Lett.*, **89** 212301, 2002. 17

[3] D. Jaksch and P. Zoller. The cold atom Hubbard toolbox. *Annals of Physics*, **315** 52, 2005. 17

[4] M. Greiner, O. Mandel, T. Esslinger, T. W. Hänsch, and I. Bloch. Quantum phase transition from a superfluid to a Mott insulator in a gas of ultracold atoms. *Nature*, **415** 39, 2002. 17, 19

[5] R. Jördens, N. Strohmaier, K. Günter, H. Moritz, and T. Esslinger. A Mott insulator of fermionic atoms in an optical lattice. *Nature*, **455** 204, 2008. 17, 20

[6] S. Bose. Plancks Gesetz und Lichtquantenhypothese. *Zeitschrift für Physik*, **26** 178, 1924. 19

[7] A. Einstein. Quantentheorie des idealen einatomigen Gases. *Sitzungsber. Preuss. Akad. Wiss.*, **3** 18, 1925. 19

[8] P. Kapitza. Viscosity of liquid helium below the λ-point. *Nature*, **141** 3558, 1938. 19

[9] M. H. Anderson, J. R. Ensher, M. R. Matthews, C. E. Wieman, and E. A. Cornell. Observation of Bose-Einstein condensation in a dilute atomic vapor. *Science*, **269** 198, 1995. 19, 62, 109

[10] C. C. Bradley, C. A. Sackett, J. J. Tollett, and R. G. Hulet. Observation of Bose-Einstein condensation in a dilute atomic vapor. *Phys. Rev. Lett.*, **75** 1687, 1995. 19

[11] K. B. Davis, M.-O. Mewes, M. A. Joffe, M. R. Andrews, and W. Ketterle. Evaporative cooling of sodium atoms. *Phys. Rev. Lett.*, **74** 5202, 1995. 19, 109, 110

[12] M. R. Andrews, C. G. Townsend, H.-J. Miesner, D. S. Durfee, D. M. Kurn, and W. Ketterle. Observation of interference between two Bose condensates. *Science*, **275** 637, 1997. 19

[13] K. W. Madison, F. Chevy, W. Wohlleben, and J. Dalibard. Vortex formation in a stirred Bose-Einstein condensate. *Phys. Rev. Lett.*, **84** 806, 2000. 19

[14] S. Burger, K. Bongs, S. Dettmer, W. Ertmer, K. Sengstock, A. Sanpera, G. V. Shlyapnikov, and M. Lewenstein. Dark solitons in Bose-Einstein condensates. *Phys. Rev. Lett.*, **83** 5198, 1999. 19

[15] L. Khaykovich, F. Schreck, G. Ferrari, T. Bourdel, J. Cubizolles, L. D. Carr, Y. Castin, and C. Salomon. Formation of a matter-wave bright soliton. *Science*, **296** 1290, 2002. 19

[16] J. Billy, V. Josse, Z. Zuo, A. Bernard, B. Hambrecht, P. Lugan, D. Clément, L. Sanchez-Palencia, P. Bouyer, and A. Aspect. Direct observation of Anderson localization of matter waves in a controlled disorder. *Nature*, **453** 891, 2008. 19

[17] G. Roati, C. D'Errico, L. Fallani, M. Fattori, C. Fort, M. Zaccanti, G. Modugno, M. Modugno, and M. Inguscio. Anderson localization of a non-interacting Bose-Einstein condensate. *Nature*, **453** 895, 2008. 19

[18] H. Feshbach. Unified theory of nuclear reactions. *Ann. Phys.*, **5** 357, 1958. 19, 20, 109

[19] S. Inouye, M. R. Andrews, J. Stenger, H.-J. Miesner, D. M. Stamper-Kurn, and W. Ketterle. Observation of Feshbach resonances in a BoseĐEinstein condensate. *Nature*, **392** 151, 1998. 19

[20] B. De Marco and D. S. Jin. Onset of Fermi degeneracy in a trapped atomic gas. *Science*, **285** 1703, 1999. 19, 110

[21] B. DeMarco, S. B. Papp, and D. S. Jin. Pauli blocking of collisions in a quantum degenerate atomic fermi gas. *Phys. Rev. Lett.*, **86** 5409, 2001. 19, 110

[22] F. Schreck, G. Ferrari, K. L. Corwin, J. Cubizolles, L. Khaykovich, M.-O. Mewes, and C. Salomon. Sympathetic cooling of bosonic and fermionic lithium gases towards quantum degeneracy. *Phys. Rev. A*, **64** 011402(R), 2001. 19, 97, 100

[23] A. G. Truscott, K. E. Strecker, W. I. McAlexander, G. B. Partridge, and R. G. Hulet. Observation of Fermi pressure in a gas of trapped atoms. *Science*, **291** 2570, 2001. 20

[24] H. Kamerlingh Onnes. On the sudden change in the rate at which the resistance of mercury disappears. *Comm. Phys. Lab. Univ. Leiden*, **124c**, 1911. 20

[25] J. Bardeen, L. N. Cooper, and J. R. Schrieffer. Theory of superconductivity. *Phys. Rev.*, **108** 1175, 1957. 20, 176

[26] D. D. Osheroff, R. C. Richardson, and D. M. Lee. Evidence for a new phase of solid ^{3}He. *Phys. Rev. Lett.*, **28** 885, 1972. 20

[27] S. Jochim, M. Bartenstein, A. Altmeyer, G. Hendl, C. Chin, J. Hecker Denschlag, and R. Grimm. Pure gas of optically trapped molecules created from fermionic atoms. *Phys. Rev. Lett.*, **91** 240402, 2003. 20

[28] C. A. Regal, C. Ticknor, J. L. Bohn, and D. S. Jin. Tuning p-wave interactions in an ultracold Fermi gas of atoms. *Phys. Rev. Lett.*, **90** 053201, 2003. 20

[29] J. Cubizolles, T. Bourdel, S. J. J. M. F. Kokkelmans, G. V. Shlyapnikov, and C. Salomon. Production of long-lived ultracold Li_2 molecules from a Fermi gas. *Phys. Rev. Lett.*, **91** 240401, 2003. 20

[30] K. E. Strecker, G. B. Partridge, and R. G. Hulet. Conversion of an atomic Fermi gas to a long-lived molecular Bose gas. *Phys. Rev. Lett.*, **91** 080406, 2003. 20

[31] D. S. Petrov, C. Salomon, and G. V. Shlyapnikov. Weakly bound dimers of fermionic atoms. *Phys. Rev. Lett.*, **93** 090404, 2004. 20

[32] M. W. Zwierlein, C. A. Stan, C. H. Schunck, S. M. F. Raupach, S. Gupta, Z. Hadzibabic, and W. Ketterle. Observation of Bose-Einstein condensation of molecules. *Phys. Rev. Lett.*, **91** 250401, 2003. 20

[33] M. Greiner, C. A. Regal, and D. S. Jin. Emergence of a molecular Bose-Einstein condensate from a Fermi gas. *Nature*, **426** 537, 2003. 20

[34] C. A. Regal, M. Greiner, and D. S. Jin. Observation of resonance condensation of fermionic atom pairs. *Phys. Rev. Lett.*, **92** 040403, 2004. 20

[35] M. W. Zwierlein, C. A. Stan, C. H. Schunck, S. M. F. Raupach, A. J. Kerman, and W. Ketterle. Condensation of pairs of fermionic atoms near a Feshbach resonance. *Phys. Rev. Lett.*, **92** 120403, 2004. 20

[36] T. Bourdel, L. Khaykovich, J. Cubizolles, J. Zhang, F. Chevy, M. Teichmann, L. Tarruell, S. J. J. M. F. Kokkelmans, and C. Salomon. Experimental study of the BEC-BCS crossover region in lithium 6. *Phys. Rev. Lett.*, **93** 050401, 2004. 20, 176

[37] M. W. Zwierlein, J. R. Abo-Shaeer, A. Schirotzek, C. H. Schunck, and W. Ketterle. Vortices and superfluidity in a strongly interacting Fermi gas. *Nature*, **435** 1047, 2005. 20

[38] M. Bartenstein, A. Altmeyer, S. Riedl, S. Jochim, C. Chin, J. Hecker Denschlag, and R. Grimm. Crossover from a molecular Bose-Einstein condensate to a degenerate Fermi gas. *Phys. Rev. Lett.*, **92** 120401, 2004. 20, 176

[39] J. Joseph, B. Clancy, L. Luo, J. Kinast, A. Turlapov, and J. E. Thomas. Measurement of sound velocity in a fermi gas near a feshbach resonance. *Phys. Rev. Lett.*, **98** 170401, 2007. 20

[40] D. E. Miller, J. K. Chin, C. A. Stan, Y. Liu, W. Setiawan, C. Sanner, and W. Ketterle. Critical velocity for superfluid flow across the BEC-BCS crossover. *Phys. Rev. Lett.*, **99** 070402, 2007. 20

[41] U. Schneider, L. Hackermüller, S. Will, T. Best, I. Bloch, T. A. Costi, R. W. Helmes, D. Rasch, and A. Rosch. Metallic and insulating phases of repulsively interacting fermions in a 3D optical lattice. *Science*, **322** 1520, 2008. 20

[42] S. Nascimbène, N. Navon, K. J. Jiang, F. Chevy, and C. Salomon. Exploring the thermodynamics of a universal Fermi gas. *Nature*, **463** 1057, 2010. 20, 176

[43] N. Navon, S. Nascimbène, F. Chevy, and C. Salomon. The equation of state of a low-temperature Fermi gas with tunable interactions. *Science*, **328** 729, 2010. 20, 176

[44] M. W. Zwierlein, A. Schirotzek, C. H. Schunck, and W. Ketterle. Fermionic superfluidity with imbalanced spin populations. *Science*, **311** 492, 2006. 20

[45] G. B. Partridge, W. Li, R. I. Kamar, Y. Liao, and Hulet R. G. Pairing and phase separation in a polarized Fermi gas. *Science*, **311** 503, 2006. 20

[46] P. Fulde and R. A. Ferrell. Superconductivity in a strong spin-exchange field. *Phys. Rev.*, **135** A550, 1964. 20

[47] A. I. Larkin and Y. N. Ovchinnikov. Inhomogeneous state of superconductors. *Sov. Phys. JETP*, **20** 762, 1965. 20

[48] W. Vincent Liu and Frank Wilczek. Interior gap superfluidity. *Phys. Rev. Lett.*, **90** 047002, 2003. 20

[49] D. S. Petrov, G. E. Astrakharchik, D. J. Papoular, C. Salomon, and G. V. Shlyapnikov. Crystalline phase of strongly interacting Fermi mixtures. *Phys. Rev. Lett.*, **99** 130407, 2007. 20

[50] U. Gavish and Y. Castin. Matter-wave localization in disordered cold atom lattices. *Phys. Rev. Lett.*, **95** 020401, 2005. 20

[51] Y. Nishida and S. Tan. Universal Fermi gases in mixed dimensions. *Phys. Rev. Lett.*, **101** 170401, 2008. 20, 176

[52] J. Deiglmayr, A. Grochola, M. Repp, K. Mörtlbauer, C. Glück, J. Lange, O. Dulieu, R. Wester, and M. Weidemüller. Formation of ultracold polar molecules in the rovibrational ground state. *Phys. Rev. Lett.*, **101** 133004, 2008. 20

[53] K.-K. Ni, S. Ospelkaus, M. H. G. de Miranda, A. Pe'er, B. Neyenhuis, J. J. Zirbel, S. Kotochigova, P. S. Julienne, D. S. Jin, and J. Ye. A high phase-space-density gas of polar molecules. *Science*, **322** 231, 2008. 20

[54] M. Aymar and O. Dulieu. Calculation of accurate permanent dipole moments of the lowest $^{1,3}\sigma^+$ states of heteronuclear alkali dimers using extended basis sets. *J. Chem. Phys.*, **122** 204302, 2005. 21, 85

[55] M. Taglieber, A.-C. Voigt, F. Henkel, S. Fray, T. W. Hänsch, and K. Dieckmann. Simultaneous magneto-optical trapping of three atomic species. *Phys. Rev. A*, **73** 011402, 2006. 21, 25, 111

[56] T. Tiecke. *PhD thesis.* University of Amsterdam, 2009. 21, 25, 34, 54, 93, 97, 109, 111, 115

[57] F. M. Spiegelhalder, A. Trenkwalder, D. Naik, G. Kerner, E. Wille, G. Hendl, F. Schreck, and R. Grimm. All-optical production of a degenerate mixture of ^{6}Li and ^{40}K and creation of heteronuclear molecules. *Phys. Rev. A*, **81** 043637, 2010. 21, 25, 111

[58] C.-H. Wu, I. Santiago, J. W. Park, P. Ahmadi, and M. W. Zwierlein. Strongly interacting isotopic Bose-Fermi mixture immersed in a Fermi sea. *arXiv:1103.4630v1*, 2011. 21, 25, 111

[59] M. Taglieber, A.-C. Voigt, T. Aoki, T. W. Hänsch, and K. Dieckmann. Quantum degenerate two-species Fermi-fermi mixture coexisting with a Bose-Einstein condensate. *Phys. Rev. Lett.*, **100** 010401, 2008. 21

[60] E. Wille, F. M. Spiegelhalder, G. Kerner, D. Naik, A. Trenkwalder, G. Hendl, F. Schreck, R. Grimm, T. G. Tiecke, J. T. M. Walraven, S. J. J. M. F. Kokkelmans, E. Tiesinga, and P. S. Julienne. Exploring an ultracold Fermi-Fermi mixture: Interspecies Feshbach resonances and scattering properties of ^{6}Li and ^{40}K. *Phys. Rev. Lett.*, **100** 053201, 2008. 21, 85, 115

[61] T. G. Tiecke, M. R. Goosen, A. Ludewig, S. D. Gensemer, S. Kraft, S. J. J. M. F. Kokkelmans, and J. T. M. Walraven. Broad Feshbach resonance in the ^{6}Li-^{40}K mixture. *Phys. Rev. Lett.*, **104** 053202, 2010. 21, 115

[62] A.-C. Voigt, M. Taglieber, L. Costa, T. Aoki, W. Wieser, T. W. Hänsch, and K. Dieckmann. Ultracold heteronuclear Fermi-Fermi molecules. *Phys. Rev. Lett.*, **102** 020405, 2009. 21, 85

[63] A. Trenkwalder, C. Kohstall, M. Zaccanti, D. Naik, A. I. Sidorov, F. Schreck, and R. Grimm. Hydrodynamic expansion of a strongly interacting Fermi-Fermi mixture. *Phys. Rev. Lett.*, **106** 115304, 2011. 21

[64] J. H. Moore, C. C. Davis, and Coplan M. A. *Building scientific apparatus.* Westview Press, 2002. 28

[65] F. Schreck. *PhD thesis.* École Normale Supérieure, Paris, 2002. 30, 36, 97

[66] S. Falke, E. Tiemann, C. Lisdat, H. Schnatz, and G. Grosche. Transition frequencies of the D lines of ^{39}K, ^{40}K, and ^{41}K measured with a femtosecond laser frequency comb. *Phys. Rev. A*, **74** 032503, 2006. 30

[67] E. A. Donley, T. P. Heavner, F. Levi, M. O. Tataw, and S. R. Jefferts. Double-pass acousto-optic modulator system. *Review of Scientific Instruments*, **76** 063112, 2005. 31

[68] R. A. Nyman, G. Varoquaux, B. Villier, D. Sacchet, F. Moron, Y. Le Coq, A. Aspect, and P. Bouyer. Tapered-amplified antireflexion-coated laser diodes for potassium and rubidium atomic-physics experiments. *Review of Scientific Instruments*, **77** 033105, 2006. 33, 35

[69] M. E. Gehm. *PhD thesis.* Duke University, 2003. 34, 51

[70] K. A. Yakimovich and A. G. Mozgovoi. Experimental investigation of the density and surface tension of molten lithium at temperatures up to 1300 K. *High Temp.*, **38** 657, 2000. 34, 47

[71] G. Ferrari, M.-O. Mewes, F. Schreck, and C. Salomon. High-power multiple-frequency narrow-linewidth laser source based on a semiconductor tapered amplifier. *Opt. Lett.*, **24** 151, 1999. 35, 36

[72] W. D. Phillips and H. Metcalf. Laser deceleration of an atomic beam. *Phys. Rev. Lett.*, **48** 596, 1982. 36, 39

[73] F. Greiner, R. Kaiser, M. Marchand, and T. Salez. *Petits problèmes de physique: du quotidien au laboratoire.* Dunod, 2011. 38, 46, 62, 64

[74] W. Ertmer, R. Blatt, J. L. Hall, and M. Zhu. Laser manipulation of atomic beam velocities: Demonstration of stopped atoms and velocity reversal. *Phys. Rev. Lett.*, **54** 996, 1985. 39

[75] H. L. Bethlem, G. Berden, and G. Meijer. Decelerating neutral dipolar molecules. *Phys. Rev. Lett.*, **83** 1558, 1999. 39

[76] H. J. Metcalf and P. van der Straten. *Laser cooling and trapping.* Springer, 1999. 41, 44, 63

[77] C. Salomon and J. Dalibard. La température limite d'un jet atomique de césium ralenti par diode laser. *C.R. Acad. Sci.*, **306** 1319, 1988. 41

[78] C. B. Alcock, V. P. Itkin, and M. K. Horrigan. Vapour pressure equations for the metallic elements: 298-2500K. *Can. Metall. Q.*, **23** 309, 1984. 46, 47

[79] A. Ridinger, S. Chaudhuri, T. Salez, U. Eismann, D. R. Fernandes, K. Magalhães, D. Wilkowski, C. Salomon, and F. Chevy. Large atom number dual-species magneto-optical trap for fermionic ^{6}Li and ^{40}K atoms. *Eur. Phys. J. D*, **DOI**: 10.1140/epjd/e2011-20069-4, 2011. 46, 61

[80] K. Dieckmann, R. J. C. Spreeuw, M. Weidemüller, and J. T. M. Walraven. Two-dimensional magneto-optical trap as a source of slow atoms. *Phys. Rev. A*, **58** 3891, 1998. 52, 53

[81] Saptarishi Chaudhuri, Sanjukta Roy, and C. S. Unnikrishnan. Realization of an intense cold Rb atomic beam based on a two-dimensional magneto-optical trap: Experiments and comparison with simulations. *Phys. Rev. A*, **74** 023406, 2006. 52

[82] A. Ridinger. *PhD thesis.* École Normale Supérieure, Paris, 2011. 54, 57, 85, 91

[83] A. Ridinger, S. Chaudhuri, T. Salez, D. R. Fernandes, N. Bouloufa, O. Dulieu, C. Salomon, and F. Chevy. Photoassociative creation of ultracold heteronuclear ^{6}Li-^{40}K* molecules. *Euro. Phys. Lett.*, **96** 33001, 2011. 61, 85

[84] N. Masuhara, J. M. Doyle, J. C. Sandberg, D. Kleppner, T. J. Greytak, H. F. Hess, and G. P. Kochanski. Evaporative cooling of spin-polarized atomic hydrogen. *Phys. Rev. Lett.*, **61** 935, 1988. 62

[85] M. S. Santos, P. Nussenzveig, L. G. Marcassa, K. Helmerson, J. Flemming, S. C. Zilio, and V. S. Bagnato. Simultaneous trapping of two different atomic species in a vapor-cell magneto-optical trap. *Phys. Rev. A*, **52** R4340, 1995. 62

[86] J. P. Gordon and A. Ashkin. Motion of atoms in a radiation trap. *Phys. Rev. A*, **21** 1606, 1980. 65, 111

[87] J. Dalibard and C. Cohen-Tannoudji. Laser cooling below the Doppler limit by polarization gradients: simple theoretical models. *J. Opt. Soc. Am. B*, **6** 2023, 1989. 66

[88] M. Drewsen, Ph. Laurent, A. Nadir, G. Santarelli, A. Clairon, Y. Castin, D. Grison, and C. Salomon. Investigation of sub-Doppler cooling effects in a cesium magneto-optical trap. *App. Phys. B*, **59** 283, 1994. 66

[89] M. Landini, S. Roy, L. Carcagní, D. Trypogeorgos, M. Fattori, M. Inguscio, and G. Modugno. Sub-Doppler laser cooling of potassium atoms. *arXiv: 1107.2337v1*, 2011. 66, 74

[90] T. Walker, D. Sesko, and C. Wieman. Collective behavior of optically trapped neutral atoms. *Phys. Rev. Lett.*, **64** 408, 1990. 66

[91] G. Labeyrie, F. Michaud, and R. Kaiser. Self-sustained oscillation in a large cloud of cold atom. *Phys. Rev. Lett.*, **96** 023003, 2006. 66

[92] C. G. Townsend, N. H. Edwards, C. J. Cooper, K. P. Zetie, C. J. Foot, A. M. Steane, Szriftgiser P., H. Perrin, and J. Dalibard. Phase-space density in the magneto-optical trap. *Phys. Rev. A*, **52** 1423, 1995. 67

[93] M. Teichman. *PhD thesis.* École Normale Supérieure, Paris, 2007. 69

[94] D. C. McKay, D. Jervis, D. J. Fine, J. W. Simpson-Porco, G. J. A. Edge, and J. H. Thywissen. Low-temperature, high-density magneto-optical trapping of potassium using the open 4S → 5P transition at 405 nm. *arXiv:1110.4067v1*, 2011. 74

[95] A. Reed. *PhD thesis.* Ohio State University, 2011. 74

[96] P. M. Duarte, R. A. Hart, J. M. Hitchcock, T. A. Corcovilos, T. L. Yang, A. Reed, and R. G. Hulet. All-optical production of a lithium quantum gas using narrow-line laser cooling. *arXiv:1109.6635v1*, 2011. 74

[97] V. Gokhroo, G. Rajalakshmi, R. Kollengode Easwaran, and C. S. Unnikrishnan. Sub-Doppler deep-cooled bosonic and fermionic isotopes of potassium in a compact $2D^+$-3D MOT set-up. *J. Phys. B: At. Mol. Opt. Phys.*, **44** 115307, 2011. 74

[98] W. Ketterle, K. B. Davis, M. A. Joffe, A. Martin, and D. E. Pritchard. High densities of cold atoms in a dark spontaneous-force optical trap. *Phys. Rev. Lett.*, **70** 2253, 1993. 81

[99] P. D. Lett, K. Helmerson, W. D. Phillips, L. P. Ratliff, S. L. Rolston, and M. E. Wagshul. Spectroscopy of Na_2 by photoassociation of laser-cooled Na. *Phys. Rev. Lett.*, **71** 2200, 1993. 83

[100] P. D. Lett, P. S. Julienne, and W. D. Phillips. Photoassociative spectroscopy of laser-cooled atoms. *Annu. Rev. Phys. Chem.*, **46** 423, 1995. 83

[101] U. Schlöder, C. Silber, T. Deuschle, and C. Zimmermann. Saturation in heteronuclear photoassociation of $^6Li^7Li$. *Phys. Rev. A*, **66** 061403, 2002. 85

[102] O. Dulieu and C. Gabbanini. The formation and interactions of cold and ultracold molecules: new challenges for interdisciplinary physics. *Rep. Prog. Phys.*, **72** 086401, 2009. 85

[103] E. R. I. Abraham, W. I. McAlexander, C. A. Sackett, and R. G. Hulet. Spectroscopic determination of the s-wave scattering length of lithium. *Phys. Rev. Lett.*, **74** 1315, 1995. 85

[104] J. R. Leroy and R. B. Bernstein. Dissociation energy and long-range potential of diatomic molecules from vibrational spacings of higher levels. *J. Chem. Phys.*, **52** 3869, 1970. 88

[105] H Wang, P. L. Gould, and W. C. Stwalley. Photoassociative spectroscopy of ultracold ^{39}K atoms in a high-density vapor-cell magneto-optical trap. *Phys. Rev. A*, **53** R1216, 1996. 90

[106] H. Wang, J. Li, X. T. Wang, C. J. Williams, P. L. Gould, and W. C. Stwalley. Precise determination of the dipole matrix element and radiative lifetime of the ^{39}K $4p$ state by photoassociative spectroscopy. *Phys. Rev. A*, **55** R1569, 1997. 90, 92, 175

[107] P. S. Julienne and J. Vigué. Cold collisions of ground- and excited- state alkali-metal atoms. *Phys. Rev. A*, **44** 4464, 1991. 90

[108] Béatrice Bussery, Yamina Achkar, and Monique Aubert-Frécon. Long-range molecular states dissociating to the three of four lowest asymptotes for the ten heteronuclear diatomic alkali molecules. *Chem. Phys.*, **116** 319, 1987. 91

[109] S. Chu, J. E. Bjorkholm, A. Ashkin, and A. Cable. Experimental observation of optically trapped atoms. *Phys. Rev. Lett.*, **57** 314, 1986. 93, 111

[110] C. J. Foot. *Atomic physics.* Oxford University Press, 2005. 94

[111] A. L. Migdall, J. V. Prodan, W. D. Phillips, T. H. Bergeman, and Metcalf H. J. First observation of magnetically trapped neutral atoms. *Phys. Rev. Lett.*, **54** 2596, 1985. 95

[112] G. Breit and I. I. Rabi. Measurement of nuclear spin. *Phys. Rev.*, **38** 2082, 1931. 95, 96

[113] W. Petrich, M. H. Anderson, J. R. Ensher, and E. A. Cornell. A stable tightly confining magnetic trap for evaporative cooling of neutral atoms. *Phys. Rev. Lett.*, **74** 3352, 1995. 97, 109

[114] B. de Marco. *PhD thesis.* JILA, 2001. 98

[115] M.-O. J. Mewes, G. Ferrari, F. Schreck, A. Sinatra, and C. Salomon. Simultaneous magneto-optical trapping of two lithium isotopes. *Phys. Rev. A*, **61** 011403(R), 1999. 99

[116] B. De Marco, J. L. Bohn, J. P. Burke, Jr., M. Holland, and D. S. Jin. Measurement of p-wave threshold law using evaporatively cooled fermionic atoms. *Phys. Rev. Lett.*, **82** 4208, 1999. 106, 110, 118, 167, 175

[117] J. E. Bjorkholm. Collision-limited lifetimes of atom traps. *Phys. Rev. A*, **38** 1599, 1988. 108

[118] D. E. Pritchard. Cooling neutral atoms in a magnetic trap for precision spectroscopy. *Phys. Rev. Lett.*, **51** 1336, 1983. 109

[119] M. Heo, J. Choi, and Y.-I. Shin. Fast production of large ^{23}Na Bose-Einstein condensates in an optically plugged magnetic quadrupole trap. *Phys. Rev. A*, **83** 013622, 2011. 110

[120] W. Ketterle and M. Zwierlein. Making, probing and understanding ultracold Fermi gases. In M. Inguscio, W. Ketterle, and C. Salomon, editors, *Proceedings of the International School of Physics Enrico Fermi on Ultracold Fermi Gases*, 2006. 110, 168

[121] S. Falke, H. Knöckel, J. Friebe, M. Riedmann, E. Tiemann, and C. Lisdat. Potassium ground-state scattering parameters and Born-Oppenheimer potentials from molecular spectroscopy. *Phys. Rev. A*, **78** 012503, 2008. 110

[122] E. Tiemann, H. Knöckel, P. Kowalczyk, W. Jastrzebski, A. Pashov, H. Salami, and A. J. Ross. Coupled system $a\,^3\sigma^+$ and $x\,^1\sigma^+$ of KLi: Feshbach resonances and corrections to the Born-Oppenheimer approximation. *Phys. Rev. A*, **79** 042716, 2009. 110, 172

[123] R. Grimm, M. Weidemüller, and Y. B. Ovchinnikov. Optical dipole traps for neutral atoms. *Advances In Atomic, Molecular, and Optical Physics*, **42** 95, 2008. 111, 112, 113

[124] S. Friebel, C. D'Andrea, J. Walz, M. Weitz, and T. W. Hänsch. CO2-laser optical lattice with cold rubidium atoms. *Phys. Rev. A*, **57** R20, 1998. 111

[125] W. H. Wright, G. J. Sonek, and M. W. Berns. Radiation trapping forces on microspheres with optical tweezers. *App. Phys. Lett*, **63** 715, 1993. 111

[126] E. A. Abbondanzieri, W. J. Greenleaf, J. W. Shaevitz, R. Landick, and S. M. Block. Direct observation of base-pair stepping by RNA polymerase. *Nature*, **438** 460, 2005. 111

[127] J. Dalibard and C. Cohen-Tannoudji. Dressed-atom approach to atomic motion in laser light: the dipole force revisited. *J. Opt. Soc. Am. B*, **2** 1707, 1985. 111

[128] A. Ashkin, J. M. Dziedzic, J. E. Bjorkholm, and S. Chu. Observation of a single-beam gradient force optical trap for dielectric particles. *Opt. Lett.*, **11** 288, 1986. 111

[129] R.J. Cook and R.K. Hill. An electromagnetic mirror for neutral atoms. *Opt. Commun.*, **43** 258, 1982. 111

[130] R. Ozeri, L. Khaykovich, and N. Davidson. Long spin relaxation times in a single-beam blue-detuned optical trap. *Phys. Rev. A*, **59** 1750, 1998. 111

[131] T. A. Savard, K. M. O'Hara, and J. E. Thomas. Laser-noise-induced heating in far-off resonance optical traps. *Phys. Rev. A*, **56** R1095, 1997. 113

[132] M. E. Gehm, K. M. O'Hara, T. A. Savard, and J. E. Thomas. Dynamics of noise-induced heating in atom traps. *Phys. Rev. A*, **58** 3914, 1998. 113

[133] M. E. Gehm, K. M. O'Hara, T. A. Savard, and J. E. Thomas. Erratum: Dynamics of noise-induced heating in atom traps [Phys. Rev. A 58, 3914 (1998)]. *Phys. Rev. A*, **61** 029902(E), 2000. 113

[134] W. S. Bakr, J. I. Gillen, A. Peng, S. Fölling, and M. Greiner. A quantum gas microscope for detecting single atoms in a Hubbard-regime optical lattice. *Nature*, **462** 74, 2009. 116

[135] C. Weitenberg, M. Endres, J. F. Sherson, M. Cheneau, P. Schauß, T. Fukuhara, I. Bloch, and S. Kuhr. Single-spin addressing in an atomic Mott insulator. *Nature*, **471** 319, 2011. 116

[136] A. M. Mazouchi. *Internship report : Feasibility of Single Atom Imaging in an Optical Lattice.* University of Toronto, 2007. 116

[137] M. Greiner, I Bloch, T. W. Hänsch, and T. Esslinger. Magnetic transport of trapped cold atoms over a large distance. *Phys. Rev. A*, **63** 031401, 2001. 119, 122

[138] H. J. Lewandowski, D. M. Harber, D. L. Whitaker, and E. A. Cornell. Simplified system for creating a Bose-Einstein condensate. *J. Low. Temp. Phys.*, **132** 309, 2003. 119

[139] B. Battelier. *PhD thesis.* École Normale Supérieure, Paris, 2007. 120

[140] T. Salez. *Internship report : Manipulations d'un mélange Li-K ultra-froid.* École Normale Supérieure, Paris, 2007. 135, 137, 162

[141] C. Cohen-Tannoudji. *Cours du Collège de France.* 2006-2007. 168, 172

Towards quantum degenerate atomic Fermi mixtures

Thomas SALEZ

During my PhD, I participated in the full setup from scratch of an experiment that aims at cooling down and manipulating two fermionic alkaline atomic species, ^6Li *and* ^{40}K. *Our goal is to study ultracold Fermi mixtures with mass imbalance, and to realize a flexible quantum analog simulator. In fact, for certain quantum many-body problems, such as high critical temperature superconductivity and frustrated anti-ferromagnetism, there is neither complete analytical nor numerical solution. Therefore, cold atoms systems, due to their purity and their high degree of tunability, even on their interaction itself, offer an interesting complementary point of view in the study of those phenomena.*

As far as the experimental setup is concerned, we built an ultra-high vacuum system, a complete and stable laser source for each species, as well as two performing atomic sources, a ^6Li *Zeeman slower and a* ^{40}K *bidimensionnal magneto-optical trap; most of the optical and electrical quantities, as well as the imaging diagnostics, being computer controlled. Once those preliminary steps have been performed and optimized, we could obtain an efficient double magneto-optical trap, containing typically* 5×10^9 *atoms of* ^6Li *and* 8×10^9 *atoms of* ^{40}K. *In this configuration, we produced the first* $^6Li^{40}K^*$ *heteronuclear molecules by photoassociation, for which we identified 70 rovibrational lines.*

In a second part, I describe in detail the magnetic transport of the atomic mixture, between the magneto-optical trap chamber and a science cell, located in an ultra-high vacuum region with large optical access. The complete setup, from its design to its experimental implementation and optimization, as well as the development of the program and the useful numerical diagnostics, are the heart of my work. The transport efficiency could be tested and optimized, allowing for an efficient transfer of the mixture in the science cell.

Thus, after this thesis, all the experimental tools are operational in order to allow for evaporative cooling of the mixture in an optically plugged magnetic trap. Therefore, the field is open for quantum simulation and understanding of many-body problems in ultracold Fermi mixtures.